

# THESE DE DOCTORAT DE

L'UNIVERSITE DE NANTES  
COMUE UNIVERSITE BRETAGNE LOIRE

ECOLE DOCTORALE N° 602  
*Sciences pour l'Ingénieur*  
Spécialité : Thermique

Par

**Taleb GHAMLOUCH**

**Analysis of convective transfer around simple molds inside a model autoclave**

**Analyse des transferts convectifs autour de moules simples dans un autoclave modèle**

Thèse présentée et soutenue à Polytech Nantes, le 20 avril 2018

Unité de recherche :LTEN UMR CNRS 6607

Thèse N° :

## Composition du Jury :

**Béatrice PATTE-ROULAND** (rapporteur)  
**Adrien TOUTANT** (rapporteur)

Professeur  
Maître de conférences (HDR)

Université de Rouen  
Université de Perpignan Via Domitia

**Dominique GOBIN** (Président du Jury)  
**Patrick GLOUANNEC**  
**Gildas LALIZEL**  
**Stéphane ROUX** (co-encadrant)

Directeur de recherche émérite  
Professeur  
Maître de conférences  
Maître de conférences

CentraleSupélec – Université Paris-Saclay  
Université de Bretagne Sud  
ISAE - ENSMA  
Université de Nantes

Directeur de thèse  
**Vincent SOBOTKA**

Professeur

Université de Nantes

Co-directeur de thèse  
**Jean-Luc BAILLEUL**

Professeur

Université de Nantes



# **Analyse des transferts convectifs autour de moules simples dans un autoclave modèle**

(Résumé du manuscrit de thèse en langue française)





## Table de matières

<b>1. INTRODUCTION .....</b>	<b>5</b>
<b>2. DIMENSIONNEMENT DU BANC D'ESSAIS .....</b>	<b>10</b>
2.1. Conception de l'autoclave modèle .....	10
2.2. Validation de l'autoclave modèle .....	14
2.3. Conception du moule et instrumentation thermique .....	16
2.3.1. Application de la similitude géométrique .....	16
2.3.2. Structure du moule et instrumentation thermique .....	16
2.4. Etude du multichargement .....	19
2.5. Etude d'un moule avec des supports .....	20
<b>3. MODELISATION NUMERIQUE DU MODELE AUTOCLAVE .....</b>	<b>21</b>
3.1. Etude monochargement .....	22
3.1.1. Modèle physique .....	22
3.1.2. Modèle numérique et conditions aux limites .....	22
3.2. Etude du multichargement .....	23
3.3. Etude du moule avec des supports .....	24
<b>4. RESULTATS ET DISCUSSION .....</b>	<b>25</b>
4.1. Etude du Monochargement .....	25
4.1.1. Etude de l'écoulement .....	25
4.1.2. Etude de la distribution des coefficients d'échange .....	28
4.2. Etude du multichargement .....	32
4.2.1. Etude de l'écoulement .....	33
4.2.2. Etude de la distribution des coefficients d'échange .....	36
4.3. Etude du moule avec des supports .....	38
<b>5. CONCLUSION ET PERSPECTIVES .....</b>	<b>42</b>
<b>LISTE DES RÉFÉRENCES .....</b>	<b>44</b>



## ***1. Introduction***

Ces dernières années, l'utilisation de matériaux composites légers et à hautes performances a considérablement augmenté dans de nombreux secteurs industriels, en raison de leurs propriétés mécaniques spécifiques supérieures à celles des métaux et des alliages conventionnels.

Cependant, et comme dans tout secteur industriel, une problématique majeure dans le domaine de la mise en forme des matériaux composites est la dualité entre l'optimisation de la qualité des pièces produites et la réduction des temps de cycle nécessaires à leur production.

Dans la filière aéronautique, la cuisson des pièces composites par autoclave est largement répandue. Cette technique permet la réalisation de pièces de grandes dimensions tout en minimisant les porosités résiduelles grâce à l'application d'un cycle de température associé à un cycle de pression.

Les autoclaves sont généralement des enceintes de forme cylindrique (cf. Figure 1) dans lesquelles circule un gaz sous pression et contrôlé en température. Ce cycle de pression et température (cf. Figure 2) permet de maîtriser le cycle de transformation, appelé classiquement cuisson, des pièces composites. Le cycle de température permet de contrôler la transformation du matériau (polymérisation dans le cas d'une résine thermodurcissable ou cristallisation dans le cas d'une matrice thermoplastique). Le cycle de pression permet d'éliminer la quasi-totalité des porosités qui peuvent être générées dans la pièce lors du procédé (présence de vapeur d'eau, dégazage des produits chimiques...). Les autoclaves conventionnels sont constitués principalement d'une section de travail centrale permettant le positionnement d'une ou plusieurs pièces composites placées dans des moules ouverts et d'un système assurant la circulation du gaz autour des pièces. Cet écoulement est assuré par un ventilateur radial situé à l'arrière de l'autoclave. Le gaz est acheminé, après avoir été chauffé par des résistances électriques, via un système de canalisation en périphérie de la section centrale. L'écoulement du gaz à travers la section de travail est principalement turbulent, ceci étant dû à la conception du système de circulation ainsi qu'aux géométries complexes et formes aérodynamiquement défavorables des moules supportant et les pièces composites [1–4].

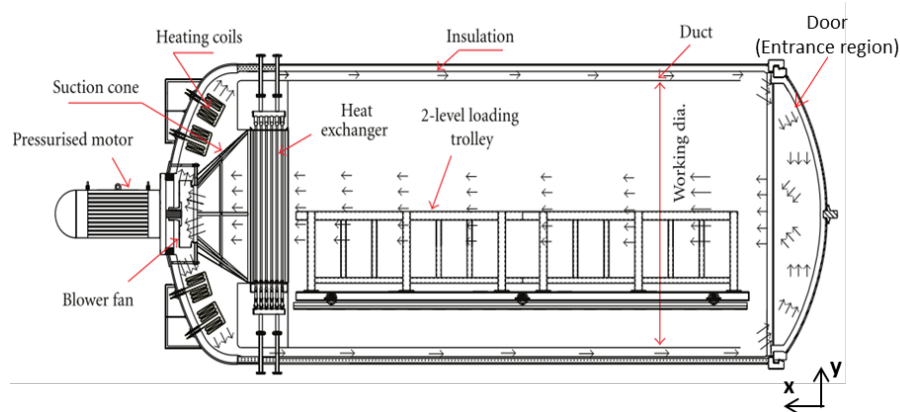


Figure 1 Schéma descriptif d'un système autoclave [5]

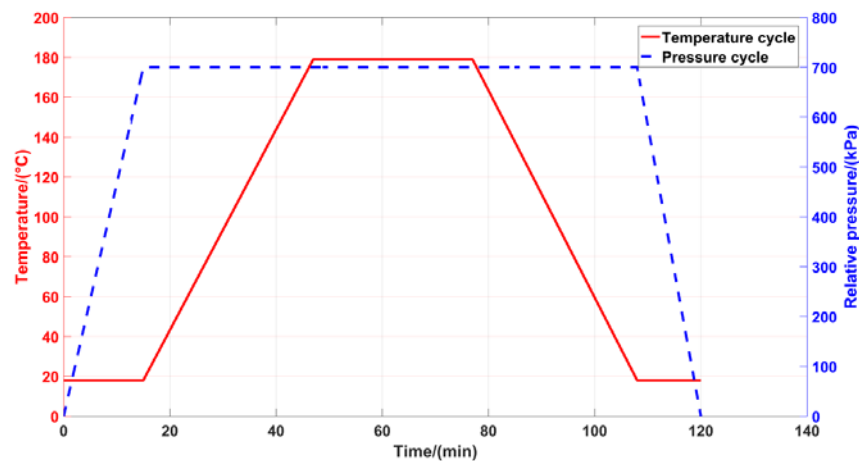


Figure 2 Cycle de cuisson typique dans un autoclave [2]

Comme dans tous les procédés de mise en forme, l'autoclave possède deux paramètres de contrôle : un mécanique et un thermique. C'est à travers le contrôle de ces deux leviers qu'il est possible d'optimiser les propriétés finales des pièces produites. Au niveau mécanique, l'usage d'une enceinte pressurisée permet le contrôle de la géométrie des pièces (la pièce composite est simplement recouverte d'une bâche puis mise sous vide), mais surtout elle permet d'éliminer la quasi-totalité des porosités et ainsi réduire les délaminages qui pourraient survenir pendant la mise en forme de ces pièces.

Au niveau thermique, la mise en forme de pièces composites met en jeu des phénomènes couplés, au sein de la pièce notamment à cause des transformations (polymérisation ou cristallisation) qui sont exothermiques et thermodépendantes. Il est évident que le contrôle du champ de température et notamment la minimisation des gradients, qu'ils soient surfaciques ou transverses, est indispensable à la bonne qualité des pièces [6,7]. Ce contrôle a pour but de garantir une transformation uniforme dans la pièce tout en conservant un temps de mise en forme raisonnable. Le non-respect de

cette condition peut conduire à différents défauts, dont le principal est le piégeage de contraintes résiduelles dans les pièces [8]. Toutefois la problématique est plus large car le contrôle du champ de température aux limites des pièces composites passe par le contrôle de la température au niveau du procédé. Il convient donc d'avoir une connaissance fine des transferts de chaleur dans l'environnement des pièces composites. En ce qui concerne les autoclaves, les transferts étant majoritairement convectifs entre la pièce composite et son environnement, il convient donc de connaître (voire d'optimiser) la distribution du coefficient d'échange autour de ces pièces.

La contribution des échanges radiatifs est également à envisager. Ceux-ci dépendent principalement de la conception de l'autoclave, notamment de la position des zones de chauffage dans l'enceinte. Selon les auteurs Monaghan *et al.* [4], pour les autoclaves conventionnels tels que ceux représentés sur la Figure 1, les résistances sont placées à l'extérieur de la section de travail et du système de canalisation du gaz. Le chauffage par rayonnement direct des éléments chauffants vers les moules ainsi que vers les parois de la section de travail est alors faible comparativement aux échanges convectifs.

Cette conclusion a été rapportée par de nombreux autres chercheurs [1,2,9] qui ont considéré la convection forcée comme la source de chaleur principale à l'intérieur d'un autoclave. De ce fait, l'étude du coefficient d'échange convectif a fait l'objet de différents travaux scientifiques [4,10,11] qui ont démontré la dépendance de ce coefficient à de nombreux paramètres. Parmi ces paramètres, on peut noter le cycle de pression, le cycle de température, l'allure et l'intensité du champ de vitesse dans l'autoclave et autour des moules [9,10,12,11].

Il ressort de ces études une forte dépendance à la pression des échanges de chaleur en raison de la densification du gaz. Ainsi, dans un autoclave, une augmentation de 0,5 MPa peut accroître d'un facteur 2,6 la valeur du coefficient d'échange. A contrario, il a été montré que ce coefficient est faiblement thermodépendant.

Au niveau de la distribution spatiale des coefficients d'échange convectifs dans l'autoclave, plusieurs études [2,4,11,13] ont mis en évidence les variations de ces coefficients selon l'axe longitudinal d'un autoclave. Ces variations sont principalement liées aux variations du champ de vitesse moyen et des niveaux de turbulence. Certaines études [1,13,14] montrent la présence de valeurs importantes des vitesses moyennes et turbulentes près de la zone d'entrée (porte) d'un autoclave (cf. Figure 1). Ce phénomène provient de la conception du système d'écoulement du gaz qui contribue à la formation de zones de recirculation et de séparation d'écoulement dans la zone d'entrée. Lorsque le gaz se déplace vers le ventilateur, l'écoulement ralentit et s'uniformise. Ce comportement conduit à des coefficients d'échange 1,3 à 3 fois plus

élevés proche de la porte d'un autoclave par rapport à ceux que l'on observe au fond de l'autoclave [10].

Weber *et al.* [10] ont étudié la variation du coefficient d'échange autour d'un moule parallélépipédique positionné sur un support et représentatif des conditions industrielles. Leur étude a montré une distribution non uniforme du coefficient d'échange entre les différentes surfaces du moule en raison de leur position face à la direction de l'écoulement (surface de stagnation, surface d'ombre, surface parallèle à la direction d'écoulement). Ils ont également montré que, dans le cas de plusieurs moules positionnés consécutivement dans l'enceinte, le coefficient d'échange autour du moule placé en avant était toujours plus élevé et plus important que celui observé sur les moules situés à l'arrière. Cela peut être attribué au phénomène de blocage [14] lorsque le moule avant bloque l'écoulement vers ceux qui sont placés derrière, créant ainsi des « effets d'ombre ».

Les travaux expérimentaux sur la mesure de l'écoulement à l'intérieur d'un autoclave restent limités en raison de la difficulté expérimentale d'instrumenter de tels appareils. Ghariban *et al.* [13] ont mesuré les vitesses et les intensités de turbulence locales le long de la direction de l'écoulement en utilisant, à différentes positions, un anémomètre à fil chaud. Les résultats de cette étude ont mis en évidence l'existence d'un écoulement complexe caractérisé par la présence de zones de séparation de l'écoulement près de la paroi de la région d'entrée. Ces zones de recirculation génèrent des niveaux de turbulence localement importants. Plus en aval, les intensités de turbulence diminuent et l'écoulement devient plus lent et plus uniforme. Olsson *et al.* [15] ont tenté de mesurer les profils de vitesse en amont d'un moule industriel situé dans un autoclave [16], en utilisant la technique PIV (Particle Image Velocimetry). Toutefois, les résultats exposés ont été jugés non pertinents et non suffisants pour l'analyse d'un écoulement autour d'un moule. Cela peut être dû à la configuration complexe de l'autoclave utilisé et dans lequel les mesures ont été effectuées.

Toutefois, quelques études expérimentales [2,4,10,11,13] ont été réalisées afin de mesurer la distribution du coefficient d'échange dans des autoclaves réels et autour des surfaces de moules. Ces mesures ont été effectuées à l'aide de calorimètres de différentes formes (plaque ou tige). Ces calorimètres ont été implantés à différents endroits à l'intérieur des autoclaves ou autour des surfaces des moules. Néanmoins, ces capteurs sont des instruments de mesure intrusifs. Ils peuvent modifier localement le champ de vitesse et donc la mesure du coefficient d'échange recherché.

En dehors de ces études expérimentales, peu des simulations numériques 3D de l'écoulement turbulent couplé avec les transferts de chaleur convectifs ont été effectués à l'échelle de l'autoclave. La principale raison est liée aux ressources de calcul requises pour de telles simulations. Zhang *et al.* [17] ainsi que Chen *et al.* [18] se sont appuyés sur des simulations en dynamique des fluides (CFD) simplifiées pour

prédire le champ de température dans un moule dans un autoclave. Weber *et al.* [10] ont proposé une méthode de calcul rapide et moins coûteuse pour simuler la réponse thermique d'un moule en ayant recours aux méthodes des éléments finis mécanique solide au lieu d'utiliser un code CFD.

D'autre part, quelques travaux [19,20] ont établi des corrélations empiriques pour l'estimation de la distribution du coefficient d'échange autour d'obstacles représentatifs de moules industriels. Néanmoins, alors que les corrélations empiriques existantes permettent l'estimation de coefficients d'échange pour des géométries simples (écoulement laminaire autour d'une plaque plane par exemple), la prédiction du coefficient d'échange est loin d'être triviale dès lors que la forme devient plus complexe. L'écoulement turbulent devient également complexe et non uniforme rendant inapplicable les corrélations existantes.

Ota [21] a réalisé une revue bibliographique sur de nombreuses études qui décrivent la structure de l'écoulement et les transferts de chaleur convectifs autour de différents obstacles représentatifs de ceux rencontrés sur des moules réels (face dirigée vers le bas, plaque plane épaisse, cylindre longitudinal...). Le long de ces obstacles, des zones de séparation et de recollement de la couche limite apparaissent.

La présence d'un tel écoulement caractérisé par des zones de séparation et de recollement de la couche limite a montré une influence forte sur les flux de chaleur convectif. Sparrow *et al.* [22] ont reporté que le coefficient d'échange atteint une valeur maximale en amont du point de recollement. D'autre part, d'autres travaux ont indiqué que le coefficient d'échange atteignait une valeur maximale au point de recollement [23] et une diminution au-delà.

Ota *et al.* [19] ont proposé une corrélation universelle pour l'estimation du coefficient d'échange convectif maximal. Ces auteurs [20] ont effectué des mesures des coefficients d'échange convectifs dans la zone de séparation et de recollement de la couche limite autour d'une plaque épaisse avec différentes formes de bord d'attaques. Leurs mesures permettent de développer une corrélation entre le coefficient d'échange convectif au point de recollement et le nombre de Reynolds indépendamment de la forme du bord d'attaque. La longueur de recollement de la couche limite a été utilisée comme la longueur caractéristique dans cette corrélation. Par ailleurs, des études ont montré que la moyenne des coefficients d'échange convectif sur toute la longueur d'une plaque épaisse est supérieure, d'environ 10-20%, à celle estimée par l'équation de Colburn pour une couche limite turbulente classique [20]. De plus, les valeurs du coefficient d'échange convectif local dans la zone de recollement de la couche limite sont supérieures de 30 à 50% à celles prédites par la formule de Colburn [23]. Ces taux de transfert de chaleur convectif relativement importants, par rapport à une couche limite turbulente classique, peuvent être dus aux taux de turbulence élevés dans la zone de recirculation [23].

Les résultats de l'étude bibliographique montrent la nécessité d'une caractérisation du coefficient d'échange autour des moules dans un autoclave. Néanmoins l'instrumentation des autoclaves industriels demeure très complexe, l'utilisation de moyens de calculs 3D très consommateurs en temps et ressources et le recours aux corrélations empiriques limité de par la complexité des formes et des écoulements à considérer.

Pour apporter des éléments de réponse à cette problématique, nous présentons dans nos travaux une approche consistant à effectuer des mesures expérimentales représentatives de celles rencontrées sur les autoclaves industriels mais en utilisant un «autoclave modèle» à échelle réduite. Cet autoclave modèle a été conçu et fabriqué en se basant sur des lois de similitude. Il permet de recréer les principaux phénomènes physiques rencontrés dans les autoclaves. En particulier l'écoulement turbulent et le transfert en convection forcée autour de moules représentatifs de cas industriels réels est abordé. Dans cette étude, des moules de formes rectangulaires (plaques épaisses) ont été utilisés. Divers chargements ont été testés.

L'un des avantages de notre configuration est la facilité d'utilisation des instruments de mesure non intrusifs et fiables tels que la technique PIV (Particle Image Velocimetry) pour la mesure des champs d'écoulement et la caméra infrarouge pour déterminer la distribution du coefficient d'échange.

Les résultats expérimentaux obtenus, aérodynamiques et thermiques, sont comparés aux résultats numériques issus des simulations réalisées sous le code RANS CFD ANSYS Fluent 16.0®. La simulation numérique permet de réaliser des études paramétriques couplées avec des algorithmes d'optimisation afin de maîtriser la distribution des coefficients d'échange thermique.

## ***2. Dimensionnement du banc d'essais***

### **2.1. Conception de l'autoclave modèle**

Un autoclave réel de forme cylindrique et dont le système de fonctionnement a été présenté dans la Figure 1, a été choisi pour servir de base à la conception de l'autoclave modèle.

La section de travail de l'autoclave à l'échelle réelle consiste en une enceinte cylindrique d'une longueur de 8 m pour un diamètre de 3 m. Le gaz (air) est pressurisé jusqu'à 7 bars et chauffé par des résistances électriques jusqu'à 180 °C. On considère que le moule installé à l'intérieur de l'autoclave est une plaque rectangulaire [10] de longueur 4 m, de largeur 2,3 m et d'épaisseur 0,13 m. La vitesse moyenne de l'air dans la section de travail de l'autoclave a été estimée à environ 3 m/s.



L'application de lois de similitude consiste à conserver les mêmes nombres adimensionnels entre l'autoclave modèle et celui à l'échelle réel, en nous plaçant dans le cas d'un écoulement gazeux incompressible dans un régime stationnaire, les nombres adimensionnels utiles pour cette étude sont le nombre de Reynolds ( $Re$ ), pour la similitude dynamique, les nombres de Prandtl ( $Pr$ ) et de Nusselt ( $Nu$ ) pour la similitude énergétique, et le coefficient d'échelle géométrique ( $k_l$ ) pour la similitude d'échelle.

Le coefficient d'échelle géométrique ( $k_l$ ) est choisi afin d'obtenir une section de travail de l'autoclave modèle compatible avec les systèmes de mesure et notamment le système PIV.  $k_l$  est ainsi fixé à 7,5. Il en résulte une section de travail de l'autoclave modèle de longueur 1,07 m et de diamètre de 0,4 m.

Cependant, il a été décidé de transformer la section de travail cylindrique obtenue, en une section de travail de forme rectangulaire, car elle est utile et pratique pour l'installation des moules et pour la réalisation des essais expérimentaux. Cette décision est justifiée par le fait que le champ d'écoulement autour d'un moule à l'intérieur d'un autoclave est considéré comme un écoulement externe [13]. Ainsi, le champ d'écoulement de l'air n'est pas influencé par la forme de la section de travail. En conséquence, la section de travail de l'autoclave modèle a été conçue comme une veine de section rectangulaire de 0,4 m de haut et de 0,315 m de large.

Compte-tenu des contraintes techniques liées à l'utilisation d'air pressurisé et chauffé dans l'autoclave modèle, la solution retenue pour notre étude est celle d'un moule chauffant échangeant avec de l'air circulant à température et pression ambiante. Cette décision a été justifiée par le fait qu'il a été montré [9,10,12,11] que la température de l'air a des effets négligeables sur les coefficients d'échange convectif. D'autre part, le fait que les transferts de chaleur convectifs dans un autoclave soient purement forcés, en dehors des zones mortes, suggère que la température du moule affecte peu les valeurs du coefficient d'échange convectif. On peut donc découpler les phénomènes de transferts de masse des phénomènes de transferts de chaleur. Afin de conserver la température constante dans la veine, un échangeur de chaleur, contrôlé par un régulateur PID, a été dimensionné et installé. Il évacue la charge thermique générée par le moteur du ventilateur et les moules chauffants.

En ce qui concerne la pression importante du gaz dans un autoclave réel, qui entraîne une augmentation du nombre de Reynolds autour des moules, cet effet a été pris en compte en augmentant la vitesse de l'air dans la section de travail de l'autoclave modèle. Ceci peut être observé par les résultats de similitude dynamique montrés et exposés ci-après.

Concernant la similitude dynamique, le nombre de Reynolds caractérisant l'écoulement dans l'autoclave réel a été calculé en se basant sur la longueur du moule

industriel ( $l = 4$  m), la vitesse moyenne de l'air dans la section de travail ( $U_{\infty} = 3$  m/s) et les propriétés de l'air à la pression et à la température spécifiées ci-dessous ( $\nu = 4,6 \times 10^{-6}$  m<sup>2</sup>/s) [24] (cf. Tableau 1). Nous obtenons ainsi  $Re = 2,6 \times 10^6$ . La conservation de la valeur de ce nombre dans l'autoclave modèle est représentée par l'Equation (1).

$$Re_{\text{autoclave modèle}} = Re_{\text{autoclave réel}}$$

Équation (1)

$$U_{\infty \text{ autoclave modèle}} = U_{\infty \text{ autoclave réel}} \frac{1}{k_l} \frac{\nu_m}{\nu_p}$$

L'application de l'Equation (1) résulte en une vitesse  $U_{\infty \text{ autoclave modèle}}$  importante et elle conduit donc à des débits volumiques supérieurs à ceux qui peuvent être obtenus avec des ventilateurs du commerce. Nous nous sommes donc contentés d'un ventilateur permettant de conserver le même ordre de grandeur du nombre de Reynolds soit  $Re_{\text{autoclave modèle}} = 1,1 \times 10^6$ . La vitesse correspondante dans la veine est alors égale à 33,7 m/s. Les résultats des similitudes dynamique et énergétique sont présentés dans le Tableau 1. Le respect des nombres adimensionnels  $Re$  et  $Pr$  implique automatiquement le respect du nombre de Nusselt ( $Nu$ ).

Tableau 1 Calcul des  $Re$  et  $Pr$  dans l'autoclave réel et l'autoclave modèle

	$T$ (°C)	$P$ (kPa)	$\nu$ (m <sup>2</sup> /s)	$l_{\text{moule}}$ (m)	$U_{\infty}$ (m/s)	$Re$	$Pr$	$\dot{Q}$ (m <sup>3</sup> /h)
<b>Autoclave Scholtz [16]</b>	180	700	$4,6 \times 10^{-6}$	4	3	$2,6 \times 10^6$	0.70	76 000
<b>Autoclave modèle</b>	20	100	$1,5 \times 10^{-5}$	0.51	33.7	$1,1 \times 10^6$	0.71	15 290

Un des objectifs de nos travaux est la confrontation des résultats numériques et expérimentaux pour les champs de vitesse et de température dans la veine d'essai et notamment autour des moules.

Pour être pertinent, les conditions aux limites expérimentales doivent être bien contrôlées, en particulier la vitesse d'entrée ainsi que l'intensité de turbulence, et représentatives des conditions réelles. Un point crucial lors de la conception du banc expérimental a donc été l'obtention d'un profil de vitesse uniforme et stable à l'entrée de l'autoclave modèle.

L'obtention d'un tel écoulement implique l'installation d'une chambre de tranquillisation conçue selon les règles données dans [25,26] et équipée de nids d'abeille et de grilles métalliques afin de réduire les échelles de turbulence et les fluctuations dans l'écoulement. Les profils de vitesse seront ainsi plus stables et plus uniformes. Elle nécessite également l'installation d'un convergent soigneusement dimensionné en raison de son rôle critique pour la qualité de l'écoulement dans la zone d'entrée de la section d'étude [27]. Enfin, elle implique l'installation d'un divergent avec une géométrie conçue afin d'éviter les zones de recirculation [26,28]. Il

permet ainsi la récupération de la pression statique, et donc la réduction de la charge du ventilateur.

La prise en compte de l'ensemble de ces contraintes a conduit à la conception d'une soufflerie en boucle fermée, présentée sur la Figure 3. Celle-ci est constituée principalement d'un ventilateur (1), d'un échangeur de chaleur (2), d'une chambre de tranquillisation (3), d'un convergent (4), de la veine d'essais ou la section de travail (5) et d'un divergent (6).

La direction  $x$  représente l'axe longitudinal parallèle à la section de travail alors que les directions  $y$  et  $z$  représentent respectivement l'axe normal vertical et l'axe normal horizontal.

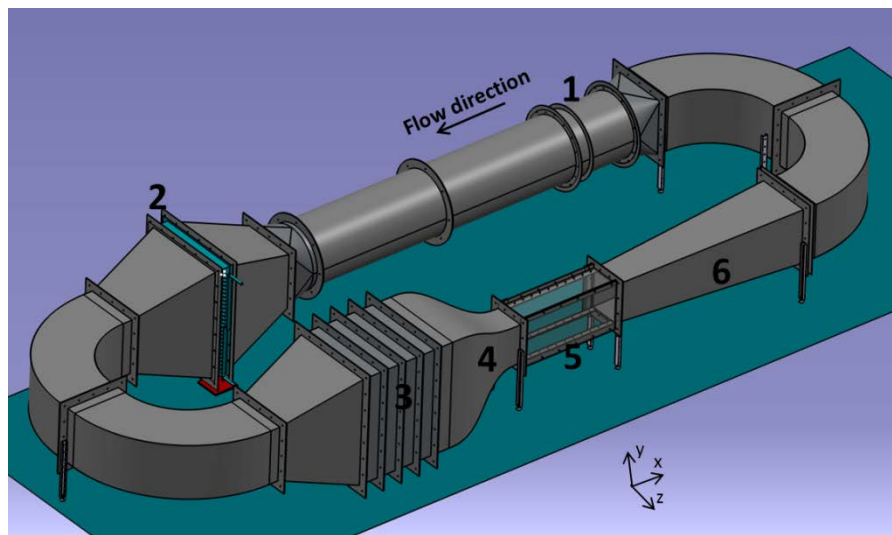


**Figure 3 Schéma de l'autoclave modèle**

Les pertes de charge ( $\Delta P$ ) dans l'autoclave modèle ont été estimées en utilisant les formules analytiques usuelles [29]. La connaissance des pertes de charge et du débit volumique nominal permet de dimensionner le ventilateur. Il convient de noter que le ventilateur est équipé d'un variateur de fréquence permettant d'atteindre différents débits dans la section de travail de l'autoclave modèle.

La Figure 4 montre l'autoclave modèle installé au laboratoire. La Figure 5 présente la veine d'essais. Remarquons que celle-ci est constituée de parois en plexiglas permettant de visualiser l'écoulement par la technique PIV. Les éléments constituant le système de mesure PIV sont visibles sur cette figure. Elle montre également un moule installé pour la réalisation des essais expérimentaux.



Figure 4 Photographie de l'autoclave modèle réalisé

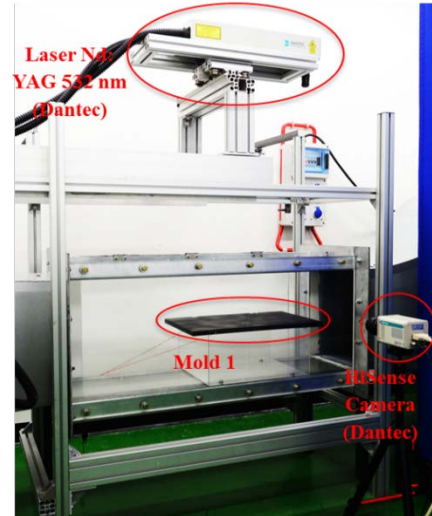


Figure 5 Photographie de la veine d'essais

## 2.2. Validation de l'autoclave modèle

La validation du banc d'essais a consisté à réaliser des mesures de profils de vitesse d'air à l'entrée de la section de travail vide en utilisant la technique PIV. L'objectif de ces mesures est de vérifier l'uniformité de l'écoulement dans la section de travail de l'autoclave modèle. Ces mesures permettent également la caractérisation de l'écoulement à l'entrée en termes de vitesse moyenne et d'intensité de turbulence. Ces valeurs serviront de conditions aux limites pour les simulations numériques CFD.

Les tests de validation ont été réalisés pour plusieurs débits (cf. Tableau 3), parmi lesquels le débit  $Q = 15\,290\text{ m}^3/\text{h}$  obtenu avec la condition de similitude dynamique (cf. Tableau 2). La chaîne PIV utilisée, de marque Dantec®, est constituée d'un laser Nd: YAG 532nm et d'une caméra HiSense ayant une résolution de  $(2048 \times 2048)\text{ px}^2$  et équipée d'un objectif de 50mm. Le laser et la caméra sont connectés à un ordinateur utilisé pour le contrôle du système et l'acquisition des images, via le logiciel DynamicStudio 3.41® fourni par Dantec®. L'ensemencement des particules dans l'écoulement a été réalisé par une machine à fumée générant un brouillard blanc dense par évaporation et condensation d'un liquide à base d'eau. La chaîne PIV utilisée permet la mesure de deux composantes du champ de vitesse. Le laser a été positionné sur un système mobile qui permet la mesure du champ de vitesse dans différentes zones de la section de travail. De plus, différents positionnements de la nappe laser permettent d'accéder séparément aux trois composantes du champ de vitesse. La zone de mesure se situe près de la zone d'entrée de la veine d'essais. Pour chaque configuration, 2 232 paires d'images sont acquises à une fréquence de 5.6 Hz. Les vitesses instantanées sont ensuite calculées par le logiciel d'acquisition puis post-

traitées afin de déduire les champs de vitesses statistiques (moyens et RMS). Ces champs statistiques sont ainsi utilisés pour déterminer les caractéristiques de l'écoulement à l'entrée. Le Tableau 2 rassemble les caractéristiques de l'écoulement à l'infini pour le débit  $Q = 15\,290\text{ m}^3/\text{h}$ .

**Tableau 2 Caractéristiques du champ d'écoulement à l'entrée de la section de travail de l'autoclave modèle**

Fréquence de rotation du moteur (Hz)	$U_\infty$ (m/s)	$V_\infty$ (m/s)	$W_\infty$ (m/s)	$u_{rms\infty}$ (m/s)	$v_{rms\infty}$ (m/s)	$w_{rms\infty}$ (m/s)	$Q$ (m <sup>3</sup> /h)
80	33,7 ±0,14	0 ±0,06	0 ±0,17	0,38 ±0,09	0	0	15 290 ±70

La faible valeur des incertitudes indique que le champ d'écoulement est uniforme à l'entrée de la section de travail. D'autre part, la comparaison entre les valeurs des trois composantes du champ de vitesse indique que l'air circule principalement le long de l'axe longitudinal de la section de travail et que l'écoulement est donc purement horizontal. La vitesse de l'air ( $U_\infty$ ) est alors égale à 33,7 m/s, ce qui correspond bien à la valeur souhaitée pour la similitude dynamique.

Les faibles valeurs des intensités de turbulence ( $u_{rms\infty}/U_\infty$ ), de l'ordre de 1%, montrent un écoulement stationnaire dans la section de travail.

L'ensemble de ces résultats indique que l'écoulement, à l'entrée de la section de travail, est uniforme et stationnaire en termes de direction, sens et d'amplitude. Ces résultats valident donc l'écoulement et la qualité de la conception de l'autoclave modèle.

D'autres débits ont également fait l'objet de mesures. Le Tableau 3 rassemble ces résultats qui présentent la même tendance.

**Tableau 3 Caractéristiques de l'écoulement à l'entrée de la section de travail pour différents débits**

Fréquence de rotation du moteur (Hz)	$U_\infty$ (m/s)	$u_{rms\infty} / U_\infty$ (%)	$Q$ (m <sup>3</sup> /h)
1.5	0,4 ±0,0	1,2 ±0,4	181 ±0,0
2	0,5 ±0,0	0,5 ±0,1	225 ±0,0
10	3,9 ±0,0	0,4 ±0,1	1 770 ± 5
30	12,3 ±0,0	0,8 ±0,1	5 580 ± 20
50	21 ±0,1	0,7 ±0,1	9 530 ± 30

## 2.3. Conception du moule et instrumentation thermique

### 2.3.1. Application de la similitude géométrique

Le même coefficient d'échelle  $k_l$  est appliqué sur le moule industriel réel présenté ci-dessus afin de dimensionner le moule à installer dans l'autoclave modèle. Le moule obtenu, est utilisé pour l'étude monochargement. Il s'agit d'une plaque rectangulaire épaisse d'une longueur de 0,51 m, d'une largeur de 0,315 m et d'une épaisseur de 0,017m. La Figure 6(a) représente le positionnement du moule dans la veine d'essais.

### 2.3.2. Structure du moule et instrumentation thermique

Afin d'estimer les coefficients d'échange convectifs, il est nécessaire de connaître le flux de chaleur échangé à la surface du moule. Comme expliqué précédemment (cf. section 2.1), l'air circulant dans la veine est maintenu à température ambiante alors qu'une source de chaleur est positionnée dans le moule.

La structure du moule est présentée sur la Figure 6(b). L'objectif est d'avoir un flux de chaleur monodimensionnel selon l'épaisseur de la plaque et évacué par la face supérieure. Le moule-plaque est ainsi constitué d'une plaque en acier inox d'épaisseur 3 mm chauffée en partie inférieure par un film résistif. Afin de minimiser les déperditions thermiques, une plaque de matériau isolant (Rohacell) de 8mm d'épaisseur est positionnée contre cette face inférieure. L'ensemble de ce système est maintenu dans un cadre de polyamide 66. Afin de quantifier les pertes thermiques par la surface inférieure du moule, il est instrumenté avec 10 thermocouples (cf. Figure 7).

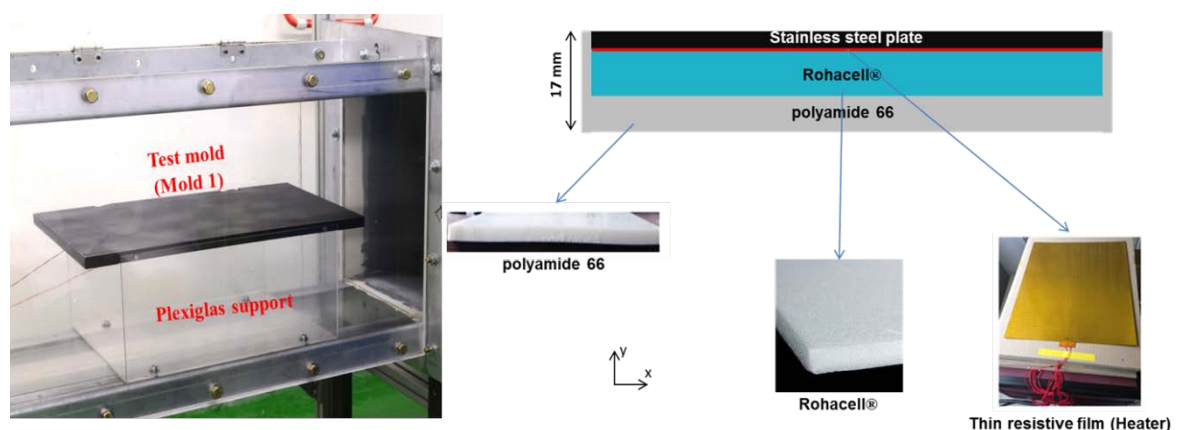


**Figure 6 (a) Photographie de l'installation du moule dans la section de travail. (b) Schéma descriptif de la structure des moules utilisés**

Une simulation numérique du moule a été réalisée. Elle montre que les transferts de chaleur dans la plaque isolante (Rohacell) peuvent être considérés unidirectionnels selon la direction de l'épaisseur de l'isolant (selon l'axe  $y$ ). Ce résultat a permis de



positionner les thermocouples de part et d'autre de la plaque isolante. La densité du flux de perte ( $\varphi_{lx}$ ) est estimée par la loi de Fourier pour les 5 positions  $x$  retenues (Equation 2). La densité flux de chaleur traversant la plaque d'acier inox ( $\varphi_{hx}$ ) est alors donnée par l'Equation 3 où  $HP$  représente la densité de flux dissipée au niveau du film résistif.

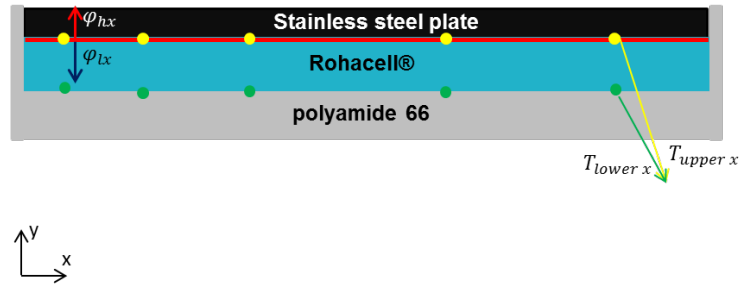


Figure 7 Schéma de l'installation des thermocouples dans le moule et des flux déduits

$$\varphi_{lx} = \left( \frac{\lambda_{Rohacell}}{e_{Rohacell}} \right) \cdot (T_{upper x} - T_{lower x}) \quad \text{Équation (2)}$$

$$\varphi_{hx} = HP - \varphi_{lx} \quad \text{Équation (3)}$$

Le problème 2D stationnaire à résoudre est alors représenté sur la Figure 8. En effet, la distribution de vitesse en surface de plaque va engendrer une distribution du coefficient d'échange conduisant à des transferts 2D dans la plaque en inox.

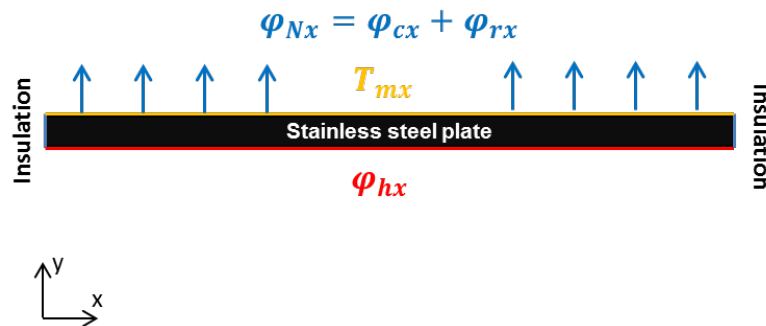


Figure 8 Schéma descriptif du modèle numérique de la plaque Inox

Ce problème est résolu à l'aide du code éléments finis Comsol®. Les mesures expérimentales, i.e. le profil de température ( $T_{mx}$ ) ainsi que le flux de chaleur local ( $\varphi_{hx}$ ), servent de conditions aux limites. La solution de l'équation de la chaleur résolue dans la plaque inox permet de déterminer la distribution du flux normal sur la surface supérieure de la plaque Inox ( $\varphi_{Nx}$ ).

Le flux échangé à la surface ( $\varphi_{Nx}$ ) est dissipé par convection ( $\varphi_{cx}$ ) et rayonnement ( $\varphi_{rx}$ ) avec l'environnement à la température  $T_{\infty}$ . Le flux radiatif est donné par :

$$\varphi_{rx}(x) = \varepsilon \cdot \sigma \cdot (T_{mx}^4(x) - T_{\infty}^4) \quad \text{Équation (4)}$$

Dans cette expression,  $T_{mx}$  représente la température de surface de la plaque,  $\sigma$  la constante de Stefan-Boltzmann ( $\sigma=5,67 \times 10^{-8} \text{ W}/(\text{m}^2 \cdot \text{K}^4)$ ) et  $\varepsilon$  l'émissivité de la peinture recouvrant la plaque en inox ( $\varepsilon = 0,89$ ).

La densité de flux convectif est alors donnée par :

$$\varphi_{cx} = \varphi_{Nx} - \varphi_{rx} \quad \text{Équation (5)}$$

Finalement, la distribution du coefficient d'échange convectif  $HTC$  est obtenue par :

$$HTC(x) = \frac{\varphi_{cx}(x)}{T_{mx}(x) - T_{\infty}} \quad \text{Équation (6)}$$

Afin de déterminer la distribution des coefficients  $HTC$  de manière précise, et étant donnée la linéarité de la relation entre la densité de flux convectif ( $\varphi_{cx}$ ) et la température de la surface ( $T_{mx}$ ), les tests ont été réalisés pour trois puissances de chauffage différentes ( $HP_1 = 714 \text{ W}/\text{m}^2$ ,  $HP_2 = 1110 \text{ W}/\text{m}^2$  et  $HP_3 = 1800 \text{ W}/\text{m}^2$ ).

Ces trois puissances permettent d'obtenir, pour chaque position  $x$ , trois valeurs différentes de température ( $T_{mx}$ ) associées aux trois valeurs différentes de densité de flux convectifs ( $\varphi_{cx}$ ). Ainsi, le coefficient d'échange convectif local ( $HTC$ ) est calculé pour chaque position  $x = x_i$  en utilisant la méthode de régression linéaire représenté par l'équation (7).

$$\begin{bmatrix} T_{1mx} \\ T_{2mx} \\ T_{3mx} \end{bmatrix}_{xi} = \frac{1}{HTC} \begin{bmatrix} \varphi_{1cx} \\ \varphi_{2cx} \\ \varphi_{3cx} \end{bmatrix}_{xi} + T_{\infty} \quad \text{Équation (7)}$$

Au niveau expérimental, le profil de température à la surface de la plaque acier ( $T_{mx}$ ) est mesuré grâce à une caméra infra-rouge (cf. Figure 9). Il est à noter que des fenêtres en silicium, transparentes à la longueur d'onde de la caméra ont dues être installées dans la veine d'essais pour permettre cette mesure.



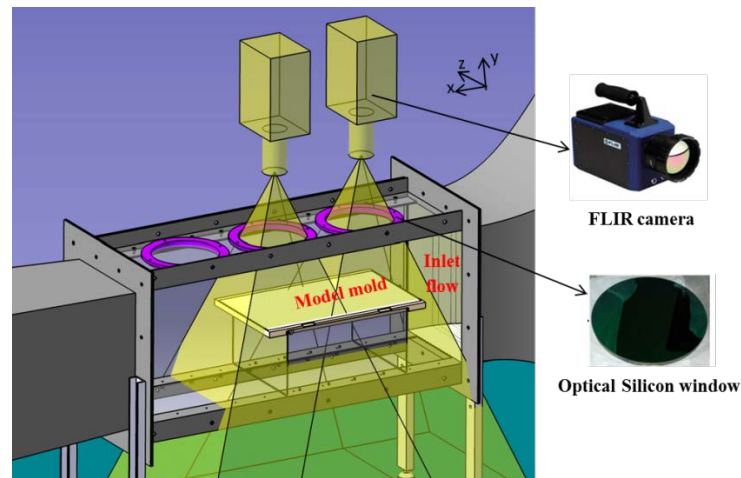


Figure 9 Mesure par caméra infrarouge de la température supérieure du moule

## 2.4. Etude du multichargement

Lors du procédé de mise en forme, plusieurs pièces composites sont chargées simultanément dans l'autoclave. Un moule placé en amont peut bloquer/perturber l'écoulement du gaz vers les moules situés en aval, créant ainsi des effets d'ombrage. Ces effets d'ombrage peuvent conduire à la présence de distributions variées du coefficient d'échange autour des différents moules, et ainsi contribuer à la production de pièces composites présentant différents états de cuisson et donc de qualités hétérogènes à la fin du cycle de cuisson.

L'objectif de l'étude multichargement est d'étudier ces effets d'ombrage. Notre étude consiste à installer un second moule, appelé Moule 2 derrière le Moule 1, présenté ci-dessus, dans la section de travail de l'autoclave modèle. Cette seconde plaque est similaire à la première, la seule différence étant une longueur deux fois plus faible.

L'étude de ces effets d'ombrage a consisté à étudier d'abord la structure de l'écoulement et le comportement de la distribution des coefficients d'échange autour du Moule 2 situé en aval du Moule 1. Les résultats aérodynamiques et thermiques ont été comparés ensuite avec ceux obtenus autour du moule placé en avant.

La Figure 10 illustre l'installation des deux moules dans la section de travail et séparés d'une distance  $d$ . Cette distance est considérée comme un paramètre d'étude.

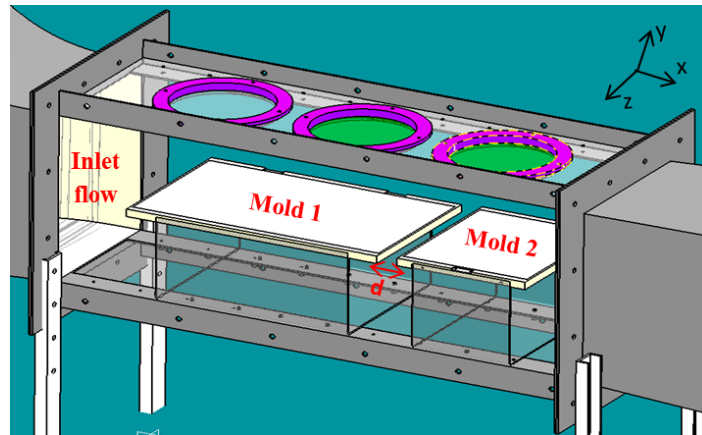


Figure 10 Schéma CAO de l'étude multichargement

## 2.5. Etude d'un moule avec des supports

Des moules avec des supports de structure complexe peuvent être utilisés lors du procédé de mise en forme (Figure 11). Ces obstacles peuvent contribuer à la présence d'un écoulement complexe et non uniforme autour des surfaces des moules ainsi qu'à l'apparition de zones mortes caractérisées par des faibles vitesses. Cette complexification de l'écoulement peut conduire à la présence de distributions variées des coefficients d'échange.



Figure 11 Photographie d'un moule industriel avec des supports [30]

Afin d'étudier l'impact de ces supports, notre étude consiste à installer des obstacles de géométrie simplifiée autour d'une plaque dans la section de travail de l'autoclave modèle comme illustré sur la Figure 12.

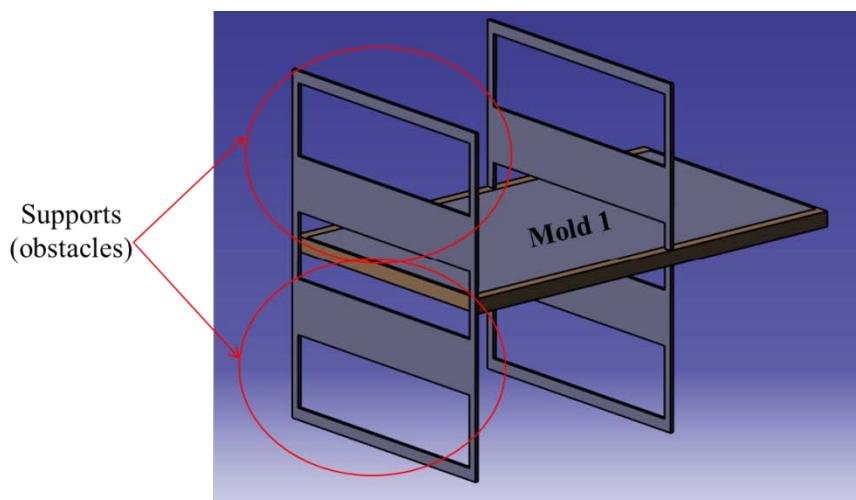


Figure 12 Schéma CAO du moule et des supports

### ***3. Modélisation numérique du modèle autoclave***

En complément des mesures expérimentales, la simulation numérique de l'écoulement autour des moules a été réalisée à l'aide du code volumes finis Ansys Fluent®. Les équations de Navier-Stokes sont résolues en employant l'approche RANS (Reynolds Averaged Navier-Stokes Simulation). Cette approche, largement utilisée pour la prédiction des écoulements et des transferts thermiques [31,32], est considérée moins coûteuse, au niveau des temps de calcul, que d'autres méthodes telles que la DNS (Direct Numerical Simulation) et la LES (Large Eddy Simulation). L'utilisation de l'approche RANS dans le cadre de nos travaux nécessite le recours à un modèle de turbulence. Parmi les différents modèles disponibles, le modèle de turbulence "SST  $k-\omega$ " a été sélectionné pour la simulation de l'écoulement turbulent et des échanges convectifs autour des moules. En effet, ce modèle permet de fournir des prédictions précises et améliorées, par rapport aux autres modèles, d'écoulements proches paroi en résolvant avec précision la sous-couche visqueuse ce qui n'est pas le cas avec la famille des modèles  $k-\varepsilon$  [33–36]. La prédiction de la sous-couche visqueuse est nécessaire pour prédire avec précision la distribution des coefficients  $HTC$  sur la surface [37].

Plusieurs modèles numériques ont été développés et correspondent aux différents cas d'études traités :

- le cas monochargement qui consiste à étudier les phénomènes physiques autour d'un seul moule dans la section de travail de l'autoclave modèle.
- le cas multichargement qui consiste à installer deux moules dans la section de travail afin de traiter des effets d'ombrage.
- le cas d'un moule avec des supports qui consiste à installer un moule équipé par des supports de structure.

### 3.1. Etude monochargement

#### 3.1.1. Modèle physique

Le domaine de calcul 2D qui représente la section de travail de l'autoclave modèle avec le moule installé est présenté sur la Figure 13. La présence d'un écoulement horizontal uniforme à l'entrée de la section de travail de l'autoclave modèle ainsi que l'utilisation d'un moule ayant la forme d'une plaque rectangulaire épaisse permettent d'obtenir des champs des vitesses 2D [38]. Les calculs numériques sont réalisés en régime stationnaire comme pour les essais expérimentaux.

Le domaine de calcul correspond aux dimensions expérimentales, soit un domaine rectangulaire de 1,07m de long et 0,4m de large. Le moule utilisé a une longueur de 0,51m et une épaisseur de 0,017m. Il a été créé selon la structure présentée dans la section 2.3 (cf. Figure 6). Les propriétés des matériaux utilisés sont correctement définies (plaque Inox, Rohacell®, polyamide 66 et le film résistif chauffant).

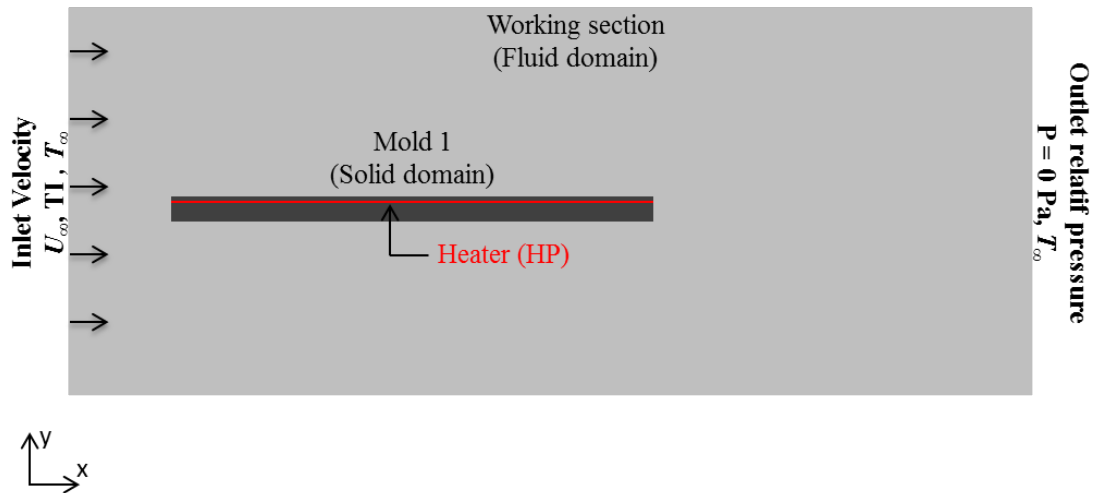


Figure 13 Domaine de calcul de la section de travail de l'autoclave modèle – Cas monochargement

#### 3.1.2. Modèle numérique et conditions aux limites

Pour les parois du domaine, une condition d'adhérence a été choisie. A l'entrée du domaine, des conditions aux limites aérodynamiques ont été imposées telles que la vitesse d'entrée ( $U_\infty$ ) et l'intensité de la turbulence ( $u_{rms}/U_\infty$ ) (cf. Figure 13). Ces quantités sont fixées en fonction des conditions expérimentales et selon les caractéristiques d'écoulement obtenues précédemment (cf. Tableau 2). En effet, de nombreux chercheurs [39,40] ont signalé l'influence du niveau de l'intensité de turbulence sur la structure de l'écoulement et par conséquent sur les coefficients d'échange convectif autour des surfaces. Compte tenu de ce fait, les conditions aux limites d'entrée doivent être cohérentes avec nos mesures expérimentales afin de

pouvoir comparer ces mesures avec nos résultats numériques. La température d'entrée du fluide ( $T_\infty$ ) et la puissance injectée dans le film résistif ( $HP$ ) ont également été définies en fonction des conditions expérimentales. Le fluide de travail est de l'air.

Le domaine fluide, au loin de la pièce, a été maillé avec des éléments triangulaires non structurés à l'aide de l'outil Ansys Workbench Meshing. Des éléments carrés structurés ont été utilisés pour mailler le domaine solide et le fluide auprès des moules. Notons ici que le maillage a été raffiné près des parois du moule (cf. Figure 14) afin de pouvoir décrire finement les phénomènes physiques qui s'y produisent. Le maillage fin près des surfaces a été créé de sorte que la distance adimensionnelle entre la paroi et le premier élément du maillage ( $y^+$ ) soit inférieur à l'unité [37,41] dans le but de résoudre avec précision, avec l'utilisation du modèle de turbulence SST k- $\omega$ , la zone proche paroi siège de forts gradients.

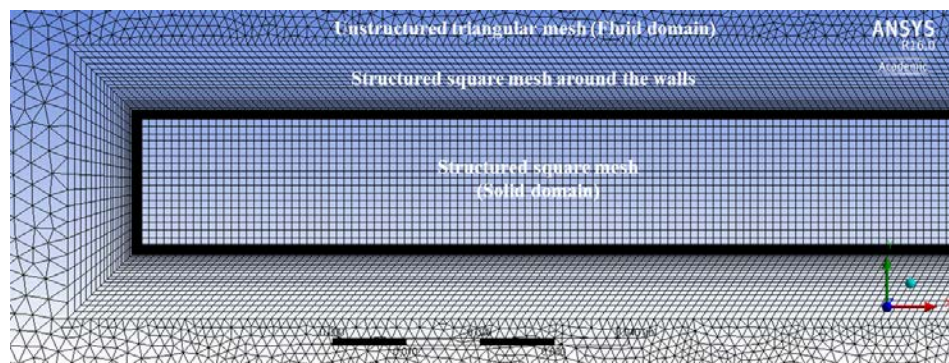


Figure 14 Zoom sur le maillage construit autour du domaine solide

Les équations d'écoulement et de l'énergie couplées avec les équations du modèle de turbulence sont résolues par une méthode de volumes finis. Les schémas de discrétisation Upwind de second ordre ont été utilisés pour toutes les variables de l'écoulement. La résolution du système d'équation est traitée de façon itérative grâce à l'algorithme de couplage pression-vitesse "COUPLE". Le critère de convergence impose une valeur normalisée pour les résidus inférieure à  $1.10^{-5}$  pour les équations d'écoulement et à  $1.10^{-8}$  pour l'équation de l'énergie. Les calculs ont été effectués sur un processeur à 3 GHz. Le temps de convergence est d'environ 15 minutes. A la fin de chaque calcul numérique, un rapport de débit a été réalisé afin de vérifier la loi de conservation du débit massique ainsi que le bilan énergétique dans l'ensemble du domaine.

### 3.2. Etude du multichargement

Comme précisé dans la partie expérimentale, section 2.4, les deux plaques Moule 1 et Moule 2 sont utilisées.

Numériquement, le modèle géométrique du Moule 2 a été réalisé de la même manière que celui du Moule 1. La Figure 15 montre le domaine du calcul qui contient le Moule 2 placé derrière le Moule 1 à l'intérieur de la section de travail de l'autoclave modèle. La distance qui sépare les deux moules est nommée  $d$ . Cette dernière est définie comme étant un paramètre d'étude. Une étude paramétrique a été réalisée afin de visualiser l'impact de cette distance sur les phénomènes physiques étudiés.

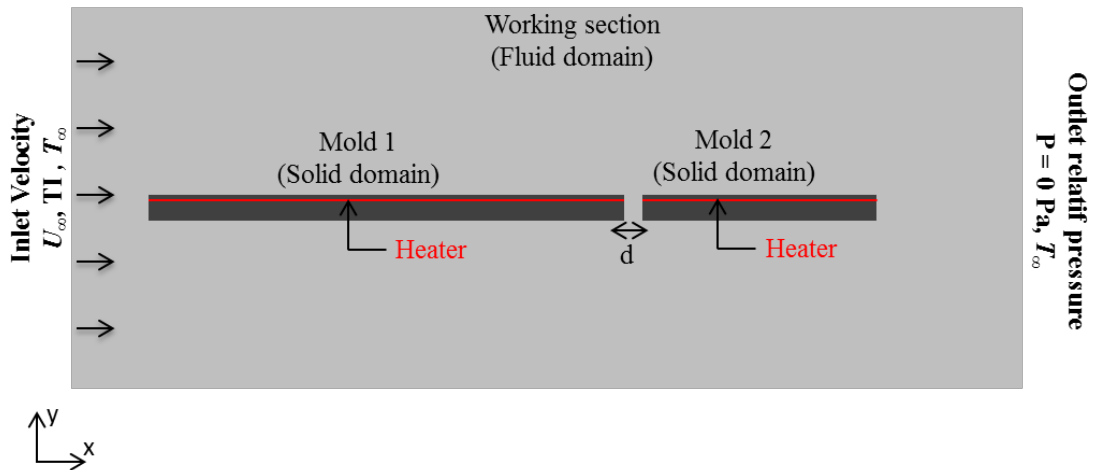


Figure 15 Le domaine de calcul de la section de travail de l'autoclave modèle – Cas multichargement

Les différentes étapes suivies et appliquées pour la création du modèle numérique, à savoir la géométrie, le maillage, les conditions aux limites, le solveur, etc., sont les mêmes que celles décrites ci-dessus pour le cas monochargement.

### 3.3. Etude du moule avec des supports

La Figure 16 montre le modèle géométrique numérique du moule avec les obstacles nommés  $O_1$ ,  $O_2$ ,  $O_3$  et  $O_4$  et installé dans la section de travail de l'autoclave modèle. Le modèle géométrique numérique correspond au schéma présenté Figure 12.



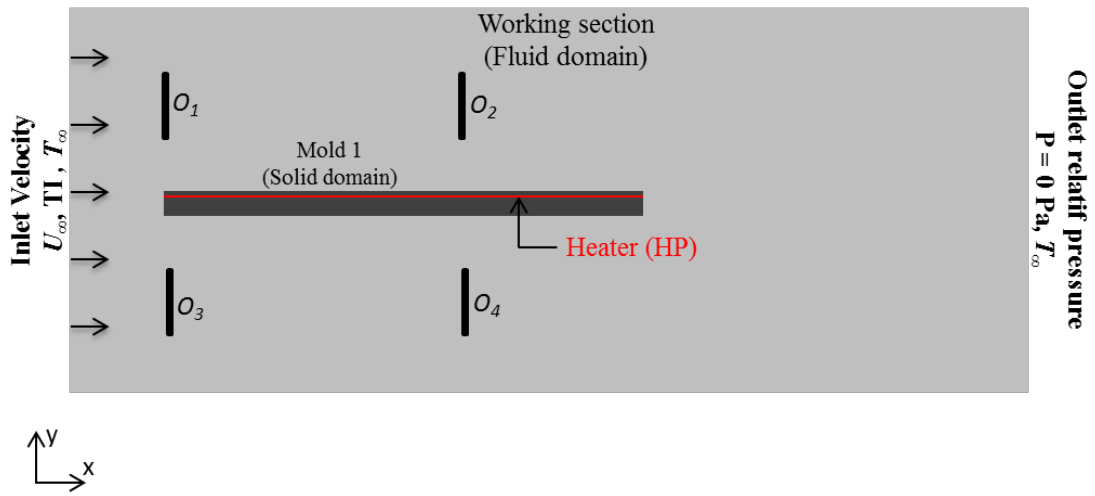


Figure 16 Domaine de calcul de la section de travail de l'autoclave modèle – Cas moule + obstacles

Les différentes étapes suivies et appliquées pour la création du modèle numérique, à savoir la géométrie, le maillage, les conditions aux limites, le solveur, etc., sont les mêmes que celles décrites ci-dessus pour les précédents cas.

## 4. Résultats et Discussion

### 4.1. Etude du Monochargement

#### 4.1.1. Etude de l'écoulement

Un système PIV est utilisé pour mesurer le champ de vitesse autour du moule. La Figure 17 montre le montage expérimental pour les mesures PIV effectuées. La nappe laser générée est normale à la surface supérieure du moule et positionnée dans la zone centrale de ce dernier, là où l'écoulement est 2D. Elle est située dans le plan de mesure ( $xy$ ) permettant de mesurer les deux composantes du vecteur vitesse selon les axes ( $x$ ) et ( $y$ ). La caméra est installée et calibrée face à la zone de mesure illuminée par le plan laser. La zone de mesure couvre le bord d'attaque du moule. Les mesures sont réalisées en régime stationnaire défini par l'obtention d'une densité homogène des particules dans l'écoulement. Le débit volumique est celui obtenu par la similitude dynamique :  $Q = 15\,290\text{ m}^3/\text{h}$ .

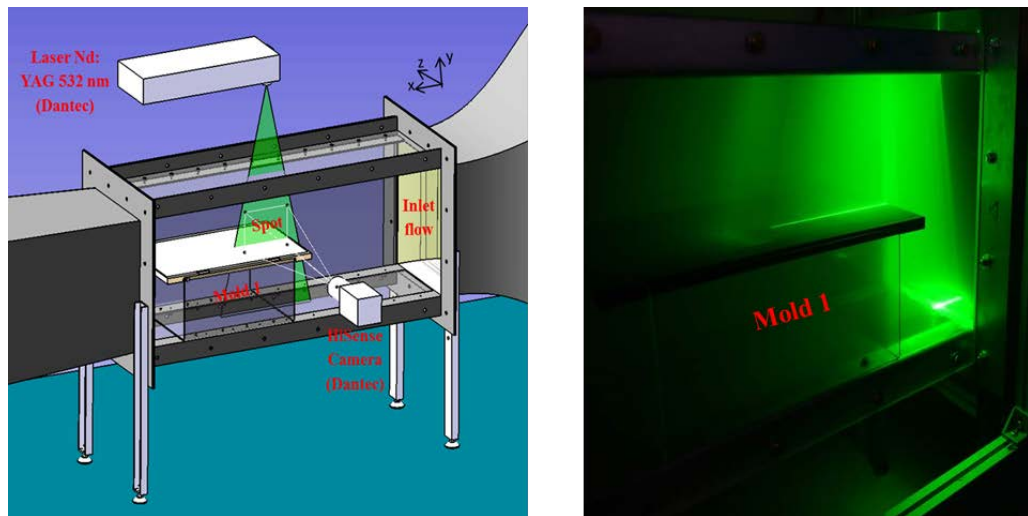


Figure 17 Mesures PIV des champs de vitesses dans le plan (xy)

Sur la Figure 18 sont représentées les lignes de courant ainsi que la norme du champ de vitesse. Ces résultats sont obtenus par une moyenne temporelle du champ de vitesse instantanée. Le point de référence ( $x/e=0$ ,  $y/e=0$ ) correspond à l'angle supérieur du bord d'attaque de la plaque.

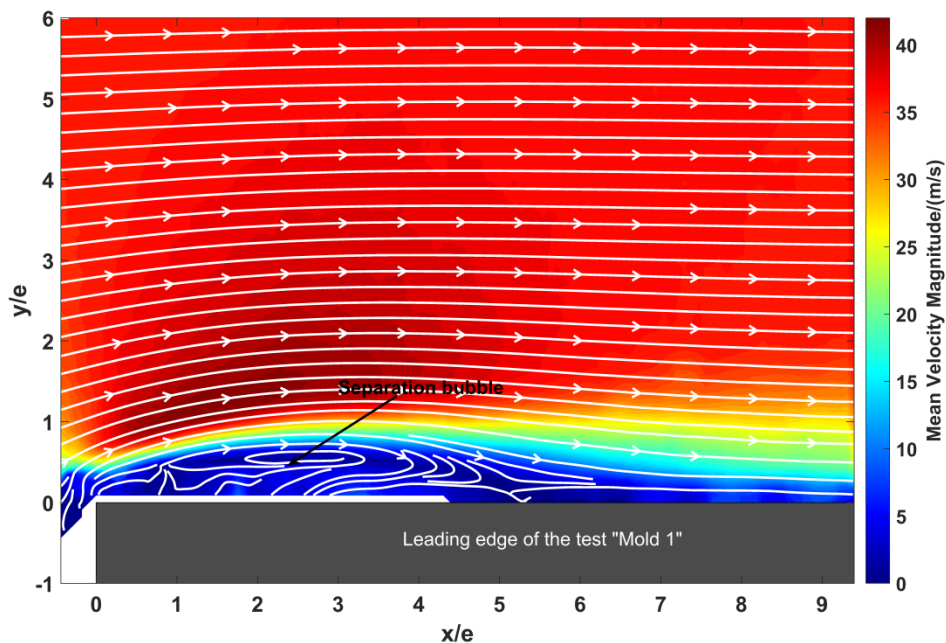


Figure 18 Norme de la vitesse et lignes de courant autour de la plaque

Les lignes de courant (Figure 18) mettent en évidence la zone de séparation depuis le bord d'attaque puis du recollement de la couche limite. Cela se manifeste par la présence d'une bulle de séparation qui se forme à partir du début de la plaque ( $x/e = 0$ ) et puis le recollement à une distance située à  $x/e = 5,2$ . Cette distance représente la longueur de recollement de la couche limite ( $X_r$ ). Elle est une longueur caractéristique



de la zone de la séparation et de recollement. La structure observée de l'écoulement autour de la plaque est bien conforme aux résultats de la littérature [21].

Cette structure d'écoulement a été validée de façon plus précise et quantitative en traçant les profils des vitesses longitudinales moyennes ( $U/U_\infty$ ) et les r.m.s ( $u_{rms}/U_\infty$ ) dans la couche limite développée autour de la plaque, cela pour différentes positions longitudinales ( $x/e$ ). Ces profils sont montrés sur les Figure 19 et Figure 20 respectivement et sont comparés aux résultats issus des simulations numériques.

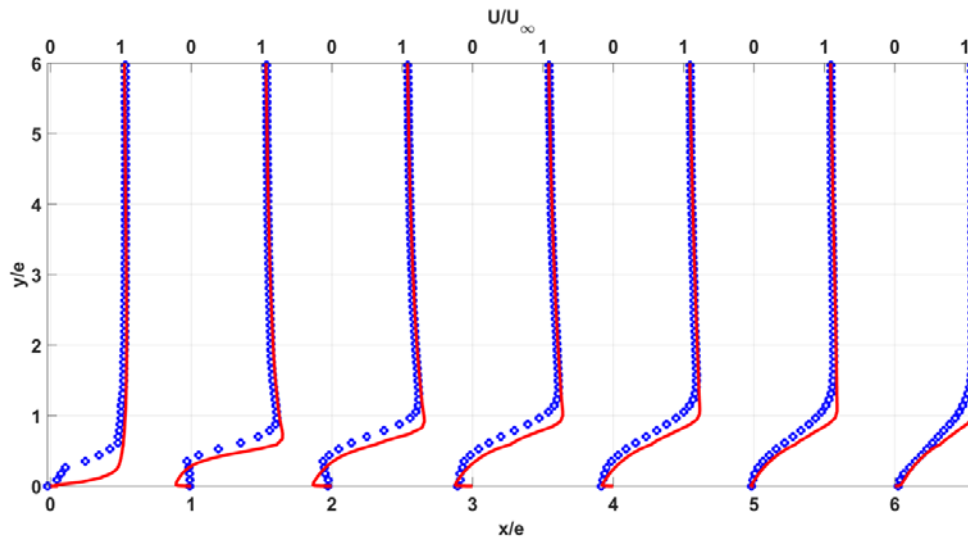


Figure 19 Profils des vitesses longitudinales moyennes  $U$ :  $\circ$ , PIV; —, CFD

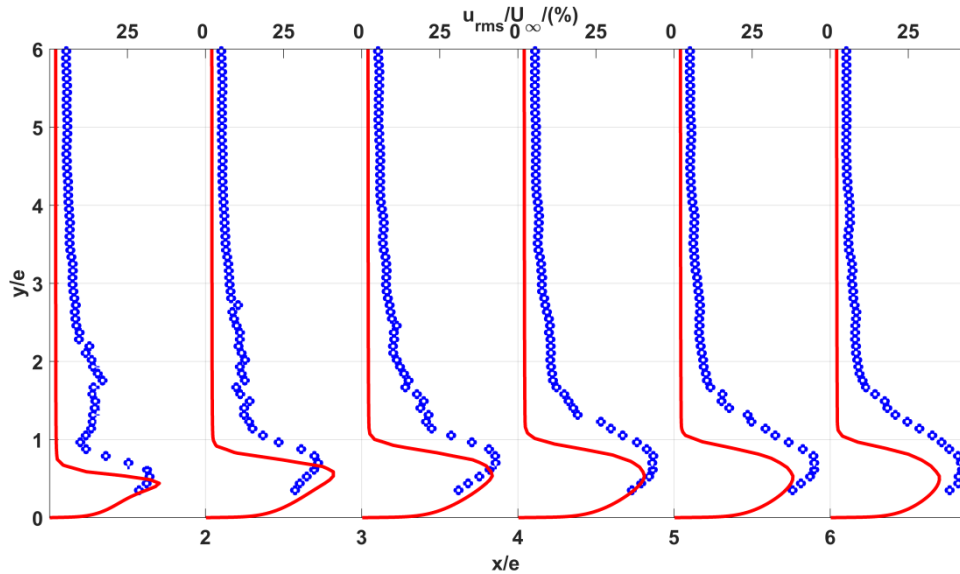


Figure 20 Profils des vitesses longitudinales r.m.s  $u_{rms}$ :  $\circ$ , PIV; —, CFD

Ces profils montrent à partir du bord d'attaque ( $x/e = 0$ ) et jusqu'au recollement de la couche limite (entre  $x/e = 5$  et  $x/e = 6$ ) des valeurs négatives de la vitesse moyenne

normalisée ( $U/U_\infty$ ) au proche de la paroi, ainsi que des valeurs significatives de l'intensité de la turbulence qui atteint plus de 25%. Ainsi, ces profils et l'apparition des points d'inflexion confirment l'apparition de la zone de séparation puis le recollement de la couche limite autour du moule.

La comparaison entre les profils de vitesse expérimentaux et ceux issus des simulations numériques montre un bon accord. Par conséquent, les simulations numériques de l'écoulement turbulent d'air isotherme autour d'un moule installé dans la section de travail sont validées grâce aux essais expérimentaux.

L'étape suivante consiste à réaliser l'étude en présence d'une source de chaleur dans le moule de façon à identifier la répartition des coefficients d'échange à la surface.

### **4.1.2. Etude de la distribution des coefficients d'échange**

L'étude expérimentale de la distribution des coefficients a été réalisée selon la méthodologie présentée et détaillée dans la Section 2.3.2. L'application de cette méthodologie permet d'abord la mesure des quantités physiques suivantes :  $\phi_{lx}$ ,  $\phi_{hx}$  et  $T_{mx}$ . Ensuite, la quantification de ces grandeurs permet de déterminer la distribution du coefficient d'échange autour de la surface supérieure du moule.

Cependant, et pendant la réalisation des mesures thermiques et en particulier pendant la thermographie infrarouge de la surface supérieure du moule, des zones froides ont été observées à côté des bords du moule. Ces zones froides sont caractérisées par des températures relativement inférieures à celles de la zone centrale. Le champ de température issu de ces mesures infrarouge, en régime stationnaire, ainsi que la localisation de ces zones froides sont montrés sur la Figure 21. Le champ de température obtenu correspond à une puissance de chauffage de  $1800 \text{ W/m}^2$  injecté dans le film résistif du moule. Le moule est refroidi par l'écoulement de l'air qui circule avec une vitesse de  $33,7 \text{ m/s}$  et avec une température constante de  $23,5^\circ\text{C}$ .

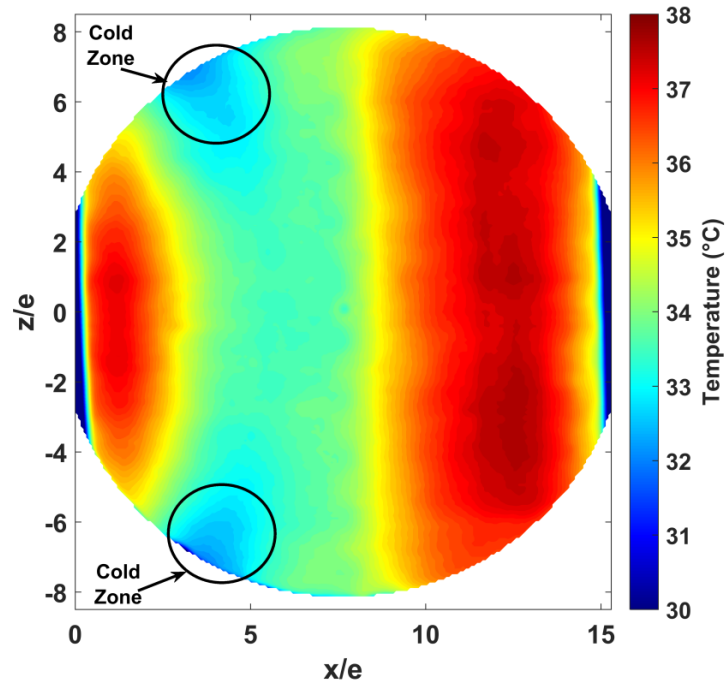


**Figure 21 Température moyenne de la surface supérieure du moule**

La thermographie infrarouge montre un champ de température unidimensionnel dans la zone centrale de la plaque et qui dépend principalement de la position longitudinale ( $x/e$ ). Les zones froides mentionnées ci-dessus sont localisées sur les bords du moule approximativement à  $x/e = 4$ . Ces zones froides caractérisées par des températures inférieures à celles proches de la région centrale (cf. Figure 21) montrent que le champ de température est bidimensionnel autour du moule sauf dans la zone centrale. L'apparition de ces zones froides peut être expliquée par les effets de bord. En effet, selon les auteurs Ota *et al.* [38], ces effets sont définis par la présence de tourbillons en fer à cheval formés autour des bords d'une plaque. L'écoulement dans la région de recirculation devient en général tridimensionnel à cause de ces tourbillons sauf dans la zone centrale. Cet effet sur l'écoulement se manifeste par la présence d'une ligne de recollement courbée [38]. De plus, ces tourbillons ont de grands effets sur les transferts de chaleur convectifs. En effet, ils provoquent une augmentation locale des transferts convectifs, donc des nombres de Nusselt. Ainsi, en supposant une densité de flux constante, les températures près des bords de la veine d'essai sont plus basses que celles proches de la région centrale, d'où l'apparition de ces zones froides.

Afin de vérifier cette hypothèse, des mesures du champ de vitesse dans un plan ( $xz$ ) parallèle à la surface supérieure du moule ont été réalisées (cf. Figure 22). La zone des mesures PIV représentée en Figure 22 est située entre  $x/e = 0$  et  $x/e = 9$ , et entre  $z/e = -2$  et  $z/e = 7$  selon le système de coordonnées défini pour la surface supérieure du moule (cf. Figure 21).

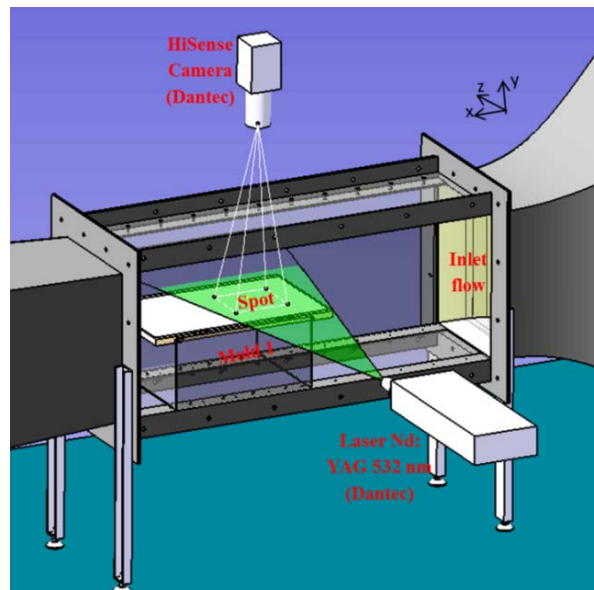


Figure 22 Mesures PIV des champs de vitesses dans le plan (xz)

La Figure 23 montre les lignes de courant de l'écoulement moyen obtenues grâce aux mesures PIV ainsi que le champ de température moyen dans la zone d'étude.

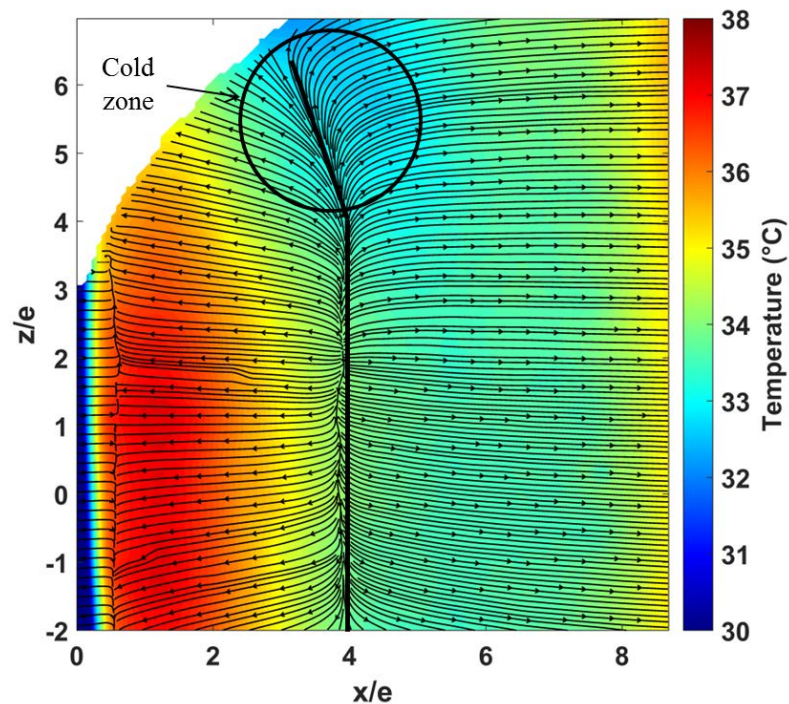


Figure 23 Température moyenne et lignes de courant du champ de vitesse autour du moule

L'analyse des lignes de courant obtenues permet l'identification d'une ligne qui correspond à l'intersection du plan laser émis avec la bulle de séparation. Cette ligne identifiée est marquée sur la Figure 23 par une ligne noire située à  $x/e = 4$ . Elle

montre un comportement constant jusqu'à la position  $z/e = 4,5$  à partir duquel elle devient courbée. Cette courbure correspond bien à la position de la zone froide (cf. Figure 23).

L'apparition d'une ligne courbée indique ainsi que la ligne de recollement de la zone de séparation est courbée aussi et est bien cohérent avec les résultats de la littérature.

Toutefois, malgré ces effets de bord, dans la zone centrale du moule, l'écoulement et les échanges thermiques convectifs restent toujours indépendants de la coordonnée  $z$ . De ce fait, le profil de température ( $T_{mx}$ ) a été extrait de la zone centrale pour déterminer ensuite la distribution des coefficients  $HTC$ . Cette distribution est montrée dans la Figure 24.

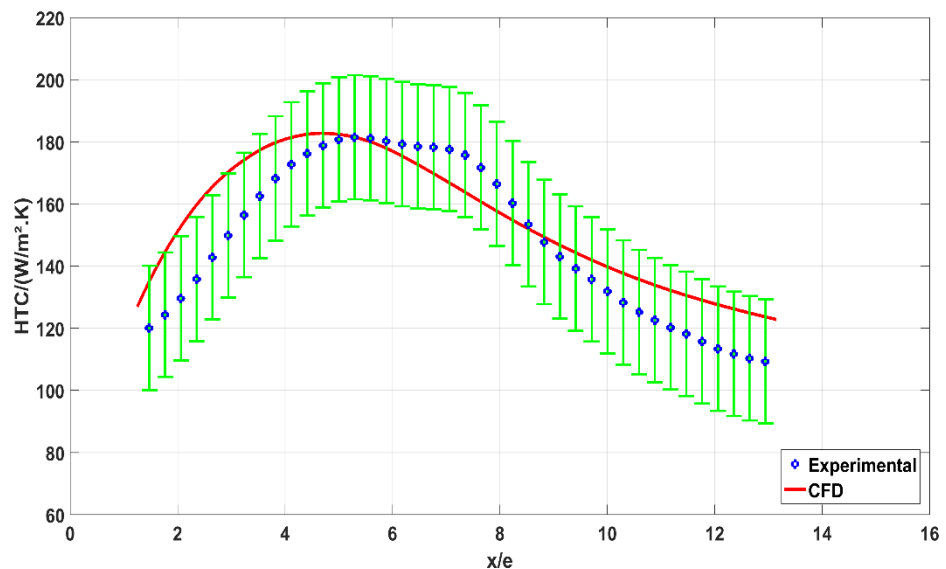


**Figure 24 Distribution des coefficients d'échange en surface du moule**

Les profils numériques et expérimentaux obtenus montrent le même comportement. Ils augmentent à partir du bord d'attaque et atteignent une valeur maximale pour  $x/e = 5,2$ , pour le profil expérimental, contre  $x/e = 4,7$  pour le profil numérique. Ensuite, ils diminuent.

Ce comportement s'explique par la structure de l'écoulement en surface du moule montrée précédemment. En effet, l'apparition de la bulle de séparation sur le bord d'attaque de la plaque épaisse est caractérisée par des niveaux de turbulence relativement importants, ce qui améliore localement les échanges convectifs [40]. Ces derniers atteignent une valeur maximale à la position du recollement de la couche limite ou juste en amont [22,23], là où la couche limite est la moins épaisse. Cependant, cette différence de position maximale a été jugée faible [21]. Rappelons que la position du point de recollement de la couche limite a été déterminée à  $x/e =$

5,2 d'après les mesures aérodynamiques. Au-delà de la zone de recollement, la croissance de la couche limite équivaut à une augmentation de la résistance thermique. Par conséquent, en aval de la zone de recollement, les coefficients d'échange diminuent.

Le comportement des coefficients d'échange, mesurés et calculés, est en cohérence avec la littérature. En effet, les valeurs maximales obtenues à partir des résultats expérimentaux et numériques, se sont révélées proche de la valeur estimée par la corrélation proposée par Ota *et al.* [20] (cf. Tableau 4). Cette corrélation est représentée par l'Equation (8) et les propriétés de l'air ( $\lambda$  et  $\nu$ ) ont été prises à la température mesurée et à la pression ambiante.

$$\frac{HTC_{max} \cdot Xr}{\lambda} = 0.0919 \left( \frac{U_{\infty} \cdot Xr}{\nu} \right)^{0.734} \quad \text{Équation (8)}$$

**Tableau 4 Coefficients d'échange dans la zone de recollement**

	Expériences	CFD	Ota <i>et al.</i>	Ecart
<b>HTC<sub>max</sub> (W/m<sup>2</sup>/K)</b>	182 (+/- 20)	183	196	7 %

Les simulations numériques ont montré leur capacité à prédire correctement la distribution du coefficient d'échange en surface de plaques épaisses. De plus, la valeur moyenne spatiale sur la longueur du moule obtenue par l'approche CFD correspond très bien à celle obtenue expérimentalement (cf. Tableau 5).

**Tableau 5 Comparaison entre les valeurs numériques et expérimentales du coefficient d'échange moyen**

	Expériences	CFD	Ecart
<b><math>\overline{HTC}</math> (W/m<sup>2</sup>.K)</b>	149 (+/- 20)	155	4 %

L'évolution des coefficients d'échange, présentée sur la Figure 24, montre une distribution non uniforme en surface du moule malgré une géométrie simplifiée. Ainsi, dans le cas d'un autoclave réel chargé avec des moules de formes plus complexes, cette hétérogénéité de distribution risque d'être plus importante et plus significative.

## 4.2. Etude du multichargement

Le moule 1 a été placé en amont du moule 2 à une distance  $d$ . Dans ces travaux,  $d$  est fixé à 3,2 cm (cf. Figure 25 et Figure 26).

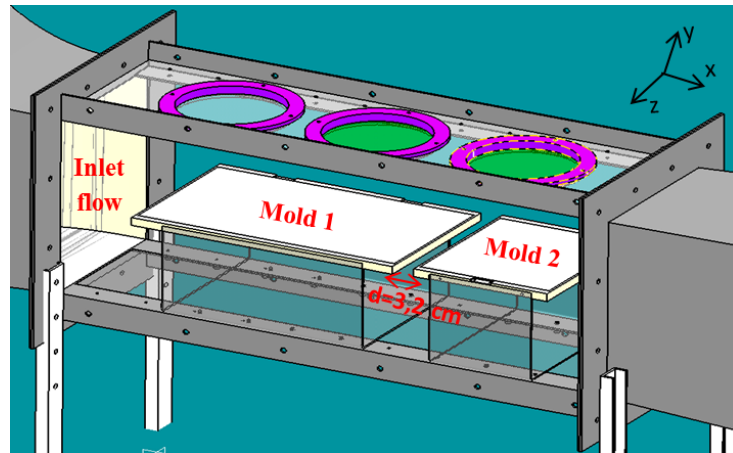


Figure 25 Schéma de la section de travail équipée de 2 moules

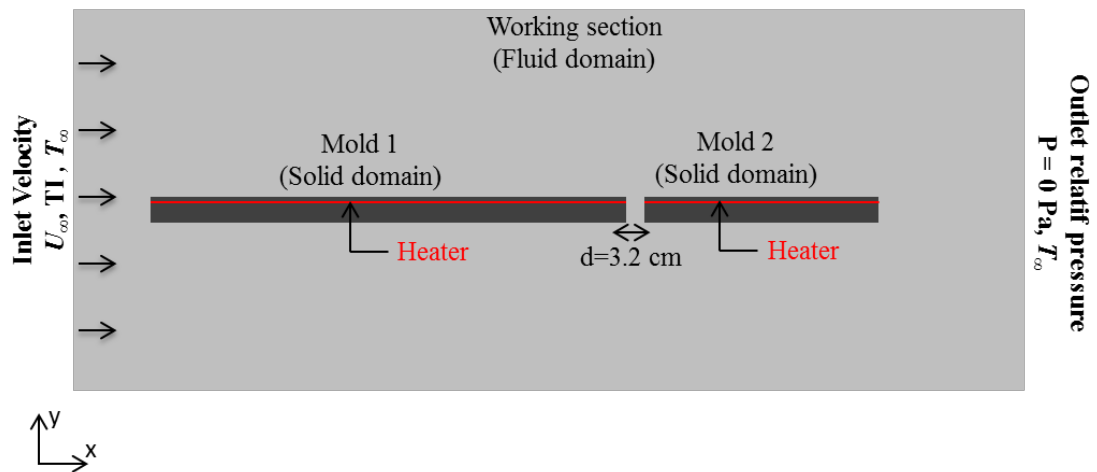


Figure 26 Modèle numérique de l'étude pour  $d=3.2$  cm

L'étude des effets d'ombrage a consisté à étudier d'abord la structure de l'écoulement et le comportement de la distribution des coefficients d'échange autour du moule 2 situé en aval du moule 1. Ensuite, les résultats aérauliques et thermiques ont été comparés à ceux obtenus autour du moule placé en amont.

#### 4.2.1. Etude de l'écoulement

La Figure 27 présente les positions du laser et de la caméra. La zone de mesure illuminée est située dans le plan (xy). Compte tenu des pertes de charge générées par la présence de deux plaques dans la section de travail, le débit mesuré qui correspond à la fréquence 80 Hz du moteur de ventilateur est réduit de 15 290 m<sup>3</sup>/h à 14 500 m<sup>3</sup>/h. Ce débit correspond à une vitesse d'entrée  $U_\infty = 32$  m/s obtenue grâce aux mesures PIV.



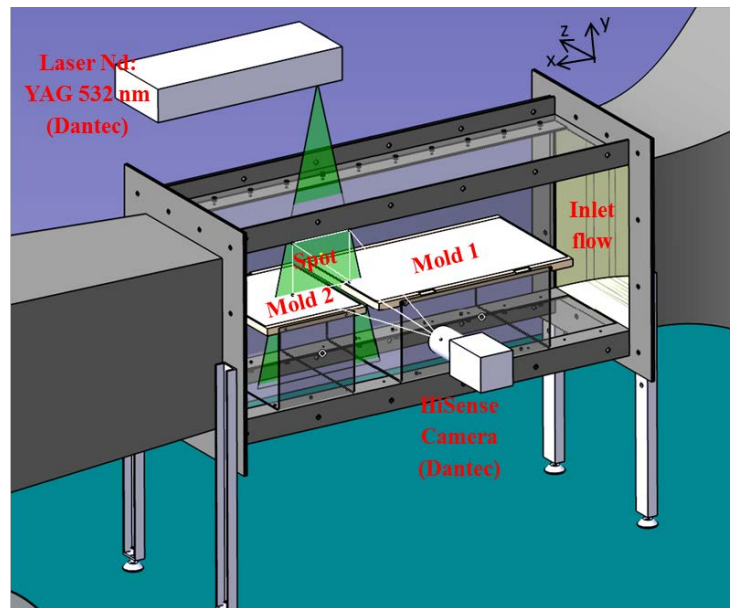


Figure 27 Procédure de mesure PIV autour du moule 2

La Figure 28 montre la norme du champ de vitesse ainsi que les lignes de courant au niveau du bord de fuite du moule amont et du bord d'attaque du moule aval. Le point de référence ( $x/e=0$ ,  $y/e=0$ ) correspond à l'angle haut du bord d'attaque du moule 2.

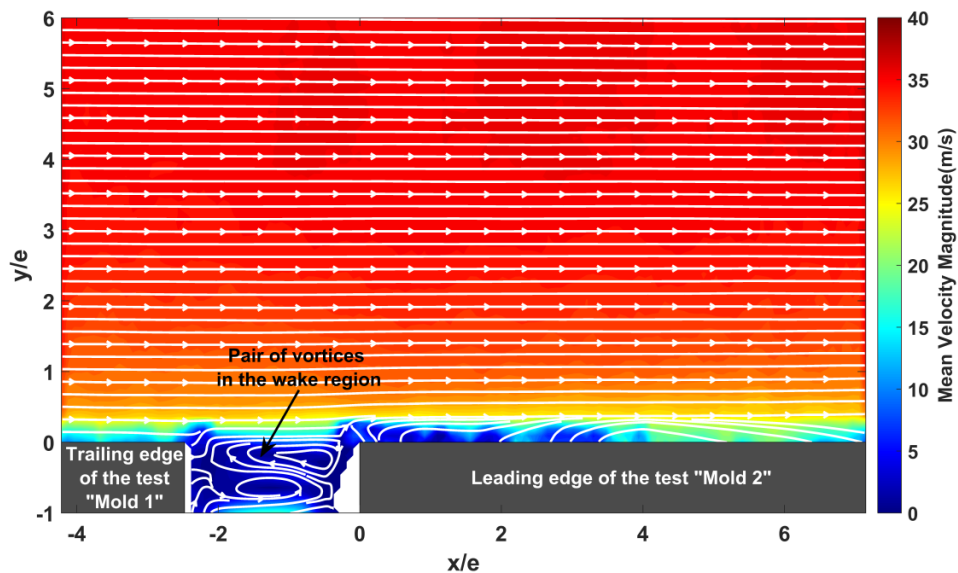


Figure 28 Norme de la vitesse et lignes de courant dans le cas d'un multichargement

Les lignes de courant montrent une paire de tourbillons formée dans le sillage du moule 1 ce qui est conforme à la description présentée par d'autres études scientifiques [42]. Les lignes de courant ne montrent pas la formation d'une bulle de



séparation significative autour du moule 2 contrairement à ce qui était détecté autour du moule 1 (cf. Figure 18) dans le cas du monochargement. L'allure de l'écoulement autour du moule 2 a été validée en traçant les profils de la vitesse moyenne longitudinale normalisée ( $U/U_\infty$ ) et de l'intensité de turbulence ( $u_{rms}/U_\infty$ ) dans la couche limite développée pour différentes positions longitudinales  $x/e$  (Figure 29 et Figure 30). Sur ces figures sont également présentés les résultats provenant des simulations numériques.

Dans la région proche paroi du moule 2, la Figure 29 montre des valeurs positives de la vitesse longitudinale sans l'existence de points d'inflexion. La Figure 30 montre des niveaux de turbulence relativement faibles. Ces comportements des profils de vitesse, contrairement à ceux obtenus pour la première plaque, montrent à nouveau l'absence de la bulle de séparation et de recollement de la couche limite autour du moule 2.

En revanche, la comparaison entre les profils de vitesses expérimentaux et numériques montre un bon accord. Par conséquent, le modèle numérique construit dans le cas des plusieurs moules dans la section de travail est validé grâce aux mesures expérimentales.

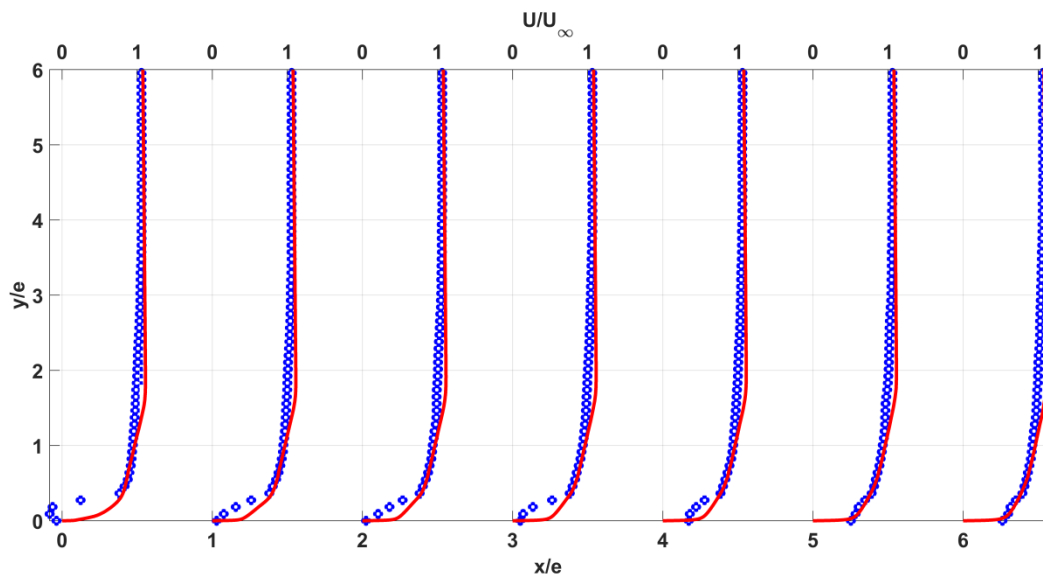


Figure 29 Profils des vitesses longitudinales moyennes  $U$ :  $\circ$ , PIV; —, CFD

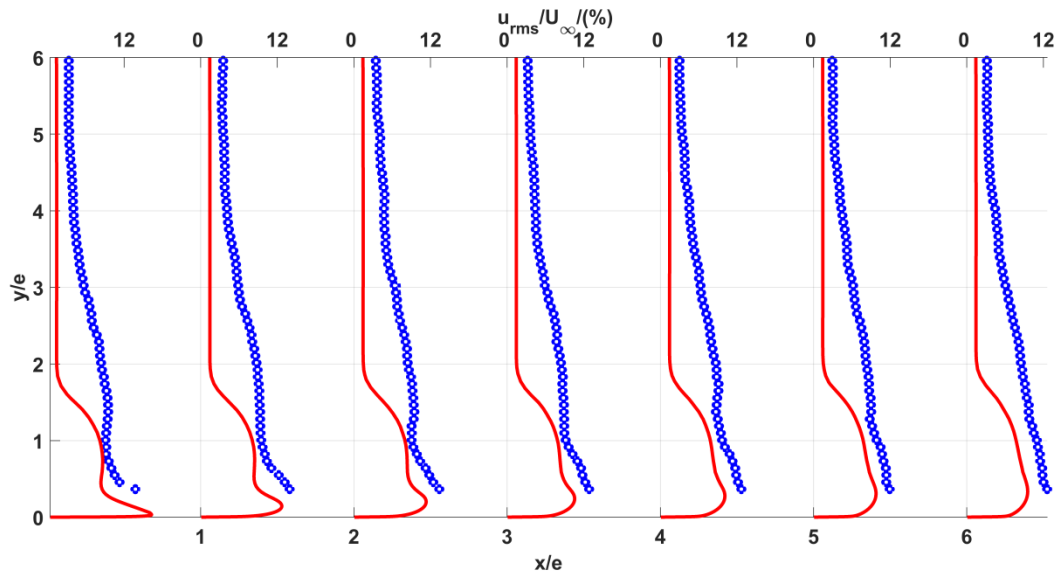


Figure 30 Profils des vitesses longitudinales r.m.s  $u_{rms}$ :  $\circ$ , PIV; —, CFD

#### 4.2.2. Etude de la distribution des coefficients d'échange

L'application de la procédure expérimentale déjà présentée permet d'obtenir la distribution des coefficients d'échange autour du moule 2. Cette distribution est représentée sur la Figure 31 et comparée aux résultats issus de la simulation numérique.

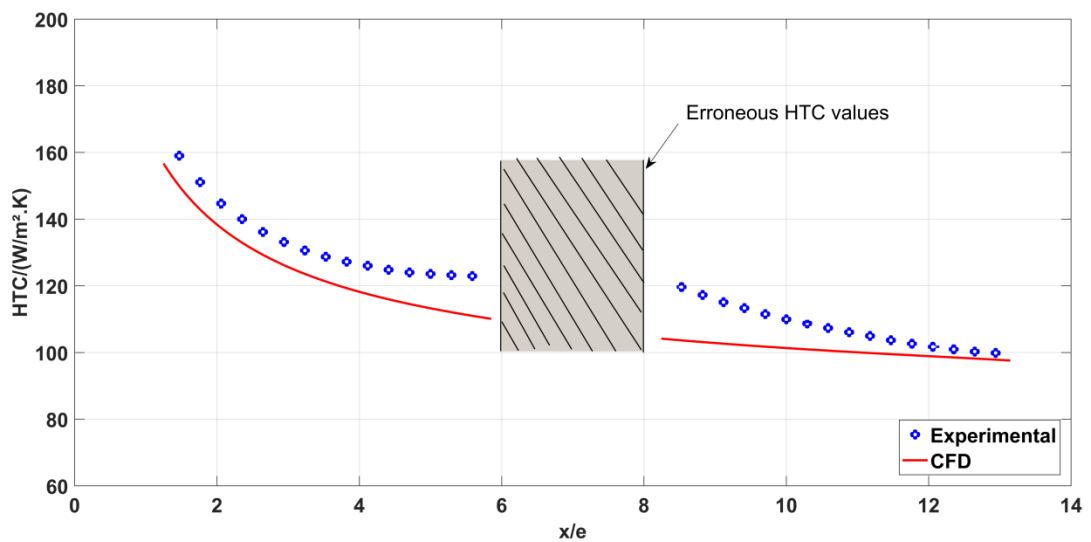


Figure 31 Distribution des coefficients  $HTC$  autour du moule 2

Les deux profils, expérimental et numérique, montrent la même évolution des coefficients d'échange convectifs, qui diminuent de manière monotone. Ce comportement s'explique à nouveau par la structure de l'écoulement autour du moule

2. En effet, l'absence de bulle de séparation de la couche limite signifie que la couche limite reste attachée et se développe en permanence. L'épaisseur de la couche limite augmente donc continument, ainsi que la résistance thermique liée, d'où la décroissance continue des coefficients d'échange.

Dans ce cas également, le modèle numérique a montré sa capacité à prédire assez correctement la distribution des coefficients d'échange convectif. De plus, les valeurs moyennes spatiales, sur la longueur des moules, des coefficients d'échange déduites de la courbe expérimentale ainsi que de la courbe numérique montrent un bon accord entre elles (cf. Tableau 6).

**Tableau 6 Comparaison entre les résultats numériques et les résultats expérimentaux**

	Expérimentation	CFD	Ecart
$\overline{HTC}$ (W/m <sup>2</sup> .K)	120 (+/- 20)	111	7.5 %

Pour visualiser l'impact du phénomène d'ombrage sur les coefficients d'échange, la courbe expérimentale des coefficients obtenue dans le cas d'un seul moule a été tracée sur le même graphique que celle obtenue autour du moule 2 placé en arrière. Les deux courbes sont présentées sur la Figure 32.

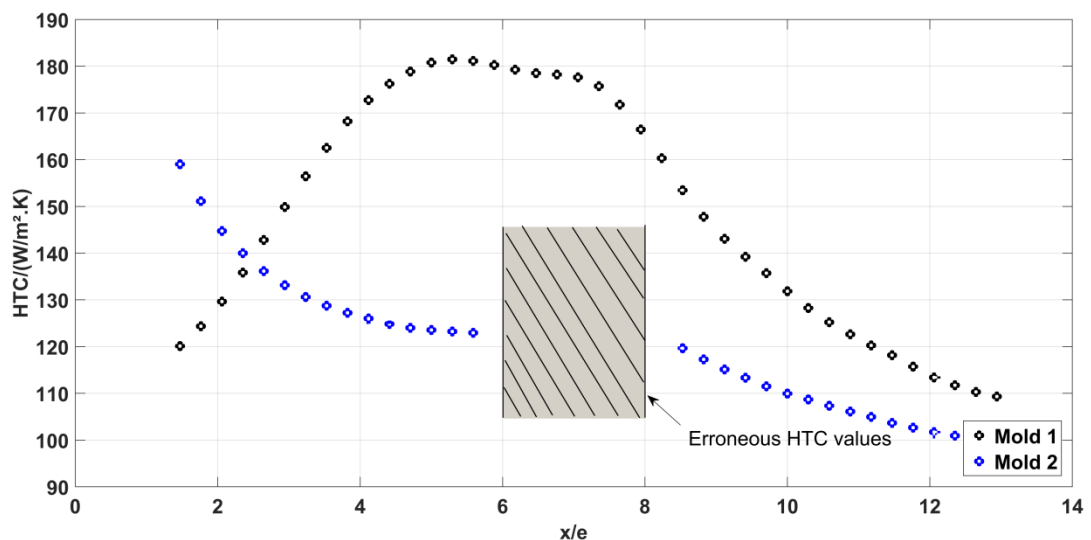


**Figure 32 Coefficients d'échange autour du moule amont (1) et du moule aval (2)**

La comparaison entre les deux courbes montre clairement des distributions de coefficients d'échange différents. Plus précisément, les valeurs autour du moule 1 sont globalement plus importantes que celles obtenues autour du moule 2, confirmant l'existence et l'impact des effets d'ombrage entre les moules.

Par conséquent, le procédé autoclave dans lequel plusieurs pièces composites sont chargées simultanément peut contribuer à l'existence de différentes distributions de coefficients d'échange convectifs autour des moules.

### 4.3. Etude du moule avec des supports

La Figure 33 montre la norme de la vitesse issue de l'analyse numérique. En ce qui concerne les conditions aux limites, la vitesse à l'entrée, l'intensité de turbulence et la température de l'air ont été fixées à 33,7 m/s, 1,1% et 27 °C respectivement. Ces valeurs assignées aux conditions limites ont été définies arbitrairement afin de démarrer les calculs numériques et de visualiser les résultats. Ils peuvent être modifiés par la suite en fonction des conditions expérimentales réelles. La puissance de chauffage ( $HP$ ) dans le film résistif est de 2000W/m<sup>2</sup>.

Comme attendu, les résultats indiquent que la présence des obstacles contribue à l'existence de zones mortes caractérisées par de faibles vitesses. De plus, ces obstacles, malgré leur géométrie simplifiée, contribuent à l'existence d'un champ d'écoulement complexe dans la section de travail de l'autoclave modèle et autour de la surface du moule. Ce résultat laisse présager de la complexité d'un écoulement réel dans un autoclave en présence de pièces plus complexes. Un tel écoulement est difficile à décrire et à mesurer ce qui explique les études en nombre limité dans la littérature liée aux autoclaves.

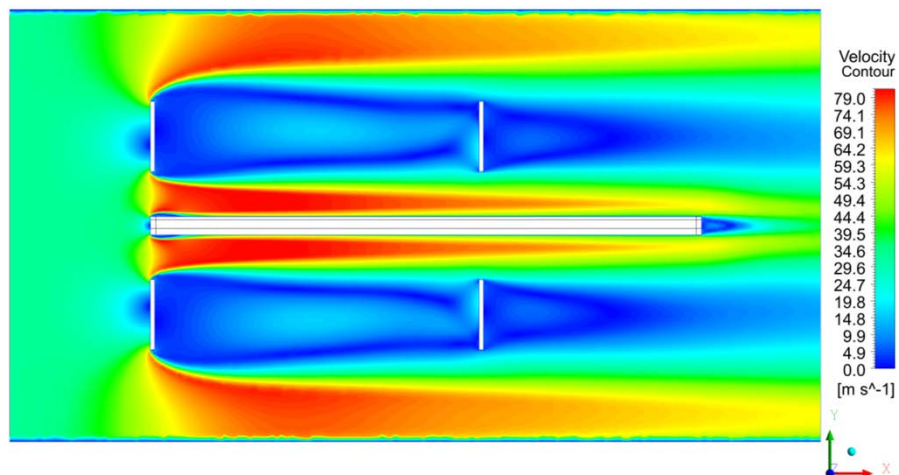
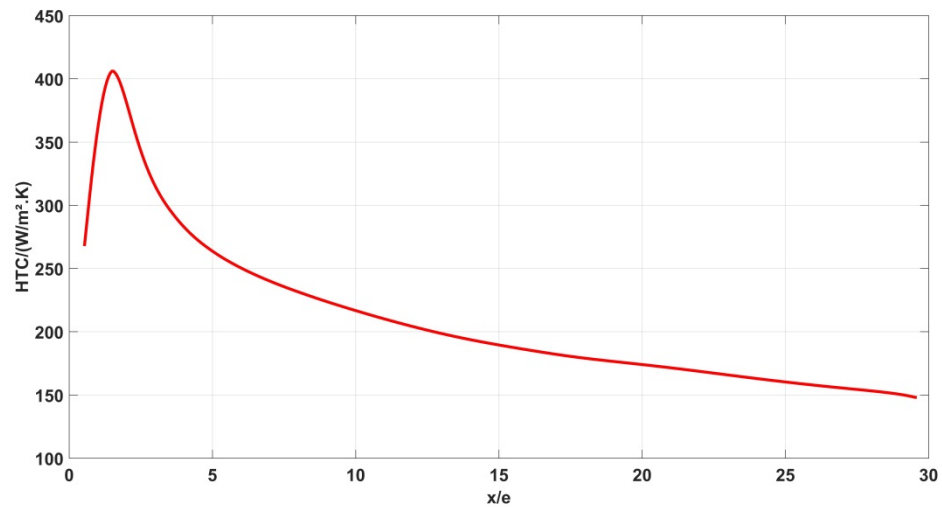


Figure 33 Champ de vitesse dans la section de travail

La Figure 34 montre le profil obtenu de  $HTC$  autour de la surface supérieure du moule. Le profil présente un comportement similaire à celui obtenu autour du moule seul (Figure 24).



**Figure 34 Distribution des *HTC* autour de la surface supérieure du moule représentatif**

Une étude paramétrique basée sur des méthodes d'interpolation et couplée avec un algorithme d'optimisation afin de trouver une conception géométrique optimale des supports ou obstacles a été menée. Ces méthodes d'interpolation s'avèrent avantageuses dans le cas où nombreux paramètres d'entrée interviennent. En effet, elles consistent d'abord à réaliser des simulations numériques automatiquement sur un ensemble de points d'échantillonnage définis dans un espace de conception appelé «Design of Experiments» (DOE). Ces points d'échantillonnage sont obtenus à partir des combinaisons des valeurs attribuées aux paramètres d'entrée nommés aussi variables de conception. Ensuite, des méthodes d'interpolation sont utilisées pour décrire la relation entre les paramètres de sortie, qui représentent les phénomènes physiques étudiés, et les paramètres d'entrée. Ces méthodes d'interpolation sont capables ainsi de fournir rapidement des valeurs approximatives des paramètres de sortie, partout dans l'espace de conception analysé, sans avoir à effectuer une simulation complète et coûteuse. Par conséquent, ces techniques permettent l'obtention des substituts rapides pour les paramètres de sortie et qui peuvent être utilisées pour l'optimisation.

Une conception géométrique optimale des supports doit permettre d'améliorer l'intensité des coefficients d'échange d'une part (caractérise la durée du cycle de cuisson) et leur distribution uniforme d'autre part autour du moule (caractérise la qualité finale des pièces).

Les paramètres d'entrée ou les variables de conception sont présentés dans la Figure 35 et sont en fait des distances géométriques qui permettent de modifier la position et la taille des obstacles.



**Figure 35 Paramètres d'entrée pour la conception des obstacles**

L'algorithme d'optimisation MOGA (Multi-Objective Genetic Algorithm) a été utilisé. Les critères de l'étude d'optimisation sont définis de la manière suivante:

- Maximiser la valeur moyenne des coefficients d'échanges  $\overline{HTC}$  permettant ainsi d'intensifier les échanges convectifs.
- Minimiser la distribution des coefficients d'échange, soit  $\sigma(HTC)$  permettant ainsi de minimiser la distribution non-uniforme des coefficients d'échange autour du moule.

Une fois la convergence des calculs d'optimisation atteinte, un point candidat qui représente une conception géométrique optimale est généré. Elle permet de respecter les critères d'optimisation définis ci-dessus. La nouvelle conception géométrique des obstacles et donc du moule représentatif est illustrée par la Figure 36. Cette dernière est relativement évidente dans le cas simple que nous avons considéré. Elle consiste à utiliser de longs obstacles en gardant de petites ouvertures près des surfaces du moule (cf. Figure 36). Avec cette conception, l'écoulement d'air est bloqué loin des surfaces du moule dans la section de travail à cause des pertes de charge importantes imposées par ces obstacles. Par conséquent, l'écoulement d'air passe à travers ces petites ouvertures mais avec une vitesse importante conduisant donc à une augmentation des coefficients d'échange convectifs.

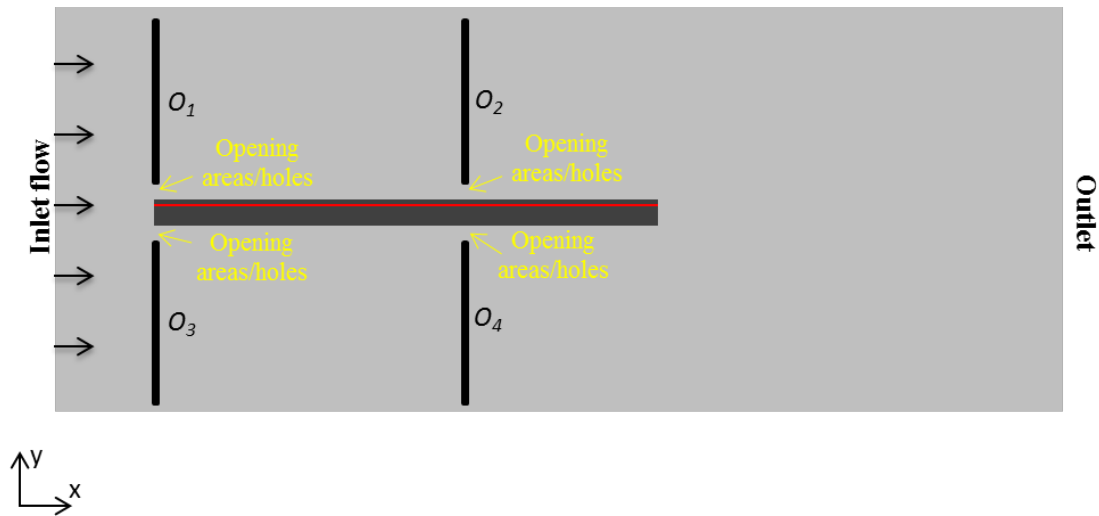


**Figure 36 La nouvelle conception géométrique optimale des obstacles**

Cette conception permet l'intensification des coefficients d'échange autour des surfaces du moule d'environ 263% par rapport à l'ancienne géométrie de base (Figure 16). La comparaison entre les quantités physiques qui caractérisent les échanges convectifs, c.à.d.  $\overline{HTC}$  et  $\sigma(HTC)$ , et issues de l'ancienne et de la nouvelle géométrie est présentée dans le Tableau 7.

**Tableau 7 Comparaison entre l'ancienne et la nouvelle géométrie**

	$\overline{HTC}$ (W/m <sup>2</sup> .K)	$\sigma$ (HTC) (W/m <sup>2</sup> .K)	CV (%)
Ancien design	210	59	28
Nouveau design	764	125	16

D'autre part, il a été constaté que le coefficient de variation (CV) a diminué avec la nouvelle conception optimale (cf. Tableau 7). Cela signifie que la dispersion des valeurs des coefficients d'échange par rapport à la valeur moyenne a été réduite. Ce résultat permet ainsi de déduire que l'uniformité des coefficients d'échange a été améliorée autour des surfaces du moule avec la nouvelle conception géométrique. Il faut noter que le coefficient de variation (CV) permet de mesurer la dispersion des points dans une série de données autour de la moyenne. Il représente le rapport de l'écart-type à la moyenne, et c'est une mesure statistique utile pour comparer le degré de variation d'une série de données à une autre, même si les moyennes sont différentes les unes des autres.

Toutefois, l'ensemble des résultats numériques obtenus dans le cas d'un moule représentatif nécessite un travail de validation par des essais expérimentaux comme il a été procédé précédemment pour les cas monochargement et multichargement.

## ***5. Conclusion et perspectives***

Un autoclave modèle à l'échelle réduite a été conçu et fabriqué en se basant sur les lois de similitude. Ce banc d'essais est capable de recréer les phénomènes physiques existant dans un autoclave réel notamment l'écoulement turbulent de gaz et les échanges thermiques convectifs autour de moules de formes et de géométries variées représentatifs d'outillages industriels. Dans cette étude, des moules simples de forme parallélépipédique ont été utilisés. Un des principaux avantages de ce système est la facilité d'utilisation d'instruments de mesure non intrusifs tels que la PIV et la caméra infrarouge pour l'étude des champs de vitesse et de la distribution des coefficients d'échange respectivement. Plusieurs configurations ont été étudiées telle que l'installation d'un ou plusieurs moules dans la section de travail de l'autoclave modèle ainsi que la définition d'un moule avec ses supports. En parallèle, des modèles numériques qui représentent les configurations d'études expérimentales ont été construits avec le code CFD Ansys Fluent 16©. L'avantage principal de ces modèles est leur capacité à mener des études paramétriques permettant d'établir des relations entre des conceptions géométriques et les phénomènes physiques étudiés.

L'ensemble des résultats aérodynamiques et thermiques obtenus montrent une bonne corrélation entre le champ de vitesse et la distribution des coefficients d'échange à la surface des moules. Ces résultats montrent un bon accord avec les conclusions rapportées par d'autres études scientifiques, concernant l'apparition de la zone de séparation et de recollement de la couche limite et son influence sur le comportement des échanges convectifs dans le cas d'un seul moule installé dans la section d'étude par exemple. De plus, la comparaison entre les résultats numériques, aérodynamiques et thermiques, et ceux issus des mesures expérimentales a montré un bon accord permettant de valider le modèle numérique.

Les résultats principaux obtenus à partir de ce travail ont montré une distribution non uniforme des coefficients d'échange convectifs autour des moules. Dans le cas d'un procédé en autoclave réel avec des pièces composites ayant des géométries plus complexes et des formes aérodynamiquement défavorables, cette hétérogénéité peut être aggravée conduisant donc à la présence de gradients de température importants au sein des pièces composites fabriquées. La présence de ces gradients thermiques peut affecter la qualité d'une pièce à la fin du cycle de cuisson.

Dans le cas d'un moule équipé par des supports et représentatif d'un cas industriel réel, les résultats numériques ont montré la présence d'un écoulement complexe et non uniforme, caractérisé par la présence des zones mortes et des points de stagnation. La projection de ces résultats sur le cas d'un moule industriel réel et caractérisé par la présence des plusieurs points d'arrêt permet de déduire que l'hétérogénéité de la distribution des coefficients d'échange est beaucoup plus importante et que ces



coefficients ont une faible intensité. De plus, la présence des points de stagnation et des zones mortes à faible vitesses peut contribuer à l'apparition de la convection mixte.

Une étude d'optimisation de la conception géométrique des supports du moule représentatif et couplée avec des méthodes d'approximations a été menée dans un cas simple. L'étude a réussi à proposer une conception géométrique des obstacles qui permet d'intensifier les coefficients d'échange convectifs autour des surfaces du moule et de minimiser leur distribution hétérogène.

Toutefois, les résultats numériques issus de l'outil CFD concernant l'étude d'un moule représentatif, et en particulier les résultats d'optimisation, nécessite un travail de validation par des essais expérimentaux. Ces essais aérodynamiques et thermiques devront être réalisés dans des futurs travaux.

Ces travaux doivent inclure ainsi une investigation des phénomènes de convection mixte permettant de déterminer leurs conditions d'apparition, surtout dans le cas de moule avec des géométries plus complexes. Une meilleure compréhension des conditions d'apparition de ces phénomènes permet de déduire l'existence ou pas d'un couplage entre l'écoulement et les mécanismes de transfert thermique. Cela peut être utile pour simplifier les modèles de simulation numériques surtout dans le cas d'un modèle complexe 3D. Physiquement, le phénomène de convection mixte dépend essentiellement de la vitesse de l'écoulement ainsi que de la température de surface. De ce fait, l'étude de la convection mixte peut être réalisée en utilisant l'autoclave modèle fabriqué. En effet, ce banc d'essais permet de varier et d'imposer différentes températures de surface et différents débits d'air. Les résultats obtenus peuvent être utilisés pour déterminer les abaques d'apparition de convection mixte.

## Liste des références

- [1] A. Johnston, An integrated model of the development of process-induced deformation in autoclave processing of composite structures, The University of British Columbia, 1997.
- [2] N. Slesinger, T. Shimizu, A. Poursartip, A.R.A. Arafath, Heat transfer coefficient distribution inside an autoclave, in: Proc. 17Th Int. Conf. Compos. Mater., Edinburgh, UK, 2009.
- [3] M.K. Telikicherla, M.C. Altan, F.C. Lai, Autoclave curing of thermosetting composites: process modeling for the cure assembly, *Int. Commun. Heat Mass Transf.* 21 (1994) 785–797.
- [4] P.F. Monaghan, M.T. Brogan, P.H. Oosthuizen, Heat transfer in an autoclave for processing thermoplastic composites, *Compos. Manuf.* 2 (1991) 233–242. <http://linkinghub.elsevier.com/retrieve/pii/0956714391901457>.
- [5] A.R. Upadhyaya, G.N. Dayananda, G.M. Kamalakannan, J. Ramaswamy Setty, J. Christopher Daniel, Autoclaves for aerospace applications: issues and challenges, *Int. J. Aerosp. Eng.* 2011 (2011) 1–11. <http://www.hindawi.com/journals/ijae/2011/985871/> (accessed January 20, 2015).
- [6] A. Labban, P. Mousseau, R. Deterre, J.-L. Bailleul, Curing cycle optimization of a thick-section rubber part, *Rubber Chem. Technol.* 83 (2010) 331–348.
- [7] A. Labban, P. Mousseau, J.L. Bailleul, R. Deterre, Optimization of thick rubber part curing cycles, *Inverse Probl. Sci. Eng.* 18 (2010) 313–340. doi:10.1080/17415971003589517.
- [8] M. Péron, R. Cardinaud, N. Lefèvre, J. Aubril, V. Sobotka, N. Boyard, S. Le Corre, PvT-HADDOC : A multi-axial strain analyzer and cure monitoring device for thermoset composites characterization during manufacturing, *Compos. Part A.* 101 (2017) 129–142. doi:10.1016/j.compositesa.2017.06.004.
- [9] V. Antonucci, M. Giordano, S. Inerraimparato, L. Nicolais, Analysis of heat transfer in autoclave technology, *Polym. Compos.* 22 (2001) 613–620. doi:10.1002/pc.10564.
- [10] T.A. Weber, J.-C. Arent, L. Münch, M. Duhovic, J.M. Balvers, A fast method for the generation of boundary conditions for thermal autoclave simulation, *Compos. Part A.* 88 (2016) 216–225. <http://dx.doi.org/10.1016/j.compositesa.2016.05.036>.
- [11] A. Johnston, P. Hubert, R. Vaziri, A. Poursartip, An investigation of autoclave convective heat transfer, in: *Des. Manuf. Compos.*, 1998: pp. 106–113.
- [12] N.E.J. Kluge, Experiments and numerical modelling of the SMC and autoclave processes, Lulea University of Technology, 2015.
- [13] N.S. Ghariban, A. Haji-Sheikh, D.Y.S. Lou, Heat transfer in autoclaves, in: *ICHMT Int. Symp. Manuf. Mater. Process.*, Dubrovnik, 1990: pp. 833–848.

- [14] F.C. Campbell, Chapter 6: Curing: It's a Matter of Time (t), Temperature (T) and Pressure (P), in: J. Flake Campbell (Ed.), *Manuf. Process. Adv. Compos.*, First ed., Elsevier Science, 2003: pp. 175–179.
- [15] N.E.J. Olsson, T.S. Lundstrom, L. Westerberg, T. Nyman, Flow and heat transfer inside an autoclave, in: *Proc. FPCM11 Conf.*, Auckland, 2012: pp. 188–195.
- [16] Scholtz Maschinenbau, (n.d.). <https://www.scholz-autoclaves.com/>.
- [17] Z. Cheng, W. Yonggui, L. Xianzhu, Z. Boming, Y. Guangquan, J. Peng, Research with CFX software on frame mould temperature field simulation in autoclave process, *Polym. Polym. Compos.* 17 (2009) 325–336.
- [18] F. Chen, L. Zhan, Y. Xu, Modelling and simulation for temperature distribution of mold during autoclave forming process, in: *Proc. 12th Int. Conf. Heat Transf. Therm. Eng. Environ.*, Geneva, 2014: pp. 80–88.
- [19] T. Ota, H. Nishiyama, A correlation of maximum turbulent heat transfer coefficient in reattachment flow region, *Int. J. Heat Mass Transf.* 30 (1987) 1193–1200. doi:10.1016/0017-9310(87)90048-2.
- [20] T. Ota, N. Kon, Heat transfer in the separated and reattached flow over blunt flat plates - Effects of nose shape, *Int. J. Heat Mass Transf.* 22 (1979) 197–206.
- [21] T. Ota, A Survey of Heat Transfer in Separated and Reattached Flows, *Appl. Mech. Rev.* 53 (2000) 219–235. doi:10.1115/1.3097351.
- [22] E.M. Sparrow, S.S. Kang, W. Chuck, Relation between the points of flow reattachment and maximum heat transfer for regions of flow separation, *Int. J. Heat Mass Transf.* 30 (1987) 1237–1246. doi:10.1016/0017-9310(87)90157-8.
- [23] T. Ota, N. Kon, Heat transfer in the separated and reattached flow on a blunt flat plate, *J. Heat Transfer.* 96 (1974) 459–462.
- [24] The Engineering ToolBox, (n.d.). [https://www.engineeringtoolbox.com/air-properties-d\\_156.html](https://www.engineeringtoolbox.com/air-properties-d_156.html).
- [25] L. Cattafesta, C. Bahr, J. Mathew, Fundamentals of wind-tunnel design, *Encycl. Aerosp. Eng.* (2010) 1–10. doi:10.1002/9780470686652.eae532.
- [26] R.D. Mehta, P. Bradshaw, Design rules for small low speed wind tunnels, *Aeronaut. J.* 83 (1979) 443–453.
- [27] J. H. Bell, R. D. Mehta, *Contraction design for small low-speed wind tunnels*, Stanford, 1988.
- [28] R.D. Blevins, Chapter 7: nozzles, diffusers, and venturis, in: N.Y.V.N. Reinhold (Ed.), *Appl. Fluid Dyn. Handb.*, New York, 1984: pp. 144–163.
- [29] I.E. Idel'cik, *Memento des Pertes de Charge: coefficients de pertes de charge singulières et de pertes de charge par forttement*, First edi, Paris, 1968.
- [30] PCM INNOVATION, (n.d.). <https://www.pcminnovation.com/en/molds-for-composites/>.

- [31] L. Jiao, Z. Yan-xuan, G. Pi-hai, G. Chang-tao, Numerical simulation and PIV experimental study of the effect of flow fields around tube artificial reefs, *Ocean Eng.* 134 (2017) 96–104. doi:10.1016/j.oceaneng.2017.02.016.
- [32] P. Singh, B.V. Ravi, S. V. Ekkad, Experimental and numerical study of heat transfer due to developing flow in a two-pass rib roughened square duct, *Int. J. Heat Mass Transf.* 102 (2016) 1245–1256. doi:10.1016/j.ijheatmasstransfer.2016.07.015.
- [33] M.L. Hoang, P. Verboven, J. De Baerdemaeker, B.M. Nicolai, Analysis of the air flow in a cold store by means of computational fluid dynamics, *Int. J. Refrig.* 23 (2000) 127–140. doi:10.1016/S0140-7007(99)00043-2.
- [34] Q. Chen, Comparison of different k- $\epsilon$  models for indoor air flow computations, *Numer. Heat Transf. Part B.* (1995) 353–369.
- [35] D.C. Wilcox, *Turbulence Modeling for C.F.D.*, DCW Industries, Inc., La cañada, California, 1994.
- [36] B.E. Launder, On the modeling of turbulent industrial flows, in: *Proc. Comput. Methods Appl. Sci.*, Elsevier, 1992: pp. 91–102.
- [37] Ansys, *Lecture 7: Turbulence modeling*, (2015).
- [38] H. Yanaoka, H. Yoshikawa, T. Ota, Numerical simulation of laminar flow and heat transfer over a blunt flat plate in square channel, *J. Heat Transfer.* 124 (2002) 8–16. doi:10.1115/1.1420715.
- [39] M. Kiya, K. Sasaki, Free-stream turbulence effects on a separation bubble, *J. Wind Eng. Ind. Aerodyn.* 14 (1983) 373–386. doi:http://dx.doi.org/10.1016/0167-6105(83)90039-9.
- [40] A. Kondjoyan, F. Péneau, H.-C. Boisson, Effect of high free stream turbulence on heat transfer between plates and air flows: a review of existing experimental results, *Int. J. Therm. Sci.* 41 (2002) 1–16. doi:10.1016/S1290-0729(01)01299-6.
- [41] J. Wen, H. Yang, G. Jian, X. Tong, K. Li, S. Wang, Energy and cost optimization of shell and tube heat exchanger with helical baffles using Kriging metamodel based on MOGA, *Int. J. Heat Mass Transf.* 98 (2016) 29–39. doi:10.1016/j.ijheatmasstransfer.2016.02.084.
- [42] J.H. Gerrard, The mechanics of the formation region of vortices behind bluff bodies, *J. Fluid Mech.* 25 (1966) 401–413. doi:10.1017/S0022112066001721.

# Table of contents

<b><u>Nomenclature.....</u></b>	<b><u>v</u></b>
---------------------------------	-----------------

<b><u>General Introduction.....</u></b>	<b><u>1</u></b>
---	-----------------

<b><u>Chapter 1 State of the art.....</u></b>	<b><u>7</u></b>
---	-----------------

<b>1.1 GENERAL CONTEXT .....</b>	<b>11</b>
1.1.1 Introduction to composite materials.....	11
1.1.1.1 Matrix materials.....	11
1.1.1.2 Reinforcing materials .....	12
1.1.1.3 Highlights and applications .....	13
1.1.2 Manufacturing methods of composite materials.....	15
1.1.3 Challenges in manufacturing of polymer matrix composites .....	18
<b>1.2 AUTOCLAVE MANUFACTURING PROCESS .....</b>	<b>20</b>
1.2.1 Functioning of autoclave systems.....	20
1.2.2 Main physical phenomena within autoclaves .....	24
1.2.2.1 Gas flow pattern.....	24
1.2.2.2 Heat transfer mechanisms.....	28
1.2.2.2.1 Convection heat transfer .....	28
1.2.2.2.2 Radiative heat transfer .....	35
1.2.2.2.3 Conduction heat transfer and chemical transformation.....	38
<b>1.3 FLOW AND HEAT TRANSFER AROUND A BLUFF BODY .....</b>	<b>44</b>
1.3.1 Introduction.....	44
1.3.2 Flow field description .....	45
1.3.3 Convective heat transfer description.....	51
1.3.4 Summary .....	54
<b>1.4 PARTIAL CONCLUSION .....</b>	<b>55</b>
<b>LIST OF REFERENCES.....</b>	<b>56</b>

<b><u>Chapter 2 Design and Fabrication of the Model Autoclave and associated instrumentation.....</u></b>	<b><u>61</u></b>
---	------------------

<b>2.1 PRINCIPLE OF THE MODEL AUTOCLAVE .....</b>	<b>65</b>
<b>2.2 DIMENSIONAL ANALYSIS AND SIMILARITY LAWS.....</b>	<b>66</b>
<b>2.3 DESIGN STRATEGY OF THE MODEL AUTOCLAVE.....</b>	<b>69</b>
2.3.1 Application of similarity laws.....	69

2.3.1.1	Prototype autoclave .....	69
2.3.1.2	Working section of the model autoclave .....	70
2.3.1.2.1	Application of the geometric similarity .....	70
2.3.1.2.2	Application of the dynamic similarity .....	71
2.3.1.2.3	Application of the energetic similarity .....	74
2.3.1.2.4	Summary of the applied similarity conditions .....	75
2.3.2	Determination of the model autoclave concept .....	77
2.3.3	Presentation of the designed model autoclave .....	78
<b>2.4</b>	<b>AERODYNAMIC INSTRUMENTATION AND MEASUREMENT METHODOLOGY .....</b>	<b>82</b>
2.4.1	Flow field measurement .....	82
2.4.2	Introduction to the PIV technique .....	82
2.4.3	Description of the employed PIV system (Laser + Camera) .....	84
2.4.4	Measurement and post-processing methodology .....	85
<b>2.5</b>	<b>VALIDATION OF THE MODEL AUTOCLAVE .....</b>	<b>88</b>
2.5.1	Procedure of the validation work .....	88
2.5.2	Results of the validation work .....	89
<b>2.6</b>	<b>DESIGN OF THE MODEL MOLD .....</b>	<b>95</b>
2.6.1	Application of the geometrical similarity condition .....	95
2.6.2	Concept of the model mold .....	95
2.6.3	Thermal instrumentation and measurement methodology .....	97
2.6.3.1	Measurement of $T_{mx}$ .....	98
2.6.3.2	Measurement of $\phi_{cx}$ .....	99
2.6.3.3	Measurement of $HTC$ .....	102
<b>2.7</b>	<b>INTER-PART SHADOWING EFFECTS INVESTIGATION .....</b>	<b>103</b>
<b>2.8</b>	<b>STUDY OF A REPRESENTATIVE MOLD .....</b>	<b>104</b>
<b>2.9</b>	<b>PARTIAL CONCLUSION .....</b>	<b>107</b>
	List of references .....	108

---

### ***Chapter 3 CFD analysis of the Model Autoclave.....111***

<b>3.1</b>	<b>CONTEXT OF THE NUMERICAL STUDY .....</b>	<b>115</b>
<b>3.2</b>	<b>NUMERICAL MODEL OF A SINGLE MOLD .....</b>	<b>116</b>
3.2.1	Geometry .....	116
3.2.2	Governing equations and numerical methods .....	117
3.2.2.1	Navier-Stokes equations .....	117
3.2.2.2	Turbulence models .....	120
3.2.2.3	Materials .....	121
3.2.2.3.1	Fluid domain .....	121
3.2.2.3.2	Solid domain .....	121
3.2.2.4	Boundary conditions .....	122
3.2.2.4.1	Flow boundary conditions .....	122
3.2.2.4.2	Thermal boundary conditions .....	123
3.2.2.5	Mesh .....	123
3.2.2.5.1	Wall modeling strategy and solid domain meshing .....	123
3.2.2.5.2	Fluid domain meshing .....	124
3.2.2.5.3	Mesh quality test .....	124

3.2.2.6	Solving.....	126
3.2.3	Numerical results and discussion.....	126
3.2.3.1	Numerical convergence of the physical quantities.....	127
3.2.3.2	Verification of the mass and energy conservation.....	128
3.2.3.3	Numerical results vs literature.....	128
3.2.3.3.1	Flow field behavior.....	129
3.2.3.3.2	Wall shear stress coefficient.....	132
3.2.3.3.3	Pressure coefficient.....	133
3.2.3.3.4	Study of $Xr$ .....	134
3.2.3.3.5	Nusselt distribution.....	136
<b>3.3</b>	<b>NUMERICAL MODEL OF THE INTER-PART SHADOWING EFFECTS INVESTIGATION .....</b>	<b>139</b>
3.3.1	Geometry.....	139
3.3.2	Governing equation and numerical method.....	139
3.3.3	Verification of the numerical model.....	140
3.3.4	Numerical results and discussion.....	140
<b>3.4</b>	<b>NUMERICAL MODEL OF THE “REPRESENTATIVE MOLD” .....</b>	<b>141</b>
3.4.1	Geometry.....	141
3.4.2	Governing equation and numerical method.....	142
3.4.3	Verification of the numerical model.....	144
3.4.4	Numerical results and discussion.....	144
<b>3.5</b>	<b>PARTIAL CONCLUSION .....</b>	<b>145</b>
	<b>List of references .....</b>	<b>146</b>

---

## ***Chapter 4 Flow Field Structure and Convective Heat Transfer Distribution around Molds .....***

---

<b>4.1</b>	<b>STUDY OF ONE MODEL MOLD.....</b>	<b>153</b>
4.1.1	Study of the flow field .....	153
4.1.1.1	Procedure of the study .....	153
4.1.1.2	Results of the flow field.....	154
4.1.2	Study of the convective heat transfer coefficient.....	161
4.1.2.1	Procedure of the study .....	161
4.1.2.2	Thermal results .....	163
4.1.2.2.1	Infrared thermography .....	163
4.1.2.2.2	Thermocouples acquisition .....	168
4.1.2.2.3	Determination of the convective heat transfer distribution ( $\phi_{cx}$ ) .....	170
4.1.2.2.4	Determination of the $HTC$ distribution .....	171
4.1.3	Summary of the results .....	174
<b>4.2</b>	<b>STUDY OF THE INTER-PART SHADOWING PHENOMENON .....</b>	<b>176</b>
4.2.1	Study of the flow field .....	177
4.2.1.1	Procedure of the study .....	177
4.2.1.2	Results of the flow field.....	178
4.2.2	Study of the convective heat transfer coefficient.....	184
4.2.2.1	Procedure of the study .....	184
4.2.2.2	Thermal results .....	184
4.2.2.2.1	Infrared thermography .....	184

4.2.2.2.2	Determination of the $HTC$ distribution .....	186
4.2.3	Summary of the results .....	187
4.2.4	Parametric study of $d$ .....	189
<b>4.3</b>	<b>STUDY OF THE “REPRESENTATIVE MOLD” .....</b>	<b>193</b>
4.3.1	Study of the flow field .....	193
4.3.2	Study of the convective heat transfer coefficient.....	195
4.3.3	Parametric study and optimization.....	195
4.3.3.1	Creation of the experimental design (DOE) .....	197
4.3.3.1.1	Design variables.....	197
4.3.3.1.2	Choice of the type of the design space .....	198
4.3.3.1.3	Objectives functions .....	199
4.3.3.1.4	Summary.....	199
4.3.3.2	Surrogate model.....	199
4.3.3.3	Optimization study .....	203
<b>4.4</b>	<b>PARTIAL CONCLUSION .....</b>	<b>209</b>
	<b>List of references .....</b>	<b>210</b>
	<b><u>General Conclusion and Perspectives.....</u></b>	<b><u>213</u></b>
	<b><u>Appendix A Design of the Model Autoclave.....</u></b>	<b><u>219</u></b>
	<b><u>Appendix B Sensitivity of mesh and turbulence model .....</u></b>	<b><u>239</u></b>



# Nomenclature

## List of dimensionless numbers

$Re$	Reynolds number ( $= U_{\infty} l_c / \nu$ )	-
$Pr$	Prandtl number ( $= C_p \mu / \lambda$ )	-
$Bi$	Biot number ( $= HTCl_c / \lambda$ )	-
$Nu$	Nusselt number ( $= HTCl_c / \lambda$ )	-
$Fr$	Froude number ( $= U_{\infty}^2 / g l_c$ )	-
$We$	Weber number ( $= \rho U_{\infty}^2 l_c / Y$ )	-
$Eu$	Euler number ( $= P / \rho U_{\infty}^2$ )	-
$Ec$	Eckert number ( $= U_{\infty}^2 / C_p T_{\infty}$ )	-
$Gr$	Grashof number ( $= \rho^2 g \beta l_c^3 (T_w - T_{\infty}) / \mu^2$ )	-
$Ri$	Richardson number ( $= Gr / Re^2$ )	-

## List of symbols

$A$	Area	m <sup>2</sup>
$BR$	Blockage ratio	-
$c$	Contraction ratio	-
$C_f$	Friction coefficient	-
$C_p$	Specific heat capacity	J/(kg.K)
$CV$	Coefficient of variation	%
$D$	Diameter	m
$d$	Distance	m
$e$	Thickness	mm

$f$	Frequency	Hz
$g$	Gravity	m/s <sup>2</sup>
$H$	Height	m
$HP$	Heating power	W/m <sup>2</sup>
$HTC$	Local heat transfer coefficient	W/(m <sup>2</sup> .K)
$k$	Turbulent kinetic energy	m <sup>2</sup> /s <sup>2</sup>
$K$	Pressure drop coefficient	-
$k_l$	Coefficient of geometric scale	-
$l$	Length	m
$L$	Width	m
$l_c$	Characteristic length	m
$N$	Number (quantity)	-
$P$	Static pressure	kPa
$\Delta P$	Pressure loss	Pa
$Pe$	Perimeter	m
$Q$	Volume flow rate	m <sup>3</sup> /h
$q$	Heat transfer rate	W
$\dot{q}$	Energy source	W/m <sup>3</sup>
$R$	Radius	m
$R^2$	Coefficient of determination	-
$T$	Temperature	°C
$t$	Time	s
$t^*$	Pseudo-time	s
$TI$	Turbulence intensity	%
$U$	Time-average value of x-component of velocity	m/s

$u$	Instantaneous value of x-component of velocity	m/s
$u_T$	Friction velocity	m/s
$V$	Time-average value of y-component of velocity	m/s
$v$	Instantaneous value of y-component of velocity	m/s
$VM$	Velocity magnitude	m/s
$VO$	Volume	m <sup>3</sup>
$W$	Time-average value of z-component of velocity	m/s
$w$	Instantaneous value of z-component of velocity	m/s
$x$	Cartesian coordinates	m
$Xr$	Reattachment length	mm
$Y$	Surface tension	N/m
$y$	Cartesian coordinates	m
$y^+$	Dimensionless distance ( $= d_w u_T / \nu$ )	-
$\beta$	Open area ratio (porosity)	-
$\beta$	Coefficient of expansion	K <sup>-1</sup>
$\Gamma_1$	Gamma 1	-
$\varepsilon$	Turbulent kinetic energy dissipation	m <sup>2</sup> /s <sup>3</sup>
$\varepsilon$	Emissivity	-
$\theta$	Half of a diffuser angle	°
$\lambda$	Thermal conductivity	W/(m.K)
$\mu$	Dynamic viscosity	Pa.s
$\mu_T$	Turbulent viscosity	Pa.s
$\nu$	Kinematic viscosity	m <sup>2</sup> /s
$\rho$	Density	Kg/m <sup>3</sup>
$\sigma$	Standard deviation	-

$\sigma_c$	Stefan-Boltzmann constant	$\text{W}/(\text{m}^2 \cdot \text{K}^4)$
$\tau_w$	Wall shear stress	Pa
$\varphi$	Heat flux density	$\text{W}/\text{m}^2$
$\omega$	Specific dissipation rate	1/s

## Subscripts/Superscripts

$\infty$	Free stream value
$(\bar{\phantom{x}})$	Space-Averaged value
$(\phantom{x})'$	Fluctuating quantity
$c$	Convection
$h$	Heating
$l$	Loss
$m$	Mold
$mo$	Model
$max$	Maximum value
$N$	Normal
$p$	Prototype
$R$	Reattachment
$r$	Radiation
$ref$	Reference
$r.m.s.$	Root Mean Square
$t$	Total
$w$	Wall

# *General introduction*



In recent years, the use of high performance and lightweight composite materials has increased considerably in many industrial sectors, e.g., aerospace, aeronautical, yachting and automotive because of their high specific mechanical properties. However the quality enhancement of composite parts with the reduction of the manufacturing time represents a challenging task for the manufacturers in order to increase their quality/cost ratio. The existing manufacturing processes can be expensive and the quality of the produced parts can be significantly affected by many parameters. Among them, the uniformity of the temperature distribution during the forming is of primary importance. In fact, presence of thermal gradients can result in non-uniform degrees of cure in the part leading to residual stresses and finally a decrease of their mechanical properties. Many research projects are conducted to answer this issue. This is also in this context that the scientific research project, named “COMPETH”, was created. This project is an academic chair which aims to better understand and control heat transfer during manufacturing of high performance composite parts. This chair is divided into three complementary axes:

- the measurement and understanding of the thermo-physical properties of the composites materials, with a particular focus on the radiative properties, the kinetics of polymerization or crystallization and the associated dimensional removals
- the thermal control of manufacturing processes.
- the development of thermal measurement instruments

The “COMPETH” project was funded by the institute of research technology “IRT Jules Verne” in Nantes. It started in 2013 for 5 years, with the contribution of four industrial members: Airbus, Airbus Group Innovations (AGI), Daher and Solvay and two academic laboratories: the Laboratoire de Thermique et Énergie de Nantes (LTEN) and the Institut de Recherche en Génie Civil et Mécanique (GeM) specialized in thermal and mechanical engineering sciences respectively.

The “COMPETH” project includes six research work packages (WP) over the three main axes studies mentioned above:

- WP 1: Identification of the kinetics of crystallization and the strains during the manufacturing processes of composite materials taking into account the coupling with heat transfers.
- WP 2: Understanding of radiative properties of carbon-reinforced composite materials.
- WP 3: Design of non-intrusive and high sensitivity heat flux sensors in order to quantify the heat flux between a composite piece and its mold on one hand and between the composite piece and its environment on the other hand.

- WP 4: Installation of a platform dedicated to thermo-kinetic characterization.
- **WP 5: Analysis of convective transfer around simple molds inside a model autoclave.**
- WP 6: Analysis of heat transfers during the laser-assisted automated-tape placement of carbon/PEEK composites.

The work presented in this manuscript is a part of WP5 and is dedicated of convective transfer in autoclaves. These devices that correspond to convection pressure ovens enable the forming of composite material while minimizing the presence of porosity. However, the complex geometries of the molds disposed inside autoclaves generate non-uniform turbulent gas flow patterns around them leading to non-uniform heat transfer coefficients distribution between the circulating gas and the composite part. The knowledge of this distribution is nevertheless essential to control heat transfer within the composite part.

Autoclaves used for aeronautics applications can reach several meters in diameter for several tens of meters. Experimental measurements in such devices remain very tricky to perform. In this thesis it was then decided to manufacture our own autoclave at reduced scale. Its design was based on geometric, dynamic and energy similarity laws. It is able to recreate the main physical phenomena existing in the full scale autoclave, i.e. the turbulent flow field and the forced convective heat transfer around representative molds; while controlling the flow conditions. One of its most important features is the ease of use of non-intrusive measuring instruments such as the Particle Image Velocimetry (PIV) technique for the measurement of the velocity field and the infrared imaging camera for the study of the convective heat transfer coefficient distribution.

In addition to the experimental measurements, numerical models based on Computational Fluid Dynamics (CFD) methods were employed to calculate the turbulent velocity fields and the convective heat transfer coefficient distributions around the molds installed within the model autoclave. Ansys Fluent 16.0® was used.

Works presented in this manuscript are divided into four chapters:

- In the first one, a state of the art exposes the general context of the thesis by highlighting the autoclave manufacturing process and the associated problematic. The existing state of the art was established in order to point out the new contribution of this work.
- In Chapter 2, the design and fabrication of the model autoclave as well as its instrumentation is presented. The validation of this device is also presented.



- Chapter 3 is dedicated to CFD modeling of the model autoclave. Several configurations are tested. A parametric study in case of multi-loading is detailed.
- Experimental results and their comparisons with numerical ones are presented in Chapter 4. As expected a non-uniform distribution of heat transfer coefficient is obtained. Experimental results point out the limitation of 2D numerical approach even in very simple cases. Experimental approach in this autoclave model can be then an alternative to numerical approach, especially for multi-loading in where different configurations can be tested easily compared to 3D simulation.

Finally, the main achieved results as well as the possible future works are gathered in conclusion and perspectives.



# *Chapter 1*

## *State of the art*



## Table of contents

<b>Chapter 1 State of the art.....</b>	<b>7</b>
<b>1.1 GENERAL CONTEXT .....</b>	<b>11</b>
1.1.1 Introduction to composite materials.....	11
1.1.1.1 Matrix materials.....	11
1.1.1.2 Reinforcing materials .....	12
1.1.1.3 Highlights and applications .....	13
1.1.2 Manufacturing methods of composite materials.....	15
1.1.3 Challenges in manufacturing of polymer matrix composites .....	18
<b>1.2 AUTOCLAVE MANUFACTURING PROCESS .....</b>	<b>20</b>
1.2.1 Functioning of autoclave systems.....	20
1.2.2 Main physical phenomena within autoclaves .....	24
1.2.2.1 Gas flow pattern.....	24
1.2.2.2 Heat transfer mechanisms.....	28
1.2.2.2.1 Convection heat transfer .....	28
1.2.2.2.2 Radiative heat transfer .....	35
1.2.2.2.3 Conduction heat transfer and chemical transformation .....	38
<b>1.3 FLOW AND HEAT TRANSFER AROUND A BLUFF BODY .....</b>	<b>44</b>
1.3.1 Introduction.....	44
1.3.2 Flow field description .....	45
1.3.3 Convective heat transfer description.....	51
1.3.4 Summary .....	54
<b>1.4 PARTIAL CONCLUSION .....</b>	<b>55</b>
<b>LIST OF REFERENCES.....</b>	<b>56</b>



## **1.1 General context**

### **1.1.1 Introduction to composite materials**

The composite materials are often defined as heterogeneous and anisotropic materials. They consist of two or more chemically distinct constituents having a distinct interface, which separates them as reinforcing particle and matrix. Also, they have a unique combination of properties that are noticeably higher than the constituent properties. Generally, a discontinuous phase (called reinforcement) is embedded into a continuous phase (called matrix) of various kinds. Charges can be added. The reinforcement may be in the form of fibers or particles. Accordingly, two broad classifications are fibrous composites and particulate composites. However, focus is directed toward the fiber-reinforced polymer composites (FRPs) as they constitute a major category of composite materials with a wide range of applications.

The reinforcement provides the essential mechanical properties by fortifying the matrix in terms of strength and stiffness. The reinforcement fiber can be cut, aligned, placed in different ways to affect the properties of the resulting composite. On the other hand, the matrix, normally in a form of polymer resin, keeps the reinforcement in the desired orientation. It protects the reinforcement from chemical and environmental attack, and it bonds the reinforcement so that applied loads can be effectively transferred.

#### **1.1.1.1 Matrix materials**

Thermosets and thermoplastics are the two basic types of resin matrix used in the manufacturing of fiber-reinforced organic polymer composites [1].

The vast majority of structural composite materials uses thermoset resins as they improve the material's mechanical properties, providing enhances chemical resistance, heat resistance and structural integrity. In fact, the thermoset resins are initially liquids and they are cured under the action of heat, a catalyst and a hardener. The chemical transformation is irreversible and forms a cross-linked three-dimensional molecular network. The cross-linking process eliminates the risk of the product remelting when heat is applied, making thermoset resins ideal for high-heat applications such as electronics and appliances. Common thermoset resins include polyester resin, vinyl ester resin, epoxy, phenolic and polyurethane.

However, the thermoplastic matrix composite materials have become, in recent years, particularly attractive in many advanced industrial sectors such as aerospace, automotive, and aeronautics. The thermoplastic resins are generally carbon containing polymers synthesized by addition or condensation polymerization. This process forms macromolecules linked together by secondary bonds (Van der Waals, dipolar force or

hydrogen bonding...). Usually, these secondary forces can be easily overcome by thermal energy, making thermoplastics moldable at high temperatures. Thus the consolidation process of thermoplastic composites is completely reversible as no chemical bonding takes place.

The use of thermoplastic resins has developed since the 1970s because they offer a number of advantages over thermosetting composites:

- Highly recyclable
- Aesthetically-superior finishes
- High-impact resistance
- Remolding/reshaping capabilities
- Chemical resistant
- Hard crystalline or rubbery surface options
- Eco-friendly manufacturing

Common thermoplastic resins used today include polyphenylene sulfide (PPS) and polyamide for the manufacturing of composites materials, PET (for water and soda bottles), polypropylene (packaging containers), polycarbonate (safety glass lenses), vinyl (window frames), polyethylene (grocery bags), PVC (piping) and nylon (footwear).

### 1.1.1.2 Reinforcing materials

Fibers, as reinforcing materials, are divided mainly into two families (see Figure 1.1):

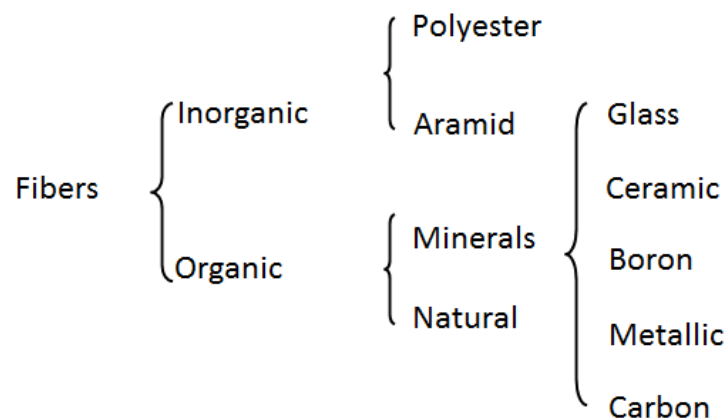


Figure 1.1 Main types of fibers [2]

As shown in Figure 1.1, the used reinforcement can be of very different natures and kinds. However, it is selected according to the desired properties required in the finished product.



Despite the existing various natures of reinforcements, three basic types of fiber, as reinforcing materials, are used in the advanced composite industries [1]:

- the carbon fibers: carbon fiber has high strength and high stiffness and used in a variety of structural and electrical applications.
- the glass fibers: It is the most common reinforcing material for polymer matrix composites, as they offer high strength at relatively low cost. However, they have poor abrasion resistance, poor adhesion to polymer matrix, and tendency to absorb moisture.
- the aramid fibers: Aramid fibers, more commonly known under the trade name of “Kevlar”, are made from aromatic polyamides and possess unique properties like high tensile strength and modulus, temperature stability, dimensional stability, flex performance, textile processability, and resistance to chemical.

We can also mention the natural fibers, which are experiencing actually a high growth. It is essentially about the vegetable fibers such as the flax fibers or the hemp fibers.

In a composite material, the fibers are generally arranged and organized in such way as to form a particular architecture. Thus the fiber architecture refers to the arrangement of fibers, which can be either linear, two-dimensional, or three dimensional [3].

### **1.1.1.3 Highlights and applications**

Composite materials have emerged as a major class of structural elements. These materials are light weight, flexible, and also have high corrosion resistance, impact strength, fatigue strength, etc... [4].

Because of these properties, composite materials are being considered as a replacement of traditional materials used in the aerospace, automotive, and other industries. The specialty of composites is that the engineering properties, which are required in the end product, can be achieved by a careful selection of matrix and reinforcement. The outstanding features of fiber-reinforced polymer composites are their high specific stiffness, high specific strength, and controlled anisotropy, which make them very attractive structural materials [4].

In fact in the aerospace industry, the benefits of exploiting the excellent specific strength and stiffness properties (strength and stiffness per unit weight) of composites in terms of lightweight structural design are immediately apparent. Indeed, the percentage of used composite materials for the construction of large aircrafts has increased significantly in recent years (see Figure 1.2 and Figure 1.3), with more than 50% for the latest Airbus A350.

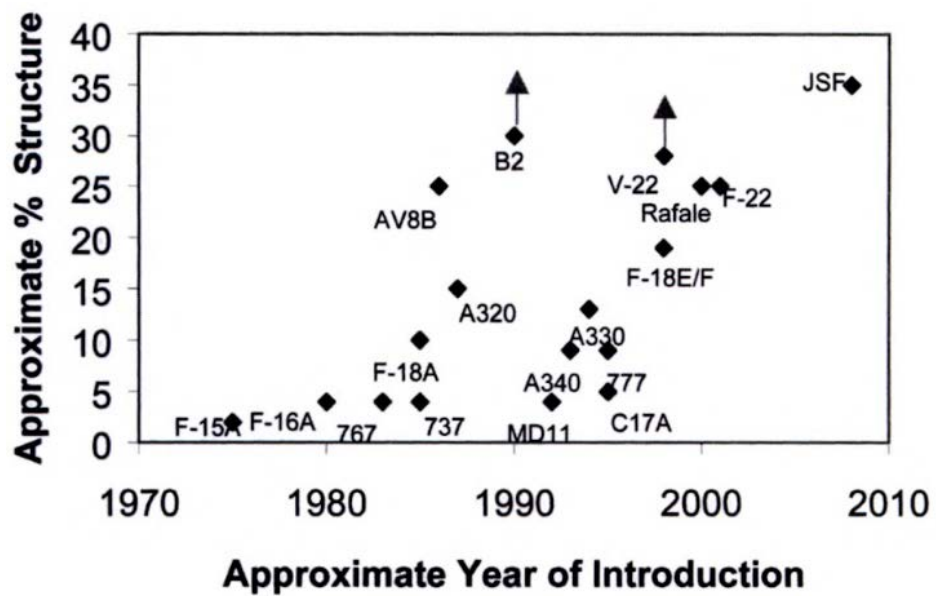


Figure 1.2 Growth of use of advanced composites in airframe structure [5]

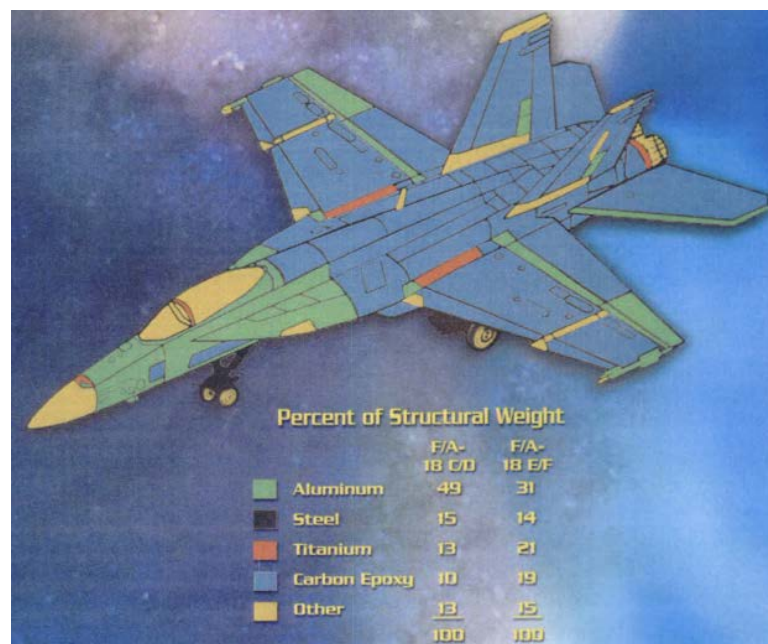


Figure 1.3 Schematic diagram of fighter aircraft F-18 E/F. For comparison details of the structure of the earlier C/D model are also provided in the inset table [5]

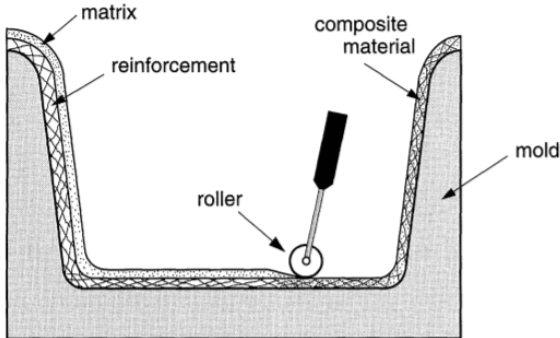
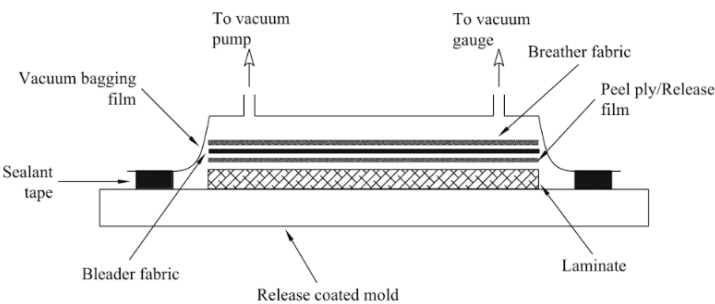
## 1.1.2 Manufacturing methods of composite materials

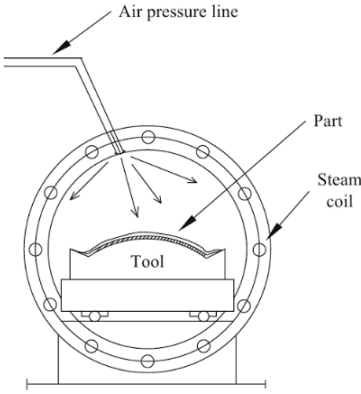
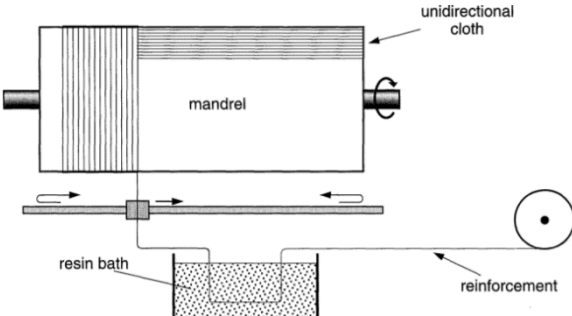
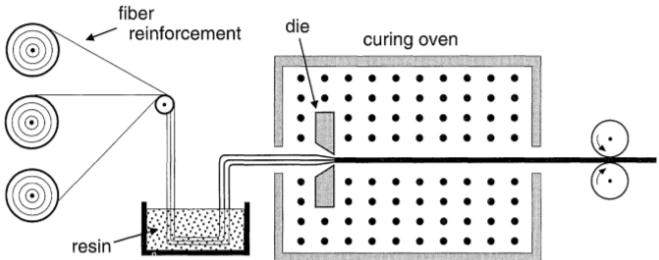
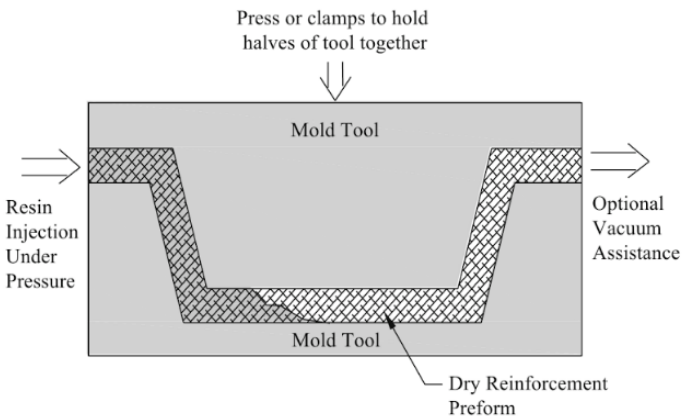
The manufacturing of polymers and the development of new technologies for their composites have contributed a lot in the composite manufacturing science. There are several methods to manufacture the fiber-reinforced polymer composites, such as vacuum bagging, autoclave, filament winding, pultrusion, resin transfer molding (RTM) and other liquid composite molding (LCM). The descriptive schemas of the main and the most often used currently available manufacturing methods for the fiber-reinforced polymer composites are presented in Table 1.1[4,6].

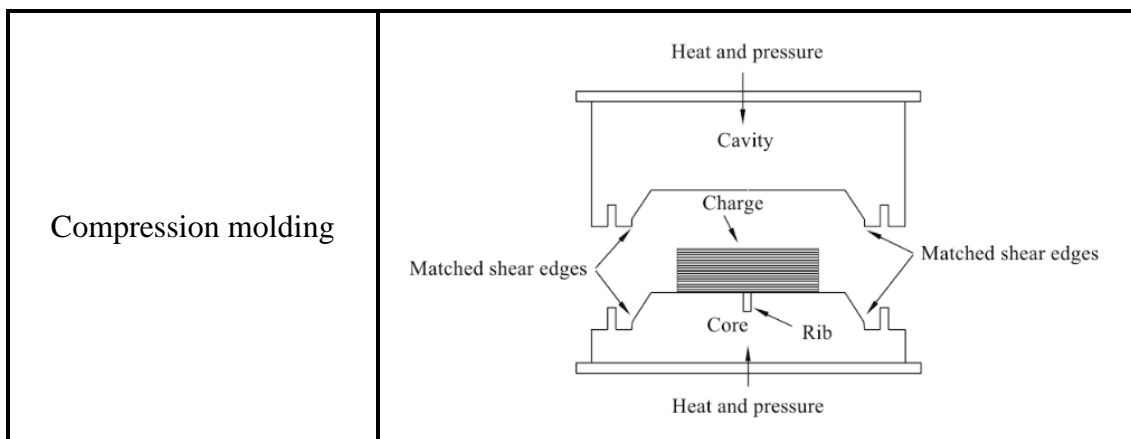
Despite the differences of the mechanisms applied during these manufacturing methods, the latter require always:

- a mechanical action, such as the application of pressing forces in order to remove the entrapped air and the excess resin, or the application of pressure injection to pump the resin.
- a thermal action, such as the application of a temperature curing cycle in order to process the resin.

**Table 1.1 The main current manufacturing methods [4,6]**

Hand layup molding	 <p>The diagram illustrates the hand layup molding process. It shows a cross-section of a mold cavity. A layer of reinforcement (represented by a cross-hatched pattern) is being applied to the inner surface of the mold. A matrix (represented by a solid grey area) is being applied over the reinforcement. A roller is shown pressing the layers together. The final product is labeled as 'composite material'.</p>
Vacuum bag molding	 <p>The diagram illustrates the vacuum bag molding process. It shows a cross-section of a mold assembly. A 'Release coated mold' is at the bottom. Above it is a 'Laminate' (cross-hatched). Above the laminate is a 'Peel ply/Release film'. Above that is a 'Breather fabric'. Above the breather fabric is a 'Vacuum bagging film'. The entire assembly is sealed with 'Sealant tape'. Arrows indicate connections: 'To vacuum pump' from the top of the bagging film, and 'To vacuum gauge' from the side of the bagging film. A 'Bleeder fabric' is also shown between the laminate and the peel ply.</p>

<p><b>Pressure bag molding</b></p>	 <p>The diagram shows a cross-section of a pressure bag molding setup. A mold tool is placed inside a bag, which is surrounded by a steam coil. An air pressure line is connected to the bag, and a part is being formed inside the bag.</p>
<p><b>Filament winding</b></p>	 <p>The diagram illustrates the filament winding process. A mandrel is rotated, and a unidirectional cloth is wound around it. A resin bath is used to impregnate the cloth, and a reinforcement is applied to the mandrel.</p>
<p><b>Pultrusion</b></p>	 <p>The diagram shows the pultrusion process. Fiber reinforcement and resin are fed into a die, which is then cured in a curing oven. The resulting part is then cut into sections.</p>
<p><b>Resin Transfer Molding (RTM)</b></p>	 <p>The diagram depicts the Resin Transfer Molding (RTM) process. A mold tool is used to shape the part, and resin is injected under pressure. A dry reinforcement preform is placed in the mold, and optional vacuum assistance is used to ensure proper filling.</p>



However, among these various existing manufacturing methods, the pressure bag molding is widely used for the production of high quality composites items. In fact, the pressure, usually provided by compressed air or water, is applied to the flexible bag that covers the prepreg composite. The application of pressure forces out the entrapped air, vapors, and excess resin. It also facilitates better wetting of fibers. Thus, the pressure bag molding produces quality composites with high fiber content and lower void content.

This method requires disposable bagging material and high skill of the operators. An improvement of pressure bag molding is the use of autoclaves for curing of the composite. An autoclave enables the curing of composite at higher temperature so that the curing reaction is more efficient and viscosity goes down enhancing wetting of fibers.

Autoclaves are basically heated pressure vessels. These are usually provided with the vacuum system. The bagged layup is cured inside the autoclave as shown in the descriptive schema of the pressure bag molding in Table 1.1. The pressures required for curing are typically in the range of one to ten bars and takes several hours to complete the curing. This method accommodates higher temperature matrix resins having properties higher than the conventional resins, such as epoxies. Component size is limited by the autoclave size. It is mostly used in the aerospace industry to manufacture high-strength/weight ratio parts from pre-impregnated high-strength fibers for aircraft, spacecraft, and missiles. Conventionally, a high pressure is achieved by pressurized air systems, which have a risk of fire occurring within the autoclave. The use of inert nitrogen instead of air eliminates the risk of fire.

Autoclaves are widely used to cure high-performance fiber-reinforcement polymer composites at high temperature and pressure. This process involves application of higher heat and uniform pressure on the component during curing, which results in a denser and low void percentage product. The autoclave equipment and tooling are expensive and it is only suitable for high-end applications.

### 1.1.3 Challenges in manufacturing of polymer matrix composites

The composite materials have many advantages and can be tailored to meet the specific functional requirements, yet they are not popular in everyday products. This is because of the manufacturing difficulties and costs associated with the production of consumer goods at competitive pricing. Traditional metallic materials still dominate at many places, where a composite material might be more appropriate with respect to material economy and function.

The major obstacle in this direction is not the material cost in general; it is the manufacturing cost and time of a composite item [4]. The existing manufacturing methods are costly thereby increasing the product cost. No doubt, the technology for manufacturing of high-quality composite products (like in aerospace and automotive sector) is available, but the equipment, tooling, and running costs are so high that the production of general purpose items is not economical.

The manufacture of advanced composite parts involves the preparation of a network of fibers according to the desired shape of the component (preforming), impregnating this fiber network with the resin, and curing of the resin while the part is being supported. The major challenges are efficient handling of the fibers, getting high volume percent of fibers in the composites and applications of uniform pressure during the curing of resin.

Appropriate curing of the matrix is required to achieve required properties in the composites. The pressure, temperature, component geometry, and distribution of pressure over the surface of component are some of the deciding factors of quality product.

Composite materials cannot be utilized to their full potential unless we have the technology for competitive production of composite items. This is a major issue today and there is a need for innovation in manufacturing technology of composites.

Therefore, the increased use and wide applications of composite materials on one hand and the faced challenges and encountered difficulties in the manufacturing of composites parts on the other have fostered the scientific researches and investigations in this field. In this context, the industrial chair named “COMPETH” was created. The project was detailed in the *General introduction* and it includes the present thesis works under the workpackage 5 which is dedicated to the study of convective transfer inside an autoclave.

In the next section, the autoclave manufacturing process will be under scope. The functioning of the autoclave systems will be detailed carefully as a first step. Then the main occurred physical phenomena will be deduced and the existing state of the art

that aims to investigate it will be established and discussed. Also, the various experimental and numerical methodologies employed in these previous research studies will be exposed.

## **1.2 Autoclave manufacturing process**

The importance of the study of the autoclave manufacturing process arises from the fact that the autoclaves have become indispensable tools/equipment for processing high quality polymer composite aerospace/air craft structural components [7]. Today, in the aircraft industry, investments in this equipment are regarded to be strategically important. Autoclaves are now being used to produce very large aircraft components such as wing and fuselage. They can process a wide variety of materials, including thermoset [8] and thermoplastic [9] based composite aircraft parts with varying contours and complex shapes.

On the other hand, the quality requirements of the present aircraft industry are indeed most stringent. Therefore, there is a dire need to improve the efficiency and cost effectiveness of aircraft structural systems apart from ensuring reliable and consistent processing methods. The desired improvement should pass through minimizing the composite pieces porosities on one hand, and an increase in the composite parts loading within autoclaves coupled with reduction in time curing cycles on the other hand.

### **1.2.1 Functioning of autoclave systems**

Autoclaves are generally considered as pressure vessels and gas convection ovens of cylindrical shape. The conventional autoclaves are divided mainly into a central working section and a gas system duct for gas circulation. The schematic is shown in Figure 1.4. The large size of the fabricated structural components (wing and fuselage) has created the need for very large size autoclaves (typically 6 to 10 meters in length and 3 to 5 meters in diameter) in the industry.

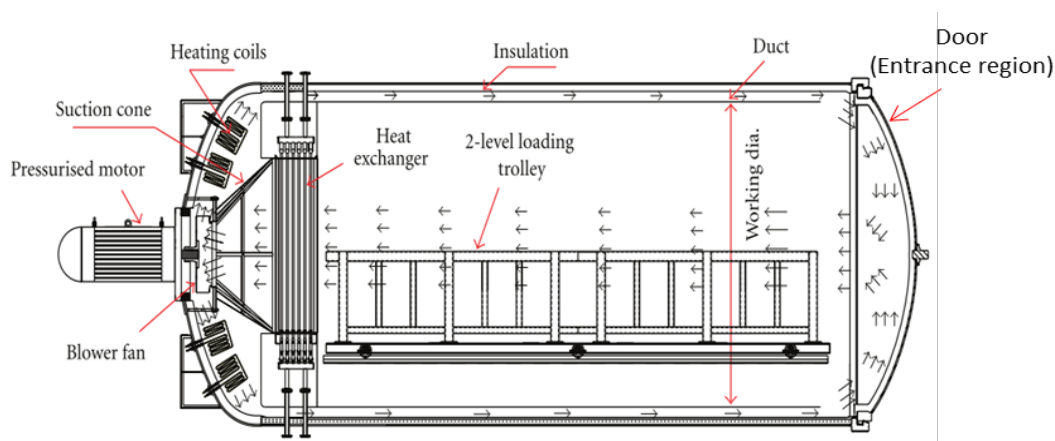
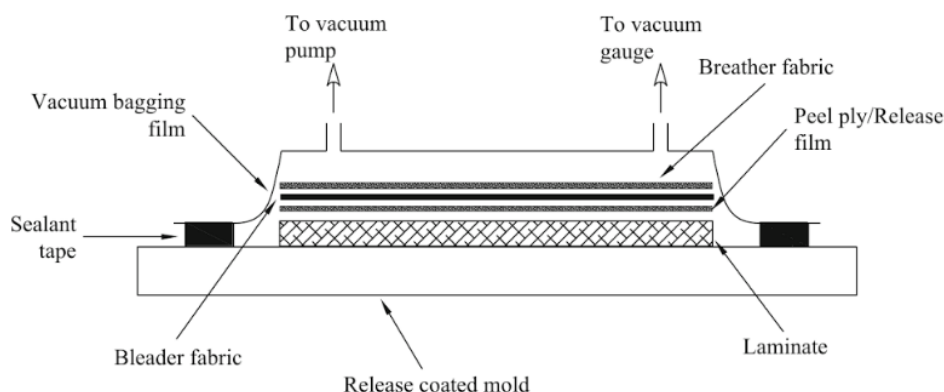


Figure 1.4 Schematic of air circulation and working section of an autoclave [10]



Composite prepregs, woven fiber mats impregnated with resin, are cut and laid up in the shape of the part. Then the laminate is placed on a mold, bagged and installed on a loading trolley and then introduced into the central working section of the autoclave. A typical schema of a bag-laminate-mold is shown in Figure 1.5.



**Figure 1.5 Schematic of a bag-laminate-mold autoclave assembly**

The polymeric composite materials are cured by exposure to various stages of elevated temperature and pressure for a predetermined length of time so-called cure cycle. A typical cure cycle for a fiber-reinforced polymer composite is shown in Figure 1.6.

The elevated temperature applied during the cure cycle provides the required heat to initiate and maintain chemical reactions, phase transitions and crystallization in the matrix material. On the other hand, the applied pressure provides the necessary force to consolidate the material, to squeeze out excess resins and to reduce the porosities in each ply in the case of thermoset polymer. The cure cycle should correspond to the resin systems used in order to produce a satisfactory laminate. For example, the epoxy resins used in the aeronautics industry require temperatures within 200 °C and pressures of 7 bars. The service temperatures of these epoxy resin-based structural components are restricted to about 120 °C. On the other hand, the cure cycle presented in Figure 1.6 corresponds to a continuous fiber-reinforced PEEK (APC-2). In fact, the magnitude and the duration of the temperature and the pressure applied during a cure cycle is a major factor in determining the quality and the performance of the finished part.

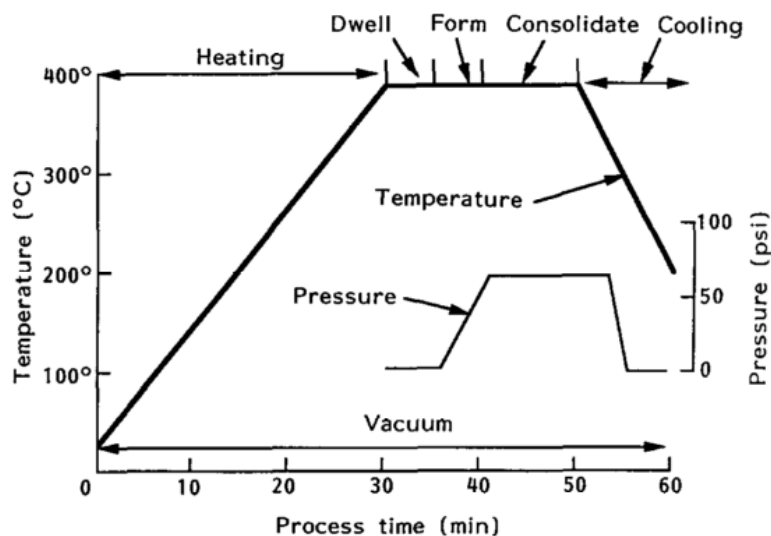


**Figure 1.6 Schematic diagram of a typical process cycle for APC-2 showing the temperature and pressure curves against time [11]**

The required cure cycle is provided by the gas temperature and pressure that flows within the working section around the composite parts thanks to the circulation system. Indeed, the forced gas (nitrogen or air) circulation systems are commonly used in autoclaves. The circulation system consists of a centrifugal blower and ducting (Figure 1.4). The heaters are placed around the impeller. The centrifugal blower takes in gas axially and discharges it radially. The gas that is discharged from the impeller passes over the heating elements and routed, after being heated, via the ducting system to the central working section in order to cure the composite materials. The blower fan is adequately sized to ensure a velocity of 1-3 m/s on the component at ambient conditions. The gas circulation unit also performs the task of accelerating the cooling process by removing the gas on the outside surface of the cooling tubes at a faster rate. Modern autoclaves have a flange-mounted blower motor, which is encased in a pressure-tight casing and connected to the rear of the autoclave. Thus, the motor rotor, stator, and the mechanical components such as the bearings directly encounter the autoclave pressure. Such blower arrangements are generally water-cooled to ensure that the motor windings and bearings are not subject to higher temperatures.

Heating the gas is achieved either electrically or by indirect gas firing (circulating externally heated or cooled thermic fluid). Electrical heating that gives precise control of autoclave ambient temperature is cleaner and more amenable to advanced computer controls. The electrical heating capacity is based on the charge and the resin system requirements of the cure cycle. Normally a number of heater elements are grouped in banks and connected in the star or the delta configuration.

On the other hand, a cooling system is used for cooling the autoclave ambient. In fact, the processing of composites requires variable cooling rates as demanded by the resin system. In electrically heated autoclaves, the heating rate is controlled by either switching off the heater banks or by varying the heater-input power. The control of cooling system is more involved as there are a number of variables that affect the cooling. They are temperature difference between the autoclave ambient and cooling medium, rate of flow of cooling medium, heat transfer area, conductivity of cooling coil material, and velocity of autoclave medium across the heat exchanger. Generally, the cooling rate is controlled by varying the flow of cooling water. In some autoclaves, both air and water are used as a cooling medium.

A pressurization system is used as well in order to ensure the required pressurization rates in the autoclave. The average pressurization rate in modern autoclaves is 2 bar/min. Nowadays, many autoclaves use nitrogen as the pressurization medium instead of air. This is because the autoclave cure consumables are highly inflammable in the air medium due to the presence of oxygen. There have been several reports of autoclave fire resulting invariably in the loss of the component. Though the nitrogen medium ensures fire-free autoclave cure cycles, care must be taken to avoid danger to personnel (possibility of asphyxiation) in nitrogen environments due to the lower oxygen levels.

The positioning of the composite laminate/molds into the central working section of the autoclave to be cured is made thanks to the loading system that consists of a loading platform. To enable easy loading of components, it is a general practice to install the autoclaves in a pit, so that the top surface of the loading platform is flush with the floor. In this case, it requires a loading bridge to be deployed to bridge the gap between autoclave door and pit (Figure 1.7).



**Figure 1.7 Image of a loading bridge system [12]**

## 1.2.2 Main physical phenomena within autoclaves

The autoclave temperature conditions strongly affect the successful manufacturing of the part, which could have high quality and good final mechanical properties if it solidifies uniformly without large thermal gradients. Therefore, during the autoclave process, the desirable state would be that an even and optimal temperature field exists in the whole manufactured part in order to improve the part quality on one hand and to reduce the manufacturing cost on the other.

Unfortunately, this is not always the case. All we need to reach this desirable state is to get a better understanding of the main occurred physical phenomena and their distribution inside an autoclave. Indeed, the autoclave process involves several chemical and physical phenomena: the flow pattern of the working gas, the heat transferred from the surrounding to the bag-composite-mold, i.e. the convective and the radiative heat transfers and the heat transfer through the bag-composite-mold coupled with the phase change [13].

In this section, the previous research works that aim to investigate the mentioned physical phenomena will be reviewed and the presented findings will be discussed and analyzed. The experimental and the numerical methodologies employed during these studies will be exposed as well.

### 1.2.2.1 Gas flow pattern

The research works on the study of the gas flow field within autoclaves have been found to be limited. Indeed, the complicated configurations of autoclave systems as well as the opaque material of the main shell prevent the use of non-intrusive and reliable measurement techniques such as the Particle Image Velocimetry (PIV) and the Laser Doppler Velocimetry (LDV) for the velocity gas flow measurements. Also, the extreme operating conditions such as the high temperature and pressure make difficult the use of traditional measurement instruments such as the hot-wire anemometer system and the Pitot probe. In addition, these techniques are known to be intrusive and unreliable especially in the case of industrial flows.

On the other hand, the large sizes of actual autoclaves make the numerical simulations of the turbulent flow field time-consuming and require more efforts and computational resources. Therefore the cost is too prohibitive.

However, many researchers have agreed that the gas flow within autoclaves is mainly turbulent due to the design of the circulation system and to the gas interaction with the installed molds of bluff bodies and complex shapes [14–17].

A description of the gas flow behavior within a standard production size autoclave has been presented by Campbell [15].

The presented description shows that the highest velocities occur near the entrance region (Door) and along the centerline of the autoclave. On the other hand, analyses have showed that recirculation regions occur at some outer radial positions where velocities were found to be low or zero.

This behavior was explained by the fact that the high-velocity region near the door is caused by the supply flow striking the autoclave door at the edges and moving towards the center to form a backward flowing high-velocity plume. As the gas moves backward, the plume dissipates and the flow becomes slower and more uniform. Indeed, the average axial velocity was found to be between 3 m/s and 5 m/s whereas velocities as high as 13.4 m/s occurred near the door. The axial variation in velocity was found to decrease approximately 4 m from the door (entrance region) and becomes more and more uniform downstream. A schematic of the gas flow behavior in a typical autoclave is shown in Figure 1.8.

This behavior of the working gas was verified by the turbulence intensity value that was found to be very high at the door region, typically 13-15%. According to the authors [15], this can be due to the separated-reattached flow or recirculation regions near the entrance and caused by the supply flow striking the autoclave door at the edges as mentioned previously. Further downstream from the door, the turbulence intensity dampens out at the same time that the velocity distribution becomes more uniform and keeps decreasing towards the rear of the autoclave.

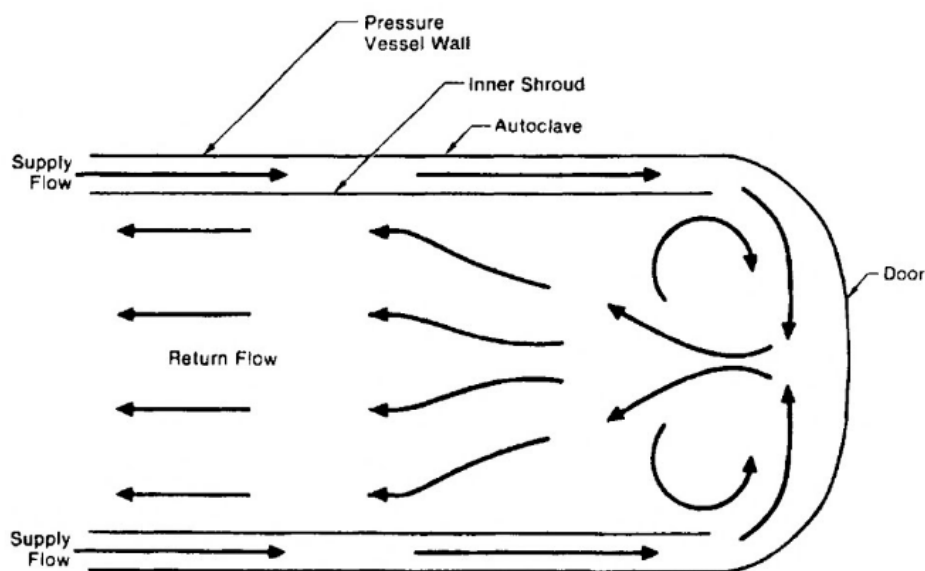


Figure 1.8 Gas flow velocity behavior in an autoclave [15]

This description of the gas flow behavior within an autoclave shows a good agreement with the experimental findings obtained by Ghariban *et al.* [14]. In fact, the authors used a three-channels hot-wire anemometer system for the measurement of

the gas flow velocity and turbulence intensity. These measurements were performed at atmospheric pressure and a temperature of 25 °C in order to have adequate conditions for using the hot-wire anemometer system. The free stream velocity within the unloaded autoclave was  $U_{\infty} = 2.05$  m/s. The obtained Reynolds number is  $Re = 36\,000$  and it was calculated based on the diameter ( $D$ ) of the working section of the autoclave.

The time-averaged velocities and the turbulence intensities were measured for nine different positions from the entrance region and along the longitudinal axis parallel to the autoclave working section (bulk flow direction) and for four different heights.

Figure 1.9 shows the measured time-averaged local velocity components for  $Re = 36\,000$ .  $U$  is the velocity component in the axial direction of the autoclave (bulk flow direction) whereas  $V$  and  $W$  are the velocity components in the vertical and the horizontal normal direction respectively.

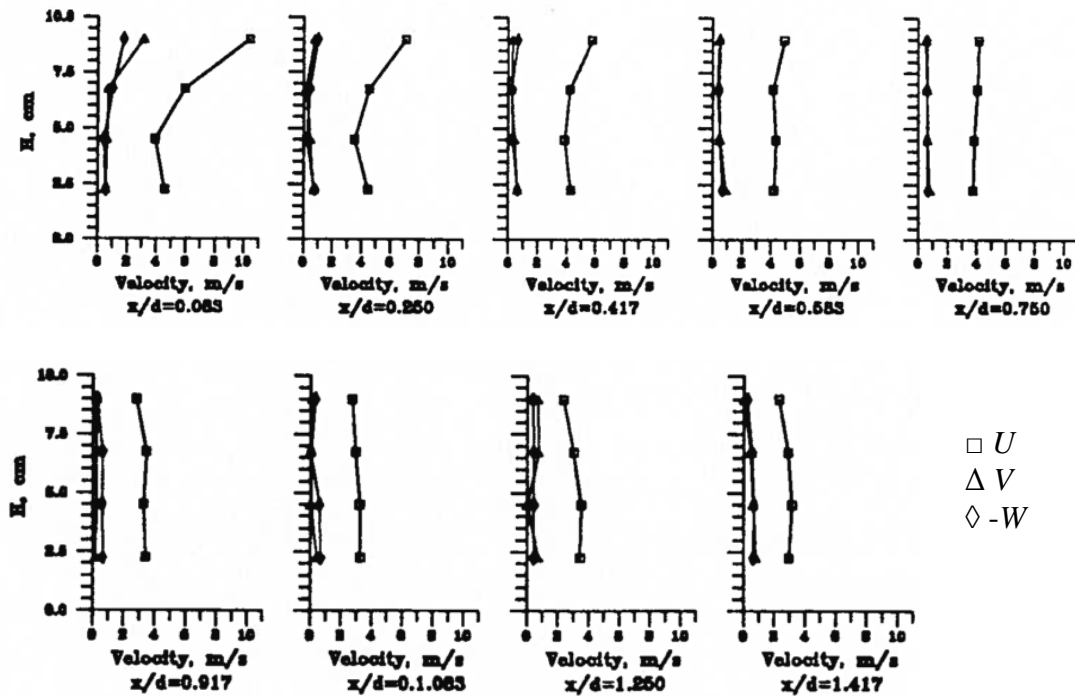


Figure 1.9 Time-averaged velocity components for  $Re = 36\,000$  [14]

The data shown in Figure 1.9 indicate that the average velocity components  $V$  and  $W$  are not negligible especially near the entrance region. This can be due to the existence of separation and recirculation zones.

These data also indicate that the mean velocity  $U$  was found to be significantly large at the center of the entrance region. This significant velocity shows thus that the flow was separated near the wall at the entrance and it moved faster in the core.

Downstream from the entrance region, the velocity in the longitudinal axis direction ( $U$ ) was found to become uniform and slower.

On the other hand, Figure 1.10 shows the values of turbulence intensity obtained at different locations along the bulk flow direction from the entrance region and at different distances from the axis of the autoclave.

The turbulence in the entrance region of the autoclave was found to be high whereas it decreases further downstream. This profile of turbulence intensity indicates again the existence of separated-reattached flow near the entrance region and characterized by high turbulence intensity [18].

The existing of such separated-reattached flow can be due to the mixing of gas flow coming from all directions creating then a rather larger turbulence level and a complex flow field.

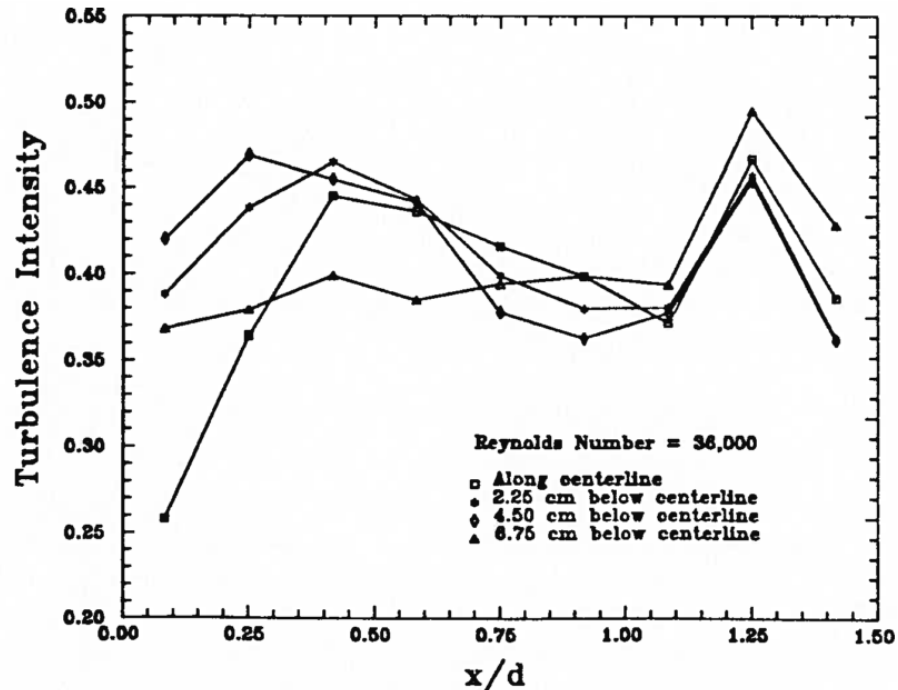


Figure 1.10 Turbulence intensity along the bulk flow direction,  $Re = 36\,000$  [14]

Based on these previous studies, it can be concluded that the gas flow field is not uniform within an autoclave and it presents a complex behavior. This behavior can be summarized as follows: the supply gas enters from all directions, via the circulation system, and strikes the autoclave door creating then recirculation regions or dead zones at some outer radial positions near the wall of the entry region (door) against high velocity at the center. On the other hand, the appearance of such separated-reattached flow leads to the existence of high turbulence intensity. As the gas moves



backward, the gas flow becomes slower and more uniform and the turbulence intensity decreases further downstream from the door.

This flow behavior of the working gas affects the distribution of the convective heat transfer coefficient inside an autoclave as this coefficient depends strongly on the type of flow, flow velocity and flow turbulence intensity [19,20]. In the next section, the previous research studies that aim to investigate these effects will be exposed.

On the other hand, no studies have been found to investigate the flow field behavior around molds during the autoclave manufacturing process.

### **1.2.2.2 Heat transfer mechanisms**

During the autoclave process, different modes of heat transfer can occur. These heat transfers from the autoclave surrounding to molds can be classified into three categories:

- forced convection heat transfer to the mold from the gas circulating through the autoclave working section.
- radiation heat transfer between the interior surfaces of the autoclave working section and the mold.
- heat transfer through the bag-laminate-mold: conduction heat transfer through the bag, composite laminate, air gaps and mold material coupled with the exothermal irreversible chemical transformation.

#### **1.2.2.2.1 Convection heat transfer**

During an autoclave process, the heat transferred between the energy carrying working gas and the bag-laminate-mold group activates exothermic curing reactions, leading to composite consolidation.

Indeed, many researchers have agreed that the convective heat transfer mechanism is the most relevant aspect controlling the rate of chemical and physical transformations associated with composite curing and that the forced convection is the main source of heat transfer into the autoclave mold [16,17,21]. The effectiveness of the forced convection is summarized by the Heat Transfer Coefficient (*HTC*) between circulating air and the mold surface.

Given this fact, several researchers have been interested to investigate the convective *HTC* during the autoclave manufacturing process. They concluded that *HTC* within a single autoclave depends on various major parameters summarized by the following points [11,16,17,19,22,23]:

- gas flow behavior and velocity
- gas static pressure
- gas temperature



- molds shapes and sizes

During their studies, the authors [11,14,16,19] have performed experimental measurements using calorimeter placed inside an autoclave in order to measure *HTC*.

Calorimeters are normally rods or plates with embedded thermocouples and they are made of relatively high thermal conductivity materials (steel or aluminum). Thus the obtained Biot number (*Bi*) of the calorimeter is small (less than 0.1) allowing then the use of the lumped thermal mass assumption for the calculation of *HTC* values. The *HTC* value, measured by a calorimeter at a specific location, is calculated by using the Equation (1.1) based on the Newton's law of cooling [11,16,17].  $VO_{calorimeter}$  and  $T_{calorimeter}$  are respectively the calorimeter volume and the calorimeter temperature taken as the average of the embedded thermocouples measurements.

$$HTC = \frac{\rho_{calorimeter} C_{p_{calorimeter}} VO_{calorimeter}}{A_{calorimeter} (T_{\infty} - T_{calorimeter})} \frac{dT_{calorimeter}}{dt} \quad \text{Equation (1.1)}$$

The influence of the gas flow behavior and velocity was observed first by measuring the *HTC* distribution within an unloaded autoclave. The authors [11,14,17,24] measured *HTC* from point-to-point and along the longitudinal axis of an autoclave by placing calorimeters at various locations.

They obtained that the heat transfer coefficient measured by a calorimeter placed near the front of an autoclave (entrance region) was consistently higher than that at the back (towards the rear) by about 33%, depending on the Reynolds number of the autoclave flow.

This non-uniform *HTC* distribution can be explained by the non-uniform behavior and velocity of the gas flow showed previously in the section 1.2.2.1. In fact, the existence of separated-reattached regions characterized by high turbulence intensities as well as the appearance of high velocities near the wall of the front (door) enhance the convective heat transfer rates [20,25]. Towards the back of the autoclave, the flow becomes more uniform and slower and the turbulence intensity decreases reducing then the heat transfer coefficient value. This variation of the flow velocity, that can be from 1.5 m/s to 18 m/s within a single autoclave sometimes, can lead to a variation of *HTC* from 20 W/m<sup>2</sup>/K to 180 W/m<sup>2</sup>/K [19].

This large variation from point-to-point of *HTC* values indicates that identical composite parts placed at different sections of the autoclave can be cured differently. So that may cause the production of identical composite pieces of different qualities at the end of the curing cycle.

Another effect of the flow velocity on  $HTC$  is encountered inside an autoclave in the case of an installed mold. This effect is summarized by the fact that the convective heat transfer coefficient has a non-uniform distribution between the different surfaces of the mold during the autoclave process. This is due to the intra-mold shadowing. In fact, shadowing effects on the leeward mold side as well as flow stagnation on the windward side will influence the local flow velocity significantly and thereby also the  $HTC$  value [16,17].

The intra-mold shadowing phenomenon was demonstrated by Weber *et al.* [19]. The authors measured the  $HTC$  over the different surfaces of an industrial test mold by means of a calorimeter placed at different positions around the mold. The used calorimeter is a steel rod with six embedded thermocouples. Figure 1.11 shows the used test mold which consist of a rectangular cross-section base plate and a rectangular box on top of the base plate. On the other hand, Figure 1.12 shows the studied test mold placed inside the autoclave with the different calorimeter positions used for the  $HTC$  measurements (position 1, 2, 3 and 5).

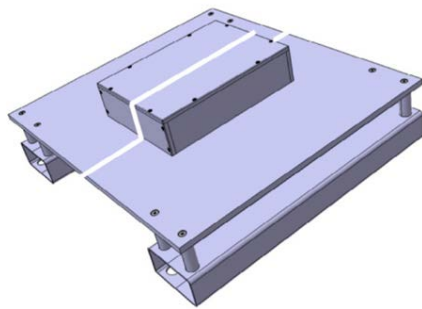


**Figure 1.11** Schema of the test mold [19]

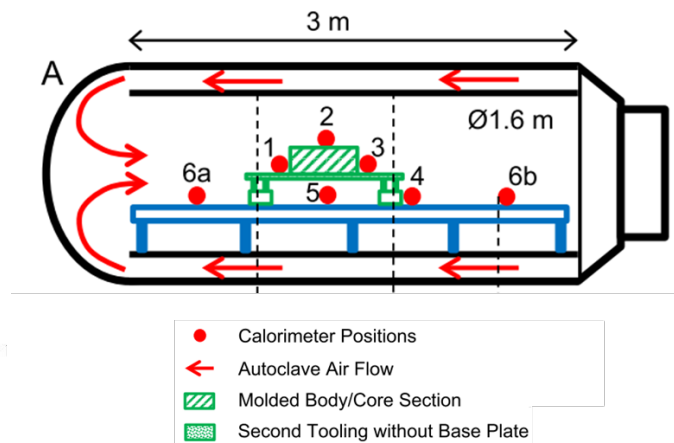


**Figure 1.12** Different calorimeter positions for the  $HTC$  measurements around the test mold [19]

The measurements of  $HTC$  were performed, during the curing cycle, for an absolute gas pressure of 5 bars and a temperature of 180 °C between 120 and 200 min (Figure 1.15). Figure 1.13 shows the corresponding relative  $HTC$  values measured for each mold surface, i.e. at position 1 to 3 and 5. The mean of position 2 (parallel flow) was taken as reference.

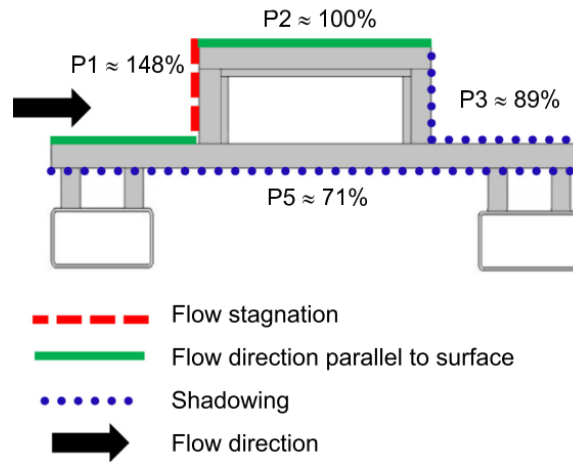


**Figure 1.13** *HTC* distribution on the representative test mold using percentage values (surfaces with parallel flow set to 100% as baseline) [19]

In the same context, the effect of the flow velocity can be encountered also when several molds are processed together. In this case, parts located forward can block the flow of gas to parts located behind them creating then shadowing effect [15].

The inter-part shadowing effect was showed also by Weber *et al.* [19]. They placed a second mold of rectangular box shape, without a base plate, behind the representative test mold showed previously in Figure 1.11. Then, the inter-part shadowing was investigated experimentally using calorimeter measurements at positions 7 and 8 (Figure 1.14).

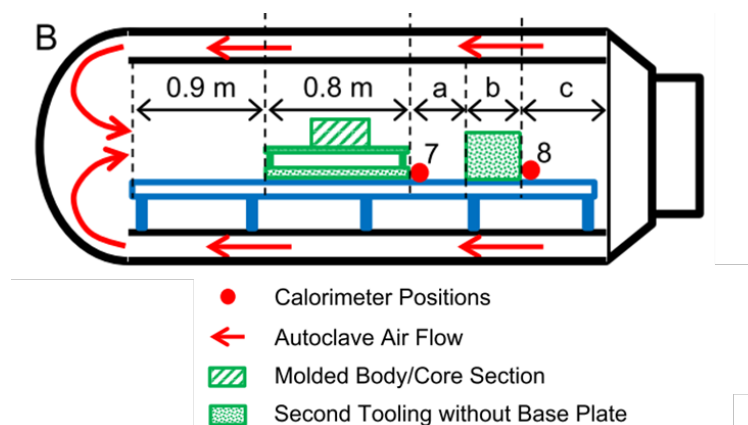


**Figure 1.14** Different calorimeter positions for the *HTC* measurements – Study of the shadowing effect [19]

Position 7 was found to encounter almost no measurable inter-part influence during the experiments. In fact, the values measured at position 7 were very similar to those at position 4 (Figure 1.12), which shows that there is enough spacing between the molds to avoid a negative inter-part influence on the forward mold. Position 8, on

the other hand, showed a significantly lower  $HTC$  than positions 3, 4, and 6b (Figure 1.12).

This finding confirms that placing molds behind one another creates additional shadowing effects.

The dependence of  $HTC$  on the gas flow velocity can best be understood by looking at the definition of the Nusselt number ( $Nu$ ). It is defined by the  $HTC$ , the characteristic length of the mold ( $l_{mold}$ ), and the conductivity of the gas ( $\lambda_{gas}$ ). The Reynolds ( $Re$ ) and Prandtl ( $Pr$ ) numbers are multiplied applying a pre-factor ( $a_{Nu}$ ) and two exponents ( $b_{Re}$ ,  $c_{Pr}$ ) to calculate the Nusselt number (Equation (1.2) taken from [23]).

$$Nu = \frac{HTC \cdot l_{mold}}{\lambda_{gas}} = a_{Nu} \cdot (Re)^{b_{Re}} \cdot (Pr)^{c_{Pr}} \quad \text{Equation (1.2)}$$

$$Re = \frac{\rho_{gas} \cdot l_{mold} \cdot U_{\infty}}{\mu_{gas}} \quad \text{Equation (1.3)}$$

$$Pr = \frac{C_{p_{gas}} \cdot \mu_{gas}}{\lambda_{gas}} \quad \text{Equation (1.4)}$$

The constants  $a_{Nu}$ ,  $b_{Re}$  and  $c_{Pr}$  will change depending on the type of flow or the geometry changes of the mold. However, no works have been found to investigate the influence of molds shapes and sizes on  $HTC$ . In an autoclave loaded with molds of different sizes and bluff body geometries, and often with aerodynamically unfavorable shapes, very complex and non-uniform turbulent gas flow structures can develop [25]. This kind of flow behavior disturbs strongly the uniform distribution of the local heat transfer coefficient around a mold surface and makes difficult then to estimate  $HTC$  precisely by limiting the application of existing correlations (Equation (1.2)). Therefore an accurate study of the local  $HTC$  distribution over a mold surface coupled with the investigation of the local velocities and gas flow structure is required.

On the other hand, the correlations mentioned previously (Equation (1.2), Equation (1.3) and Equation (1.4)) show that  $HTC$  depends also on the thermal and physical properties of the working gas. In turn, these properties, such as heat capacity ( $C_{p_{gas}}$ ), dynamic viscosity ( $\mu_{gas}$ ) and thermal conductivity ( $\lambda_{gas}$ ) depend on temperature and pressure. Their influence, however, is rather small compared to the influence of temperature and pressure on the density of the gaseous medium ( $\rho_{gas}$ ) [26].

Given this fact, several researchers [27,19,28,24] have observed the influence of the gas temperature and pressure cycles on the convective heat transfer coefficient

(*HTC*). They concluded that the pressure cycle has a significant impact on the convective heat transfer due to the increase of the convected fluid density. Indeed, Jimmy Kluge [28] shows that increasing the autoclave gas pressure from 1 bar to 7 bars approximately increases the overall heat transfer coefficient by a factor of about 2.6. Weber *et al.* [19] mentioned that the *HTC* in an autoclave, with approximately 4 m/s mean flow velocity, is between 20 and 40 W/m<sup>2</sup>.K for ambient pressure and between 60 and 100 W/m<sup>2</sup>.K for an absolute pressure of 5 bars. On the other hand, the temperature cycle has shown to have a negligible influence.

These effects of the gas pressure and temperature cycles can be observed by examining the *HTC* curves evaluated by the calorimeter at position 2 (Figure 1.12) for three different autoclave pressure cycles. Comparing temperature and pressure changes during those cycles with the *HTC* variation reveals the small influence of temperature compared to the more dominant influence of a pressure change. This can be seen during the temperature increase from 20 °C to 80 °C in the first 25 min of the cycle, which only has a minimal influence on the *HTC*, whereas the pressure increase from 1 bar to 5 bars absolute pressure shows an increase of the *HTC* by a factor of approximately 2.5.

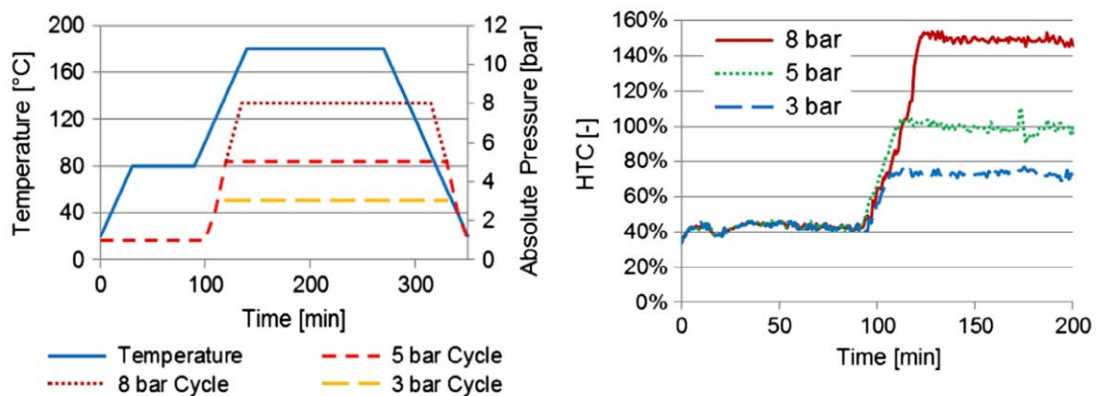


**Figure 1.15** Autoclave cycles used (left) and comparison of *HTC* measurements for those cycles at positions 2 (right) (100% reference: 5 bar *HTC* curve between 120 and 200 min) [19]

Based on all of these above presented studies, it can be concluded, in terms of actual *HTC* values, that *HTC* shows a large variation around the molds within a single autoclave and thus a fixed or a universal value cannot be determined.

Furthermore, the convective heat transfer coefficient was found to depend strongly on the different autoclave geometries and their gas circulating system designs [29,30]. In this context, Johnston [16] was the first to compare three different autoclaves and was able to show some differences between them. In fact, he conducted measurements of *HTC* value in three different autoclaves by means of an aluminum plate calorimeter

paced at the same position. The size and performance of the utilized autoclaves are summarized in Table 1.2.

**Table 1.2 Comparison of the *HTC* measured in different autoclaves**

<b>Autoclave</b>	<b>Dimensions (Internal)</b>	<b><i>HTC</i> ( 3.75 bar)</b>
Autoclave 1	1.8 × 4.5 m	100 W/m <sup>2</sup> K
Autoclave 2	0.9 × 1.8 m	100 W/m <sup>2</sup> K
Autoclave 3	1.5 × 2.4 m	25 W/m <sup>2</sup> K

All autoclaves were of the same type and working principle and also the measurement conditions were controlled accurately. However, two of the measured autoclaves showed identical behavior whereas the average heat transfer coefficient in the third autoclave was significantly lower after the pressure is increased to 3.75 bars. A variation by about a factor of 4 was founded.

This difference can be due to the mean flow velocity changing during the pressure ramp-up. The change in flow velocity is most likely caused by the insufficient blower power to compensate the increasing drag [16,19]. On the other hand, this finding allows the presumption that a transfer to different autoclaves is not easily possible.

The investigation works exposed previously on the convective heat transfer coefficient helps to understand better the thermal boundary conditions existing around molds during the autoclave manufacturing process. These thermal boundary conditions allow the prediction of the temperature field within composite laminates.

However, the use of intrusive instruments such as calorimeters during these studies for the *HTC* measurements limits the accuracy of the obtained values. In fact, the flow interaction with the calorimeter surfaces can generate complex flow structures affecting then the convective heat transfer rates [25]. In addition, these previous studies have shown no interest in investigating the distribution behavior of the local heat transfer coefficient around a representative industrial mold although the latter can represent a bluff body. Based on these facts, further investigations are necessary and reliable experimental methodologies are required in order first to study, accurately, the *HTC* distribution behavior over molds of bluff body shapes and then to predict precisely the temperature field within composite parts and molds.

#### 1.2.2.2.2 Radiative heat transfer

Given the fact that the forced convection is considered the main source of heat transfer into the autoclave mold, the question about the radiant contribution to heat transfer becomes particularly important.

The convective heat transfer within autoclaves depends mainly on the different autoclave geometries, mold shapes and sizes, the gas velocity and the processing pressure cycle used as showed previously. In turn, the radiative heat transfer to molds depends mainly on the view factors between the mold and autoclave surfaces and the emissivities of the mold and autoclave materials. The autoclave and mold surfaces are usually made from either mild or stainless steels and the emissivities of the surfaces may vary from 0.16 for polished stainless steel to 0.81 for highly oxidized steel [31].

In addition, the relative importance of radiative heating of the mold depends on the location of the resistance heaters as autoclaves are normally heated tanks to these band heaters.

In typical autoclaves, three such locations can be identified [11]:

- band heaters in the working section walls [9]. In this case both the mold and working section walls receive radiant heat direct from the resistance heaters.
- resistance heaters placed in the air ducts which are located parallel to the working section [30]. In this case some of the working section walls receive radiant heat direct from the resistance heaters.
- resistance heaters placed outside the working section and ducts [29]. In this case, there is no (or very little) direct radiant heating of either the mold or working section walls by the resistance heaters.

The estimation of the relative importance of convection and radiation heat transfer was studied by Monaghan *et al.* [11] by carrying out experimental tests inside a research laboratory autoclave developed by the authors (Figure 1.16) [9]. The autoclave was designed to operate at pressures up to 20.6 bars and temperatures up to 400 °C. The heating system chosen is a circular band heating system comprising three heater bands installed in the working section walls (Figure 1.16).



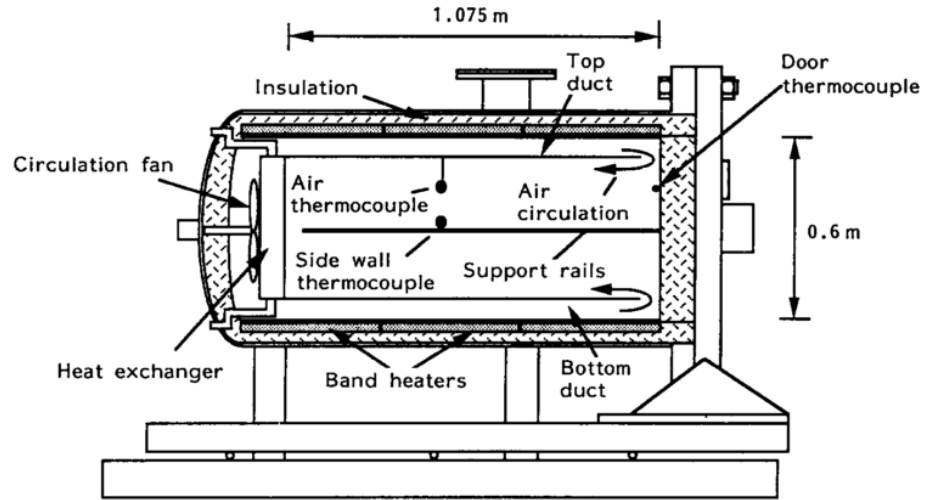


Figure 1.16 Schema of the used experimental autoclave [11]

Their experimental approach consists of using two plate calorimeters of the same dimensions and thermal properties but with different surface emissivities. The surface of the first plate calorimeter was highly polished providing then a low emissivity surface of about 0.028 [31]. On the other hand, the surface of the second plate was treated by a thin layer of carbon which has a high emissivity of about 0.95 [31].

The energy balance on a plate calorimeter heated in an autoclave gives the Equation (1.5). The total rate of heat transfer ( $q_t$ ) can be estimated by recording the temperature results and then by using the Equation (1.6) based on the lumped thermal mass assumption.

$$q_t = q_c + q_r \quad \text{Equation (1.5)}$$

$$q_t = m_{\text{calorimeter}} \cdot C_{p_{\text{calorimeter}}} \cdot \frac{dT_{\text{calorimeter}}}{dt} \quad \text{Equation (1.6)}$$

The convection heat transfer ( $q_c$ ) was estimated first by placing the plate with the low emissivity surface in the autoclave assuming then that the radiative heat transfer is negligible. Thus the convective heat transfer coefficient was determined using the Equation (1.1) allowing the deduction of the convection heat transfer. In turn, the radiation heat transfer ( $q_r$ ) was estimated, in a second step, by using the plate with the high emissivity surface. In this case,  $q_r$  in Equation (1.5) became not equal to zero and it was calculated by knowing the convection heat transfer from the first step.

The authors found that the radiation heat transfer from the interior surfaces to the plate calorimeter of high emissivity surface reaches an average of 29% of the total heat transfer within the experimental autoclave.

However, the radiation heat transfer within the used autoclave may be somewhat higher than in other autoclaves due to the direct heating of the side walls and the



location of the heaters as explained previously. Furthermore, the authors mentioned in their study that the presented results are for their autoclave which is not of conventional design [29,30]. For autoclaves such as those fabricated by the manufacturer Scholtz Maschinenbau [29], the radiant contribution to heat transfer would normally tend to be lower.

In the same context, Kluge *et al.* [32] investigated the effect of thermal radiation on the temperature distribution on a mold during an autoclave run by means of computational fluid dynamics simulations. These simulations have been performed with two different methods: with and without the thermal radiation model. Then, the calculated mold temperature was compared to experimental results [33].

The experimental work was carried out at full-scale industrial conditions [29] with a proper 11m long cylindrical hot gas autoclave having a diameter of 3 m. The resistance heaters are placed outside the working section and ducts. A description of the used autoclave can be seen in Figure 1.4. On the other hand, the mold, presented in Figure 1.17, represents an industrial mold with a rather complex geometry and it was placed in the center of the autoclave.

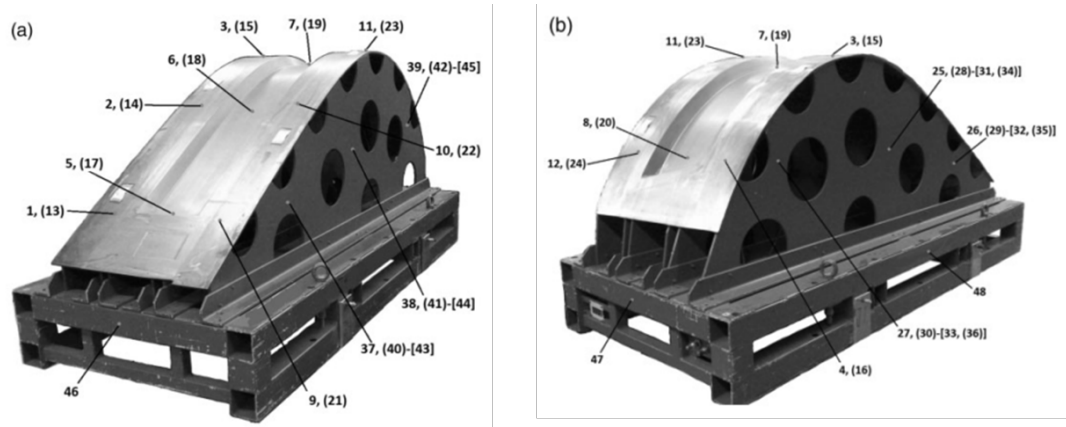


**Figure 1.17 The front (a) and the back (b) of the mold seen from lateral viewpoints and measurement positions [33]**

The experimental measurements of the temperature distribution on the selected mold were monitored at 48 positions by means of thermocouples (Figure 1.17). On the other hand, the numerical study was performed with the commercial code STAR-CCM© 8.04 both with and without modeling thermal radiation as mentioned previously.

Figure 1.18 shows the spatially averaged experimental temperatures, from all monitored points, over time against the average values derived from the two types of simulations.

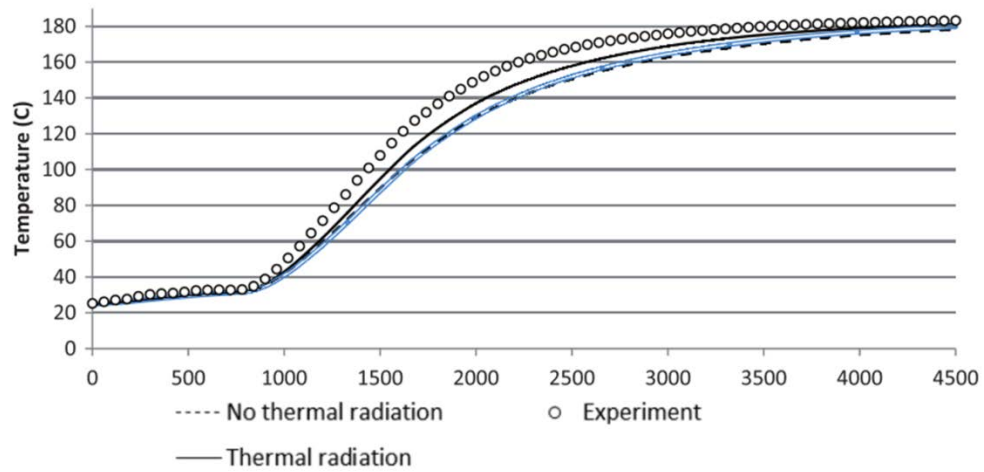


**Figure 1.18 The average temperature over time (s) for all monitored positions for the simulations and the experiment [32]**

As seen, the spatially averaged experimental temperature cannot be captured with any of the performed simulations. However, the simulation with applied thermal radiation is the closest but it does not present a noticeable difference with the no thermal radiation.

Based on these exposed studies, it can be concluded at the end that the radiation heat transfer contribution tends to be lower inside the autoclaves of conventional designs, especially with the use of no high emissivity mold surfaces. Therefore the forced convection heat transfer remains undoubtedly the major heat transfer process inside an autoclave.

#### 1.2.2.2.3 Conduction heat transfer and chemical transformation

The heat exchanges between the autoclave surrounding and the assembly bag-composite-mold have shown to affect strongly the temperature field within the composite laminates. However, the energy transfer through the composite, the bagging and the mold plays a key role as well in determining the temperature field behaviors within the manufactured composite parts, especially in the case of manufacturing of thick thermoset composite laminates. These thermal phenomena through the nonhomogeneous autoclave assembly (mold, laminate and bag) are influenced by the heating rate or the cure cycle, the laminate thickness, the vacuum bag and obviously the convective exchange. A schematic of the analyzed autoclave assembly is showed in Figure 1.19.

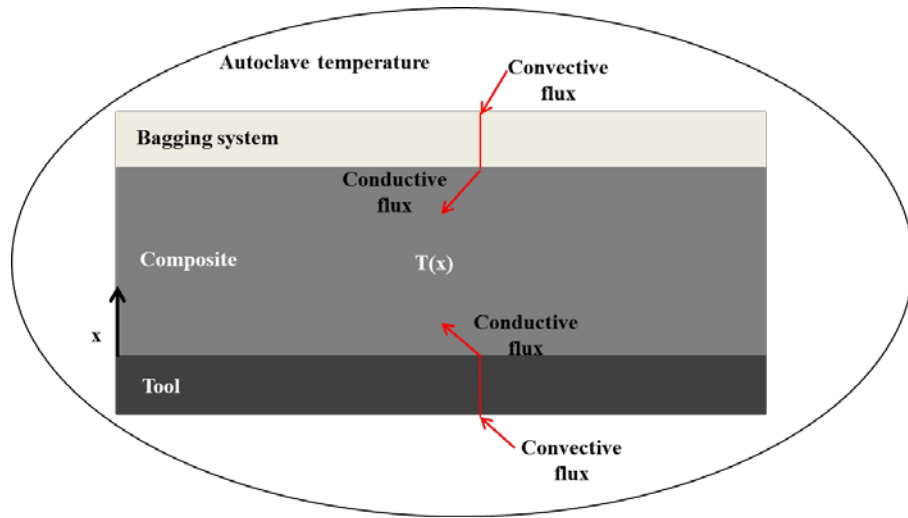


**Figure 1.19** Schematic of the analyzed system [34]

As explained previously, during the autoclave process, consolidation of the composite takes place by applying a temperature and pressure cycle to the laminate, which has been preshaped according to the desired part, located on a mold and bagged. The processing cycle involves the development of the non-reversible resin polymerization reaction, which is an exothermic reaction activated by the convective heat transport with the autoclave environment and the conduction from the bag and the mold layers.

However, the conventional autoclave cure cycle recommended by the laminate manufacturer is only used for fabricating thin laminates. If thick laminates are cured by the conventional cure cycle, temperature overshoot or high exothermal peaks through the thickness of the laminate arises during the exothermic reaction because the low thermal conductivity of matrices of composite materials acts as a thermal barrier.

The presence of such large thermal gradients leads to a non-uniform solidification and transformation of the manufactured part which can affect its quality and its final mechanical properties by the presence of residual stresses.

Given this fact, many researchers have developed physical models, analyzed after by finite element methods, to predict the temperature history of the composite during the curing stage [35–38] and methodologies to select the proper autoclave temperature cycle able to limit the thermal gradients along the part thickness [39–42].

These physical models are based essentially on the heat transfer equation and including the heat generation term ( $\dot{q}$ ) due to the exothermic reaction of the polymerization reaction (see Equations (1.7) and (1.8)). The physical quantities  $da/dt$  and  $Q_r$  are the cure rate and the heat of reaction per unit mass of resin respectively. The resolution of such model requires the knowing of the surface boundary conditions

of the autoclave assembly. These boundary conditions are mainly the convective heat exchanges and controlled through the convective heat transfer coefficient  $HTC$ .

$$\frac{\partial}{\partial x} \left( \lambda_x \frac{\partial T}{\partial x} \right) + \frac{\partial}{\partial y} \left( \lambda_y \frac{\partial T}{\partial y} \right) + \frac{\partial}{\partial z} \left( \lambda_z \frac{\partial T}{\partial z} \right) + \dot{q} = \rho C_p \frac{\partial T}{\partial t} \quad \text{Equation (1.7)}$$

$$\dot{q} = \rho Q_r \frac{d\alpha}{dt} \quad \text{Equation (1.8)}$$

In this context, Loos *et al.* [35] developed models which describe the curing process of composites constructed from continuous fiber-reinforced, thermosetting resin matrix prepreg materials. The models consisted of different submodels, each describing the different phenomena occurring during the resin polymerization: the “thermochemical” submodel, providing the temperature, the viscosity and the degree of conversion, the “flow” submodel, giving the pressure distribution, the resin flow and the compaction and the “void” submodel, resulting in the void size. It should be outlined that, however, that the heat transfer analysis performed by the authors was only for the curing laminate accounting for the one dimensional heat conduction, along the thickness direction, and the contribution of the polymerization reaction. Further, the temperature at the bottom and at the top of the composite surface was specified as function of the time without considering the local forced convective exchange and its complex distribution around an autoclave assembly as showed previously. This assumption neglects also the heterogeneity nature of the autoclave assembly consisting of the mold and the bagging layer.

Joshi *et al.* [36] simulated the three-dimensional transient energy transfer (see Equations (1.7) and (1.8) ) through the composite, the bagging and the mold by finite element (FE) methods. The FE numerical procedure was demonstrated to be stable and accurate by the comparison between the numerical and experimental temperature at the center of a thick graphite-epoxy laminate. However, a constant and uniform heat transfer coefficient of 85 W/(m<sup>2</sup>.K) was used between the autoclave air and either the mold or the bagging material which is not the case during an autoclave molding.

A similar two-dimensional heat transfer model was used also by Telikicherla *et al* [37] to simulate the thermal phenomena through the nonhomogeneous autoclave assembly (mold plate, composite laminate and vacuum bag). On the other hand, Antonucci *et al.* [34] formulated in their work a transient energy balance between the convective heat fluxes from the autoclave environment and the conductive fluxes from the composite for the bagging and the tool layer. The absence of conductive internal gradients was assumed and thermal boundary conditions were provided thanks to thermocouples installed within the thick autoclave element. Further, the thermal evolution of the composite was described by considering the through thickness conduction and the polymerization reaction contribution. Experimental data

from industrial autoclave cure cycle of two identical thick composite laminates based on epoxy resin and carbon fiber reinforcement were collected and analyzed to validate the method.

Many other studies [43–49] have worked as well on the development of numerical simulations for the prediction of the temperature field of thick thermoset matrix laminates manufactured by the autoclave vacuum bag process. The authors concluded, based on the obtained temperature results, that conventional cure cycles recommended by prepreg manufacturers for thin laminates should be modified to reduce out-of-plane temperature gradient.

Against this background, Kim *et al.* [39] developed an autoclave cure cycle to reduce the temperature overshoot of thick laminates during the exothermic reaction by introducing cooling and reheating steps into the conventional cure cycle. The cure rate and temperature at the midpoint of the laminate were used as control variables. The prediction of the temperature distribution of the thick thermosetting composite laminates during cure was ensured by the simulation of the heat transfer equation, including the heat generation term as explained above. The developed cure cycle was used to cure 15 and 30 mm (100 and 200-ply) thick laminates and it was found to be effective for the reduction of temperature overshoot. On the other hand, simplified assumptions were considered once again by the authors during their work, such as the uniform distribution in the plane of the composite laminate which is not encountered, during the process, due to the non-uniform *HTC* distribution over the mold.

Despite the importance of the several research studies exposed above in the prediction of the temperature history of the cured laminate coupled with the chemical transformations during an autoclave process, however, these studies were carried out with a poor description and inappropriate value of the *HTC* distribution over molds surfaces. In fact, the convective heat transfer coefficient represents the surface thermal boundary conditions required for the resolution of the energy equation. Thus, an inaccurate prediction of the interaction between the energy carrier fluid and the processing part can affect the accuracy of the simulation results and limit the correct description of the thermal evolution of the autoclave assembly. In this context, Hudek [50] showed that a predicted *HTC* value, which is  $\pm 30\%$  too high, will almost cause a doubling of the error in temperature prediction.

On the other hand, the estimation of the heat exchange convective properties is difficult to achieve due to the local flow dynamic and the interaction between the part and the autoclave fluid. Therefore, this difficulty makes the real application of the developed models to industrial manufacturing cycles not attainable.

To overcome these hurdles in the prediction of the interaction between the energy carrier fluid and the processing part, some authors drew on computational fluid

dynamic (CFD) simulations to generate a three-dimensional representation of the temperature field within an autoclave mold.

Against this background, Xie *et al.* [21,51] simulated the turbulent flow field coupled with the thermal transfers phenomena and polymerization reaction through a composite component placed on a mold within an autoclave. The authors attempted to optimize, numerically, the composite curing temperature field by adjusting variables such as the time of heat preservation and heating rate. Similarly, Chen *et al.* [52] and Cheng *et al.* [53] established numerical calculations for a frame mold temperature field in an autoclave process and the impact of the mold design parameters on the temperature field was investigated.

However, there are several disadvantages linked to such a CFD approach. Although the current standards in CFD allow an accurate autoclave simulation, a calibration with flow measurements is often necessary to cover all effects like the complex and non-uniform behavior of the gas flow near the entrance region as showed previously. Moreover, the CFD model requires an extensive model set-up including the autoclave working section, autoclave loading tools, and all the molds that might be processed together. On the other hand, an adapted mesh must be constructed carefully with high precision around the molds in order to predict accurately the *HTC* distribution and then the temperature field. Based on these facts, the computation time of CFD is rather high and it requires more efforts and computational resources and therefore the cost is too prohibitive.

Instead of using lengthy CFD evaluations or additional software tools, Weber *et al.* [19] presented a fast method for estimating thermal boundary conditions that combines low numerical and testing effort with reasonable accuracy. The method consists first of identifying and summarizing the most important factors that can influence the convective heat exchanges and thus the mold heat-up. These factors, which were listed above in the section 1.2.2.2.1, are essentially the flow phenomena (e.g. the intra-part shadowing, the inter-part shadowing and the longitudinal positions within the autoclave), the mold material and shape and the autoclave curing cycle. Thermal measurements were performed to quantify the impact of these various parameters. Finally, the gained knowledge was applied to develop a semi-empirical approach for boundary condition estimation that enables a simple and fast thermal simulation of the mold temperature field with reasonably high accuracy and using a solid mechanics finite element method instead of CFD simulations. This approach developed by the authors was found to reduce the model set-up and computation times to the level of those applying only a constant *HTC* throughout the complete simulation.

However, the *HTC* measurements performed by the authors were carried out by means of calorimeters as showed previously in the section 1.2.2.2.1. These intrusive

instruments limit the accuracy of the obtained *HTC* values and thus the correct description of the thermal evolution of the mold.

Furthermore, the authors have not taken into account the complex behavior of the turbulent flow structure around the mold and its impact on the local distribution of the heat transfer coefficient around the mold surfaces.

Indeed, the gas interaction with molds of bluff body shapes and aerodynamically unfavorable geometries can result in flow accompanying a separation and reattachment regions along the mold. Such a flow is characterized by a bubble just behind the separation point and the redevelopment of flow downstream of the reattachment point. This kind of flow can disturb the heat transfer rates in the separated, reattached, and redeveloping regions over the mold surfaces. Furthermore, the use of molds with excessive support structures can result in the presence of dead zones characterized by low velocities and thus low convective heat transfer rates. Subsequently, a deeper and more correct investigation of the local *HTC* distribution along bluff body surfaces is required. This subject will be discussed in the following section.



## **1.3 Flow and heat transfer around a bluff body**

### **1.3.1 Introduction**

The incoming fluid over a relatively thick body generates a flow which is not of a boundary layer type and is accompanied by fluid separation and reattachment. Flow accompanying a separation and reattachment along a body is characterized by a bubble just behind the separation point and the redevelopment of flow downstream of the reattachment point.

In the flow at a high Reynolds number, the separated shear layer is, in general, very unstable, and transits easily to the turbulent flow state. Accordingly, the turbulent shear layer reattaches to the surface. Subsequently, a large scale vortex structure is shed almost periodically from the reattachment region to the downstream region, producing reverse flow. These flow behaviors represent the complexity of the separated, reattached and redeveloping flow and it is not easy to measure the flow field with high reliability.

On the other hand, such a flow influences the rate of heat transfer from the body. Indeed, so many experimental works reveal that the heat transfer coefficient ( $HTC$ ) attains a maximum in the neighborhood of the time-averaged reattachment point, where the time averaged wall shear stress becomes zero [25].

The separation and reattachment of flow occurs in the flow around many geometrical configurations and it is widely observed in nature and also in a wide variety of engineering and technology applications.

In the case of an autoclave filled with parts and molds of varying size and shape and often with aerodynamically unfavorable geometries, this kind of very complex gas flow patterns and heat transfer rates can develop especially with the presence of a pressurized and thus a high Reynolds number working gas. This complexity limits the application of the existing empirical correlations for the calculation of the local heat transfer coefficient distribution over the molds surfaces and thus making  $HTC$  not easy to predict.

From this point of view, an accurate knowledge of fluid flow structure and heat transfer rates between bluff bodies and surrounding gas is required. Figure 1.20 shows the most basic flow configurations such as the downward facing step, the sudden expansion plane channel, the abrupt expansion tube, the blunt flat plate, the longitudinal blunt circular cylinder and the surface mounted obstacle.

The blunt flat plate or rectangular box was chosen to be under scope in the present study as it can often be a representative shape of an industrial mold [19]. Furthermore, the investigation of the local heat transfer rates over a blunt flat plate can reveal the



reliability or not of the  $HTC$  measurements performed in the previous research works by means of plate calorimeters.

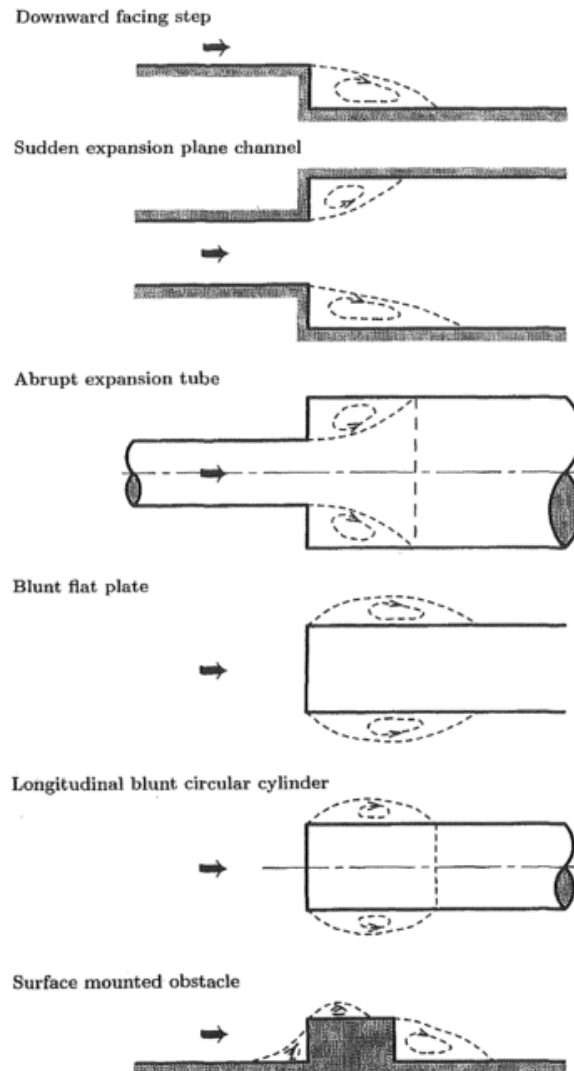


Figure 1.20 Flow configurations [25]

### 1.3.2 Flow field description

The separated and reattached flow and also the heat transfer around the blunt flat plate with finite thickness have been investigated comprehensively by Ota *et al.* [54]. In fact, Ota [54] analyzed the flow in a parallel walled channel and showed the time-averaged separated streamline and the reattachment length. As a distinct feature of this flow, the boundary layer is very thin at the corner of the plate leading edge, where the flow separates. Just downstream of the flow separation, the thin separated shear layer rapidly changes flow direction. Accordingly, the separated shear layer is severely unstable and easily transits to the turbulent one even at relatively low

Reynolds number. Subsequently, the turbulent shear layer reattaches onto the plate surface.

Further, details of the time-averaged flow field were clarified by Ota *et al.* [55], and they showed the mean velocity distribution, as shown in Figure 1.21, the pressure distribution, and also the development of the reattached turbulent boundary layer to the downstream. The variable  $(2h)$  and  $(U_m)$  signifies the thickness of the plate and the free stream velocity respectively according to the authors' nomenclature. The study was performed for a Reynolds number of  $2.69 \times 10^4$  based on the plate thickness.

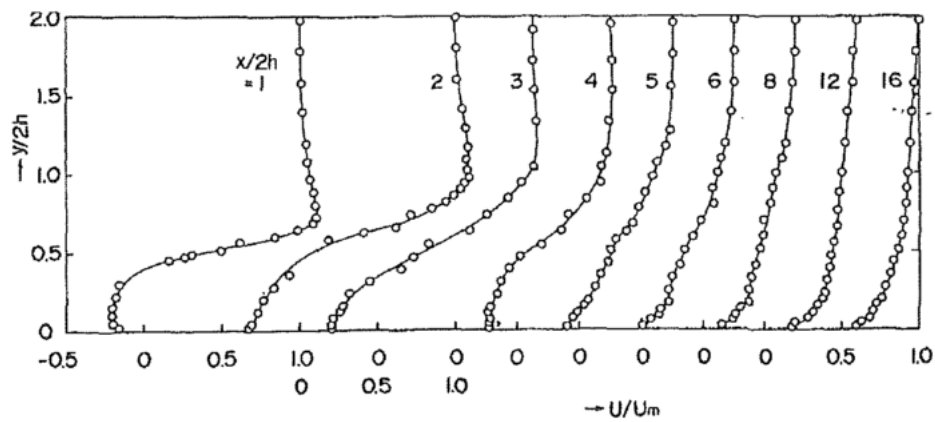


Figure 1.21 Velocity distribution over a blunt flat plate for  $Re = 2.69 \times 10^4$  [55]

In the same context, Kiya *et al.* [56] reported on a comprehensive set of measurements in which directionally sensitive split-film sensors were used in conjunction with hot-wire anemometry. Mean and fluctuating velocities and forward flow fraction data were presented.

Djilali *et al.* [18] detailed also in their work an experimental investigation of the two-dimensional flow around a long bluff rectangular plate placed at zero incidence in a uniform low-turbulence stream inside a wind tunnel. The measurements were made using conventional hot-wire anemometry, directionally sensitive pulsed wire anemometers and surface shear stress probes. The authors exposed the results of the flow field and the surface measurements (Figure 1.22, Figure 1.23, Figure 1.24, Figure 1.25 and Figure 1.26) made in a highly turbulent and unsteady separated-reattaching flow region. Their measurements were made for a Reynolds number of  $5 \times 10^4$  based on the plate thickness.  $D$  and  $U_{ref}$  are the plate thickness and the free stream velocity respectively according to the authors' nomenclature.

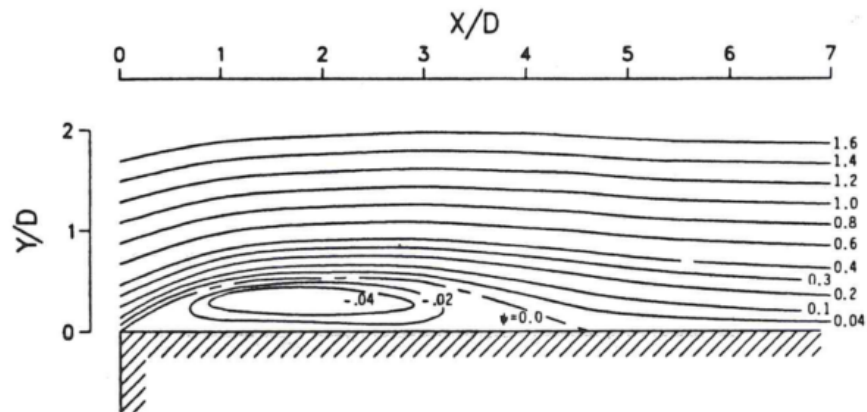


Figure 1.22 Mean streamlines deduced from pulsed-wire measurements [18]

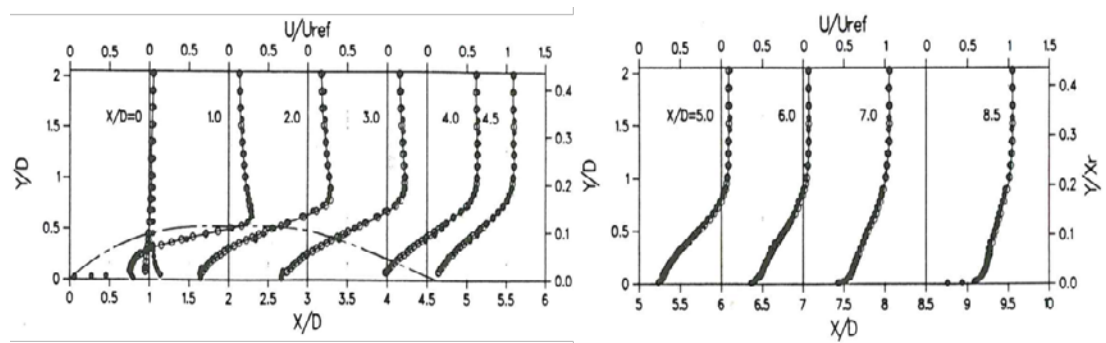


Figure 1.23 Mean longitudinal velocity profiles and separation streamlines [18]

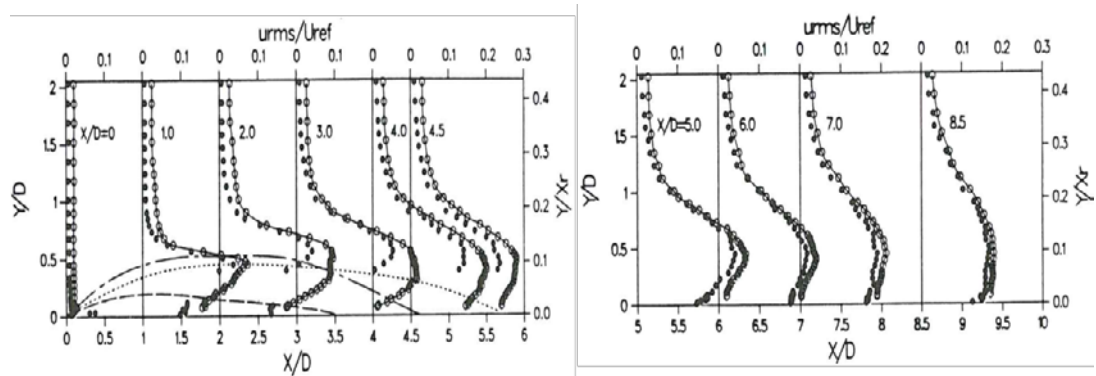


Figure 1.24 Fluctuating (r.m.s) longitudinal velocity profiles and separation streamlines [18]

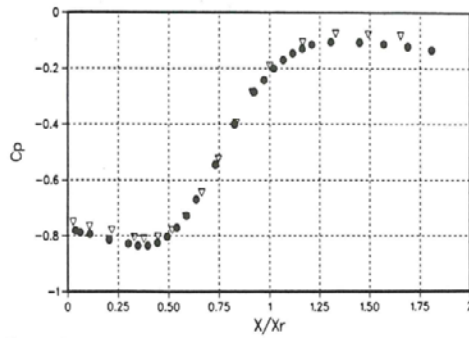


Figure 1.25 Distribution of surface pressure coefficient [18]

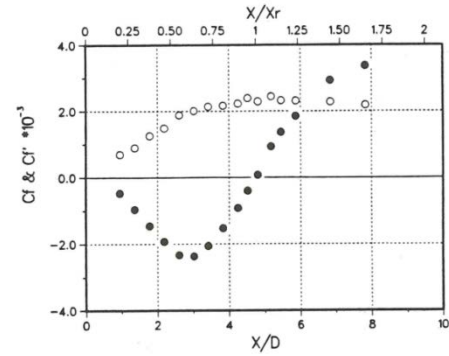


Figure 1.26 Distribution of wall shear stress coefficient: O, r.m.s; ●, mean [18]

The characteristic scale for the separation region is the reattachment length ( $X_r$ ). This is measured from the line of separation (the sharp leading edge) to the time-averaged reattachment line which is defined as the location where the time-averaged wall shear stress ( $\overline{\tau_w}$ ) vanishes (Figure 1.26). The reattachment length can be deduced as well from the surface flow visualization of the mean streamlines and the mean and fluctuating (r.m.s) longitudinal velocity profiles (Figure 1.22, Figure 1.23 and Figure 1.24).

The reattachment length ( $X_r$ ) of the separated-reattaching flow over a blunt flat plate depends mainly on the Reynolds number, the free stream turbulence intensity and the blockage ratio ( $BR$ ) defined as the tunnel height per the plate thickness.

The effect of Reynolds number was investigated by Ota *et al.* [57]. Using flow visualization (with aluminum powder), they observed three flow régimes:

- The *laminar separation – laminar reattachment* régime at low Reynolds number, in which, in agreement with the observations of Lane *et al.* [58], the reattachment length increases with the Reynolds number.
- The *laminar separation – turbulent reattachment* régime, in which the reattachment length decreases steeply as the Reynolds number increases. This régime is characterized by the appearance of instabilities in the shear layer near separation and transition to turbulence before reattachment.
- The *turbulent separation – turbulent reattachment* régime ( $Re \geq 2 \times 10^4$  based on the plate thickness) where the separated shear layer becomes turbulent very soon after separation. The Reynolds number was found to have no effect on the reattachment length in this last flow régime.

The Reynolds-number-independent regime was also observed by Hillier *et al.* [59]. They noted that the flow is essentially Reynolds number independent in the range  $3.4 \times 10^4 < Re < 8.0 \times 10^4$ , with a weak elongation appearing only when  $Re \geq 8.0 \times 10^4$ .

In the same paper, Hillier *et al.* [59] showed that the flow is very sensitive to free-stream-turbulence levels. Indeed, the reattachment length ( $X_r$ ) was found to decrease with increasing the free stream turbulence intensity. The effect of the free stream turbulence was also investigated by Kiya *et al.* [60]. They used a rod upstream of the plate to generate the turbulence and obtained results similar to those of Hillier *et al.*

On the other hand, the reattachment length was seen to decrease with increasing the solid blockage ratio ( $BR$ ) [61,62]. This can be observed by the data compiled by Cherry *et al.* [61] and showed in Figure 1.27. These data were obtained in low free stream turbulence intensity.

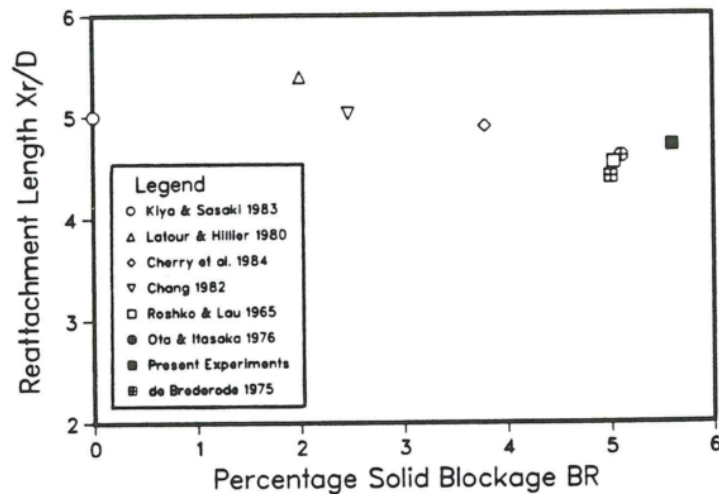
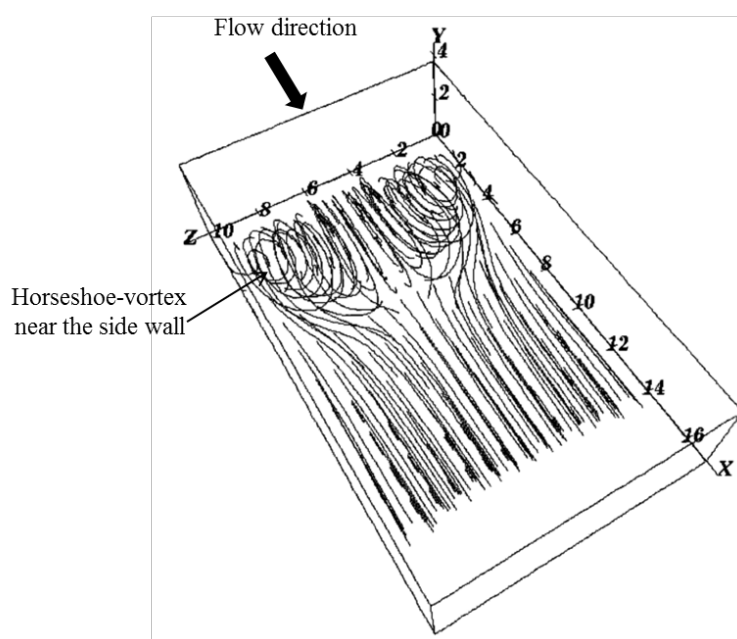


Figure 1.27 Reattachment lengths found for various solid blockage ratios [61]

The experiments conducted by Djilali *et al.* [18] reported a reattachment length of  $4.7D$  at a Reynolds number of  $5.0 \times 10^4 \pm 0.1 \times 10^4$  with a free stream turbulence intensities in the range of 0.25-0.4 percent and a solid blockage ratio ( $BR$ ) of 5.6 percent. Further, they observed that the reattachment length remains unchanged over the Reynolds number range  $2.5 \times 10^4$  to  $9.0 \times 10^4$  confirming then the observation of Hillier *et al.* [59] that the flow is essentially Reynolds number independent for  $Re \geq 2.7 \times 10^4$ . On the other hand, Ota *et al.* [63] observed that the flow reattachment occurs at about four plate thickness downstream from the leading edge. The turbulence level of the uniform flow was about 0.8 percent throughout their investigation with a Reynolds number of  $3.58 \times 10^4$  and a blockage ratio of 5 percent. It should be recalled that the Reynolds number ( $Re$ ) in such studies was calculated based on the plate thickness.

However, the separated-reattaching flow, over a blunt flat plate, is three-dimensional despite the presence of a horizontal uniform velocity field upstream of the plate within the test section.

Indeed, Yanaoka *et al.* [64] carried out three-dimensional numerical simulations of the separated and reattached flow over a blunt flat plate in a square channel. These numerical calculations of Navier-Stokes equations and energy equation were carried out using the finite difference method. It was clarified from the obtained results that the two-dimensionality of the flow is reduced as Reynolds number increases and the flow in the recirculation region becomes three-dimensional. This three-dimensionality of the flow is due to the side wall effects. The latter are explained by the presence of horseshoe-vortices formed near the side walls of the plate (Figure 1.28), resulting then in the presence of a curved reattachment line. However, the authors mentioned that the flow is three-dimensional except in the neighborhood of the plate center.



**Figure 1.28 Numerical mean streamlines over the blunt flat plate for  $Re=400$  [64]**

Given this fact, researchers [18,63] equipped bluff flat plates, during the experiments, with side plates or endplates in order to overcome the side wall effects and thus to ensure the two-dimensionality of the flow. Dziomba [65] indicated that the use of endplates is crucial to this purpose.

The complexity and the unpredictability of the gas flow pattern that can develop over molds of different sizes and shapes within an autoclave can be perceptible as well by investigating the effect of small geometrical changes on the flow field structure.

Against this background, Ota [66] and Djilali *et al.* [67] measured effects of the nose shape of a bluff flat plate upon the turbulence characteristics and showed the large effects of the nose shape in the separated and reattached regions and also far

downstream. It has been found from their obtained results that the reattachment length increases with the wedge angle ( $\alpha$ ) showed in Figure 1.29.

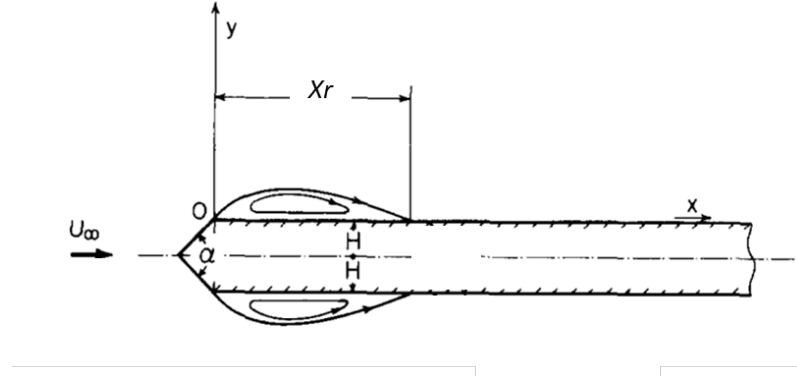


Figure 1.29 Nose shape of wedge angle ( $\alpha$ ) [68]

Beside the experimental works, numerical calculations of the separated-reattaching flow have been performed as well. Djilali *et al.* [69] made a numerical analysis with a  $k-\epsilon$  turbulence model and compared with the measured data. Li *et al.* [70] applied a scale-method to the Navier-Stokes (NS) equations for the separated and reattached flow around various configurations. Tafti *et al.* [71,72] made a “Direct Numerical Simulation” (DNS) of NS equations for two and three dimensional flows. They clarified clearly the reattachment length, the forming process of large scale vortices, the low-frequency motion of the separated shear layer, and the shedding frequency of large scale vortices.

### 1.3.3 Convective heat transfer description

The characteristic behavior of the separated shear layer exposed above sets out key questions about the local heat transfer coefficient ( $HTC$ ) distribution that can exist over the body as this behavior plays very important role upon the heat transfer in the separated and reattached regions.

Based on this principle, experimental studies of heat transfer around the blunt flat plate were first conducted by Ota *et al.* [63]. The authors made measurements of the heat transfer coefficient ( $HTC$ ) by means of thermocouples in the separated, reattached, and redeveloped regions of a two-dimensional air flow on a flat plate with blunt leading edge. The obtained  $HTC$  distribution is shown in Figure 1.30 in the form of  $Nu/Re^{2/3}$  for various Reynolds numbers. The dimensionless numbers, i.e.  $Re$  and  $Nu$ , were calculated based on the half of the plate thickness ( $H$ ). The used symbol is according to the authors nomenclature.



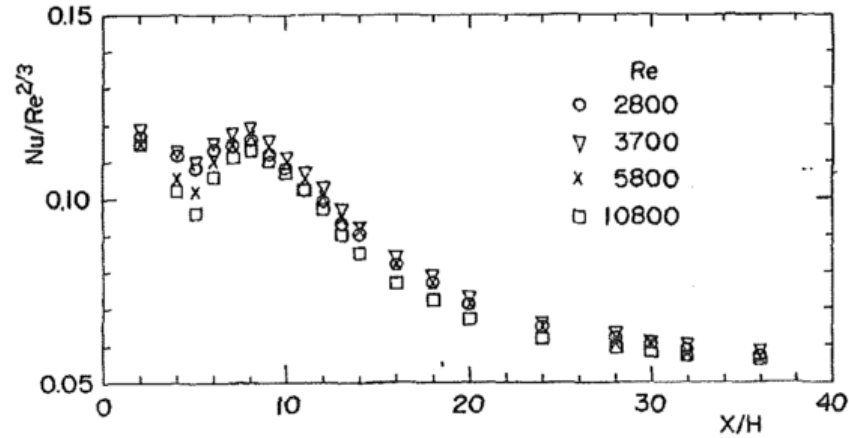


Figure 1.30 Local Nusselt number distribution [63]

Figure 1.30 shows that the ratio  $Nu/Re^{2/3}$  is independent of the Reynolds number with some scatters and it is a function of only the distance from the leading edge. Indeed,  $HTC$  increases sharply near the leading edge and reaches a maximum value at a position that corresponds to the reattachment point. The latter was found, according to the authors, to be at about four plate thickness downstream from the leading edge. Hereafter the Nusselt number at this position is called as the reattachment Nusselt ( $Nu_R$ ). However, Sparrow *et al.* [73] reported that the position of the maximum heat transfer coefficient is located somewhat upstream of the time-averaged reattachment point but this difference is generally small. Downstream from the reattachment point, the heat transfer coefficient decreases and approaches the value for the turbulent boundary layer on a flat plate. The conventional correlation of Colburn for the local Nusselt ( $Nu_x$ ) and Reynolds ( $Re_x$ ) numbers was shown in Figure 1.31 versus those obtained from measurements at the downstream region ( $x/H = 20$ ).

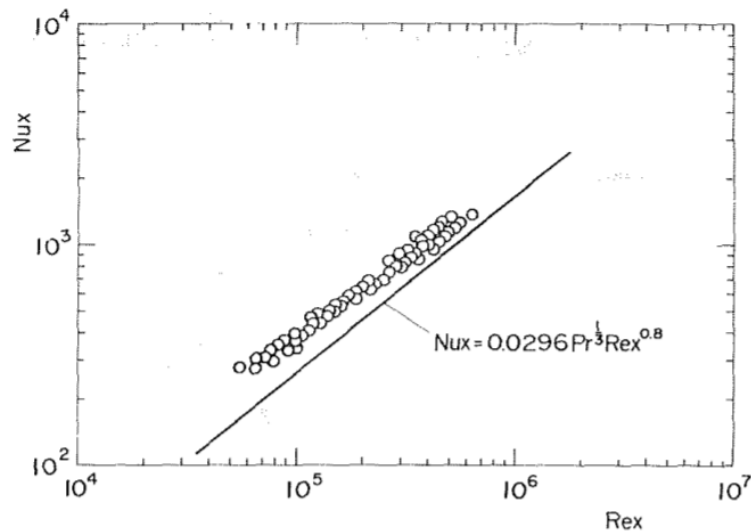


Figure 1.31 Local Nusselt number distribution in downstream region [63]



However, it was found that the present results were about 30 to 50 percent larger than the Colburn equation for the turbulent boundary layer on the flat plate. Further, Ota *et al.* [68] founded that the mean heat transfer coefficient over the whole plate length is larger by about 10-20% than the value estimated by the Colburn equation.

These findings affirm the assumption mentioned before that the existing correlations are unable to predict accurately the heat transfer coefficient distribution over molds of bluff body shape placed within an autoclave. This complexity of the heat transfer coefficient prediction can be perceptible as well by observing the effects of the nose shape of a blunt plate (Figure 1.29) upon the heat transfer characteristics in the separated, reattached, and redeveloping flow regions [68].

Given this fact, the authors Ota *et al.* [74] worked on a universal correlation formula for the estimation of the maximum turbulent heat transfer coefficient in the reattachment flow region around bluff bodies. More specifically, in the case of a blunt flat plate with leading edges of various shapes (Figure 1.29), Ota *et al.* [68] developed a correlation between the reattachment Nusselt number and the Reynolds number independently of the nose shape (Equation (1.9)). The reattachment length ( $X_r$ ) is employed as the reference length.

$$Nu_R = \frac{HTC_R \cdot X_r}{\lambda} = 0.0919 \left( \frac{U_\infty \cdot X_r}{\nu} \right)^{0.734} \quad \text{Equation (1.9)}$$

In the case of a three-dimensional separated and reattached flow over a blunt flat plate as showed previously, Yanaoka *et al.* [64] observed numerically that the horseshoe-vortices formed near the side walls have great effects upon the heat transfer in the redeveloping region. Indeed, they explained that the horseshoe-vortices cause an increase of the streamwise velocity and also the transverse one near the side walls. Therefore these flows bring about a great increase of Nusselt number near the side walls than the channel center. These effects are illustrated in Figure 1.32 which shows the local Nusselt number distribution from the channel center to the side wall of the plate. A schema of the plate with the coordinate system was presented previously in Figure 1.28. Results of two-dimensional calculations were included in this figure for comparison. It can be seen clearly that the difference between the two and the three dimensional results for the Nusselt number is relatively small near the channel center but increases greatly near the side walls. These thermal findings affirm the two-dimensionality of the flow near the plate center.

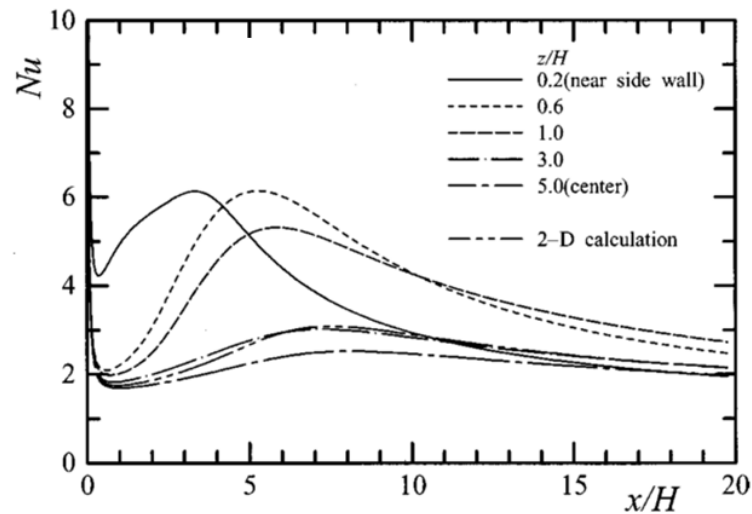


Figure 1.32 Nusselt number distribution [64]

### 1.3.4 Summary

This exposed survey of the numerous previous research works allow to understand the characteristics of the turbulent gas flow along a bluff body as well as the heat transfer behavior in the separated, reattached and redeveloping flow regions. The complexity and the unpredictability of these phenomena explained above lead to deduce that the assumption of a uniform and constant heat transfer coefficient over molds surfaces placed inside an autoclave is not adequate. Thus, it can result in inaccurate prediction of the thermal history of the manufactured composite parts. On the other hand, the heat transfer coefficient has shown to depend strongly upon the behaviors of the turbulent separated shear layers. Therefore the thermal analysis of the temperature field within a composite part should pass essentially through a better understanding of the flow field behavior around bluff body molds coupled with the investigation of the convective heat transfer coefficients distribution.

However, these experimental investigations of the flow and heat transfer in the separated, reattached, and redeveloping regions have been carried out by means of intrusive instruments such as Pitot tube, hot-wire anemometer and thermocouples respectively. These techniques are known to be unreliable in this kind of flow. Additionally, important three-dimensional effects are likely to have been present as explained previously. Based on these challenges, alternative approaches and new experimental methodologies are necessary.

## **1.4 Partial conclusion**

The survey of the numerous previous research studies on the heat transfer analysis within autoclaves, exposed in section 1.2.2.2, has shown that the convective heat transfer mechanism, modeled through the convective heat transfer coefficient, is one of the most relevant aspect controlling the rate of chemical and physical transformations associated with composite parts curing in autoclave. An accurate knowledge of the local convective heat transfer coefficient distribution constitutes thus an essential element to generate appropriate boundary conditions over the autoclave assembly (bag-composite laminate-mold) and therefore to predict accurately the temperature field with composites parts. However, the use of molds of various bluff body shapes and often with aerodynamically unfavorable geometries can develop very complex turbulent flow along the body and often characterized by the presence of separated-reattaching regions. Such a flow has shown to affect strongly the convective heat transfer coefficient distribution that becomes non-uniform and unpredictable over the mold surfaces. The heterogeneity of this distribution can generate thermal gradients within a manufactured composite part. The presence of thermal gradients can result in non-uniform degrees of cure leading potentially to residual stresses in the final part which can reduce its quality and its final mechanical properties. On the other hand, the different presented previous studies have been carried out by means of intrusive instruments. These techniques are known to be unreliable in this kind of conditions. Based on these challenges, alternative approaches and new experimental methodologies have been developed in the presented thesis study. These measurement methodologies will be detailed and exposed in *Chapter 2*.

## List of references

- [1] S.T. Peters, Handbook of Composites, second ed., Chapman & Hall, London, 1998.
- [2] L. Gornet, Généralités sur les matériaux composites, 2008. <https://cel.archives-ouvertes.fr/cel-00470296v1>.
- [3] P.K. Mallick, Composites Engineering Handbook, first ed., Marcel Dekker, New York, 1997.
- [4] K.K. Kar, Composite Materials: processing, Applications, Characterizations, first ed., Springer, Berlin, 2017.
- [5] A. Baker, S. Dutton, D. Kelly, Composite Materials for Aircraft Structures, second ed., American Institute of Aeronautics and Astronautics, Virginia, 2004.
- [6] J.-M. Berthelot, Composite Materials: Mechanical Behavior and Structural Analysis, first ed., Springer, New York, 1999.
- [7] G.N. Dayananda, M. Subba Rao, B.R. Somashekar, Indigenous development of autoclave technology, in: Proc. Natl. Symp. Dev. Adv. Compos. Struct., 1994.
- [8] S.G. Advani, E.M. Sozer, Processing advanced thermo set fiber composites, in: Process Model. Compos. Manuf., 2002: pp. 339–343.
- [9] P.J. Mallon, M.R. Monaghan, Development of a computer controlled autoclave for forming thermoplastic composites, Compos. Manuf. 1 (1990) 8–14.
- [10] A.R. Upadhyay, G.N. Dayananda, G.M. Kamalakannan, J. Ramaswamy Setty, J. Christopher Daniel, Autoclaves for aerospace applications: issues and challenges, Int. J. Aerosp. Eng. 2011 (2011) 1–11. <http://www.hindawi.com/journals/ijae/2011/985871/> (accessed January 20, 2015).
- [11] P.F. Monaghan, M.T. Brogan, P.H. Oosthuizen, Heat transfer in an autoclave for processing thermoplastic composites, Compos. Manuf. 2 (1991) 233–242. <http://linkinghub.elsevier.com/retrieve/pii/0956714391901457>.
- [12] <http://www.boeingimages.com/archive/Massive-Autoclave-for-Curing-Composite-Materials-2F3XC55WX12.html>, (n.d.).
- [13] N.E.J. Olsson, T.S. Lundstrom, L. Westerberg, T. Nyman, Flow and heat transfer inside an autoclave, in: Proc. FPCM11 Conf., Auckland, 2012: pp. 188–195.
- [14] N.S. Ghariban, A. Haji-Sheikh, D.Y.S. Lou, Heat transfer in autoclaves, in: ICHMT Int. Symp. Manuf. Mater. Process., Dubrovnik, 1990: pp. 833–848.
- [15] F.C. Campbell, Chapter 6: Curing: It's a Matter of Time (t), Temperature (T) and Pressure (P), in: J. Flake Campbell (Ed.), Manuf. Process. Adv. Compos., First ed., Elsevier Science, 2003: pp. 175–179.
- [16] A. Johnston, An integrated model of the development of process-induced deformation in autoclave processing of composite structures, The University of

- British Columbia, 1997.
- [17] N. Slesinger, T. Shimizu, A. Poursartip, A.R.A. Arafath, Heat transfer coefficient distribution inside an autoclave, in: Proc. 17Th Int. Conf. Compos. Mater., Edinburgh, UK, 2009.
  - [18] N. Djilali, I.S. Gartshore, Turbulent flow around a bluff rectangular plate. Part I: experimental investigation, *J. Fluids Engineering*. 113 (1991) 51–59.
  - [19] T.A. Weber, J.-C. Arent, L. Münch, M. Duhovic, J.M. Balvers, A fast method for the generation of boundary conditions for thermal autoclave simulation, *Compos. Part A*. 88 (2016) 216–225. <http://dx.doi.org/10.1016/j.compositesa.2016.05.036>.
  - [20] A. Kondjoyan, F. Péneau, H.-C. Boisson, Effect of high free stream turbulence on heat transfer between plates and air flows: a review of existing experimental results, *Int. J. Therm. Sci.* 41 (2002) 1–16. doi:10.1016/S1290-0729(01)01299-6.
  - [21] G. Xie, J. Liu, W. Zhang, Simulation and thermal analysis on temperature fields during composite curing process in autoclave technology, in: Proc. ASME 2012 Int. Mech. Eng. Congr. Expo. IMECE2012, Houston, Texas, USA, 2012: pp. 1–9.
  - [22] M.K. Telikicherla, M.C. Altan, F.C. Lai, Autoclave curing of thermosetting composites: process modeling for the cure assembly, *Int. Commun. Heat Mass Transf.* 21 (1994) 785–797.
  - [23] T.L. Bergman, A.S. Lavine, F.P. Incropera, D.P. DeWitt, *Fundamentals of Heat and Mass Transfer*, Seventh, John Wiley & Sons, Jefferson, 2011. <http://books.google.com/books?id=vvyIoXEywMoC&pgis=1>.
  - [24] A. Johnston, P. Hubert, R. Vaziri, A. Poursartip, An investigation of autoclave convective heat transfer, in: *Des. Manuf. Compos.*, 1998: pp. 106–113.
  - [25] T. Ota, A Survey of Heat Transfer in Separated and Reattached Flows, *Appl. Mech. Rev.* 53 (2000) 219–235. doi:10.1115/1.3097351.
  - [26] G.W.C. Kaye, T.H. Laby, *Tables of physical and chemical constants, and some mathematical functions*, second ed, Kessinger Publishing, Whitefish, 2008.
  - [27] V. Antonucci, M. Giordano, S. Inserraimparato, L. Nicolais, Analysis of heat transfer in autoclave technology, *Polym. Compos.* 22 (2001) 613–620. doi:10.1002/pc.10564.
  - [28] N.E.J. Kluge, *Experiments and numerical modelling of the SMC and autoclave processes*, Lulea University of Technology, 2015.
  - [29] Scholtz Maschinenbau, (n.d.). <https://www.scholz-autoclaves.com/>.
  - [30] ASC Process Systems, (n.d.). <http://www.aschome.com/index.php/en/>.
  - [31] J.R. Howell, R. Siegel, M.P. Menguc, *Thermal Radiation Heat Transfer*, fifth ed, Taylor & Francis Group, Boca Raton, n.d.
  - [32] J.N.E. Kluge, T. Lundström, L. Westerberg, T. Nyman, *Modelling heat transfer*

- inside an autoclave: Effect of radiation, *J. Reinf. Plast. Compos.* 0 (2016) 1–17. doi:10.1177/0731684416641333.
- [33] N.E.. Kluge, T.. Lundstrom, A. Ljung, L.. Westerberg, T. Nyman, An experimental study of temperature distribution in an autoclave, *J. Reinf. Plast. Compos.* 35 (2016) 566–578. doi:10.1177/0731684415624768.
- [34] V. Antonucci, M. Giordano, S.I. Imparato, L. Nicolais, Autoclave manufacturing of thick composites, *Polym. Compos.* 23 (2002) 902–910. doi:10.1002/pc.10487.
- [35] A.C. Loos, G.S. Springer, Curing of epoxy matrix composites, *J. Compos. Mater.* 17 (1983) 135–169. doi:10.1177/002199838301700204.
- [36] S.C. Joshi, X.L. Liu, Y.C. Lam, A numerical approach to the modeling of polymer curing in fibre-reinforced composites, *Compos. Sci. Technol.* 59 (1999) 1003–1013.
- [37] M.K. Telikicherla, M.C. Altan, F.C. Lai, Autoclave curing of thermosetting composites: process modeling for the cure assembly, *Int. Commun. Heat Mass Transf.* 21 (1994) 785–797.
- [38] M. Péron, R. Cardinaud, N. Lefèvre, J. Aubril, V. Sobotka, N. Boyard, S. Le Corre, PvT-HADDOC : A multi-axial strain analyzer and cure monitoring device for thermoset composites characterization during manufacturing, *Compos. Part A.* 101 (2017) 129–142. doi:10.1016/j.compositesa.2017.06.004.
- [39] J.S. Kim, D.G. Lee, Development of an Autoclave Cure Cycle with Cooling and Reheating steps for Thick Thermoset Composite Laminates, *J. Compos. Mater.* 31 (1997) 2264–2282.
- [40] L. Kalra, M.J. Perry, L.J. Lee, Automation of autoclave cure of graphite-epoxy composites, *J. Compos. Mater.* 26 (1992) 2567–2584.
- [41] A. Labban, P. Mousseau, R. Deterre, J.-L. Bailleul, Curing cycle optimization of a thick-section rubber part, *Rubber Chem. Technol.* 83 (2010) 331–348.
- [42] A. Labban, P. Mousseau, J.L. Bailleul, R. Deterre, Optimization of thick rubber part curing cycles, *Inverse Probl. Sci. Eng.* 18 (2010) 313–340. doi:10.1080/17415971003589517.
- [43] Z. Guo, S. Du, B. Zhang, Temperature field of thick thermoset composite laminates during cure process, *Compos. Sci. Technol.* 65 (2005) 517–523. doi:10.1016/j.compscitech.2004.07.015.
- [44] D.C. Blest, B.R. Duffy, S. Mckee, A.K. Zulkifle, Curing simulation of thermoset composites, *c* (1999) 1289–1309.
- [45] a Cheung, Y. Yu, K. Pochiraju, Three-dimensional finite element simulation of curing of polymer composites, *Finite Elem. Anal. Des.* 40 (2004) 895–912. doi:10.1016/S0168-874X(03)00119-7.
- [46] A.C. Loos, G.S. Springer, Epoxy Matrix Composites of, 17 (1983) 135–169.
- [47] S. Yi, H.H. Hilton, M.F. Ahmad, A finite element approach for cure simulation

- of thermosetting matrix composites, *Comput. Struct.* 64 (1997) 383–388. doi:10.1016/S0045-7949(96)00156-3.
- [48] J.H. Oh, D.G. Lee, Cure Cycle for Thick Glass / Epoxy Composite Laminates, *J. Compos. Mater.* 36 (2002) 19–45. doi:10.1106/00219980202330.
- [49] V. a F. Costa, a. C.M. Sousa, Modeling of flow and thermo-kinetics during the cure of thick laminated composites, *Int. J. Therm. Sci.* 42 (2003) 15–22. doi:10.1016/S1290-0729(02)00003-0.
- [50] M. Hudek, Examination of heat transfer during autoclave processing of polymer composites, 2001.
- [51] G.N. Xie, J. Liu, W.H. Zang, G. Lorenzini, C. Biserni, Simulation and improvement of temperature distributions of a framed mould during the autoclave composite curing process, *J. Eng. Thermophys.* 22 (2013) 43–61. doi:10.1134/S1810232813010062.
- [52] F. Chen, L. Zhan, Y. Xu, Modelling and simulation for temperature distribution of mold during autoclave forming process, in: *Proc. 12th Int. Conf. Heat Transf. Therm. Eng. Environ.*, Geneva, 2014: pp. 80–88.
- [53] Z. Cheng, W. Yonggui, L. Xianzhu, Z. Boming, Y. Guangquan, J. Peng, Research with CFX software on frame mould temperature field simulation in autoclave process, *Polym. Polym. Compos.* 17 (2009) 325–336.
- [54] T. Ota, A separated and reattached flow on a blunt flat plate in a tunnel, *Q. J. Mech. Appl. Math.* 27 (1974) 379–386.
- [55] T. Ota, M. Itasaka, A separated and reattached flow on a blunt flat plate, *J. Fluids Eng.* 98 (1976) 79–86.
- [56] M. Kiya, K. Sasaki, Structure of a turbulent separation, *J. Fluid Mech.* 137 (1983) 83–113.
- [57] T. Ota, Y. Asano, J. Okawa, Reattachment length and transition of the separated flow over blunt flat plates, *Bull. JSME.* 24 (1981) 941–947.
- [58] J.C. Lane, R.I. Loehrke, Leading edge separation from a blunt flat plate at low reynolds number, *J. Fluids Eng.* 102 (1980) 494–496.
- [59] R. Hillier, N.. Cherry, The effects of stream turbulence on separation bubbles, *J. Wind Eng. Ind. Aerodyn.* 8 (1981) 49–58.
- [60] M. Kiya, K. Sasaki, Free-stream turbulence effects on a separation bubble, *J. Wind Eng. Ind. Aerodyn.* 14 (1983) 373–386. doi:http://dx.doi.org/10.1016/0167-6105(83)90039-9.
- [61] N.J. Cherry, R. Hillier, M.E.M.P. Latour, Unsteady measurements in a separated and reattaching flow, *J. Fluid Mech.* 144 (1984) 13–46. doi:10.1017/S002211208400149X.
- [62] E. Velayati, M. Yaghoubi, Numerical study of convective heat transfer from an array of parallel bluff plates, *Int. J. Heat Fluid Flow.* 26 (2005) 80–91. doi:10.1016/j.ijheatfluidflow.2004.05.001.



- [63] T. Ota, N. Kon, Heat transfer in the separated and reattached flow on a blunt flat plate, *J. Heat Transfer*. 96 (1974) 459–462.
- [64] H. Yanaoka, H. Yoshikawa, T. Ota, Numerical simulation of laminar flow and heat transfer over a blunt flat plate in square channel, *J. Heat Transfer*. 124 (2002) 8–16. doi:10.1115/1.1420715.
- [65] B. Dziomba, Experimental investigation of bluff body separation regions, in: *CASI Aerodyn. Symp.*, Montréal, 1985.
- [66] T. Ota, Nose shape effects on turbulence in the separated and reattached flow over blunt flat plates, *Zeit Flugwiss Weltraumforsch.* 7 (1983) 316–321.
- [67] N. Djilali, I.S. Gartshore, Effect of leading-edge geometry on a turbulent separation bubble, *AIAA J.* 30 (1992) 559–561.
- [68] T. Ota, N. Kon, Heat transfer in the separated and reattached flow over blunt flat plates - Effects of nose shape, *Int. J. Heat Mass Transf.* 22 (1979) 197–206.
- [69] N. Djilali, I.S. Gartshore, M. Salcudean, Turbulent flow around a bluff rectangular plate. Part II : numerical predictions, *J. Fluids Eng.* 113 (1991) 60–67. doi:10.1115/1.2926498.
- [70] X. Li, N. Djilali, On the scaling of separation bubbles, *JSME Int. J.* 38 (1995) 541–548. doi:10.1248/cpb.37.3229.
- [71] D.K. Tafti, S.P. Vanka, A three-dimensional numerical study of flow separation and reattachment on a blunt plate, *Phys. Fluids A.* 3 (1991) 2887–2909. doi:10.1063/1.858208.
- [72] D.K. Tafti, S.P. Vanka, A numerical study of flow separation and reattachment on a blunt plate, *Phys. Fluids A.* 3 (1991) 1749–1759.
- [73] E.M. Sparrow, S.S. Kang, W. Chuck, Relation between the points of flow reattachment and maximum heat transfer for regions of flow separation, *Int. J. Heat Mass Transf.* 30 (1987) 1237–1246. doi:10.1016/0017-9310(87)90157-8.
- [74] T. Ota, H. Nishiyama, A correlation of maximum turbulent heat transfer coefficient in reattachment flow region, *Int. J. Heat Mass Transf.* 30 (1987) 1193–1200. doi:10.1016/0017-9310(87)90048-2.



*Chapter 2*  
*Design and Fabrication of  
the Model Autoclave  
and associated  
instrumentation*



## Table of contents

<b><i>Chapter 2 Design and Fabrication of the Model Autoclave and associated instrumentation.....</i></b>	<b><i>61</i></b>
<b>2.1 PRINCIPLE OF THE MODEL AUTOCLAVE .....</b>	<b>65</b>
<b>2.2 DIMENSIONAL ANALYSIS AND SIMILARITY LAWS.....</b>	<b>66</b>
<b>2.3 DESIGN STRATEGY OF THE MODEL AUTOCLAVE.....</b>	<b>69</b>
2.3.1 Application of similarity laws.....	69
2.3.1.1 Prototype autoclave .....	69
2.3.1.2 Working section of the model autoclave .....	70
2.3.1.2.1 Application of the geometric similarity .....	70
2.3.1.2.2 Application of the dynamic similarity.....	71
2.3.1.2.3 Application of the energetic similarity.....	74
2.3.1.2.4 Summary of the applied similarity conditions .....	75
2.3.2 Determination of the model autoclave concept .....	77
2.3.3 Presentation of the designed model autoclave .....	78
<b>2.4 AERODYNAMIC INSTRUMENTATION AND MEASUREMENT METHODOLOGY .</b>	<b>82</b>
2.4.1 Flow field measurement.....	82
2.4.2 Introduction to the PIV technique.....	82
2.4.3 Description of the employed PIV system (Laser + Camera) .....	84
2.4.4 Measurement and post-processing methodology .....	85
<b>2.5 VALIDATION OF THE MODEL AUTOCLAVE .....</b>	<b>88</b>
2.5.1 Procedure of the validation work.....	88
2.5.2 Results of the validation work .....	89
<b>2.6 DESIGN OF THE MODEL MOLD .....</b>	<b>95</b>
2.6.1 Application of the geometrical similarity condition .....	95
2.6.2 Concept of the model mold.....	95
2.6.3 Thermal instrumentation and measurement methodology.....	97
2.6.3.1 Measurement of $T_{mx}$ .....	98
2.6.3.2 Measurement of $\varphi_{cx}$ .....	99
2.6.3.3 Measurement of $HTC$ .....	101
<b>2.7 INTER-PART SHADOWING EFFECTS INVESTIGATION .....</b>	<b>103</b>
<b>2.8 STUDY OF A REPRESENTATIVE MOLD .....</b>	<b>104</b>
<b>2.9 PARTIAL CONCLUSION .....</b>	<b>107</b>
<b>LIST OF REFERENCES.....</b>	<b>108</b>



## **2.1 Principle of the Model Autoclave**

The discussions and the analyzes, presented in the *chapter 1*, of the previous research studies have shown the lack of precise investigation of the velocity field and the local heat transfer coefficient distribution around molds of bluff body shape inside an autoclave. Such kind of investigation represents a key element to obtain appropriate boundary conditions of the mold and thus to predict accurately the temperature history of the composite part.

On the other hand, the previous research works on the study of flow field and heat transfer behaviors along bluff bodies, such as blunt flat plate, were found to use techniques which are unreliable, intrusive and difficult to implement.

Given this fact, the achievement of the main objective of the thesis project should pass essentially through precise measurements of the velocity field and the local *HTC* distribution along molds of bluff body shape installed inside an autoclave, and by means of non-intrusive measuring instruments.

However, the complicated configuration systems of autoclaves as well as their expensive time and cost consuming make technically difficult the performing of experimental tests as well as the instrumentation by advanced and non-intrusive measurement techniques. As a result, performing experimental measurements inside full scale autoclaves becomes a challenging area and thus an alternative approach is necessary.

To overcome this challenge, the alternative and the new approach proposed in this thesis study consists in developing a home-made model autoclave to perform the required experimental measurements. The developed test bench represents in fact a reduced scale autoclave designed and then manufactured based on similarity laws applied on a full scale actual autoclave. The application of the similarity laws enables to obtain the same main physical phenomena that exist in the full scale one such as the turbulent flow field and the forced convective heat transfer. Representative real industrial molds of various shapes can be installed within the working section of the model autoclave for the experimental tests.

Further, one of its most important advantages is the ease of use of non-intrusive and reliable measuring instruments such as the Particle Image Velocimetry (PIV) technique for the measurement of the velocity field and the infrared imaging camera for the study of the convective heat transfer coefficient distribution over molds.

The various steps followed during the thesis study for the design of the proposed Model Autoclave will be detailed in the next sections. The associated instrumentation

and the developed experimental methodologies for the flow field and heat transfer measurements will be exposed as well.

## **2.2 Dimensional analysis and similarity laws**

The dimensional analysis consists of reducing the number and complexity of experimental variables, which affect a given physical phenomenon, and group them in dimensionless form. The dimensional analysis requires the resort to compacting techniques and methods such as the “Buckingham pi theorem” [1].

The main benefit of the dimensional analysis is that it provides “scaling or similarity laws” which can convert data from a cheap, small model to design information for an expensive, large prototype. Thus it allows an enormous savings in time and cost.

In fact, when the actual geometrical size of a problem does not match the laboratory scale and it presents complicated configurations, which is the case for an actual autoclave, it should have recourse to experimental tests performed on a model. In this case, the experimenter must respect certain functioning conditions that link the study on the model to its prototype transposition. These conditions are defined by the “similarity laws”. When the scaling law is valid, then it can be said that a condition of similarity exists between the model and the prototype [1].

The main types of similarities that must exist for a complete similitude between a model and its prototype are the following:

- Geometric similarity
- Dynamic similarity
- Energetic similarity

In the case of fluid mechanics problems coupled with heat transfers mechanisms, these conditions of similarity as well as the main associated dimensionless parameters are listed in Table 2.1. These dimensionless numbers will be employed for the sizing of the model autoclave.

Table 2.1 Dimensionless groups in fluid mechanics and heat transfers [1]

Similarity condition	Parameter	Definition	Qualitative ratio of effects	Importance
Geometric	linear-scale	$k_l = \frac{l_{mo}}{l_p}$	Distance ratio	Always
Dynamic	Reynolds number	$Re = \frac{\rho U_\infty l_c}{\mu}$	Inertia/ Viscosity	Always
	Froude number	$Fr = \frac{U_\infty^2}{g l_c}$	Inertia/ Gravity	Free-surface flow
	Weber number	$We = \frac{\rho U_\infty^2 l_c}{Y}$	Inertia/ Surface tension	Free-surface flow
	Euler number	$Eu = \frac{P}{\rho U_\infty^2}$	Pressure/ Inertia	Cavitation
Energetic	Prandtl number	$Pr = \frac{\mu c_p}{\lambda}$	Dissipation/ Conduction	Heat convection
	Nusselt number	$Nu = \frac{HTC \cdot l_c}{\lambda}$	Convection/ Conduction	Forced convection
	Grashof number	$Gr = \frac{\rho^2 g \beta l_c^3 \Delta T}{\mu^2}$	Buoyancy/ Viscosity	Natural convection
	Richardson number	$Ri = \frac{Gr}{Re^2}$	Natural/ Forced	Mixed convection
	Eckert number	$Ec = \frac{U_\infty^2}{c_p \Delta T}$	Kinetic energy/ Enthalpy	Dissipation
	Temperature ratio	$\frac{T_w}{T_\infty}$	Wall temperature/ Stream temperature	Heat transfer

For the dynamic similarity conditions, it is common to characterize an incompressible gaseous flow such as air, which is the kind of flow that circulates within an autoclave, primarily by its Reynolds number ( $Re$ ) [2]. The incompressibility of the flow is due to its lower Mach number (below unity). Then, the  $Re$  is considered

as the key dimensionless parameter of interest while the other numbers, i.e.  $Fr$ ,  $Eu$ , and  $We$  drop out entirely especially if there are no free surfaces [1].

However, achieving Reynolds number similarity is a difficult task, even in incompressible flows, and thus the only way to match  $Re$  is to increase the velocity within the model [2].

On the other hand, for the energetic similarity conditions, the Grashof and the Richardson numbers drop out also as the investigated phenomenon is purely forced convection as shown in *Chapter 1*.



## ***2.3 Design strategy of the model autoclave***

### **2.3.1 Application of similarity laws**

#### **2.3.1.1 Prototype autoclave**

The prototype full-scale autoclave, chosen for the design of the model autoclave, represents a conventional actual autoclave manufactured by Scholtz Maschinenbau [3]. The prototype autoclave is shown in Figure 2.1.

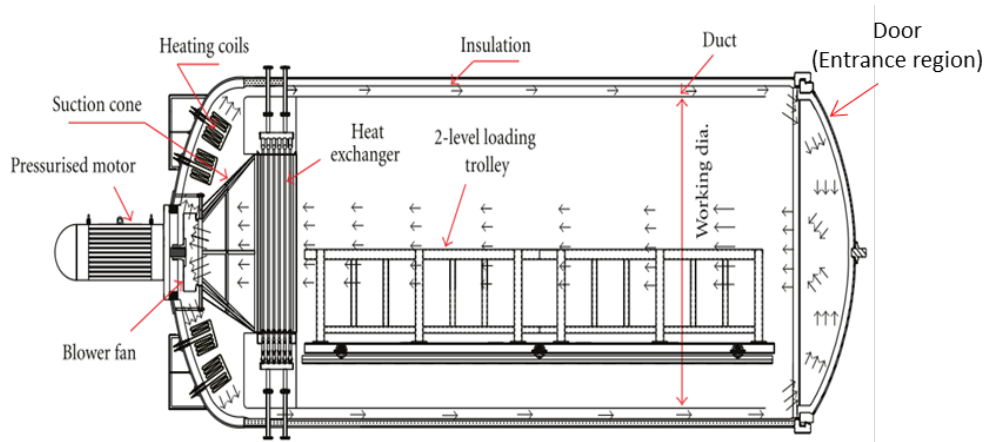


**Figure 2.1 Schematic of the prototype autoclave [4]**

The working section of the prototype autoclave is a cylindrical vessel with a length of 8 m and a diameter of 3 m. Air is the used gas and its mean velocity through the loaded working section of the autoclave was estimated to be approximately 3 m/s.

On the other hand, the adopted curing cycle is shown in Figure 2.2.

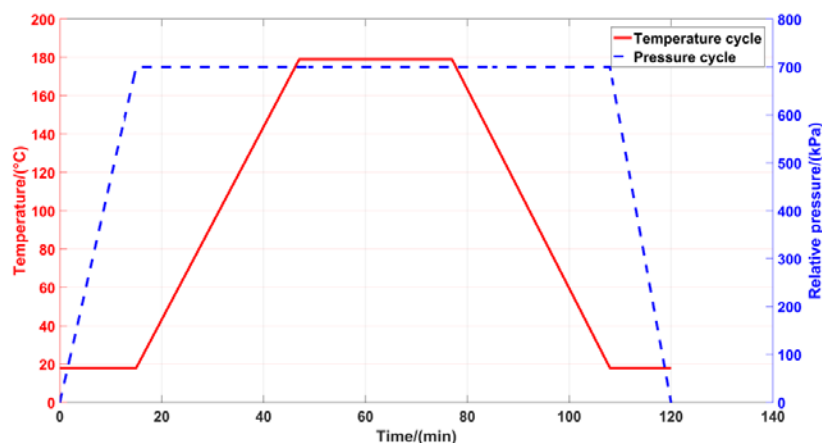


**Figure 2.2 The air curing cycle [5]**

During this curing cycle, the air can be pressurized up to 700 kPa and heated by electrical resistance heaters up to 180 °C.

Further, an industrial simplified prototype mold was chosen and it is supposed to be a rectangular box-shaped mold, such as the one used by previous researchers [6–8], with a length of 4 m, a width of 2.3 m and a thickness of 130 mm.

### **2.3.1.2 Working section of the model autoclave**

#### **2.3.1.2.1 Application of the geometric similarity**

The geometric similarity between the working section of the prototype autoclave and the model requires the use of the dimensionless parameter  $k_l$  which represents the distance scale as showed in section 2.2. This parameter was chosen carefully in order to obtain a working section dimensionally adapted for the test room. It was selected also to obtain appropriate dimensions for the implementation and the efficiency use of the PIV technique.

Given this fact,  $k_l$  was chosen to be 7.5. This resulting in a model working section of cylindrical shape with a length of 1.07 m and a diameter of 0.4 m. However, it was decided to transform the obtained cylindrical working section to a rectangular shape working section as it is helpful and practical for the installation of the model molds and the performing of the experimental measurements. This decision was justified by the fact that the flow field around a mold within an autoclave is considered as an external flow [9]. Further, the study of the boundary layers thicknesses growth over the different inner walls of the working section of the model autoclave has shown no interactions [10]. Thus the flow field pattern is not influenced by the working section shape. As a result, the working section of the model autoclave was designed as a rectangular section shape vessel of high 0.4 m and width 0.315 m, which allows the obtaining of a section area equivalent to the 0.4 m diameter.

On the other hand, the sizing work of the model mold installed within the working section and used for performing experimental measurements will be presented in section 2.6.

The summary of the application of the geometric similarity condition is exposed in the Table 2.2 which shows the dimensions of the obtained model working section.

**Table 2.2 Application of the geometric similarity condition**

	<b>Geometric similarity parameter</b>	<b>Dimensions of the working section</b>	
	$k_l$	$D$ (m)	$l$ (m)
<b>Prototype autoclave</b>	7.5	3	8
<b>Model autoclave</b>		0.4, $\Rightarrow$ $L = 0.315$ m and $H = 0.4$ m	1.07

#### 2.3.1.2.2 Application of the dynamic similarity

The dynamic similarity for an incompressible and no free surface gaseous flow problem, which is the encountered case within an autoclave, is governed essentially by the Reynolds number ( $Re$ ) as shown above.

Given this fact, the similarity condition requires the respect of the Reynolds number value between the prototype and the model. This parameter was calculated based on the length of the mold ( $l$ ), the free stream velocity ( $U_\infty$ ) and the kinematic viscosity ( $\nu = \mu/\rho$ ) either for the prototype or the model autoclave. The subscripts  $m$  and  $p$  mean model and prototype respectively.

$$Re_{mo} = Re_p$$

**Equation (2.1)**

$$U_{\infty mo} = U_{\infty p} \frac{l_p}{l_{mo}} \frac{\nu_{mo}}{\nu_p} = U_{\infty p} \frac{1}{k_l} \frac{\nu_{mo}}{\nu_p}$$

This similarity condition represented by the Equation (2.1) was used to estimate the free stream velocity ( $U_{\infty mo}$ ) within the working section of the model autoclave. The remaining unknown variable is the gas kinematic viscosity  $\nu_{mo}$ . The latter is a function of the working gas pressure and temperature within the model autoclave. The used gas is the air as in the prototype autoclave.

The choice of the temperature of the air that flows within the working section of the model autoclave was made by taking into account many considerations. First, the previous research studies on the convective heat transfer within an autoclave, presented in section 1.2.2.2.1, have shown a negligible influence of the temperature cycle on the velocity field and the convective heat transfer coefficient. Thus, using air

at ambient temperature or high temperature will not affects the physical phenomena under investigation.

On the other hand, heating the air requires the installation of a heating system which would be highly time- and cost- consuming, especially that the heat delivered by such a system will contribute also to heat the shell of the model autoclave, and therefore a good thermal isolation of the all shell must be expected in this case.

Given these facts and taking into account the technical constraints associated with the use of a heated gas, it was decided that the air will flow within the working section of the model autoclave at a low ambient temperature, between 20°C and 25°C, and controlled thanks to the installation of a cooling heat exchanger (see Appendix A). On the other hand, the used model mold will be heated thanks to thin film resistive heaters allowing then the presence of convective heat transfer mechanisms between the air and the mold at steady state regime. This decision can be justified also by the fact that in the case of a purely forced convective heat transfer,  $HTC$  depends mainly on the mold shape and geometry and no on the surface temperature. The detailed description of the heated model mold is presented in the section 2.6.

Concerning the pressure, it was shown also that using pressurized gas within the model autoclave can generate technical constraints and risks. First, a high air pressure requires an increasing in the model autoclave shell thickness to ensure its robustness facing the flow. Further, increasing the gas pressure within the model autoclave and then make it under pressure can prevent the injection and the seeding of particles used for the PIV measurements. Based on these elements, it was decided also to keep the air at its ambient pressure.

However, the previous research works exposed in section 1.2.2.2.1 have proved the strong impact of the gas pressure on the heat transfer coefficient ( $HTC$ ) [11–13]. This effect was expressed by increasing the convected fluid density and thus by decreasing its kinematic viscosity resulting then in an increase of the Reynolds number around a mold within a prototype autoclave. This effect of the pressure was taken into account in the model autoclave by increasing the main air velocity while the air flows at ambient pressure in order to match the prototype Reynolds number. This can be observed by the respect of the dynamic similarity condition expressed by the Equation (2.1).

The determination of the temperature and pressure of the circulating air within the model autoclave enables then the estimation of its kinematic viscosity ( $\nu_{mo}$ ). The latter was found to be  $15.11 \times 10^{-6} \text{ m}^2/\text{s}$  [14]. The other known variables of the Equation (2.1) are listed in the Table 2.3. Therefore, the free stream velocity ( $U_{\infty mo}$ ) within the working section of the model autoclave was calculated and it was found to be 76.7 m/s which corresponds to a volume flow rate ( $Q_{mo}$ ) of about 34 800 m<sup>3</sup>/h. The

delivery of such important volume flow rate and the corresponding pressure drop in the whole model autoclave was found to be unrealizable by the existing commercial fans.

Given this fact,  $U_{\infty mo}$  was recalculated by reducing the model Reynolds number ( $Re_{mo}$ ) in a manner to keep the order of magnitude of the prototype Reynolds number (Equation 2.2) on one hand, and on the other hand to obtain the maximum realizable volume flow rate ( $Q_{mo}$ ) that can be provided by the existing commercial fan.

$$Re_{mo} \sim Re_p \sim 10^6 \quad \text{Equation (2.2)}$$

Based on this strategy, the founded velocity was 33.7 m/s which corresponds to a volume flow rate of about 15 290 m<sup>3</sup>/h and a model Reynolds number of about  $1,1 \times 10^6$ . The calculation of the corresponding pressure drop ( $\Delta P$ ) in the whole model autoclave and the characteristics of the chosen commercial fan are detailed in Appendix A.

**Table 2.3 Application of the dynamic similarity condition**

		<b>Prototype autoclave</b>	<b>Model autoclave</b>
<b>Air properties</b>	$T$ (°C)	180	$20 < T < 25$
	$P$ (kPa)	700	100
	$\nu$ (m <sup>2</sup> /s)	$4.6 \times 10^{-6}$	$1.5 \times 10^{-5}$
<b>Flow properties</b>	$U_{\infty}$ (m/s)	3	33.7
	$\dot{Q}$ (m <sup>3</sup> /h)	76 000	15 290
<b>Characteristics length of the mold</b>	$l$ (m)	4	0.51
<b>Dynamic similarity parameters</b>	$Re$	$2.6 \times 10^6$	$1.1 \times 10^6$

### 2.3.1.2.3 Application of the energetic similarity

According to the Table 2.1, the energetic similarity occurs by the respect of the Prandtl number ( $Pr$ ), the Eckert number ( $Ec$ ) and the wall temperature ratio ( $T_w/T_{ref}$ ) between the model and the prototype autoclave.  $T_w$  and  $T_{ref}$  represent the wall mold and the free stream temperature respectively.

Knowing the air temperature and pressure within the prototype and the model autoclaves allows the determination of the air properties and thus the calculation of the model and the prototype Prandtl numbers ( $Pr_p$  and  $Pr_{mo}$ ). The calculation of these dimensionless parameters (Table 2.4) shows a quite good respect of the Prandtl number and thus the respect of one of the energetic similarity conditions.

However, the Eckert number ( $Ec$ ) and the wall temperature ratio ( $T_w/T_{ref}$ ) cannot be matched between the model and the prototype autoclave. In fact, the air within the prototype autoclave heats the mold, thus, in the steady state regime, the ratio of temperatures tends to unity. On the other hand, the air within the model autoclave

flows at low controlled temperature around the heated walls of the model mold as explained previously. Thus the temperatures ratio is evidently larger than 1.

These unmatched values between some dimensionless parameters, i.e.  $Ec$  and  $T_w/T_{ref}$ , illustrate the fact that the general condition of similarity is rarely possible to respect it entirely as mentioned previously, and it is often difficult to keep the similarity constant for all physical quantities.

In addition, the constants  $Ec$  and  $T_w/T_{ref}$  were found not to affect the main heat transfer phenomenon under investigation which is the study of the convective heat transfer coefficient ( $HTC$ ).

**Table 2.4 Application of the energetic similarity condition**

	Air properties					Energetic similarity parameters		
	$\mu$ (Pa.s)	$C_p$ (J/kg.K)	$\lambda$ (W/m.K)	$U_\infty$ (m/s)	$T_\infty$ (°C)	$Pr$	$Ec$	$T_w/T_{ref}$
<b>Prototype autoclave</b>	$2.5 \times 10^{-5}$	1005	0.034	3	180	0.70	$2 \times 10^{-5}$	$\approx 1$
<b>Model autoclave</b>	$1.82 \times 10^{-5}$	1005	0.0257	33.7	$20 < T < 25$	0.71	$> 3.8 \times 10^{-3}$	$> 1$

#### 2.3.1.2.4 Summary of the applied similarity conditions

The similarity laws, i.e. the geometric, the dynamic and the energetic similarity conditions, were applied in the case of an incompressible gaseous flow and convective heat transfers in order to size the working section of the model autoclave. The required free stream velocity of the circulating air ( $U_{\infty mo}$ ) was estimated as well, and the air flows at ambient pressure and controlled low temperature.

Figure 2.3 shows a CAD drawing of the obtained working section of the model autoclave derived from the sizing work exposed above.

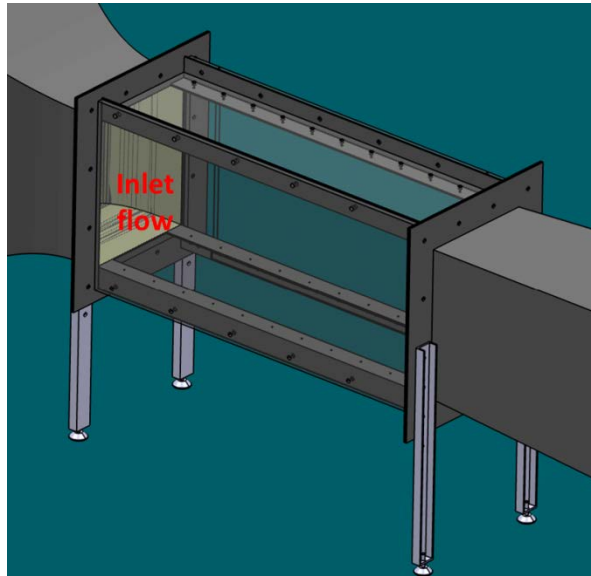


Figure 2.3 CAD drawing of the designed working section of the model autoclave



### 2.3.2 Determination of the model autoclave concept

In the light of the action plan determined in the thesis study and exposed in the section 1.4, CFD calculations will be performed using the RANS computer code ANSYS Fluent 16.0® and the aerodynamic and thermal numerical results will be compared to those deduced from experimental measurements carried out on the model autoclave.

An essential element for the comparison and thus for the validation of the numerical simulations is to obtain controlled experimental boundary conditions in order to use it as boundary conditions in the CFD calculations. Among these experimental boundary conditions, the most important one is the existence of a uniform and controlled flow field at the inlet of the working section of the model autoclave.

Indeed, a uniform and controlled flow allows a precisely determination of the free stream velocity and turbulence intensity. These measured physical quantities will be used then as velocity inlet boundary conditions in the numerical model as they affect significantly the flow field structure and the *HTC* distribution behavior [15–17].

To reach this objective, the working section flow should be devoid of any unintended unsteadiness at the inlet. Flow separation should be avoided inside the model autoclave to prevent flow unsteadiness and associated noise, as well as to minimize losses. Further, the turbulence intensity in the working section should be low enough to facilitate study of the physical phenomena of interest [2].

On the other hand, the gas within an autoclave circulates generally in a closed tunnel, according to its functioning description presented in section 1.2.1 and illustrated in Figure 2.1.

Based on the above facts, the model autoclave should be designed also as a closed tunnel with in addition the presence of uniform and controlled velocity profiles at the inlet of its working section.

Therefore, the concept of the model autoclave should represent practically a closed wind tunnel. In fact, a quality closed wind-tunnel facility provides flow uniformity and low turbulence intensities within its test section. A schematic of a closed wind tunnel with the main components is shown in Figure 2.4.

In the field of closed wind tunnels, the obtaining of test section uniform flow at the inlet with low turbulence levels should pass through the respect of the design guidelines of the main wind-tunnel components. The latter include essentially the flow conditioners, the contraction, the test section, the diffuser, the drive system (fan), and other optional components (Figure 2.4).

These design guidelines are exposed in the Appendix A. They have been applied in order to size main components that should be implemented in the model autoclave in order to meet the flow specifications.

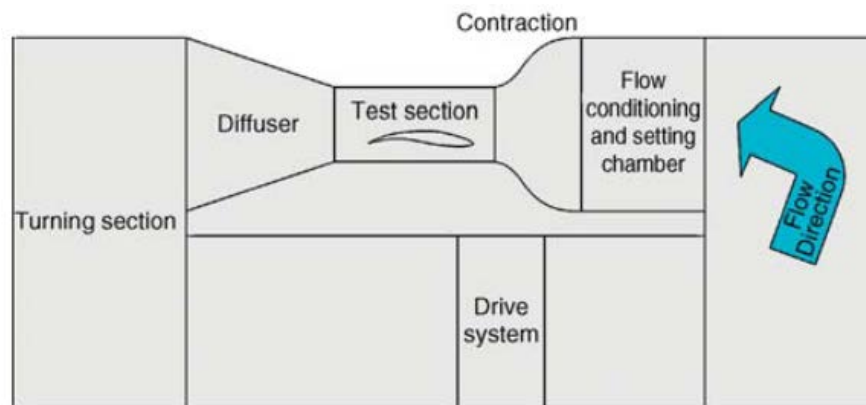


Figure 2.4 Schematic of a closed-circuit wind tunnel [2]

### 2.3.3 Presentation of the designed model autoclave

The application of the different followed steps showed above, such as the application of the similarity laws for the design of the working section and the application of the various design guidelines for the sizing of the main components, results in a model autoclave represented by the CAD drawing in Figure 2.5. A summary of the characteristics of the main components that constitute the designed model autoclave is presented in Table 2.5. It can be clearly seen that the obtained model autoclave represents in fact a close-wind tunnel.

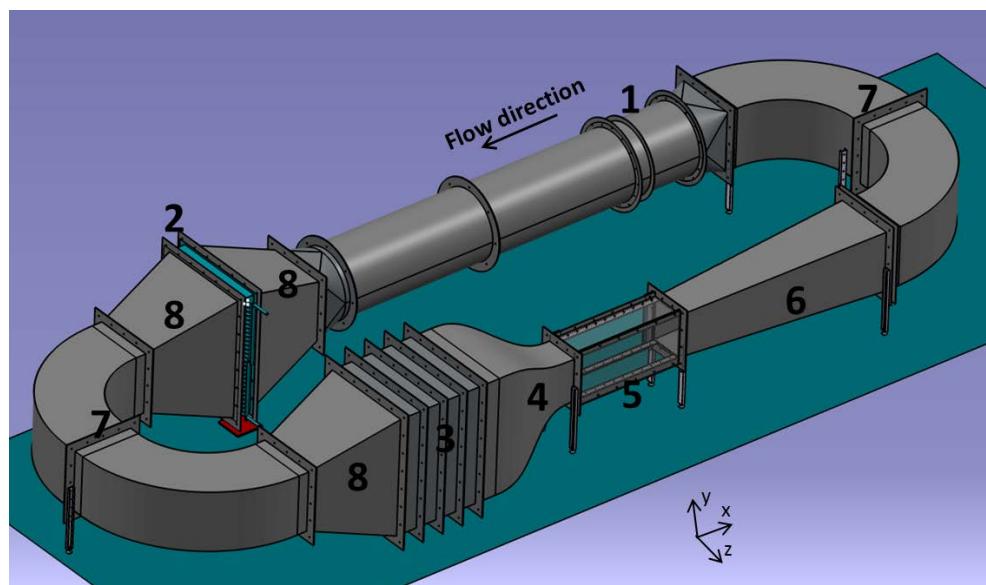


Figure 2.5 CAD schema of the designed model autoclave

Table 2.5 Characteristics of the main components of the model autoclave

Component	Noun	Characteristics
1	Axial fan	$D = 0.63 \text{ m}$
		Nominal flow ( $Q$ ): $15\,290 \text{ m}^3/\text{h}$
		Nominal Pressure drop ( $\Delta P$ ): $600 \text{ Pa}$
2	Heat exchanger	Nominal power: $5\,500 \text{ W}$
		$L \times H = 0.833 \times 1.058 \text{ m}^2$
3	Settling chamber	$l \times L \times H = 0.93 \times 0.833 \times 1.058 \text{ m}^2$
4	Contraction	Inlet section: $L \times H = 0.833 \times 1.058 \text{ m}^2$
		Outlet section: $L \times H = 0.315 \times 0.4 \text{ m}^2$
		$l = 0.94 \text{ m}$
5	Working section	$l \times L \times H = 1.07 \times 0.315 \times 0.4 \text{ m}^2$
6	Diffuser	Inlet section: $L \times H = 0.315 \times 0.4 \text{ m}^2$
		Outlet section: $L \times H = 0.56 \times 0.56 \text{ m}^2$
		$l = 2 \text{ m}$
7	Radius elbow	Square section: $L \times H = 0.56 \times 0.56 \text{ m}^2$
		$R = 1.1 \text{ m}$
8	Wide-angle diffuser	Inlet section: $L \times H = 0.56 \times 0.56 \text{ m}^2$
		Outlet section: $L \times H = 0.833 \times 1.058 \text{ m}^2$
		$l = 0.5 \text{ m}$

After obtaining and approving the final design of the model autoclave, the latter was manufactured and then installed. Figure 2.6 shows the manufactured model autoclave which is in accordance with the CAD drawing showed above. Figure 2.7 shows the working section of the model autoclave which is in accordance with the CAD drawing showed in Figure 2.3. The different components and ducts used in the

model autoclave were fabricated of galvanized steel. On the other hand, the walls of the working section were made from acrylic glass (Plexiglas) in order to be transparent for the use of the PIV technique.

Also, Figure 2.7 shows the installation of a model mold within the working section, for carrying out experimental measurements, and the mounting of the PIV technique.

In the following sections, the used model mold as well as the installed measurement instruments, especially the PIV technique, will be carefully explained and exposed.



**Figure 2.6 Picture of the manufactured model autoclave**

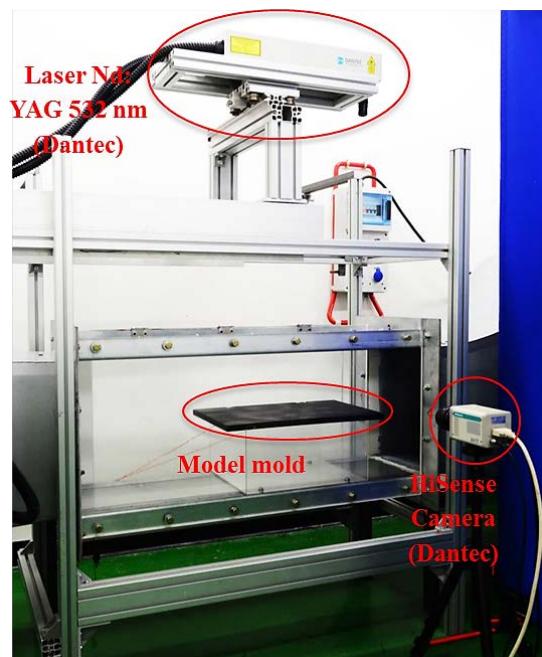


**Figure 2.7** Picture of the working section of the model autoclave

## **2.4 Aerodynamic instrumentation and measurement methodology**

### **2.4.1 Flow field measurement**

The Particle Image Velocimetry (PIV) technique is employed for the measurement of the flow field structure around model molds installed within the working section of the model autoclave.

In the following, the main features of the PIV technique are presented.

### **2.4.2 Introduction to the PIV technique**

The experimental setup and the functioning of a PIV system typically consists of several subsystems. Figure 2.8 briefly sketches a typical setup for PIV recording in a wind tunnel.

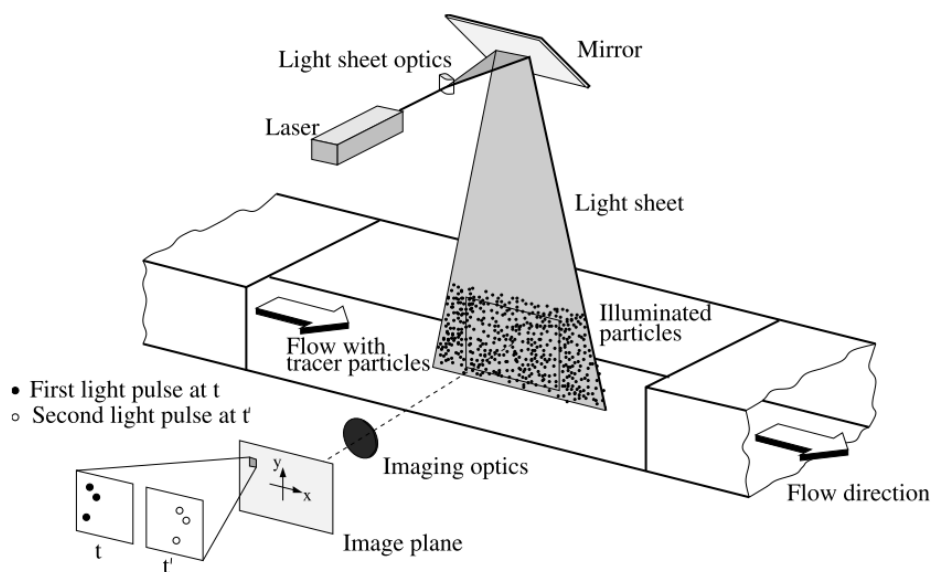


**Figure 2.8 Experimental arrangement for particle image velocimetry in a wind tunnel [18]**

First, small tracer particles are added to the flow. These particles are illuminated in a plane of the flow (light sheet) twice and by means of a laser. The time delay between pulses depends on the mean flow velocity and the magnification at imaging. It is assumed that the tracer particles move with local flow velocity between the two illuminations. The light scattered by the tracer particles is recorded then via a high quality lens either on a single frame (e.g. on a high-resolution digital or film camera) or on two separate frames on special cross-correlation digital cameras. After, the

photo-graphical PIV recording is digitized by means of a scanner. The output of the camera is transferred to the memory of a computer directly. The displacement of the particle images between the light pulses is determined through evaluation of the PIV recordings. In order to be able to handle the great amount of data which can be collected employing the PIV technique, sophisticated post-processing is required.

More precisely, for evaluation of the digital PIV recording, the latter is divided in small subareas called “interrogation areas”. The local displacement vector for the images of the tracer particles of the first and second illumination is determined for each interrogation area by means of statistical methods (auto- and cross-correlation). It is assumed that all particles within one interrogation area have moved homogeneously between the two illuminations. The projection of the vector of the local flow velocity into the plane of the light sheet (two-component velocity vector) is calculated taking into account the time delay between the two illuminations and the magnification at imaging.

The PIV technique presents general aspects and features. The most important one are listed below:

- **Non-intrusive velocity measurement:** as mentioned previously, the PIV technique is an optical technique that works non-intrusively in contrast to techniques employing probes such as pressure tubes or hot wires.
- **Indirect velocity measurement:** the PIV technique measures the velocity of a fluid element indirectly by means of the measurement of the velocity of tracer particles within the flow, which in most applications have been added to the flow before the experiment starts.
- **Illumination:** for applications in gas flows, a high power light source (laser) for illumination of the tiny tracer particles is required in order to well expose the photographic film or the video sensor by scattered light.
- **Duration of illumination pulse:** the duration of the illumination light pulse must be short enough to “freeze” the motion of the particles during the pulse exposure in order to avoid blurring of the image (“no streaks”).
- **Time delay between illumination pulses:** the time delay between the illumination pulses must be long enough to be able to determine the displacement between the images of the tracer particles with sufficient resolution, and short enough to avoid particles with an out-of-plane velocity component leaving the light sheet between subsequent illuminations.
- **Distribution of tracer particles in the flow:** for PIV technique, a homogeneous distribution of medium density is desired for high quality PIV recordings in order to obtain optimal evaluation.



- **Density of tracer particle images:** Qualitatively three different types of image density can be distinguished, which is illustrated in Figure 2.15. Medium image density is required to apply the standard statistical PIV evaluation techniques.

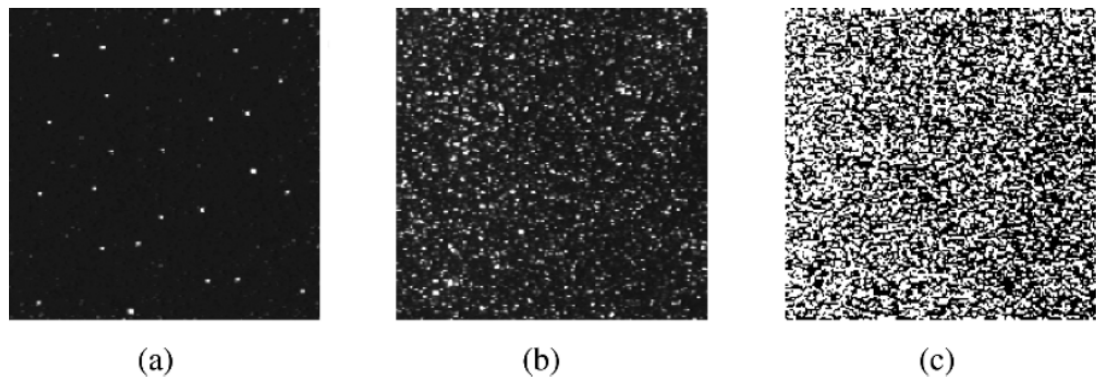


Figure 2.9 The three modes of particle image density: (a) low, (b) medium, and (c) high image density [18]

- **Number of components of the velocity vector:** due to the planar illumination of the flow field, only two (in plane) components of the velocity vector can be determined in standard two-component PIV.
- **Temporal resolution:** most PIV systems allow to record with high spatial resolution, but at relative low frame rates. However, the recent development of high-speed lasers and cameras allows time resolved measurements of most liquid and low-speed aerodynamic flows.
- **Spatial resolution:** the size of the interrogation areas during evaluation must be small enough for the velocity gradients not to have significant influence on the results.

### 2.4.3 Description of the employed PIV system (Laser + Camera)

The used PIV system is a standard two-component PIV provided by Dantec®. It is illustrated in Figure 2.7.

The illumination source consists of a dual power laser of dual-cavity Nd: YAG 532 nm, with pulse energies up to 65 mJ and frequency or repetition rate of 5.6 Hz. The laser is mounted over a movable system which allows the measurement of the velocity fields at different locations within the working section of the model autoclave. In addition, the laser sheet can be emitted in two positions: the first one is a vertical position in the (xy) plane for the detection of  $u$  and  $v$  components (Figure



2.10) while the second one is horizontal in the ( $xz$ ) plane for the measurement of  $u$  and  $w$  (Figure 2.11). The  $x$  direction represents the longitudinal axis parallel to the working section whereas the  $y$  and the  $z$  directions represent the vertical and the horizontal normal axis respectively (Figure 2.5).

A “HiSense” camera is used with a sensor resolution of  $(2048 \times 2048)$  px<sup>2</sup> fitted with a 50 mm lens. The camera is placed and calibrated in front of the illuminated particles.

The laser and the camera are connected to a computer used for the record of the output double-frame images, and they are controlled by a data acquisition program using the DynamicStudio 3.41® software provided by Dantec®.

The tracer particles seeded in the flow and illuminated by the laser are small droplet water-based fog liquid of type “Extra Clean” [19]. The mean droplet size is around 1  $\mu\text{m}$ . In fact, small particles follow the flow better. The seeding of the flow was done by using a fog generator that generates a dense white fog by evaporation and condensation of the water-based fog liquid. The particles injection is located upstream of the motor fan in the aspiration region.

#### **2.4.4 Measurement and post-processing methodology**

As mentioned above, only two (in plane) components of the velocity vector can be determined by the employed PIV 2C 2D system. Thus the resulting velocity fields derived from the PIV measurements, at a specific planar-spot within the working section, are two-dimensional (2D).

After switching on the fan motor of the model autoclave, the tracer particles are seeded in the flow thanks to the fog generator. Few minutes are required before performing the PIV measurement campaigns in order to obtain a homogeneous density distribution of the tracer particles in the flow within the working section, and to reach also the steady-state regime.

According to the volume flow rate and the spatial resolution of the images, the time delay between the illumination pulses was defined in the DynamicStudio 3.41® software. The latter allows the recording of just 372 double-frame images per single measurement campaign. Thus, for each case study, six measurement campaigns were carried out resulting then in a total of 2 232 double-frame images. The main objective is to verify the repeatability of the aerodynamic results and to verify also the statistical convergence of the calculated velocity and turbulence fields.

After the acquisition, the output double-frame images were recorded in the computer. These images were used then to calculate the instantaneous 2D velocity

vector fields using the DynamicStudio 3.41® software. Two steps analysis were followed:

- image pre-processing: background image subtraction using the minimum value according the time series.
- correlation calculation: four steps adaptive correlation (initial pass  $64 \times 64$ , final pass  $16 \times 16$  doubled, 50% overlap).

This analysis work results in a data of 2 232 instantaneous velocity fields. Table 2.6 shows an example of information that is provided by an instantaneous velocity field calculated by DynamicStudio 3.41®. The example illustrates a case study where PIV measurements are performed in the  $(xy)$  plane. “Length” signifies the velocity magnitude. “Status” can be “0” to indicate that the velocity vector has been calculated by the correlation analysis, otherwise, it can be “16” or “1” to signify that the velocity vector has been substituted or rejected respectively.  $t^*$  is actually the pseudo time and represents in fact the different instantaneous measurements.

**Table 2.6 Velocity vector calculated in an instantaneous velocity field and given by the PIV data**

Variables			Functions			
$t^*$ (s)	$x$ (mm)	$y$ (mm)	$u$ (m/s)	$v$ (m/s)	length (m/s)	Status

The DynamicStudio 3.41® provides, after the calculation work, many options such as the calculation of the time-mean velocity fields and the fluctuating (r.m.s) velocity fields. These statistical physical quantities are considered essential to calculate, especially in the case of a statistical steady state regime study.

However, it was found that during the correlation analysis work performed by the software, erroneous velocity vectors can be obtained and which can affect therefore the statistical calculations.

Given this fact, it was decided to create home-made Matlab® routines. The latter were used first to eliminate the erroneous velocity vectors, and then to carry out statistical calculations such as the determination of the time-mean and r.m.s velocity fields in the investigated planar – spot. The calculation of these quantities is explained by the formulas expressed in the Equation 2.3. The given formulas illustrate again an example of a case study where PIV measurements are performed in the  $(xy)$  plane.

$$U(x, y) = \frac{1}{N} \sum_{i=1}^N u(x, y, t_i^*)$$

$$V(x, y) = \frac{1}{N} \sum_{i=1}^N v(x, y, t_i^*)$$

$$u_{rms}(x, y) = \sqrt{\frac{1}{N} \sum_{i=1}^N \left( u(x, y, t_i^*) - U(x, y) \right)^2}$$

$$v_{rms}(x, y) = \sqrt{\frac{1}{N} \sum_{i=1}^N \left( v(x, y, t_i^*) - V(x, y) \right)^2}$$

**Equations (2.3)**

$U$  and  $V$  can be considered then as the local time-mean values of  $x$  and  $y$ -component of velocity respectively. On the other hand,  $u_{rms}$  and  $v_{rms}$  represent the local r.m.s. values of  $x$  and  $y$ -component of velocity respectively.  $N$  is the number of instantaneous validated vectors after filtration among the measured one, i.e.  $N \leq 2232$ .

Furthermore, the statistical convergence of these calculated quantities was verified using these routines. The statistical convergence signifies that the mean and r.m.s values do not vary with the sample size. This can be verified by considering first several samples of different sizes ( $N'$ ) among the validated vectors, i.e.  $N' \leq N$ . Then, for each sample, the mean and r.m.s values were calculated. Finally, the obtained results were plotted against  $N'$  in order to verify their constant behavior, and thus to verify the statistical convergence. An example of the statistical convergence study is shown below in Figure 2.16 and Figure 2.17.

## ***2.5 Validation of the model autoclave***

The installed PIV system described above was used, as a first step, to validate the model autoclave.

The validation work of the model autoclave consists of verifying the features of the fabricated model autoclave according to the fixed design guidelines showed above. The main design guideline was the presence of a uniform velocity field and low turbulence level at the inlet of the working section of the model autoclave. Thus, the validation work requires, primarily, the measurement of the inlet flow field.

The PIV system was therefore used to check the uniformity and the steadiness of the flow field at the inlet of the working section. During the validation work, the flow field was characterized quantitatively at the inlet by determining the free stream velocity and the free stream turbulence intensity.

### **2.5.1 Procedure of the validation work**

The validation procedure consisted of carrying out PIV measurement campaigns in the  $(xy)$  plane, for the measurement of the instantaneous and local velocity vectors  $u(x,y,t^*)$  and  $v(x,y,t^*)$ , and in the  $(xz)$  plane for the components  $u(x,y,t^*)$  and  $w(x,y,t^*)$ .

The tracer particles were illuminated then in planar-spots located in the  $(xy)$  and  $(xz)$  planes near the inlet of the working section (Figure 2.10 and Figure 2.11).

For the  $(xy)$  plane measurements, the camera was placed in front of the side wall of the working section at a distance of 30 cm, and calibrated in front of the illuminated spot (Figure 2.10), resulting then in an image of  $11.79 \times 11.79 \text{ cm}^2$ . For the  $(xz)$  plane measurements, the camera was placed in front of the upper wall of the working section at a distance of 33 cm, and calibrated in front of the illuminated spot (Figure 2.11), resulting then in an image of  $14.88 \times 14.88 \text{ cm}^2$ .

The validation task was carried out for the volume flow rate of interest derived from the dynamic similarity condition, i.e.  $Q = 15\,300 \text{ m}^3/\text{h}$ . The latter was estimated then by using the installed flow meter. It was found that it corresponds to a motor frequency ( $f$ ) of 80 Hz. The time delay between the illumination pulses was defined as  $10 \mu\text{s}$ .

Thereafter, the measurement campaigns of the flow field were performed according to the methodology defined in section 2.4.4.

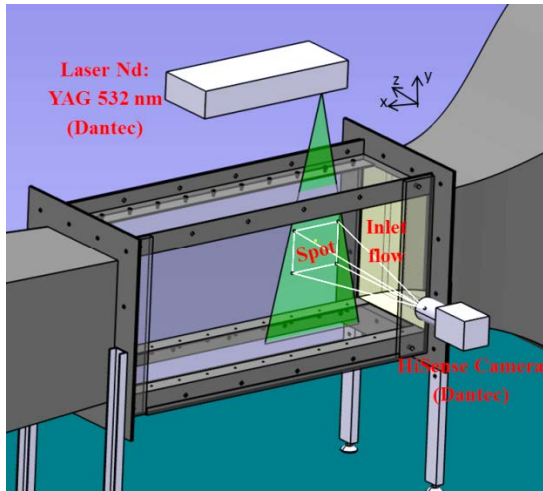


Figure 2.10 The principle of PIV measurements in the (xy) plane during the validation procedure (CAD drawing)

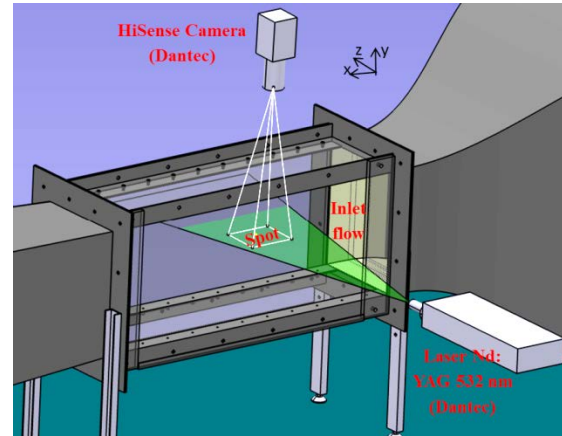


Figure 2.11 The principle of PIV measurements in the (xz) plane during the validation procedure (CAD drawing)

## 2.5.2 Results of the validation work

Figure 2.12 and Figure 2.13 show the contours and the streamlines of the local mean velocities  $U(x,y)$  and  $V(x,y)$ . The latter were calculated using the Matlab routines according to the Equation (2.3), and based on the PIV obtained data (Table 2.6). On the other hand, Figure 2.14 and Figure 2.15 show the contours and the streamlines of the local mean velocities  $U(x,y)$  and  $W(x,y)$  obtained in the same way. Figure 2.16 and Figure 2.17 illustrate the statistical convergence reached during the measurements of the mean longitudinal velocity ( $U$ ) and the turbulence intensity ( $TI$ ). The example was applied at the point ( $x = 0.06$  m,  $y = 0.06$  m).

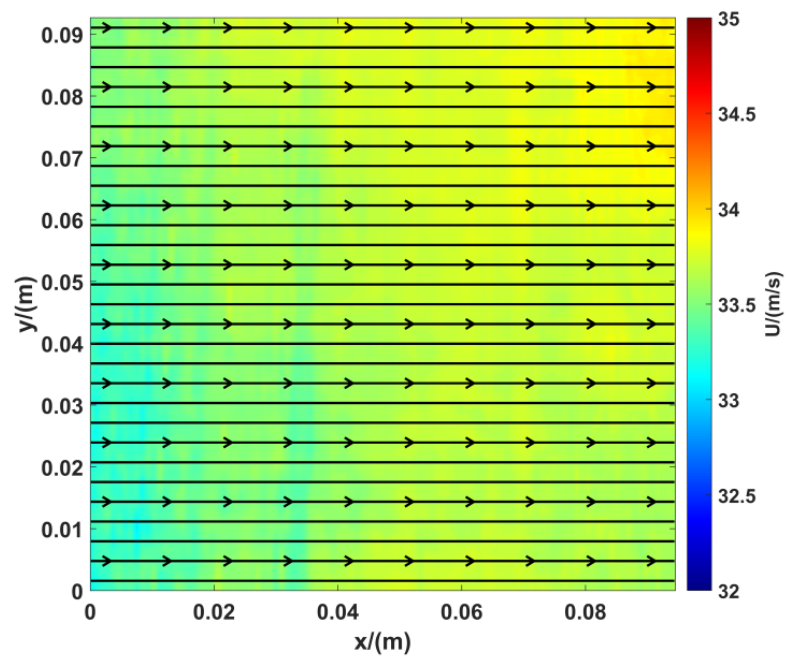


Figure 2.12 Contour + Streamlines of the mean velocity  $U(x,y)$  in the investigated spot in the  $(xy)$  plane

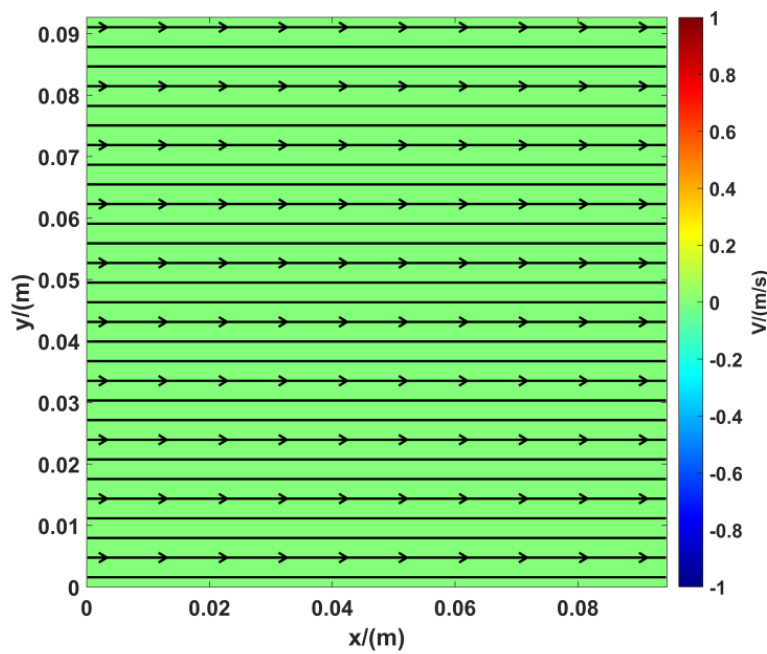


Figure 2.13 Contour + Streamlines of the mean velocity  $V(x,y)$  in the investigated spot in the  $(xy)$  plane

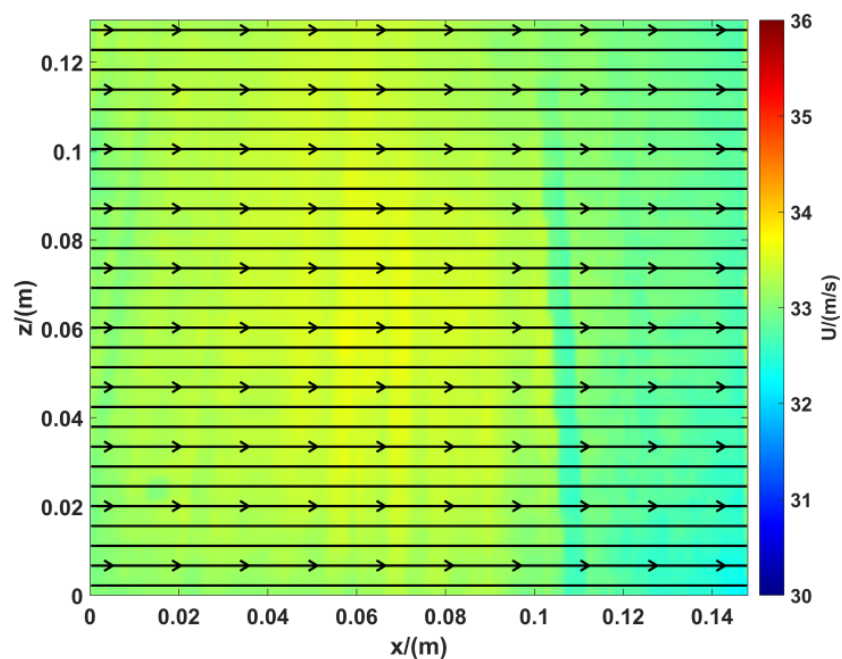


Figure 2.14 Contour + Streamlines of the mean velocity  $U$  ( $x,y$ ) in the investigated spot in the  $(xz)$  plane

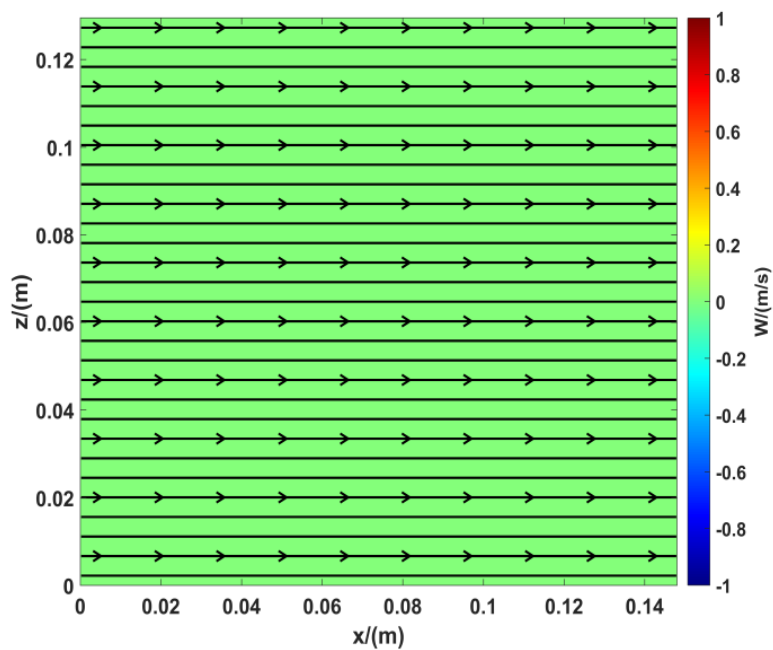
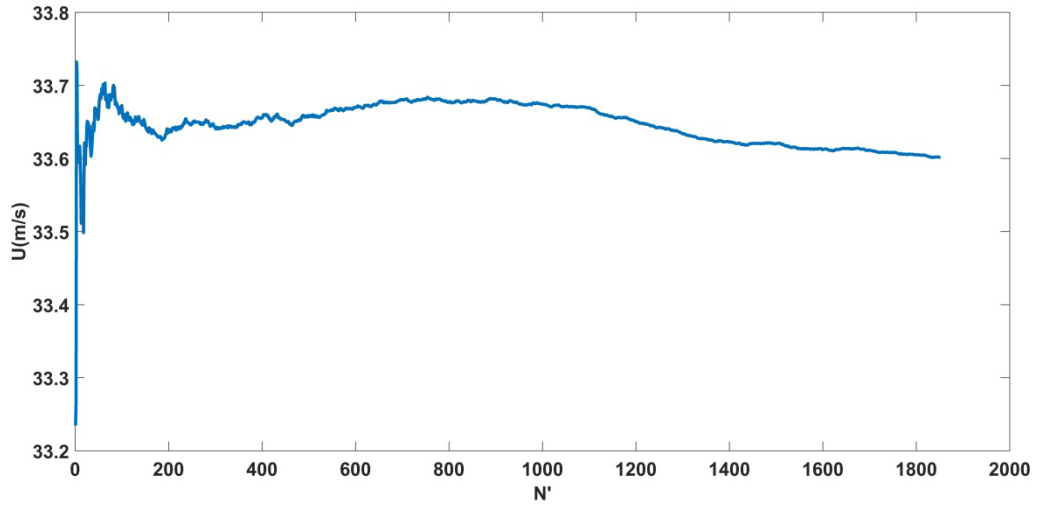
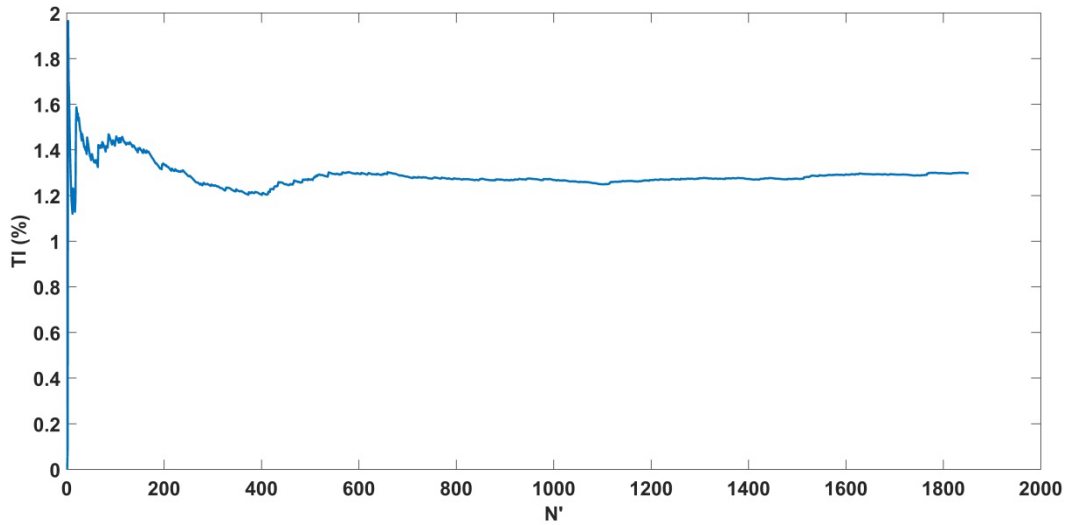


Figure 2.15 Contour + Streamlines of the mean velocity  $W$  ( $x,y$ ) in the investigated spot in the  $(xz)$  plane



**Figure 2.16 Statistical convergence of U at the point (0.06 m, 0.06 m)**



**Figure 2.17 Statistical convergence of turbulence intensity at the point (0.06 m, 0.06 m)**

These obtained velocity results allow the characterizations of the flow field at the inlet, i.e. the determination of the both free stream mean and free stream fluctuating velocities:  $U_\infty$ ,  $V_\infty$ ,  $W_\infty$ ,  $u_{rms\infty}$ ,  $v_{rms\infty}$  and  $w_{rms\infty}$ . These free stream values were obtained by the space averaging of the local mean velocities over the studied spots. The uncertainties of the obtained free stream values correspond to standard deviation calculations ( $\sigma$ ). The calculation of the free stream values and their uncertainties is given by the formulas shown in Equation (2.4). They were applied for the calculation of the  $x$ -component velocity.  $U_{ij}$  is equivalent to  $U(x,y)$  and  $N_x$  and  $N_y$  are the image pixel numbers in the  $x$  and  $y$  directions respectively.



$$U_{\infty} = \frac{1}{N_x} \frac{1}{N_y} \sum_{i=1}^{N_x} \sum_{j=1}^{N_y} U_{ij}$$

Equation (2.4)

$$\sigma_{U_{\infty}} = \sqrt{\frac{1}{N_x} \frac{1}{N_y} \sum_{i=1}^{N_x} \sum_{j=1}^{N_y} (U_{ij} - U_{\infty})^2}$$

Table 2.7 gathers the obtained free stream characteristics of the flow field at the inlet of the working section.

**Table 2.7 Characteristics of the flow field at the inlet of the working section**

Motor rotation frequency (Hz)	$U_{\infty}$ (m/s)	$V_{\infty}$ (m/s)	$W_{\infty}$ (m/s)	$u_{rms\infty}$ (m/s)	$v_{rms\infty}$ (m/s)	$w_{rms\infty}$ (m/s)	$Q$ (m <sup>3</sup> /h)
80	33.7 ±0.14	0 ±0.06	0 ±0.17	0.38 ±0.09	0	0	15 300 ±63

The low values of uncertainties show well that the flow field is spatially uniform. This can be observed, for example, by examining the contour of  $U(x,y)$ ,  $V(x,y)$  and  $W(x,y)$  plotted above (Figure 2.12, Figure 2.13, Figure 2.14 and Figure 2.15).

The comparison between the values of the three components of the free stream velocity, i.e.  $U_{\infty}$ ,  $V_{\infty}$  and  $W_{\infty}$ , indicates that the air flows mainly along the longitudinal axis of the working section of the model autoclave and thus the flow field is mainly horizontal. This can be observed, for example, by examining the black horizontal mean velocity streamlines plotted above (Figure 2.12).

Furthermore, the magnitude of the main air free stream velocity has been found to be 33.7 m/s which respect well the dynamic similarity condition presented in section 2.3.1.2.2.

The free stream turbulence intensity ( $TI$ ) was calculated according to the Equation (2.5). Thus the free stream turbulence intensity was found to be in order of 1%.

$$TI = \frac{u_{rms\infty}}{U_{\infty}} \quad \text{Equation (2.5)}$$

Therefore, the obtained result indicates that the turbulence level within the working section is level and that the flow field is steady.

These results set indicate that the flow field, at the inlet of the working section, is uniform and steady regarding the direction and the magnitude of the flow. Further, a low turbulence level has been achieved. Consequently, these findings show that the

fabricated model autoclave respects well the set of design specifications defined previously and thus the model autoclave is validated.

This validation work and thus the characterization of the flow have been performed also for other volume flow rates. The results are shown in Table 2.8. The validation of the model autoclave at low, medium and high velocities allows therefore the performing of experimental tests with different flow regimes.

**Table 2.8 Characteristics of the flow field at the inlet of the working section**

<b>Motor rotation frequency (Hz)</b>	<b><math>U_{\infty}</math> (m/s)</b>	<b><math>TI</math> (%)</b>	<b><math>Q</math> (m<sup>3</sup>/h)</b>
1.5	0.4 ±0.00	1.18 ±0.39	181
2	0.5 ±0.00	0.5 ±0.05	227
10	3.9 ±0.01	0.44 ±0.05	1 770 ± 5
30	12.3 ±0.04	0.77 ±0.12	5 580 ± 18
50	21 ±0.07	0.71 ±0.07	9 530 ± 32

## **2.6 Design of the model mold**

### **2.6.1 Application of the geometrical similarity condition**

The geometry of the model mold, which will be installed within the working section of the model autoclave, was obtained by applying the geometrical similarity condition on a prototype industrial mold with a simplified geometry. The latter is a rectangular box-shaped mold with a length of 4 m, a width of 2.3 m and a thickness of 130 mm as presented in section 2.3.1.1.

Therefore, the respect of the parameter  $k_l$  ( $k_l = 7.5$ ) results in a model mold of rectangular box shape also with a length of 0.51 m, a width of 0.315 m and a thickness of 17 mm. The obtained mold represents in fact a rectangular bluff plate.

### **2.6.2 Concept of the model mold**

According to the main objectives of the thesis study, the model mold will be installed within the model autoclave and experimental measurements will be carried out in order to investigate the flow field structure and the convective heat transfer coefficient distribution around it.

For the convective heat transfer study, in a steady state regime, it was decided in section 2.3.1.2.2 that the mold will be heated while the air flows at low and controlled temperature.

For this purpose, a thin film resistive heater was inserted and installed within the mold. The film resistive heater provides a heating power ( $HP$ ) or heat flux density to heat the mold surfaces.  $HP$  can be controlled thanks to a variable power supply.

However, an accurate measurement of the convective heat fluxes between the mold surfaces and the circulating air requires an accurate knowledge of the thermal energy balance in the whole heated mold. Thus, a complete thermal instrumentation of the whole mold is required.

Given this fact, and in order to simplify the thermal problem, it was decided to use insulating materials on the lateral and lower surfaces of the mold whereas the upper surface is made from a thermally conductive metal. In this case, the thermal instrumentation is limited on the upper surface, allowing then a better control of the thermal energy balance of the mold. Thus, the  $HTC$  distribution study will be enable around the upper surface of the mold. This method that consists of using isolating materials on the lower and the lateral surfaces, for the  $HTC$  study, has been applied by other researchers [9,20,21].

Based on the above discussion, the upper surface of the mold was made from a 3 mm thickness stainless steel plate. The thin film resistive heater was pasted at the lower part of the stainless steel plate. The stainless steel plate and the heater were all insulated in the lower and lateral parts by a polyamide 66 envelope. The lower part was also insulated with a Rohacell® foam plate of 8 mm thickness.

The final structure and concept of the model mold, according to the specifications showed above, is shown in Figure 2.18.

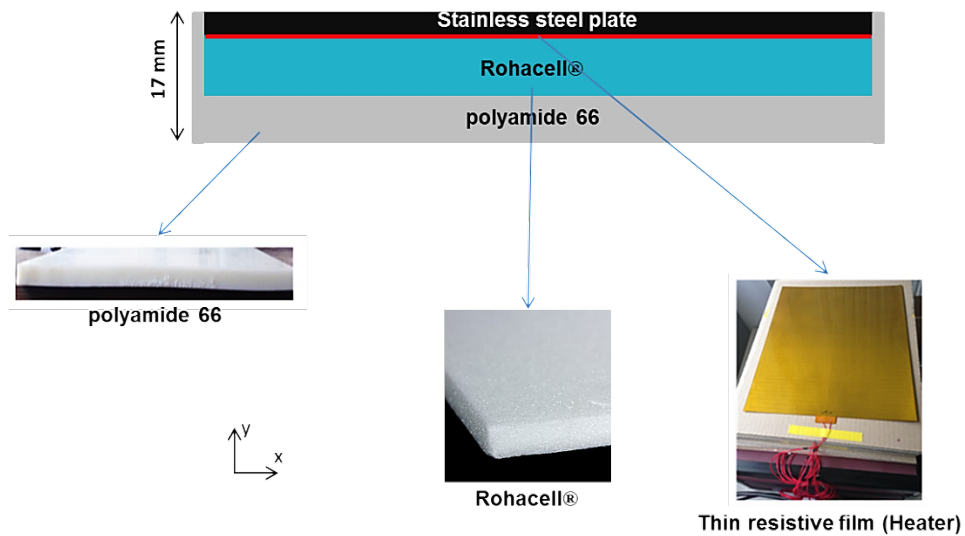


**Figure 2.18 Structure and concept of the used model mold**

The obtained model mold can be installed within the working section of the model autoclave thanks to an acrylic glass (Plexiglas) support (Figure 2.19). It should be noticed that the mold was painted mat black in order to avoid laser reflection during the PIV measurement.

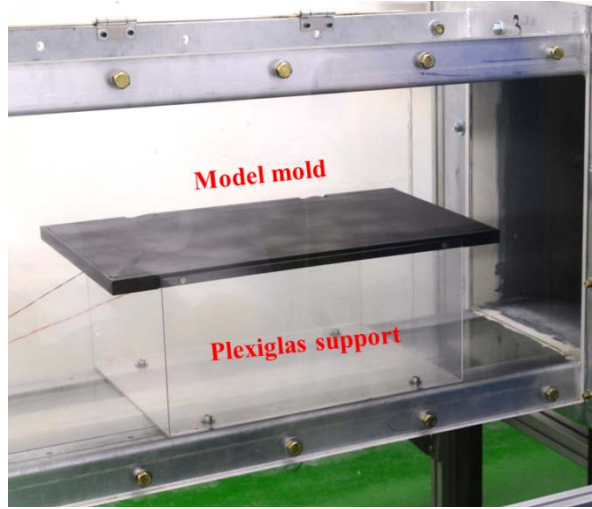


Figure 2.19 Installation of the model mold within the working section

### 2.6.3 Thermal instrumentation and measurement methodology

As mentioned previously, the thermal study aims essentially to investigate the *HTC* distribution around the mold, more precisely, around its upper surface for a defined volume flow rate ( $Q$ ). The investigation is performed in the steady-state regime.

The local convective heat transfer coefficient was determined based on the Newton's law of cooling [22] applied on the upper surface of the model mold:

$$\varphi_{cx} = HTC \cdot (T_{mx} - T_{\infty}) \quad \text{Equation (2.6)}$$

$\varphi_{cx}$  represents the density of the local forced convective heat flux from the upper surface to the air.  $T_{mx}$  and  $T_{\infty}$  are the local temperature of the upper surface of the mold and the free stream air temperature respectively.  $T_{\infty}$  was measured thanks to a PT100 sensor installed near the inlet of the working section.

The use of a mold of rectangular box shape within a working section of uniform flow at the inlet, according to the validation results showed in section 2.5.2, allows the assumption of the presence of one dimensional (1D) convective heat transfers around the mold. This assumption is applied especially near the center region of the mold, whereas near the side walls, horseshoe-vortices can be formed and thus two dimensional (2D) convective heat transfers can occur according to Yanaoka *et al.* [23]. Given these facts,  $\varphi_{cx}$  and  $T_{mx}$  depend mainly on the longitudinal position ( $x$ ) especially near the center region of the mold.

According to the Equation (2.6), the determination of  $HTC$  involves the knowledge of  $\varphi_{cx}$  and  $T_{mx}$ .

### 2.6.3.1 Measurement of $T_{mx}$

The surface temperature measurements of the upper surface of the mold, i.e. the upper surface of the heated stainless steel plate, was conducted by using a FLIR SC7500 InSb® infrared imaging camera of  $(320 \times 256)$  px<sup>2</sup> resolution. The camera was equipped with a 50 mm lens.

The camera was installed above the upper wall of the working section and calibrated in front of the mold (Figure 2.20). Thus the temperature measurements are performed in the  $(xz)$  plane.

Since the walls of the working section of the model autoclave are opaque for the infrared radiations, it was decided to install an optical circular silicon window on the upper wall of the working section for the infrared imaging measurements (Figure 2.20). It should be noticed that the infrared transmittance of the used optical window was measured using a spectrometer (Bruker®) and the obtained IR spectrum matches closely that of the used infrared imaging camera.

For each measurement campaign in the steady state regime, 300 thermal images of the upper surface were acquired by the camera with a frequency of 25 Hz. The obtained instantaneous surface temperature fields were provided by the Altair® software. Table 2.9 illustrates an example of the data provided by Altair® software after the acquisition.

**Table 2.9 Data of an instantaneous thermal image**

$t^*$	$x$	$z$	$T$
(s)	(mm)	(mm)	(°C)

Home-made Matlab® routines were created and used to carry out statistical calculations, such as the determination of the time-mean temperature fields as well as the root mean square (r.m.s) fields. Equation 2.7 shows the formulas used for these calculations. These routines were used also for plotting the mean temperature contours.

$$\bar{T}(x, y) = \frac{1}{N} \sum_{i=1}^N T(x, y, t_i^*) \quad \text{Equation (2.7)}$$

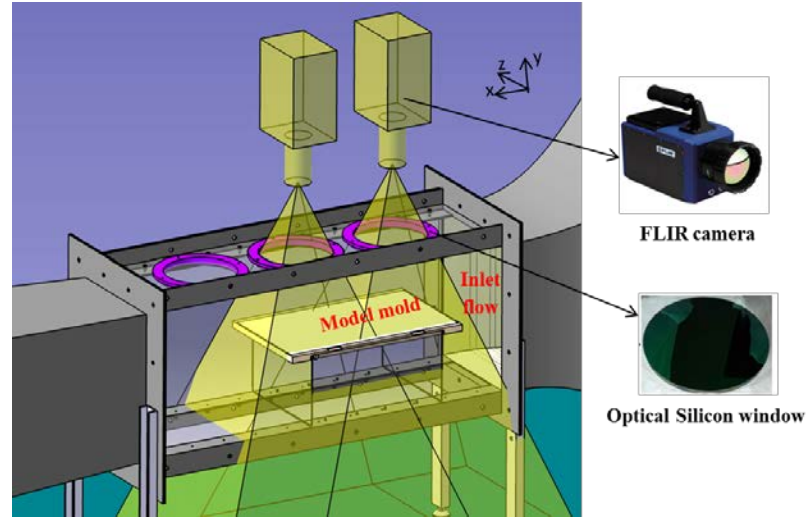


Figure 2.20 Infrared thermography of the upper surface of the mold (CAD drawing)

The obtained mean surface temperature is mainly one dimensional (1D), as explained before, especially near the center region.

Therefore,  $T_{mx}$  which represents the mean temperature profile of the stainless steel plate can be deduced. It was extracted near the center region of the mold in the  $x$  direction.

### 2.6.3.2 Measurement of $\phi_{cx}$

The determination of the local convective heat flux ( $\phi_{cx}$ ) requires an accurate knowledge of the thermal balance of the mold. The latter is heated, as mentioned before, by an energy source defined as  $HP$  and which is supplied by the film resistive heater.

Thus, the first step for the study of the thermal balance consists of the measurement of the local thermal losses ( $\phi_{lx}$ ) through the Rohacell® foam plate placed below the heater. These local heat losses were determined by applying the Fourier's law of heat conduction, in a steady state regime, through the Rohacell® foam plate thickness (Equation (2.8)).

$$\varphi_{lx} = \left( \frac{\lambda_{Rohacell}}{e_{Rohacell}} \right) \cdot (T_{upper\ x} - T_{lower\ x}) \quad \text{Equation (2.8)}$$

$T_{upper\ x}$  and  $T_{lower\ x}$  signifie the local temperatures of the upper and lower surfaces respectively of the Rohacell® foam plate. These temperatures were measured thanks to K-type thermocouples of 80  $\mu\text{m}$  in diameter and installed across the length of the Rohacell® foam plate at its upper and lower surfaces near the center region (Figure 2.21). The acquisition of the thermocouples temperatures was performed in the steady state regime thanks to a LabVIEW acquisition system.  $e_{Rohacell}$  and  $\lambda_{Rohacell}$  are 8 mm and 0.057 W/m<sup>2</sup>/K respectively.

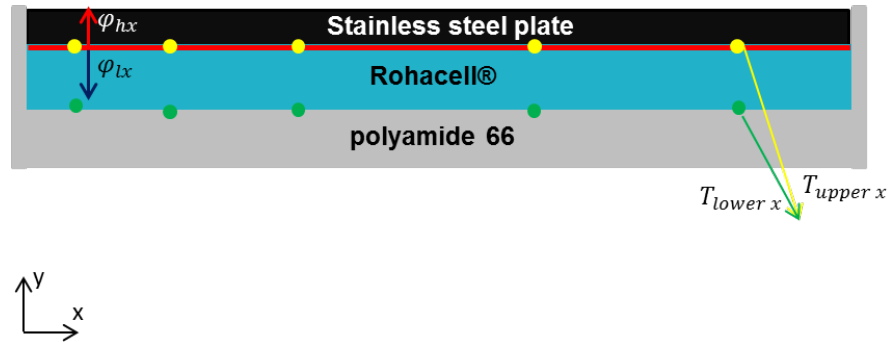


**Figure 2.21. Descriptive schematic of the installed thermocouples within the mold**

The measurement of the local thermal losses ( $\varphi_{lx}$ ) allows the deduction of the local heat fluxes ( $\varphi_{hx}$ ) from the heater towards the stainless steel plate (Figure 2.21).  $\varphi_{hx}$  is determined according to the following equation:

$$\varphi_{hx} = HP - \varphi_{lx} \quad \text{Equation (2.9)}$$

Given the fact that the stainless steel plate is thermally conductive, two-dimensional (2D) heat fluxes can exist within the plate: through the thickness (y) and along the length (x). Thus the estimation of the local convective heat flux ( $\varphi_{cx}$ ) on the upper surface of the mold, i.e. the upper surface of the stainless steel plate, is not easy and not intuitive to carry out.

Therefore, it was decided to resolve numerically the heat equation in the stainless steel plate. The resolving of the heat equation allows the determination of the local normal heat flux to the upper surface and thus the deducing of the local convective heat flux ( $\varphi_{cx}$ ).



Figure 2.22 illustrates the numerical model of the stainless steel plate. The measured physical quantities  $\varphi_{hx}$  and  $T_{mx}$  were imposed as boundary conditions on the lower and upper surfaces of the plate respectively.  $\varphi_{hx}$  was determined using the Equation (2.9). The measurement methodology of  $T_{mx}$  was exposed in section 2.6.3.1. The lateral surfaces were considered insulated due to the polyamide 66 envelope.

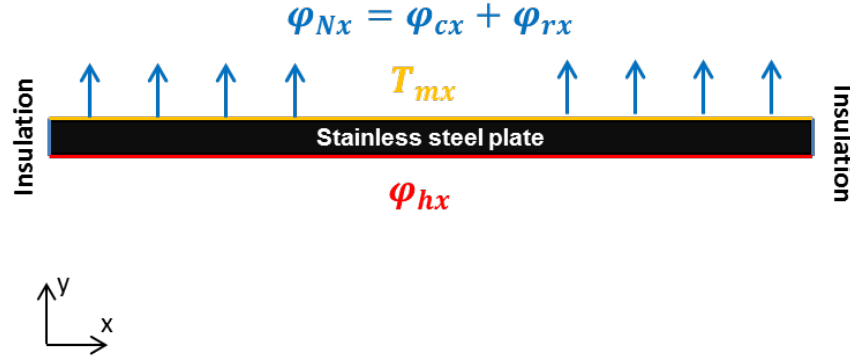


Figure 2.22. Descriptive schema of the applied thermal energy balance

The obtained 2D numerical model, illustrated in Figure 2.22, was solved using Finite Element Analysis (FEA) methods carried out on COMSOL Multiphysics 4.3a® software. The obtained solution allows the determination of the local normal heat flux on the upper surface of the stainless steel plate ( $\varphi_{Nx}$ ). The latter represents in fact the sum of the local convective heat transfer ( $\varphi_{cx}$ ) and the local radiative heat transfer ( $\varphi_{rx}$ ) with the surroundings inside the working section.

The local radiative heat flux ( $\varphi_{rx}$ ) was determined using the Equation (2.10) [22], with  $\sigma$  and  $\varepsilon$  are respectively the Stefan-Boltzmann constant ( $\sigma = 5.67 \times 10^{-8} \text{ W/(m}^2\cdot\text{K}^4)$ ) and the emissivity of the upper surface of the stainless steel plate. The surface was painted black as explained before and the emissivity of the paint is 0.89.

$$\varphi_{rx} = \sigma \varepsilon (T_{mx}^4 - T_{\infty}^4) \quad \text{Equation (2.10)}$$

$$\varphi_{cx} = \varphi_{Nx} - \varphi_{rx} \quad \text{Equation (2.11)}$$

Therefore, knowing  $\varphi_{Nx}$  and  $\varphi_{rx}$  provides the deduction of  $\varphi_{cx}$ , according to the Equation (2.11), and for a defined volume flow rate ( $Q$ ).

### 2.6.3.3 Measurement of $HTC$

The measurement of the physical thermal quantities  $\varphi_{cx}$  and  $T_{mx}$  provides the determination of  $HTC$  distribution on the upper surface of the mold according to the Equation (2.6).

In order to determine  $HTC$  accurately, for a defined volume flow rate in the model autoclave, the adopted method consists of applying three different values of heating powers ( $HP$ ) to the heater.

For each heating power ( $HP$ ), the fields of  $(T_{mx})$  and  $(\phi_{cx})$  are determined according to the steps explained previously in section 2.6.3.1 and section 2.6.3.2 respectively. Therefore for each longitudinal position ( $x_i$ ) on the upper surface, three different temperature values ( $T_{mx}(x)$ ) were obtained, and which correspond to three different convective fluxes ( $\phi_{cx}(x)$ ).

On the other hand, Equation (2.6) shows a linear relationship between the temperature and the convective flux for a defined longitudinal position ( $x$ ). As a result, the value of  $HTC$ , for each longitudinal position, is determined using the linear fitting data method [24] as it represents the slope of the linear equation. The value of  $T_\infty$  can be deduced as well.

Another advantage of this method is the ability to verify the convective heat flux mode (purely forced or mixed convection). In fact, a high value of the coefficient of determination ( $R^2 \approx 1$ ) indicates that the data are well fitted and therefore the convection heat transfer is purely forced.

## **2.7 Inter-part shadowing effects investigation**

During the autoclave process of multiple composites parts simultaneously, a forward mold can block the flow of gas to molds located behind it creating then shadowing effects.

In the thesis study, the inter-part shadowing effects are investigated. The investigation consists first of placing two molds of different size, one behind another, within the working section of the model autoclave. Then, experimental measurement of the flow field structure and *HTC* distribution around the mold placed at the back are performed. These measurements are carried out according to the experimental, aerodynamic and thermal, methodologies showed above.

The first used mold is the model mold described in section 2.6. Henceforth, it will be called Mold 1. A second mold, called Mold 2, was fabricated and it has also a rectangular box shape. Its structure and their geometrical dimensions (width and thickness) are identical to those of the Mold 1 (see Figure 2.19 and Figure 2.18) but shorter: Mold 2 is 0.26 m long. Mold 2 was thermally instrumented by thermocouples for the measurement of *HTC* (Figure 2.21).

Figure 2.23 shows a CAD drawing that illustrates the installation of the Mold 2 at the back behind the Mold 1 within the working section of the model autoclave in order to investigate the inter-part shadowing effects.  $d$  is the distance between the two molds and it is considered as a parameter study.

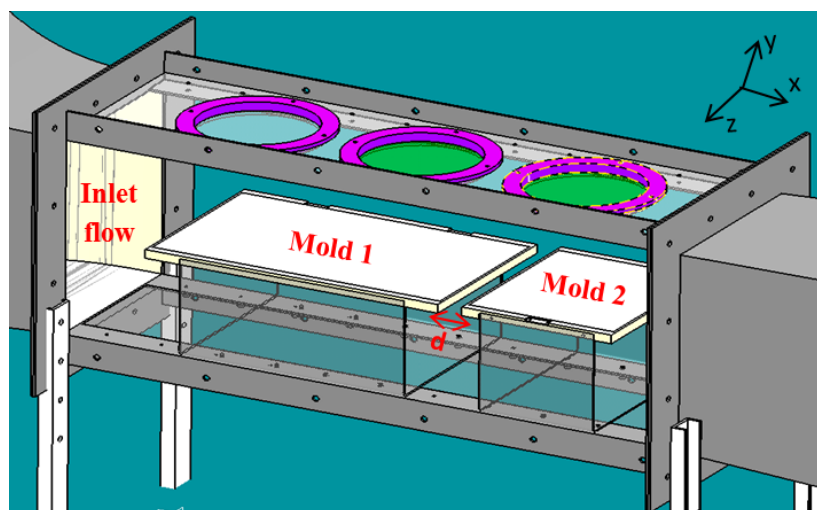


Figure 2.23 CAD drawing for the inter-part shadowing study

## **2.8 Study of a representative mold**

In this section, we are interested in the study of the turbulent flow field and the convective heat transfer coefficient distribution around a mold equipped with excessive support structure that can represent actual industrial conditions. Figure 2.24 shows an example of an industrial mold equipped with such supports and used in the aerospace industry. The main interesting questions revealed in such configuration are the impacts of these support structures on the behaviors of the flow field and the  $HTC$  distribution over the mold surface.



**Figure 2.24** Picture of an industrial mold equipped with excessive support structure [25]

To investigate these questions, a “representative mold” with a simplified geometry and which can represent in fact a mold equipped with supports was used. The geometry of the employed “representative mold” is shown in Figure 2.25.

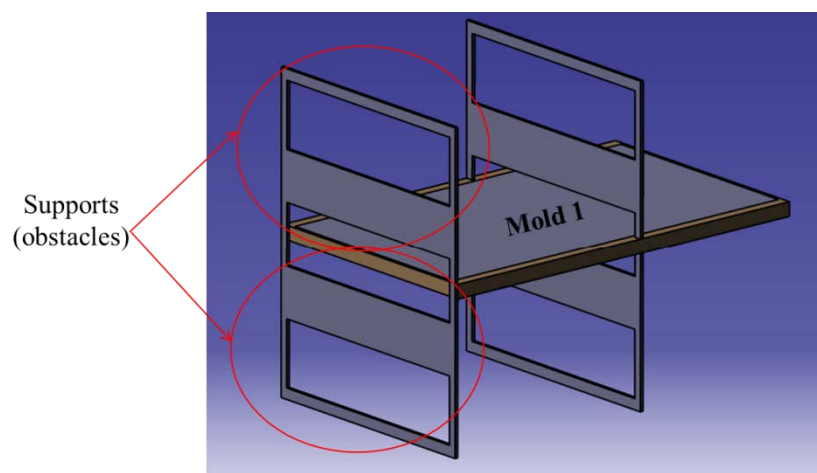


**Figure 2.25** CAD drawing of the “representative mold”

In fact, the “representative mold” is constituted essentially from the “Mold 1”, which is a blunt flat plate as presented previously, and equipped with four perforated obstacles: two on the top surface of the “Mold 1” and two on its lower surface in order to represent the industrial mold shown previously in Figure 2.24.

These obstacles are in fact flat plates that contain several rectangular section holes (Figure 2.25). The first obstacle is installed at the leading edge corner of the “Mold 1” while the second one is installed downstream of the first one with a distance  $dO_1O_2$  (Figure 2.26). The third and the fourth obstacles, i.e.  $O_3$  and  $O_4$ , were installed similarly but in the lower part (Figure 2.25 and Figure 2.26). The nomenclature  $O_1$  is referred to the first obstacle while  $O_2$  to the second obstacle.

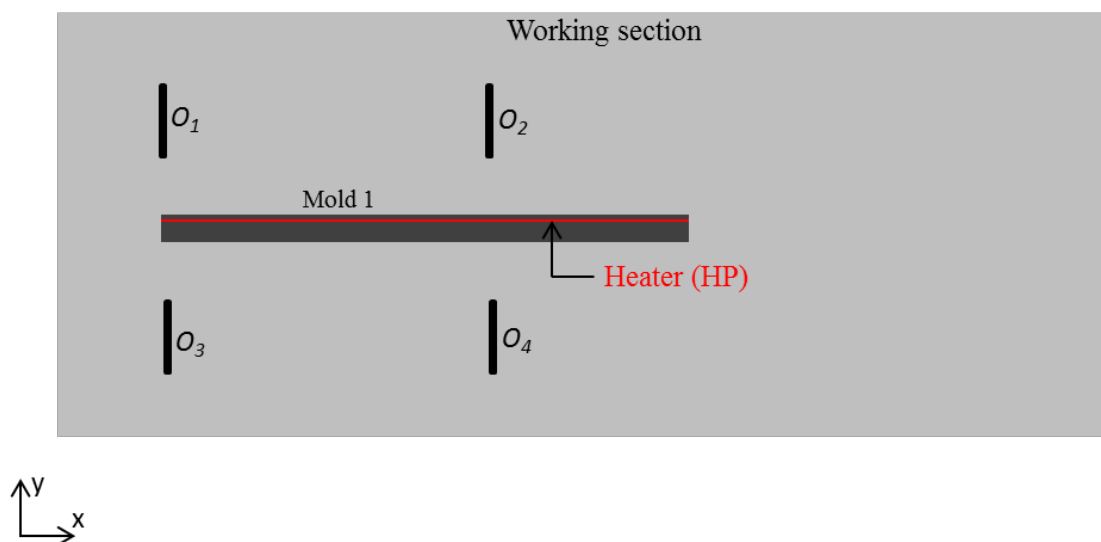
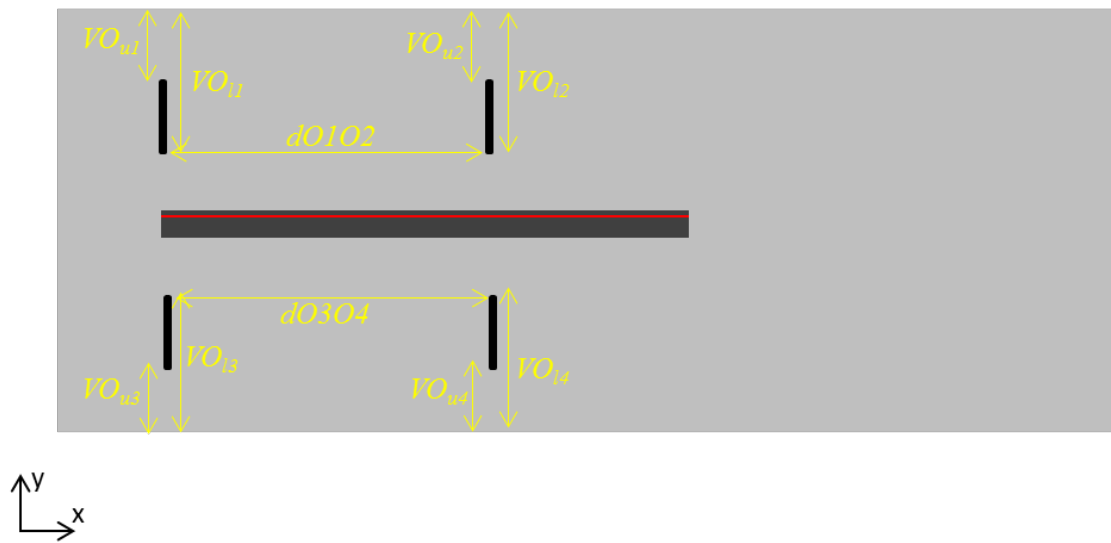


Figure 2.26 Descriptive schematic of the “representative mold” installed within the working section

These obstacles were installed around the “Mold 1” according to the Figure 2.27 and Table 2.10. The different defined geometric parameters presented in Figure 2.27 allow the control of the sizes and the positions of the obstacles. The impact of these geometric design parameters on the physical phenomena of interest, i.e. the flow field and the convective heat transfer coefficient distribution, will be investigated.



**Figure 2.27** Definition of the dimensions of the obstacles

**Table 2.10** Geometric dimensions of the obstacles

Geometric parameter	Value
$VO_{u2} = VO_{u3} = VO_{u4} = VO_{u1}$	0.085 m
$VO_{l2} = VO_{l3} = VO_{l4} = VO_{l1}$	0.15 m
$dO_3O_4 = dO_1O_2$	0.3 m

## **2.9 Partial Conclusion**

In this chapter, an autoclave model which represents an actual autoclave at reduced scale has been sized and fabricated. The design guidelines followed during the sizing works, especially the respect of similarity laws and the control of the inlet flow field, have been detailed and explained. The final design of the model autoclave and its features and characteristics have been presented. The obtained model autoclave represents in fact a closed-circuit wind tunnel. One of its important advantages is the ease of use of non-intrusive and reliable measuring instruments such as the PIV technique and the infrared imaging camera for the investigation of the turbulent velocity field and the convective heat transfer coefficient respectively around model molds. The different measurement instruments as well as the applied experimental procedures for the study of these physical phenomena have been presented and described. Finally, primary PIV measurements of the velocity field at the inlet of the working section have been performed in order to validate the model autoclave. The obtained aerodynamic results fit well with the technical specifications defined at the beginning allowing then the validation of the model autoclave. Different configuration studies have been prepared according to the experimental plan, such as the installation of one mold within the working section of the model autoclave, the installation of two molds for the study of the inter-part shadowing effects and the use of a mold with obstacles (representative mold).

## List of references

- [1] F. White, Chapter 5: Dimensional Analysis and Similitude, in: *Fluid Mech.*, Seventh ed, McGraw-Hill, New York, 2010: pp. 277–324. doi:10.1111/j.1549-8719.2009.00016.x.Mechanobiology.
- [2] L. Cattafesta, C. Bahr, J. Mathew, Fundamentals of wind-tunnel design, *Encycl. Aerosp. Eng.* (2010) 1–10. doi:10.1002/9780470686652.eae532.
- [3] Scholtz Maschinenbau, (n.d.). <https://www.scholz-autoclaves.com/>.
- [4] A.R. Upadhyay, G.N. Dayananda, G.M. Kamalakannan, J. Ramaswamy Setty, J. Christopher Daniel, Autoclaves for aerospace applications: issues and challenges, *Int. J. Aerosp. Eng.* 2011 (2011) 1–11. <http://www.hindawi.com/journals/ijae/2011/985871/> (accessed January 20, 2015).
- [5] N. Slesinger, T. Shimizu, A. Poursartip, A.R.A. Arafath, Heat transfer coefficient distribution inside an autoclave, in: *Proc. 17Th Int. Conf. Compos. Mater.*, Edinburgh, UK, 2009.
- [6] T.A. Weber, J.-C. Arent, L. Münch, M. Duhovic, J.M. Balvers, A fast method for the generation of boundary conditions for thermal autoclave simulation, *Compos. Part A* 88 (2016) 216–225. <http://dx.doi.org/10.1016/j.compositesa.2016.05.036>.
- [7] F. Chen, L. Zhan, Y. Xu, Modelling and simulation for temperature distribution of mold during autoclave forming process, in: *Proc. 12th Int. Conf. Heat Transf. Therm. Eng. Environ.*, Geneva, 2014: pp. 80–88.
- [8] Z. Cheng, W. Yonggui, L. Xianzhu, Z. Boming, Y. Guangquan, J. Peng, Research with CFX software on frame mould temperature field simulation in autoclave process, *Polym. Polym. Compos.* 17 (2009) 325–336.
- [9] N.S. Ghariban, A. Haji-Sheikh, D.Y.S. Lou, Heat transfer in autoclaves, in: *ICHMT Int. Symp. Manuf. Mater. Process.*, Dubrovnik, 1990: pp. 833–848.
- [10] H. Schlichting, *Boundary-Layer Theory*, 7th ed., New York, 1979.
- [11] V. Antonucci, M. Giordano, S. Inserraimparato, L. Nicolais, Analysis of heat transfer in autoclave technology, *Polym. Compos.* 22 (2001) 613–620. doi:10.1002/pc.10564.
- [12] N.E.J. Kluge, Experiments and numerical modelling of the SMC and autoclave processes, Lulea University of Technology, 2015.
- [13] A. Johnston, P. Hubert, R. Vaziri, A. Poursartip, An investigation of autoclave convective heat transfer, in: *Des. Manuf. Compos.*, 1998: pp. 106–113.
- [14] The Engineering ToolBox, (n.d.). [https://www.engineeringtoolbox.com/air-properties-d\\_156.html](https://www.engineeringtoolbox.com/air-properties-d_156.html).
- [15] M. Kiya, K. Sasaki, Free-stream turbulence effects on a separation bubble, J.



- Wind Eng. Ind. Aerodyn. 14 (1983) 373–386.  
doi:[http://dx.doi.org/10.1016/0167-6105\(83\)90039-9](http://dx.doi.org/10.1016/0167-6105(83)90039-9).
- [16] R. Hillier, N.. Cherry, The effects of stream turbulence on separation bubbles, J. Wind Eng. Ind. Aerodyn. 8 (1981) 49–58.
- [17] A. Kondjoyan, F. Péneau, H.-C. Boisson, Effect of high free stream turbulence on heat transfer between plates and air flows: a review of existing experimental results, Int. J. Therm. Sci. 41 (2002) 1–16. doi:10.1016/S1290-0729(01)01299-6.
- [18] M. Raffel, C. Willert, S. Wereley, J. Kompenhans, Particle Image Velocimetry, second ed, Springer, New York, 2007.  
<http://ebooks.cambridge.org/ref/id/CBO9781107415324A009>.
- [19] Fog Generators - Dantec, (n.d.). <https://www.dantecdynamics.com/fog-generators>.
- [20] P.F. Monaghan, M.T. Brogan, P.H. Oosthuizen, Heat transfer in an autoclave for processing thermoplastic composites, Compos. Manuf. 2 (1991) 233–242.  
<http://linkinghub.elsevier.com/retrieve/pii/0956714391901457>.
- [21] A. Johnston, An integrated model of the development of process-induced deformation in autoclave processing of composite structures, The University of British Columbia, 1997.
- [22] T.L. Bergman, A.S. Lavine, F.P. Incropera, D.P. DeWitt, Fundamentals of Heat and Mass Transfer, Seventh, John Wiley & Sons, Jefferson, 2011.  
<http://books.google.com/books?id=vvyIoXEywMoC&pgis=1>.
- [23] H. Yanaoka, H. Yoshikawa, T. Ota, Numerical simulation of laminar flow and heat transfer over a blunt flat plate in square channel, J. Heat Transfer. 124 (2002) 8–16. doi:10.1115/1.1420715.
- [24] S. Roux, M. Fénot, G. Lalizel, L. Brizzi, E. Dorignac, Experimental investigation of the flow and heat transfer of an impinging jet under acoustic excitation, Int. J. Heat Mass Transf. 54 (2011) 3277–3290.  
doi:10.1016/j.ijheatmasstransfer.2011.03.059.
- [25] PCM INNOVATION, (n.d.). <https://www.pcminnovation.com/en/molds-for-composites/>.



# *Chapter 3*

## *CFD analysis of the Model Autoclave*



## Table of contents

<b><i>Chapter 3 CFD analysis of the Model Autoclave</i></b>	<b><i>111</i></b>
<b>3.1</b>	<b>CONTEXT OF THE NUMERICAL STUDY .....115</b>
<b>3.2</b>	<b>NUMERICAL MODEL OF A SINGLE MOLD .....116</b>
3.2.1	Geometry..... 116
3.2.2	Governing equations and numerical methods..... 117
3.2.2.1	Navier-Stokes equations ..... 117
3.2.2.2	Turbulence models ..... 120
3.2.2.3	Materials ..... 121
3.2.2.3.1	Fluid domain..... 121
3.2.2.3.2	Solid domain..... 121
3.2.2.4	Boundary conditions..... 122
3.2.2.4.1	Flow boundary conditions..... 122
3.2.2.4.2	Thermal boundary conditions ..... 123
3.2.2.5	Mesh ..... 123
3.2.2.5.1	Wall modeling strategy and solid domain meshing ..... 123
3.2.2.5.2	Fluid domain meshing ..... 124
3.2.2.5.3	Mesh quality test..... 124
3.2.2.6	Solving..... 126
3.2.3	Numerical results and discussion..... 126
3.2.3.1	Numerical convergence of the physical quantities ..... 127
3.2.3.2	Verification of the mass and energy conservation..... 128
3.2.3.3	Numerical results vs literature ..... 128
3.2.3.3.1	Flow field behavior..... 129
3.2.3.3.2	Wall shear stress coefficient ..... 132
3.2.3.3.3	Pressure coefficient..... 133
3.2.3.3.4	Study of $Xr$ ..... 134
3.2.3.3.5	Nusselt distribution ..... 136
<b>3.3</b>	<b>NUMERICAL MODEL OF THE INTER-PART SHADOWING EFFECTS INVESTIGATION .....139</b>
3.3.1	Geometry..... 139
3.3.2	Governing equation and numerical method..... 139
3.3.3	Verification of the numerical model ..... 140
3.3.4	Numerical results and discussion..... 140
<b>3.4</b>	<b>NUMERICAL MODEL OF THE “REPRESENTATIVE MOLD” .....141</b>
3.4.1	Geometry..... 141
3.4.2	Governing equation and numerical method ..... 142
3.4.3	Verification of the numerical model ..... 144
3.4.4	Numerical results and discussion..... 144
<b>3.5</b>	<b>PARTIAL CONCLUSION .....145</b>
	<b>LIST OF REFERENCES.....146</b>



### **3.1 Context of the numerical study**

In *chapter 2*, the design and the fabrication of a test bench that represents an autoclave at reduced scale was presented and carefully detailed. The employed experimental methodologies for the measurement of the flow field and the convective heat transfers around model molds, and which based on non-intrusive measurement instruments, have been exposed as well.

However, and despite the existence of such instrumented test bench, the resort to numerical computations remains important and useful as they allow rapid and low-cost investigations of various configuration studies than experimental tests. In addition, they provide the ability to carry out fast parametric studies. The latter can be helpful thereafter to find an optimization design solution to reach the desired state. In this case, it could be the enhancement of the convective heat transfer coefficient distribution around molds during an autoclave process.

In the same time, the reliability of the numerical simulation final results is essential, and a complete awareness of the assumptions, the procedure and the various settings is crucial. This can be achieved by validating the numerical findings by experimental measurements.

In this chapter, the various aspects and features of the implemented numerical models in the thesis work as well as the different configuration studies are carefully exposed and detailed.

These numerical models were built in order to represent the experimental configuration studies exposed in *chapter 2*. These configuration studies are the investigation of the turbulent flow field and the convective heat transfer coefficient distribution around one or multiple molds (inter-part shadowing effects) within the working section of the model autoclave. Furthermore, in this chapter, a third configuration will be tested. It consists of using a mold with excessive support structure (obstacles) in order to be more representative of actual industrial conditions.

The main purpose of the numerical computations is to simulate the fluid flow and the convective heat transfers around the molds installed within the working section of the model autoclave. In other words, the performed numerical simulations aim to reproduce the same experimental configurations and investigations showed in *chapter 2*.

Then, the accuracy of the derived numerical results will be inspected by comparing it to those obtained from experimental measurements. The comparison and the validation work are showed in *chapter 4*.

First at all, a CFD tool must be selected. In this work, the commercial CFD tool ANSYS FLUENT 16.0® was used for the simulation of the physical phenomena. It

was widely known and successfully used both for research and industrial purposes [2,3].

## **3.2 Numerical model of a single mold**

### **3.2.1 Geometry**

The presence of a horizontal uniform flow at the inlet of the working section of the model autoclave, according to the validation results presented in section 2.5, and the use of rectangular box shape molds allow to consider that the turbulent flow field and the convective heat transfers around a model mold are two-dimensional (2D) and one-dimensional (1D) respectively and homogeneous in the  $z$  direction. Except near the side walls of the mold where horseshoe vortices can appear, according to Yanaoka *et al.* [4], creating then three-dimensional (3D) effects.

Given these facts on one hand, and on the other hand the efforts and computational resources and thus the prohibitive cost required by the 3D simulations, a 2D numerical model has been created. The latter is able to represent the physical phenomenon that occur near the center region of the mold [4].

Therefore, the geometrical 2D model of the working section of the model autoclave to be simulated is shown as in Figure 3.1. The geometrical model of the mold was created as well.

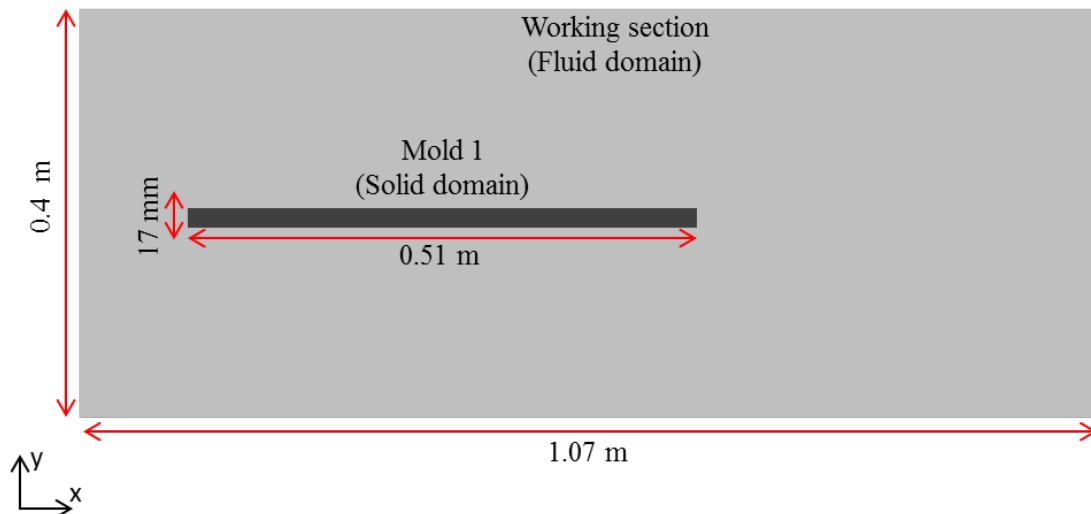


**Figure 3.1 The computational domain for the model autoclave**

The experimental actual dimensions presented previously of the working section and the mold were respected in the geometrical model: the length of the working section is 1.07 m and its width, which represents the high in actual dimension, is 0.4 m. Also, the mold, which is the “Mold 1” in this case, is 0.51 m and 17 mm in length



and thickness respectively. It was created according to the structure showed in the section 2.6.2 (see Figure 2.22).

## 3.2.2 Governing equations and numerical methods

### 3.2.2.1 Navier-Stokes equations

The basic governing equations for continuity, momentum and energy in the fluid domain, for an incompressible flow in a steady state regime with no external forces, can be expressed as follows [5][6] :

$$\text{Continuity :} \quad \frac{\partial u_i}{\partial x_i} = 0 \quad \text{Equation (3.1)}$$

$$\text{Momentum:} \quad \rho u_k \frac{\partial u_i}{\partial x_k} = -\frac{\partial P}{\partial x_i} + \mu \frac{\partial^2 u_i}{\partial x_k \partial x_k} \quad \text{Equation (3.2)}$$

$$\text{Energy:} \quad \rho c_p u_i \frac{\partial T}{\partial x_i} = \frac{\partial}{\partial x_i} \left( \lambda_f \frac{\partial T}{\partial x_i} \right) \quad \text{Equation (3.3)}$$

In Equation (3.3), the temperature in the fluid is considered as a passive scalar, with no large density changes.

In the solid domain, the energy equation (Poisson's equation) is solved:

$$\begin{aligned} \text{Energy in the heater:} \quad & -\frac{\partial}{\partial x_i} \left( \lambda_h \frac{\partial T}{\partial x_i} \right) = \frac{HP}{e_h} \\ \text{Energy elsewhere:} \quad & -\frac{\partial}{\partial x_i} \left( \lambda_s \frac{\partial T}{\partial x_i} \right) = 0 \end{aligned} \quad \text{Equations (3.4)}$$

The energy source ( $HP/e_h$ ) occurs only in the resistive film in order to model the heater.

The RANS (**R**eynolds **A**veraged Navier-Stokes **S**imulation) approach was used to solve these governing equations in the steady-state regime. In fact, RANS is the most widely used approach for industrial flows [5,7] and it is less time-consuming than other methods such as the DNS (Direct Numerical Simulation) and the LES (Large Eddy Simulation). The latter require more efforts and computational resources and the cost is too prohibitive [8]. This can be due to the fact that DNS and LES solve numerically the Navier-Stokes equations while RANS solves the Reynolds time-averaged Navier-Stokes equations. The difference between these three basic approaches can be illustrated by the schematic presented in Figure 3.2.

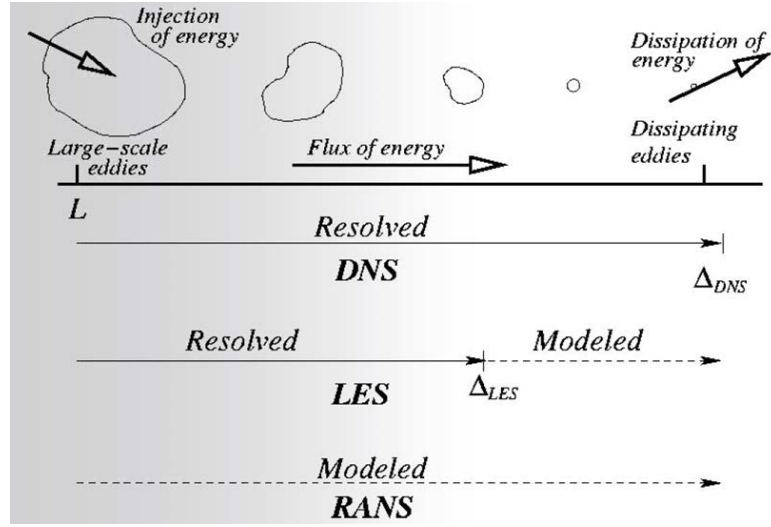


**Figure 3.2 Prediction methods of the three approaches [8]**

The RANS approach is based on the decomposition of the velocity into mean and turbulent parts. Thus, the Navier-Stokes equations (Equation (3.2)) may be rewritten as Reynolds-averaged Navier-Stokes equations (Equation 3.5).  $R_{ij}$  is the Reynolds stress tensor.

$$\rho \bar{u}_k \frac{\partial \bar{u}_i}{\partial x_k} = -\frac{\partial \bar{P}}{\partial x_i} + \mu \frac{\partial^2 \bar{u}_i}{\partial x_j \partial x_j} + \frac{\partial R_{ij}}{\partial x_j} \quad \text{Equations (3.5)}$$

$$R_{ij} = -\rho \overline{u'_i u'_j}$$

The Reynolds stresses are additional unknowns introduced by the averaging procedure, hence they must be modeled in order to close the system of governing equations. The RANS equations can be closed then in two ways: Reynolds-Stress Models (RSM) where  $R_{ij}$  is directly solved via transport equations, or Eddy Viscosity Models where Reynolds stresses are modeled using an eddy or turbulent viscosity ( $\mu_T$ ). However, RSM is advantageous in complex 3D turbulent flows, with large streamline curvature and swirl, but the model is more complex, computationally intensive and more difficult to converge than eddy viscosity models. Given these facts, it was decided to employ the Eddy Viscosity Models.

According to the Eddy Viscosity Models,  $R_{ij}$  is solved by the Equation (3.6):

$$R_{ij} = -\rho \overline{u'_i u'_j} = \mu_T \left( \frac{\partial \bar{u}_i}{\partial x_j} + \frac{\partial \bar{u}_j}{\partial x_i} \right) - \frac{2}{3} \mu_T \frac{\partial \bar{u}_k}{\partial x_k} \delta_{ij} - \frac{2}{3} \rho k \delta_{ij} \quad \text{Equation (3.6)}$$

On the other hand, the calculation of  $\mu_T$  requires the solving of two transport equations. These transport equations constitute what is called a “Turbulence Model”.

Therefore, the use of the RANS- Eddy Viscosity Models approach requires the resort to a “Turbulence Model” to model the Navier-Stokes equations. There are many turbulence models available and the choice of the model strongly influences the accuracy of the results and it depends on the case of study.

Among the many different available turbulence models, the most important kinds are the standard  $k$ - $\varepsilon$ , RNG  $k$ - $\varepsilon$ , realizable  $k$ - $\varepsilon$ , standard  $k$ - $\omega$  and SST  $k$ - $\omega$ .  $k$  is the turbulent kinetic energy,  $\varepsilon$  is the dissipation rate and  $\omega$  is the specific dissipation rate. The  $k$ - $\varepsilon$  and the  $k$ - $\omega$  transport equations to resolve  $\mu_T$  are given by the Equation (3.7) and Equation (3.8) respectively [8]. The coefficients used in these equations are empirical constants determined from experiments.

$$\begin{aligned}\mu_T &= \rho C_\mu \frac{k^2}{\varepsilon} \\ \rho \frac{Dk}{Dt} &= \frac{\partial}{\partial x_j} \left[ \left( \mu + \frac{\mu_T}{\sigma_k} \right) \frac{\partial k}{\partial x_j} \right] + \mu_T S^2 - \rho \varepsilon \\ \rho \frac{D\varepsilon}{Dt} &= \frac{\partial}{\partial x_j} \left[ \left( \mu + \frac{\mu_T}{\sigma_\varepsilon} \right) \frac{\partial \varepsilon}{\partial x_j} \right] + \frac{\varepsilon}{k} (C_{1\varepsilon} \mu_T S^2 - \rho C_{2\varepsilon} \varepsilon) \\ S &= \sqrt{2S_{ij}S_{ij}}; \quad S_{ij} = \frac{1}{2} \left( \frac{\partial \bar{u}_i}{\partial x_j} + \frac{\partial \bar{u}_j}{\partial x_i} \right)\end{aligned}\tag{Equations (3.7)}$$

$$\begin{aligned}\mu_T &= \rho \alpha^* \frac{k}{\omega} \\ \rho \frac{Dk}{Dt} &= \frac{\partial}{\partial x_j} \left[ \left( \mu + \frac{\mu_T}{\sigma_k} \right) \frac{\partial k}{\partial x_j} \right] + \tau_{ij} \frac{\partial \bar{u}_i}{\partial x_j} - \rho \beta^* f_\beta \cdot k \omega \\ \rho \frac{D\omega}{Dt} &= \frac{\partial}{\partial x_j} \left[ \left( \mu + \frac{\mu_T}{\sigma_\omega} \right) \frac{\partial \omega}{\partial x_j} \right] + \alpha \frac{\omega}{k} \tau_{ij} \frac{\partial \bar{u}_i}{\partial x_j} - \rho \beta f_\beta \cdot \omega^2\end{aligned}\tag{Equations (3.8)}$$

In the following section, the behavior and the usage of these various turbulence models will be discussed in order to select the appropriate one for our application.

### 3.2.2.2 Turbulence models

The most important used turbulence models and their suitable applications are listed as follows [8]:

- **Standard  $k-\varepsilon$ :** widely used despite the known limitations of the model. Performs poorly for complex flows involving severe pressure gradient, separation, and strong streamline curvature.
- **Realizable  $k-\varepsilon$ :** suitable for complex shear flows involving rapid strain, moderate swirl, vortices, and locally transitional flows (e.g. boundary layer separation, massive separation, and vortex shedding behind bluff bodies, stall in wide-angle diffusers, room ventilation).
- **RNG  $k-\varepsilon$ :** offers largely the same benefits and has similar applications as Realizable. Possibly harder to converge than Realizable.
- **Standard  $k-\omega$ :** superior performance for wall-bounded boundary layer, free shear, and low Reynolds number flows compared to models from the  $k-\varepsilon$  family. Suitable for complex boundary layer flows under adverse pressure gradient and separation (external aerodynamics and turbomachinery). Separation can be predicted to be excessive and early.
- **SST  $k-\omega$ :** Offers similar benefits as standard  $k-\omega$ . Not overly sensitive to inlet boundary conditions like the standard  $k-\omega$ . Provides more accurate prediction of flow separation than other RANS models.

Further, several research studies have been performed in order to investigate the potential of these turbulence models. Almost all of them [9–17] have reported that the  $k-\varepsilon$  turbulence models family failed to predict accurately the complex flow structures such as the flow separation, the detachment of a jet from a surface, the presence of a secondary recirculating flow.

The poor predictions given by these two-equation turbulence models can be explained by the overly diffusive character of these models. Authors [14,15] stated that the  $k-\varepsilon$  model significantly over-predicts shear-stress levels and thereby delays or completely prevents separation. This trend can be more pronounced in the presence of an adverse pressure gradient and leads to over-prediction of the wall shear-stress [16].

Given this inability and this inadequately prediction of  $k-\varepsilon$  turbulence models family in such applications, it was decided to use the turbulence model “SST  $k-\omega$ ” to simulate the turbulence flow within the working section of the model autoclave and around the mold. Indeed, it is recommended to predict more accurately the flow separation than other RANS models [8].

In fact, the “SST  $k-\omega$ ” turbulence model provides improved predictions of near-wall flow, and it is able to predict accurately the viscous sublayer and therefore the

boundary layer growth on the mold surface. The prediction of the viscous sublayer is a requirement to predict then accurately the  $HTC$  distribution on the mold surface.

### 3.2.2.3 Materials

#### 3.2.2.3.1 Fluid domain

The air was defined as the used gas in the fluid domain of the geometrical model of the working section (see Figure 3.1). Its properties were defined as ambient temperature ( $20^{\circ}\text{C} < T_{air} < 25^{\circ}\text{C}$ ) and pressure as follows [18] (see Table 3.1):

**Table 3.1 Defined air properties**

$\rho$ (kg/m <sup>3</sup> )	$C_p$ (J/kg/K)	$\lambda$ (W/m/K)	$\nu$ (m <sup>2</sup> /s)	$\beta$ (1/K)
1.2	1005	0.0257	$15.11 \times 10^{-6}$	$3.43 \times 10^{-3}$

#### 3.2.2.3.2 Solid domain

The solid domain represents in fact the geometrical model of the mold “Mold 1” (see Figure 3.1). This geometrical model respects the actual structure and the actual dimensions of the “Mold 1” presented previously in section 2.6.2 (see Figure 2.22). The properties of the different materials used were defined as follows [18] (see Table 3.2):

**Table 3.2 Defined properties for the solid domain**

	$\rho$ (kg/m <sup>3</sup> )	$C_p$ (J/kg/K)	$\lambda$ (W/m/K)
<b>Stainless Steel plate</b>	8030	502.5	16.27
<b>Rohacell</b>	52	2394	0.057
<b>Polyamide 66</b>	1130	1670	0.25

### 3.2.2.4 Boundary conditions

The required boundary conditions for the resolution of the governing equations exposed above are divided mainly into flow and thermal boundary conditions. The latter are illustrated in Figure 3.3 and explained in the below sections.

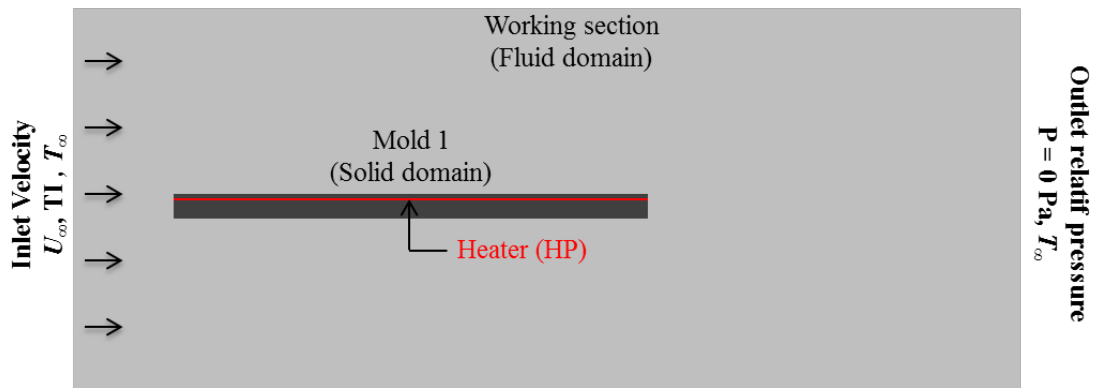


Figure 3.3 Flow and thermal boundary conditions

#### 3.2.2.4.1 Flow boundary conditions

The boundary conditions of the working section inlet and outlet were set as velocity inlet and pressure outlet, respectively (Figure 3.3). This kind of boundary conditions allow a more rapid numerical convergence and avoid numerical errors [8].

The velocity inlet boundary conditions require the definition of the main following quantities (see Table 3.3):

Table 3.3 Flow boundary conditions

Inlet		Outlet
$U_\infty$ (m/s)	TI (%)	$P$ (Pa)
33.7	1.1	0

The inlet free stream velocity ( $U_\infty$ ) and the inlet free stream turbulence intensity ( $u_{rms}/U_\infty$ ) were set according to the flow characteristics obtained previously from the experimental validation results (see Table 2.11). They correspond in this chapter to the volume flow rate of interest  $Q = 15\,290\text{ m}^3/\text{h}$ .

In fact, many researchers [19–21] have reported the effect of the free stream turbulence intensity on the flow behavior and the heat transfer coefficient ( $HTC$ ) around surfaces. Given this fact, the numerical inlet boundary conditions must be derived from experimental measurements in order to obtain comparable results.

#### 3.2.2.4.2 Thermal boundary conditions

The air inlet temperature ( $T_\infty$ ) was defined normally according to the experimental result. In this chapter,  $T_\infty$  was defined at temperature of 300 K. In the *chapter 4*,  $T_\infty$  will be modified according to the experimental measures.

The heating power or the heat flux density ( $HP$ ), injected in the film resistive heater as explained before, was defined as an energy source in the numerical model (Figure 3.3). In this chapter,  $HP$  was set at 700 W/m<sup>2</sup> to visualize numerical results. In the *chapter 4*,  $HP$  will be modified according to the experimental conditions.

#### 3.2.2.5 Mesh

##### 3.2.2.5.1 Wall modeling strategy and solid domain meshing

The choice of the mesh is a key element that can affect the accuracy of the results at the end of the numerical computations. It should be constructed and build according to the physical phenomena under investigation.

In our case study, these physical phenomena are the turbulent flow field and the convective heat transfer around the mold surfaces. Thus, an accurate prediction of the near-wall flow is required in order to predict precisely the flow separation structures and the convective heat transfer coefficient distribution.

Despite the choice of an adequate turbulence model, which is the “SST  $k-\omega$ ” turbulence model, the corresponding wall modeling strategy should be defined as well as it affects also the near-wall resolution and thus the success of the entire simulation.

In the near-wall region, where the solution gradients are very high, the resolving of the viscous sublayer is necessary to investigate properly the heat transfer and the flow structure on the wall [8].

However, to resolve this viscous sublayer, the first grid cell needs to be at  $y^+ \leq 1$  and a prism layer mesh with growth rate no higher than 1.2 should be used [7,8].  $y^+$  is the wall coordinate defined according to the Equation (3.9) for the first grid cell [22].  $d_w$  is the distance from the first cell mesh to the wall,  $u_\tau$  is the friction velocity,  $\tau_w$  is the wall shear stress and  $C_f$  is the friction coefficient. The correlation for the calculation of  $C_f$  is applied in the case of a turbulent flow over a plate with a Reynolds number range of  $5 \times 10^5 < Re_l < 10^7$  [22].

$$y^+ = \frac{u_\tau d_w}{\nu} \leftrightarrow d_w = \frac{y^+ \nu}{u_\tau}$$

Equations (3.9)

$$u_\tau = \sqrt{\frac{\tau_w}{\rho}}$$

$$\tau_w = \frac{1}{2} C_f \rho U_\infty^2$$

$$C_f = 0.058 Re_{l_c}^{-0.2}$$

$y^+$  for the first grid cell was fixed at 1. Table 3.4 gathers the numerical values of the different variables used in the Equation (3.8). The main objective at the end is to determine  $d_w$  in order to construct the mesh.

**Table 3.4 Calculation of the first cell mesh distance to the wall ( $d_w$ )**

$\rho$ (kg/m <sup>3</sup> )	$\nu$ (m <sup>2</sup> /s)	$U_\infty$ (m/s)	$l$ (m)	$Re_l$	$C_f$	$\tau_w$ (kg/m/s <sup>2</sup> )	$u_\tau$ (m/s)	$y^+$	$d_w$ (m)
1.2	$15.11 \times 10^{-6}$	33.7	0.51	$1.1 \times 10^6$	$3.6 \times 10^{-3}$	2.44	2.03	1	$7.41 \times 10^{-6}$

This condition of the distance ( $d_w$ ) between the first cell mesh and the mold surfaces was respected during the mesh construction, and it requires the use of a finer structured square mesh around the mold surfaces. Also, a structured square mesh was used for meshing the solid domain (Figure 3.4). The mesh was created using the ANSYS Workbench Meshing tool. The influence of the mesh on the velocity field profile has been studied (Appendix B).

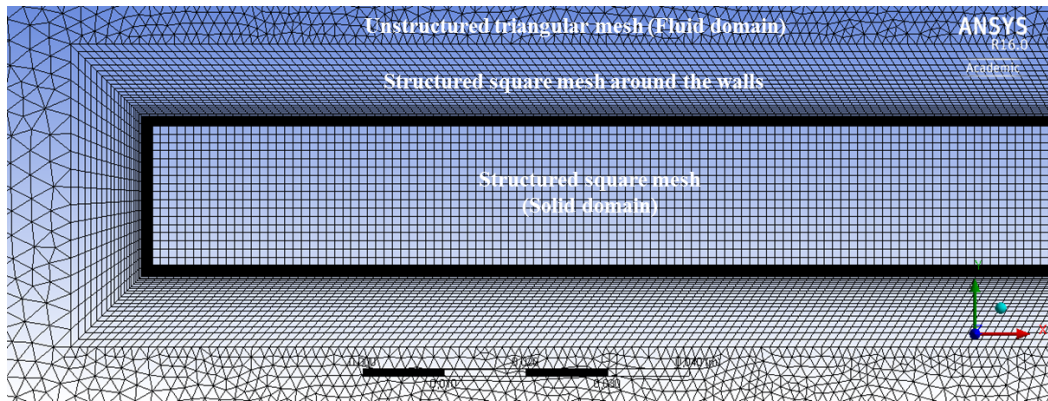


**Figure 3.4 Zoom on the constructed mesh in the computational domain**

### 3.2.2.5.2 Fluid domain meshing

The fluid computational domain was meshed with unstructured triangular grids (Figure 3.4). This type of mesh was selected as it is more flexible to use and to construct and it allows also a rapid numerical convergence.

### 3.2.2.5.3 Mesh quality test

The obtained mesh of the computational domain is shown in Figure 3.4. It contains in total 138 100 elements.



To inspect the mesh quality, as a first step, various criteria can be referred to. Among them, the most important one are the “Orthogonal quality” and the “Skewness quality” of the mesh.

The orthogonal quality of a given cell is based on the calculation of the following quantities for each face ( $i$ ).

- The normalized dot product of the area vector of a face ( $\vec{A}_i$ ) and a vector from the centroid of the cell to the centroid of that face ( $\vec{f}_i$ ):

$$\frac{\vec{A}_i \cdot \vec{f}_i}{|\vec{A}_i| |\vec{f}_i|} \quad \text{Equation (3.10)}$$

- The normalized dot product of the area vector of a face ( $\vec{A}_i$ ) and a vector from the centroid of the cell to the centroid of the adjacent cell that shares that face ( $\vec{c}_i$ ):

$$\frac{\vec{A}_i \cdot \vec{c}_i}{|\vec{A}_i| |\vec{c}_i|} \quad \text{Equation (3.11)}$$

The minimum value that results from calculating Equation (3.10) and Equation (3.11) for all the faces is then defined as the orthogonal quality for the cell. Therefore, the worst cells have an orthogonal quality closer to 0 and the best cells will have an orthogonal quality closer to 1. Figure 3.5 illustrates the relevant vectors.

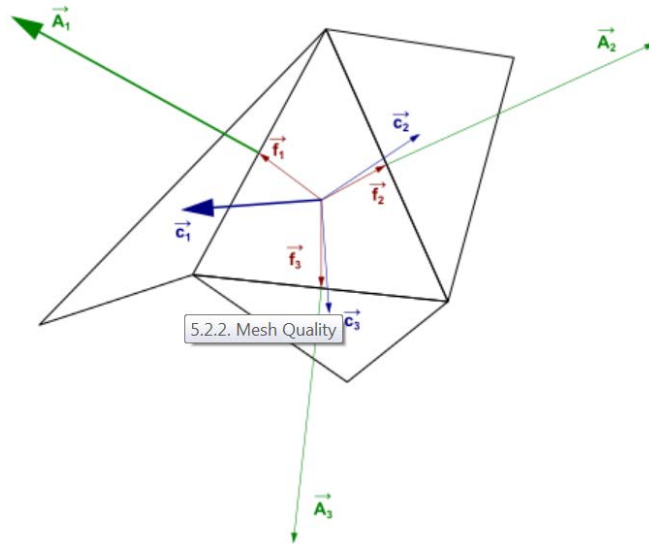


**Figure 3.5 The vectors used to compute Orthogonal quality**

Skewness is defined as the difference between the shape of the cell and the shape of an equilateral cell of equivalent volume. Highly skewed cells can decrease accuracy and destabilize the solution. For example, optimal triangular meshes should

preferably have angles of close to 60 degrees and have all angles less than 90 degrees. A general rule is that the maximum skewness for a triangular mesh in most flows should be kept below 0.95, with an average value that is significantly lower. A maximum value above 0.95 may lead to convergence difficulties and may require changing the solver controls, such as reducing under-relaxation factors and/or switching to the pressure-based coupled solver.

Table 3.5 contains the average values of these two quantities over the constructed mesh cells.

**Table 3.5 Quality of the constructed mesh**

	Orthogonal quality		Skewness	
	Average	Standard deviation	Average	Standard deviation
<b>Constructed mesh</b>	0.94	$7.5 \times 10^{-2}$	0.13	0.15

Based on the above discussion, the obtained high values of orthogonal quality for the mesh cells (close to 1) and the obtained low values of skewness (close to 0) indicate that the constructed mesh respects well the defined criteria.

### 3.2.2.6 Solving

The computer code ANSYS FLUENT 16.0® was used to calculate the flow and heat transfers as mentioned previously.

The governing equations were iteratively solved by the finite-volume-method with “COUPLED” pressure-velocity coupling algorithm. The latter is recommended for the simulation of incompressible gaseous flows [23].

“Second Order Upwind” schemes were used as they are recommended for the spatial discretization of all flow variables [24].

The convergence criterion was that the normalized residuals are less than  $10^{-5}$  for the flow equations and  $10^{-8}$  for the energy equation. The computations were performed with a workstation with CPU frequency of 3 GHz.

### 3.2.3 Numerical results and discussion

In this section, the obtained numerical results of the flow field behavior and the *HTC* distribution around the mold surfaces will be presented. They will be compared to those obtained by previous research works in the literature in order to pre-validate the computational model and the adopted numerical methods.

The final validation of the numerical model will be ensured by comparing the CFD results to those obtained from experimental measurements performed on the model autoclave. The validation work will be presented in *chapter 4*.

### 3.2.3.1 Numerical convergence of the physical quantities

The investigated physical quantities, such as the air velocity in the computational domain, the temperature of the mold and the *HTC* distribution, have shown a constant behavior against the iteration numbers at the end of the simulation. Thus the numerical convergence is an index of the quality of the realized computational model.

Figure 3.6 and Figure 3.7 shows an example of the numerical convergence for the space-average of the velocity magnitude of the air over the computational domain and for the space-average of *HTC* values over the length of the upper surface of the “Mold 1” respectively. It can be clearly seen that these plotted physical quantities present a constant behavior without fluctuations against the iteration calculations at the end of a simulation.

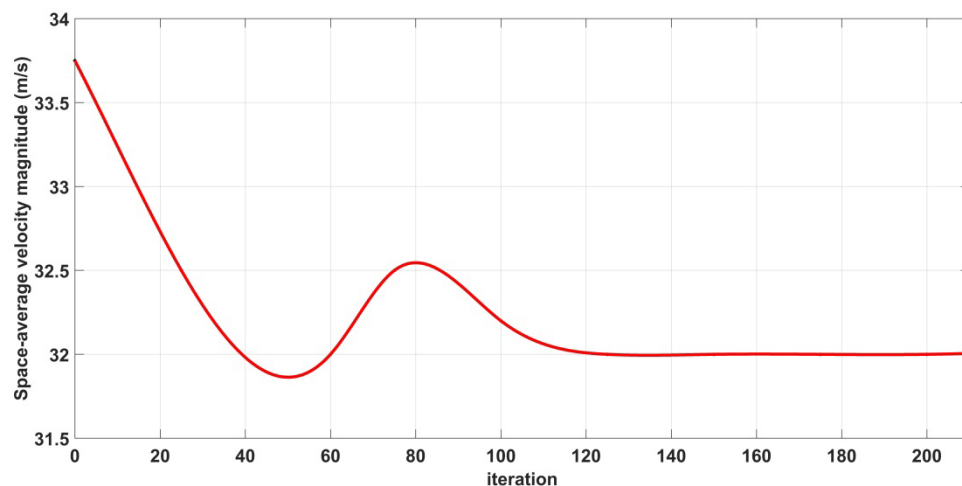
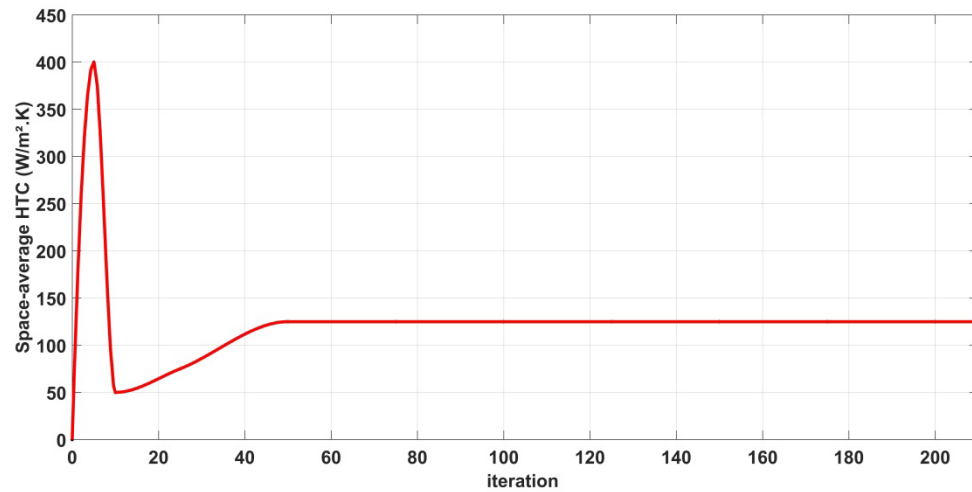


Figure 3.6 Numerical convergence – Velocity

Figure 3.7 Numerical convergence -  $HTC$ 

### 3.2.3.2 Verification of the mass and energy conservation

The accuracy of the numerical model can be verified as well by checking the energy and the mass balances in the computational domain. This is shown in Table 3.8. For the masse balance, the “Net result” signifies the difference between the volume flow rate at the inlet and at the outlet. The best value is 0. On the other hand, for the energy balance, it signifies the difference between the output and the inlet energy in the whole domain. The energy source is equivalent to the injected heating power ( $HP$ ).

The low values of “Net result” signify that the conservation of mass and energy has been respected in the simulation.

Table 3.6 Net result of the energy and mass balance in the computational domain

	Net result
Volume flow rate ( $m^3/h$ )	$10^{-6}$
Energy source ( $W/m^2$ )	0.5

### 3.2.3.3 Numerical results vs literature

In this section, the behaviors and values of some physical quantities derived from the numerical model will be compared to those obtained by previous research works found in the literature, in particular those carried out by Djilali *et al.* [25]. In summary, the authors reported measurements of the separated reattaching flow around a long rectangular plate placed in a test section corresponding to a solid blockage ratio

(*BR*) of about 5.6%. The measurements were conducted in a low-turbulence stream in the range 0.25-0.4% and at Reynolds number, based on the plate thickness, of  $5 \times 10^4$ .

On the other hand, the present numerical calculation was performed at Reynolds number based on the plate thickness of  $3.8 \times 10^4$ , with a turbulence intensity of 1.1% and with a *BR* of 4.25%.

It should be recalled that the effects of these various parameters on the separated-reattaching flow around a blunt plate have been exposed in section 1.3.

### 3.2.3.3.1 Flow field behavior

Figure 3.8 shows the streamlines of the velocity field around the leading edge of the “Mold 1”, in the steady state regime, and obtained from the CFD computations.

The obtained velocity streamlines shows the appearance of a separated-reattached flow region over the leading edge of the mold. This obtained flow structure from the numerical calculations matches the description of the flow structure around a rectangular bluff plate stated by several previous research studies [25–27] (Figure 3.9).

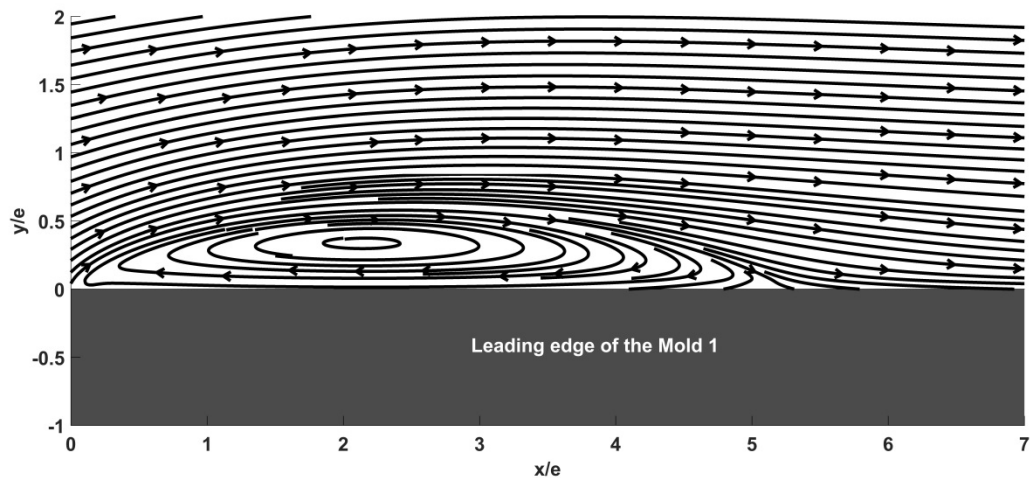
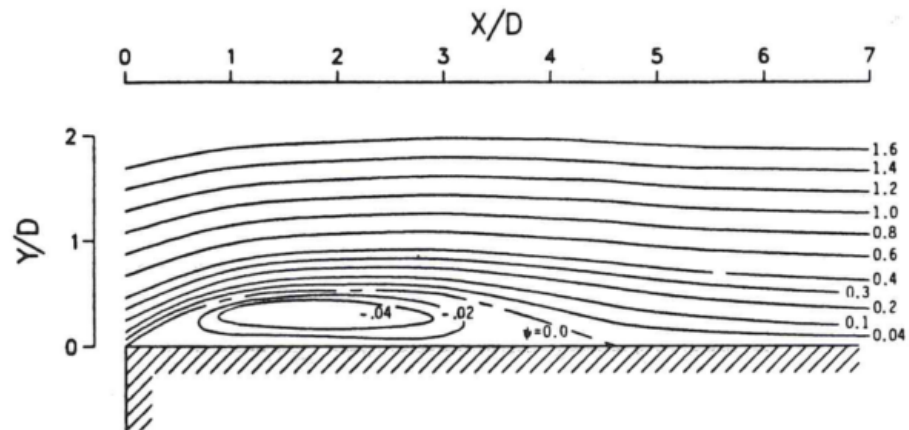


Figure 3.8 Separated-reattached flow region over the leading edge of the mold: CFD results



**Figure 3.9 Separated-reattached flow region over the leading edge of a plate (Djilali et al. [25])**

Further, the mean and r.m.s longitudinal velocity profiles have been plotted numerically in order to investigate the characteristics of the obtained separated-reattached flow region (Figure 3.10 and Figure 3.12). These profiles have been extracted in the boundary layer developed around the “Mold 1” for different dimensionless  $x$ -positions ( $x/e$ ). The reference point ( $x/e=0$ ,  $y/e=0$ ) corresponds to the leading edge corner of the mold.

The obtained profiles were compared then to those found in the literature (Figure 3.11 and Figure 3.13). The comparison shows a good agreement in the behaviors.

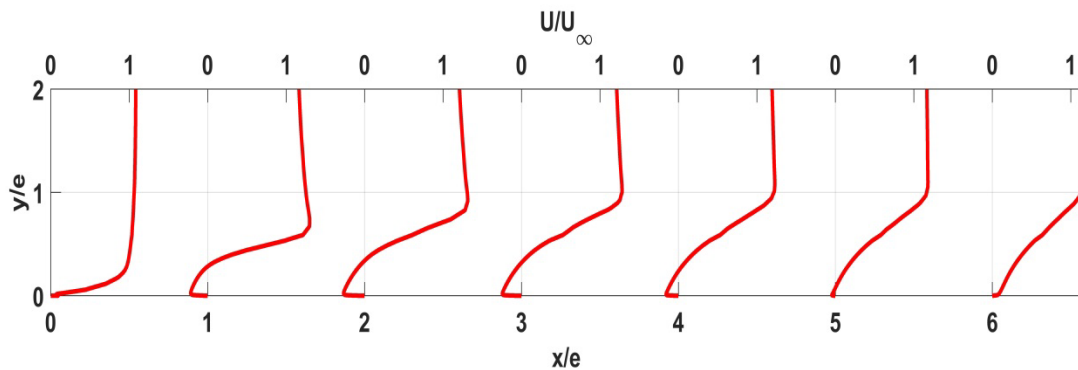


**Figure 3.10 Longitudinal velocity profiles: CFD results**

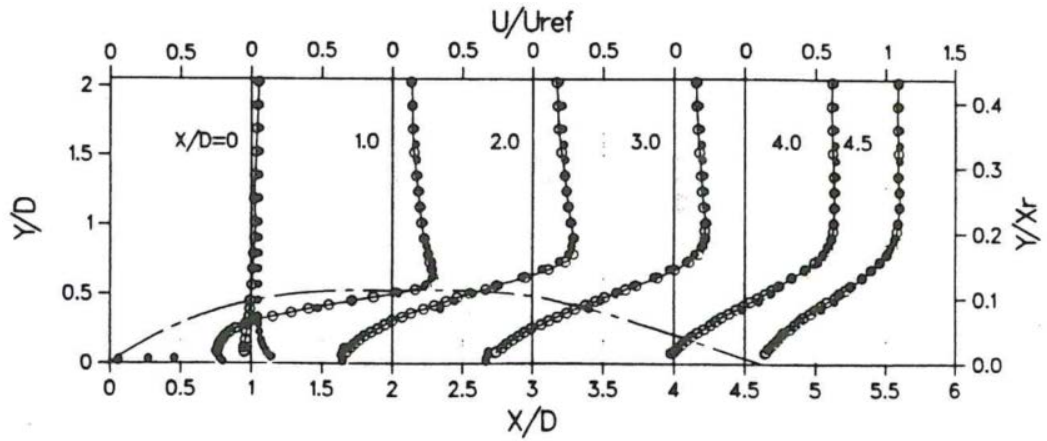


Figure 3.11 Longitudinal velocity profiles: measurements of Djilali et al. [25]

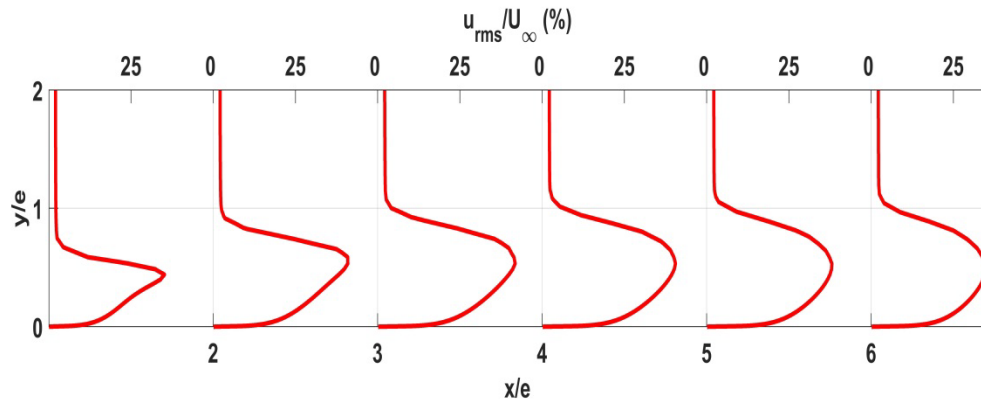


Figure 3.12 Fluctuating (r.m.s) longitudinal velocity profiles: CFD results

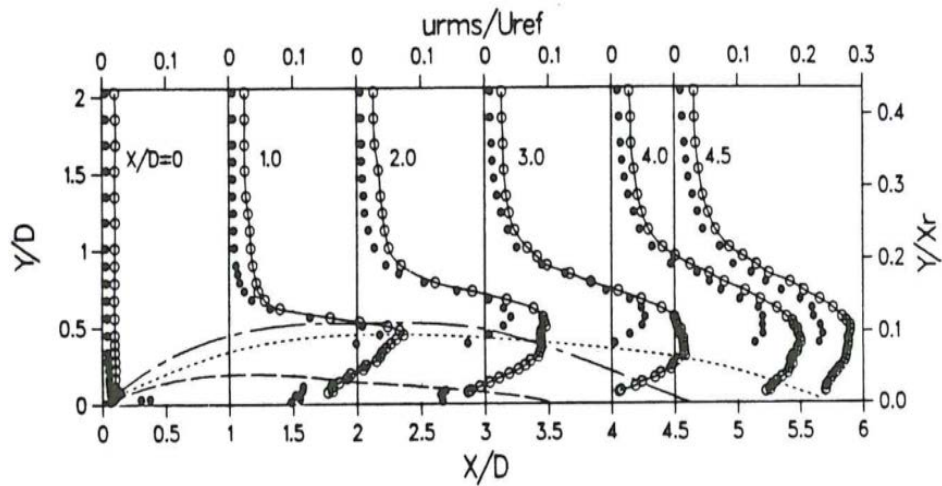


Figure 3.13 Fluctuating (r.m.s) longitudinal velocity profiles: measurements of Djilali et al. [25]

The plotted profiles in Figure 3.10 show that at the beginning of the mold, i.e.  $x/e = 0$ , and until a distance  $x/e$  between 5 and 6, the normalized  $x$ -velocities ( $U/U_\infty$ ) near

the wall present negative values. The presence of such inflexions points in these profiles indicates the existence of backflow velocities and thus the appearance of the separated-reattached flow region. The velocities further away from the wall remain slightly higher than the free stream as a result of blockage effects.

On the other hand, the profiles of turbulence intensities show the presence of significant values near the wall region which reach over 25%. However, the turbulence intensities decay fairly rapidly in the outer region of the shear layer. The presence of such high turbulence intensities indicates again the formation of separation bubbles over the leading edge of the mold [28].

The separated-reattached flow region appeared over the mold is characterized by the reattachment length ( $Xr$ ). It is measured from the line of separation, i.e. the sharp leading edge of the plate, to the reattachment line. In this simulation,  $Xr$  can be deduced to be in the range of  $5e$  to  $6e$  according to the velocity profiles shown in Figure 3.10.

The exact location of the reattachment line corresponds to the location at which the wall shear stress ( $\tau_w$ ) vanishes [25]. Knowing this location allows the deduction of the reattachment length ( $Xr$ ). Given this fact, the wall shear stress over the mold will be computed in the following in order to determine the exact value of  $Xr$ . The results of  $\tau_w$  and  $Xr$  will be compared also to those found in the literature.

### 3.2.3.3.2 Wall shear stress coefficient

Figure 3.14 shows the distribution of the skin friction coefficient ( $C_f$ ), which is proportional to the wall shear stress coefficient ( $\tau_w$ ), over the upper surface of the “Mold 1”. The obtained distribution was compared to that obtained by the measurement of Djilali *et al.* [25] (Figure 3.15) and the comparison shows again a good agreement qualitatively in the behaviors.

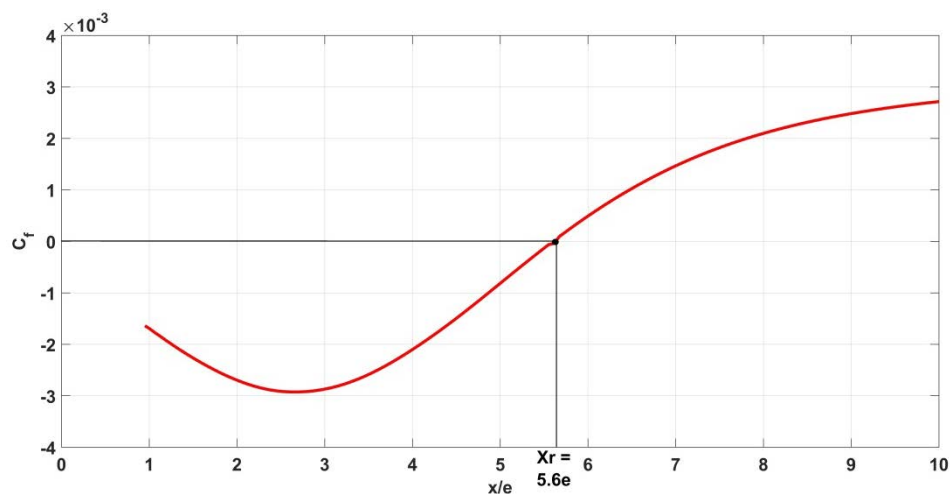
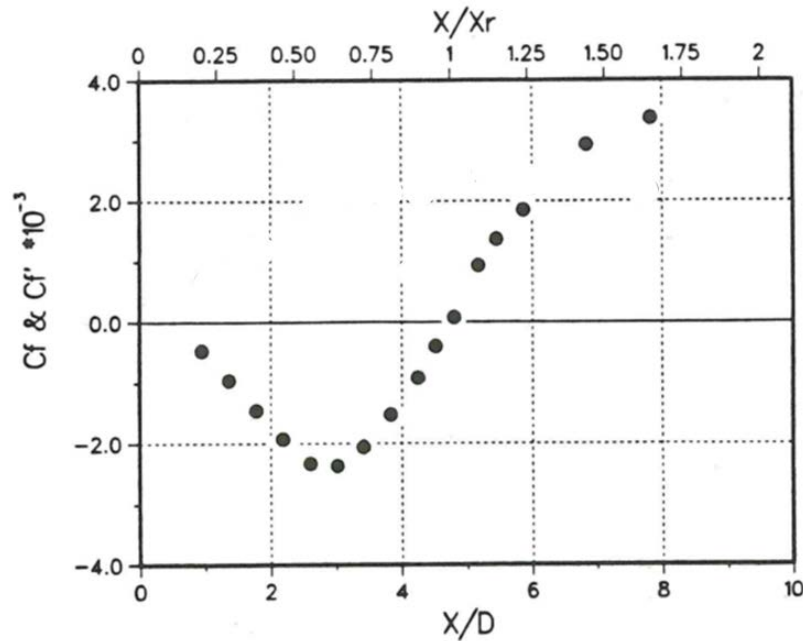


Figure 3.14 Distribution of skin friction coefficients: CFD results





**Figure 3.15 Distribution of skin friction coefficients: measurements of Djilali et al. [25]**

According to the obtained numerical result showed in Figure 3.14, the wall shear stress coefficient was found to vanish at  $x/e=5.58$ . Thus,  $Xr = 5.58e = 94.86$  mm.

On the other hand, the authors Djilali *et al.* [25] found a reattachment length of about  $4.7e$ . This deviation in the value of  $Xr$  can be due to differences in the operation conditions such as the free stream turbulence intensity and the blockage ratio. The latter have shown to affect  $Xr$  as explained previously in section 1.3.

### 3.2.3.3.3 Pressure coefficient

The distribution of the pressure coefficient over the upper surface of the “Mold 1” is shown in Figure 3.16. The numerical model has shown again to predict quite well the behavior of the pressure coefficient distribution. The latter was plotted also according to the measurement of Djilali *et al.* [25] (Figure 3.17).

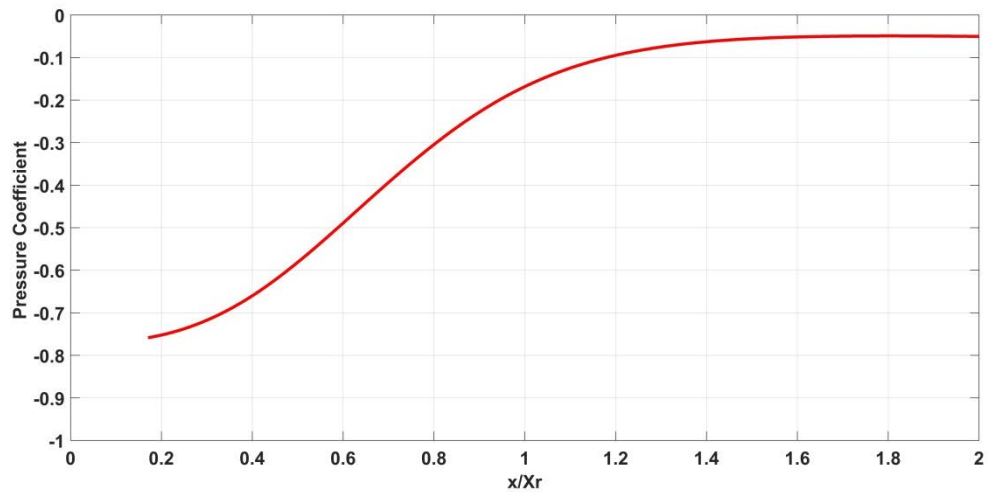


Figure 3.16 Distribution of surface pressure coefficient: CFD results

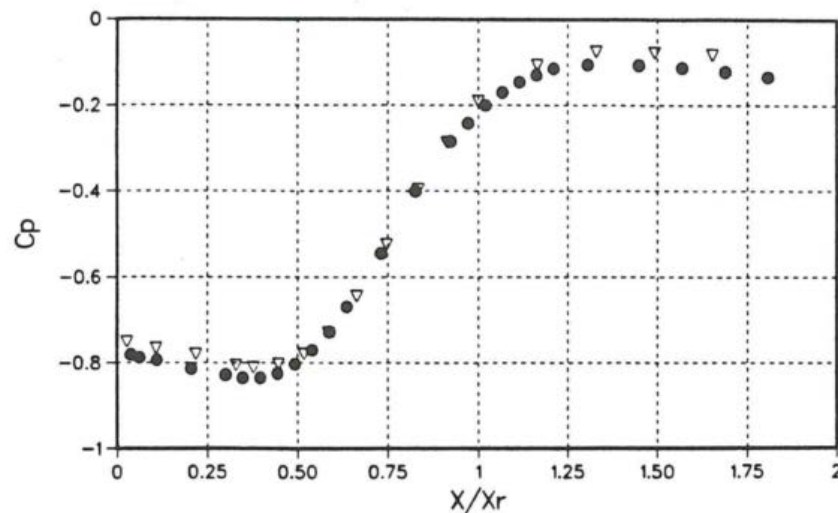


Figure 3.17 Distribution of surface pressure coefficient: measurements of Djilali et al. [25]

#### 3.2.3.3.4 Study of $X_r$

The various factors that affect the separated-reattached flow region and thus the reattachment length ( $X_r$ ) have been investigated numerically. These factors have been listed in *chapter 1*, section 1.3.

##### 3.2.3.3.4.1 Effect of $Re$ number

Previous research works [20,29] deduced that the reattachment length ( $X_r$ ) decreases as the Reynolds number ( $Re$ ) increases in the laminar separation – turbulent reattachment régime. Starting from  $Re \geq 2 \times 10^4$  based on the plate thickness and which corresponds to the turbulent separation – turbulent reattachment régime, the Reynolds number was found to have no effect on the reattachment length.

This effect of Reynolds number was investigated by running four numerical simulations that corresponds for four different  $Re$  numbers. At the end of each simulation, the reattachment length ( $X_r$ ) was determined by using the wall shear stress profile as mentioned above. Figure 3.18 shows the obtained value of  $X_r$  that correspond for each flow  $Re$  number. The latter was calculated based on the plate thickness  $e = 17$  mm.

The plotted results show that  $X_r$  decreases with increasing the  $Re$  number until  $Re = 2.36 \times 10^4$  at which  $X_r$  remains constant. This finding matches the conclusions reported in the literature.

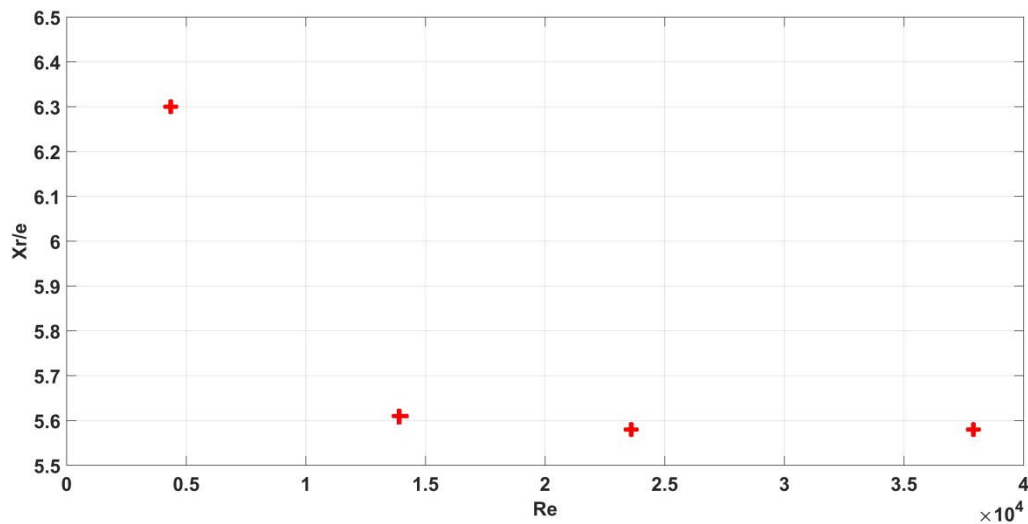


Figure 3.18 Effect of  $Re$  on the reattachment length ( $X_r$ )

#### 3.2.3.3.4.2 Effect of free stream turbulence intensity

According to several authors [19,20], properties of the separation bubble such as the reattachment length ( $X_r$ ) are correlated fairly well with the turbulence level in the working section. In fact, they reported that the length of the separation bubble reduces significantly with increasing turbulence intensity.

This finding was verified by the present numerical model. Indeed, seven numerical simulations have been performed by modifying the turbulence intensity ( $TI$ ) at the inlet (Table 3.3). For each numerical computation, the length of the separation bubble ( $X_r$ ) was determined. At the end, the evolution of  $X_r$  against the free stream turbulence intensities was plotted. The obtained correlation is shown in Figure 3.19.

This obtained correlation issued from the numerical simulations shows the reduction of  $X_r$  with increasing the turbulence level. Therefore, the numerical results match closely the conclusions reported by the previous studies.

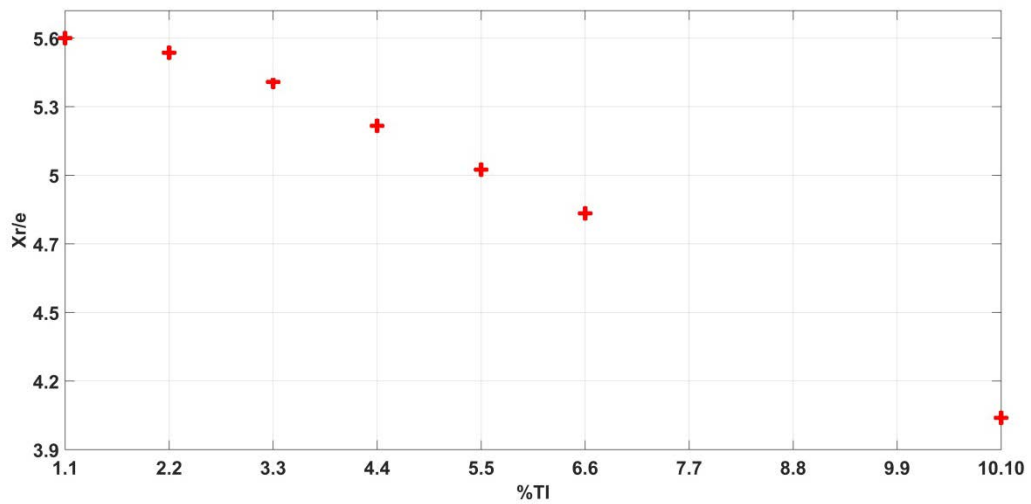


Figure 3.19 Effect of free stream turbulence intensity on  $Xr$

### 3.2.3.3.5 Nusselt distribution

Figure 3.20 shows the distribution of the dimensionless quantity  $Nu/Re^{2/3}$  over the upper surface of the mold.  $Nu$  and  $Re$  were calculated based on the half thickness of the plate ( $0.5e$ ). The obtained behavior of  $Nu/Re^{2/3}$ , which is proportional to the convective heat transfer coefficient ( $HTC$ ), shows a good agreement with that obtained by Ota *et al.* [30] (Figure 3.21).

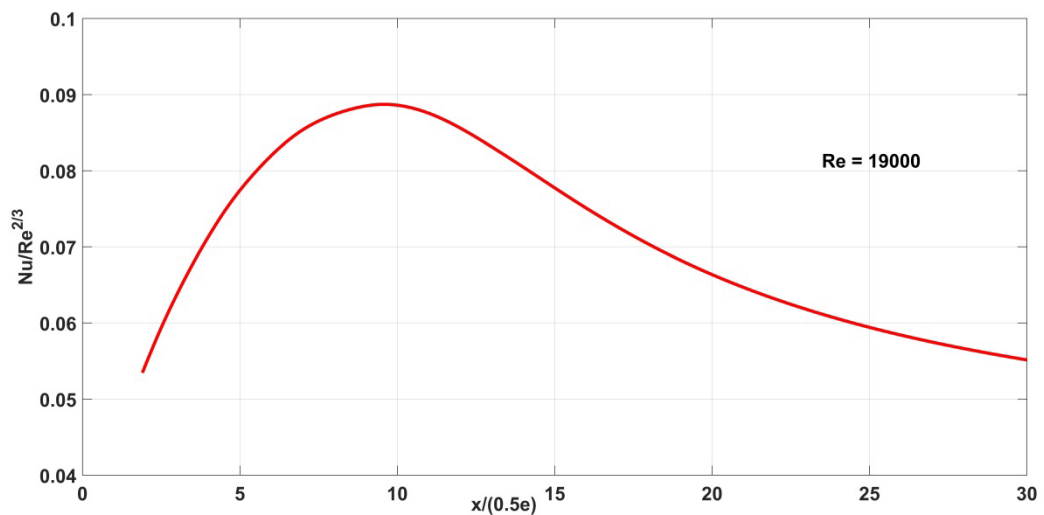


Figure 3.20 Local  $Nu$  distribution: CFD result

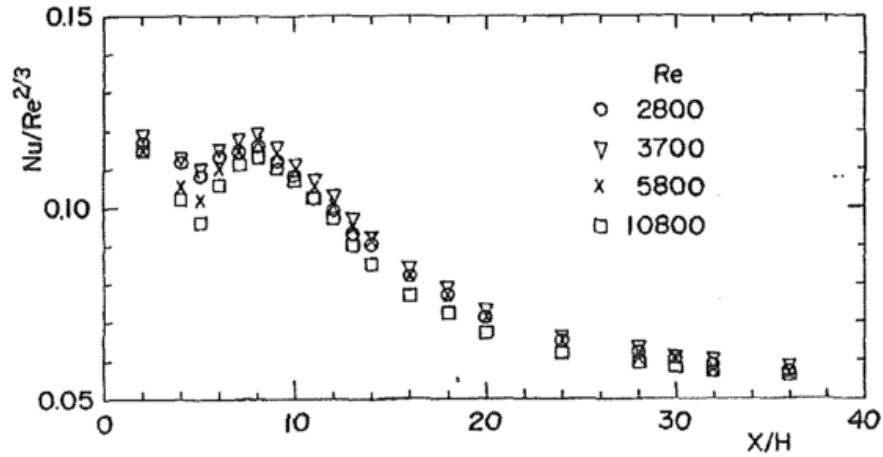


Figure 3.21 Local  $Nu$  number distribution: measurement of Ota *et al.* [30]

The obtained numerical result shows that  $HTC$  increases starting from the beginning of the “Mold 1” and reaches a maximum value at about  $x = 9.4 \times (0.5e) = 4.7e$ . Afterwards  $HTC$  decreases. This behavior correlates with the description of Sparrow *et al.* [31] who stated that  $HTC$  increases starting from the beginning of the plate and reaches a maximum value somewhere upstream of the reattachment point and after that  $HTC$  decreases. The reattachment point was found previously to be located at  $x = 5.58e$ . On the other hand, Ota *et al.* [30] mentioned that the heat transfer coefficient becomes maximum at the reattachment point. The latter occurs at about four plate thicknesses downstream from the leading edge according to the authors (Figure 3.21). They stated also that the dimensionless quantity  $Nu/Re^{2/3}$  is independent of the Reynolds number which ranged from 2720 to 17900 in their investigation, and is a function of only the distance from the leading edge. This finding was not encountered with the obtained numerical result performed at  $Re = 19\,000$ .

Furthermore, Ota *et al.* [32] worked on a universal correlation formula for the estimation of the maximum turbulent heat transfer coefficient in the reattachment flow region around bluff bodies (Equation (3.12)), in particular, in the case of a blunt flat plate. The reattachment length ( $Xr$ ) was employed as the reference length.

$$Nu_{max} = \frac{HTC_{max} \cdot Xr}{\lambda} = 0.0919 \left( \frac{U_{\infty} \cdot Xr}{\nu} \right)^{0.734} \quad \text{Equation (3.12)}$$

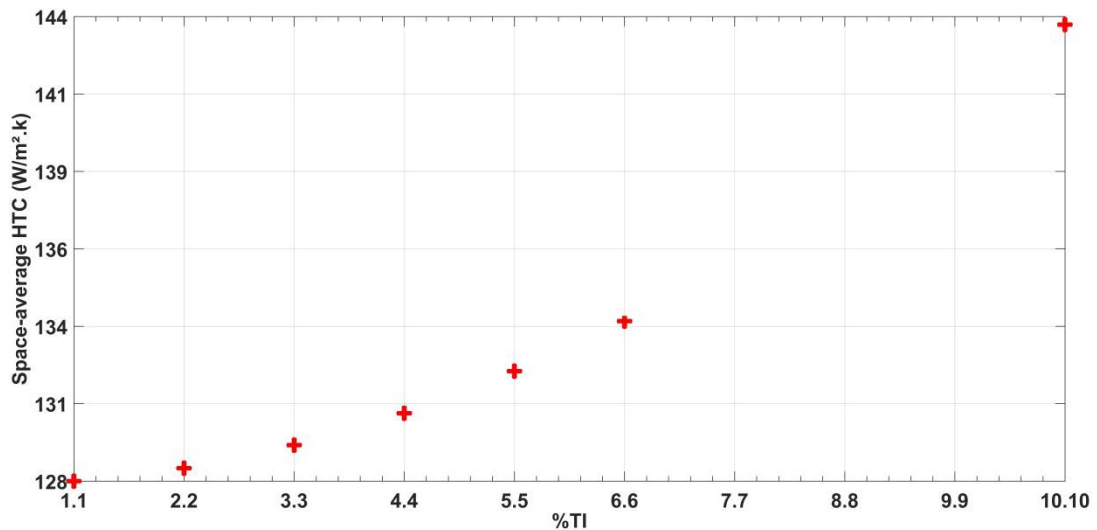
Table 3.7 shows the maximum turbulent heat transfer coefficient obtained from the numerical model and that calculated according to the above correlation. The comparison between the two values show a small error percentage, and thus the calculated  $HTC$  values show a good agreement with the proposed correlation.

Table 3.7 Calculation of the maximum  $HTC$ 

	CFD	Correlation	Deviation
$HTC_{max}$	190	204	7 %

Kondjoyan *et al.*[21] reported that free stream turbulence levels lead to an increase in the heat transfer coefficient. This conclusion has been verified by carrying out several numerical simulations with different free stream turbulence intensities at the inlet. For each simulation, the spatial average of  $HTC$  over the length of the mold was calculated. At the end, the obtained heat transfer coefficient values were plotted against the inlet free stream turbulence intensity. The obtained correlation between the heat transfer coefficient and the turbulence level is shown in Figure 3.22.

This obtained correlation matches the findings reported by previous research studies that increasing the turbulence levels within the test section leads to an increase in the heat transfer coefficients.

Figure 3.22 Effect of turbulence intensity on  $HTC$ : CFD result

### **3.3 Numerical model of the inter-part shadowing effects investigation**

The inter-part shadowing effects were investigated numerically by building the numerical model of the “Mold 2” shown previously in section 2.7.

As in the experimental work, the objectives of the numerical model of the inter-part shadowing study are to investigate, numerically, the flow field structure and  $HTC$  distribution around the “Mold 2” placed at the back within the working section.

#### **3.3.1 Geometry**

The computational domain of the “Mold 2” was created as the same manner as that for the “Mold 1”. Figure 3.23 shows the geometrical model of the “Mold 2” placed within the working section of the model autoclave and behind the “Mold 1”. The separation distance between the two plates is called “ $d$ ” and it was defined as a parameter. In the following example,  $d$  is fixed at 3.2 cm.

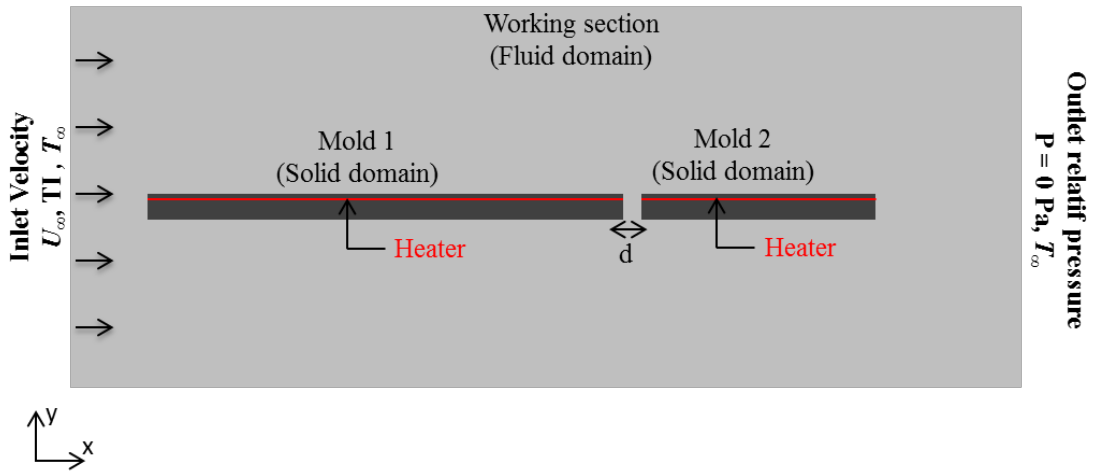


Figure 3.23 The computational domain for the inter-part shadowing study

#### **3.3.2 Governing equation and numerical method**

The various steps followed in this section, i.e. the choice of the turbulence model, the definition of the different materials, the setting up of the aerodynamic and thermal boundary conditions and the choice of the solver, are identical to those applied in the case of a single mold.

Concerning the mesh, it was constructed in the same manner as for the case of a single mold: the fluid domain was meshed with unstructured triangular grids and a structured square mesh was used for meshing the solid domains of the two molds as well as to create a finer mesh near the surface walls (Figure 3.24) such that  $y^+$  is



below unity. Table 3.8 mentions the quality of the constructed mesh according to the quality criteria defined previously (Orthogonal quality and Skewness).

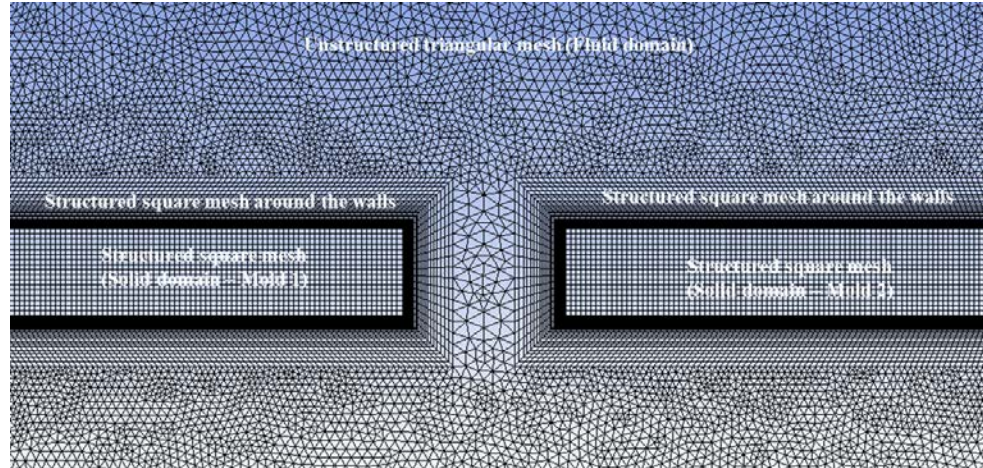


Figure 3.24 Zoom on the constructed mesh in the computational domain

Table 3.8 Quality of the constructed mesh

	Orthogonal quality		Skewness	
	Average	Standard deviation	Average	Standard deviation
<b>Constructed mesh</b>	0.93	$7.8 \times 10^{-2}$	0.14	0.15

### 3.3.3 Verification of the numerical model

Numerical simulations have been carried out, with arbitrary boundary conditions, in order to verify the convergence of the constructed numerical model. As for the case of a single model, the numerical model for the inter-part shadowing study has shown a numerical convergence of the investigated physical phenomena such as the velocity magnitude and the heat transfer coefficient in the computational domain. At the end of the calculations, the energy and the mass balance have been verified as well in the computational domain.

### 3.3.4 Numerical results and discussion

The obtained numerical results of the flow field and the convective heat transfer coefficients (*HTC*) around the “Mold 2” will be presented in *chapter 4* and compared to the experimental measurements for validation.



As mentioned before, the distance between the two molds ( $d$ ) was considered as a parameter. Therefore, it was interesting to investigate the impact of the distance  $d$  on the studied physical phenomena, in particular on the distribution of the convective heat transfer coefficients over the backward mold. This parametric study which consists of varying the distance  $d$  and the obtained results will be exposed and analyzed also in *chapter 4*.

### **3.4 Numerical model of the “representative mold”**

The velocity field and the distribution of the convective heat transfer coefficient around a mold equipped with obstacles were investigated numerically by building the numerical model of the “representative mold” shown previously in section 2.8.

#### **3.4.1 Geometry**

Numerically, the 2D geometrical model of the “representative mold” to be simulated within the working section of the model autoclave is shown in Figure 3.27.

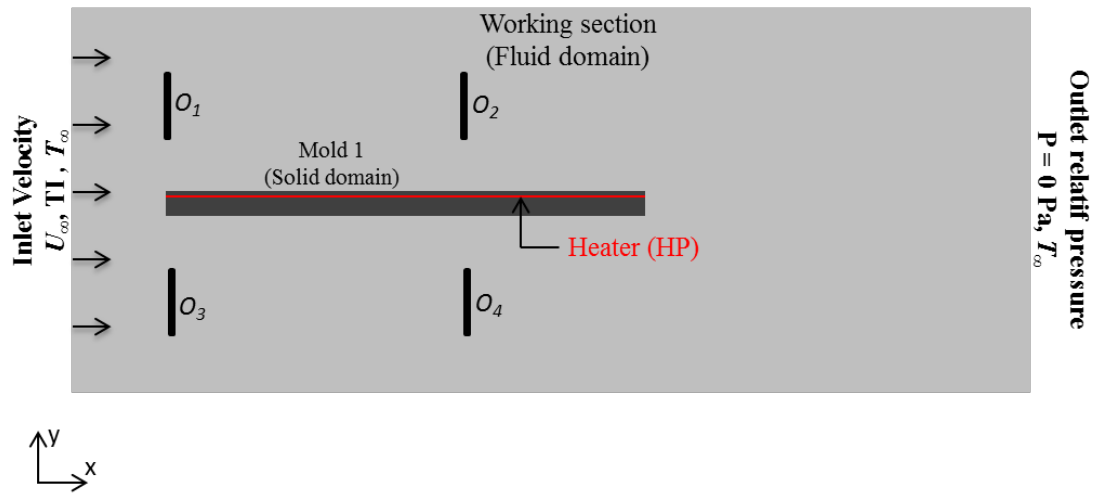


**Figure 3.25 The geometrical model of the “representative mold” installed within the working section**

The real geometrical dimensions of the “representative mold” as well as of the working section were respected in the numerical model as done before in sections 3.2 and 3.3. However, the geometrical models of the obstacles were simplified, as showed in Figure 3.27, in a manner to take into account just the significant elements that can affect the flow field. In addition, this geometrical simplification allows to reduce the time consuming of performed numerical calculations. The nomenclatures  $O_1$ ,  $O_2$ ,  $O_3$  and  $O_4$  are referred to the first, second, third and fourth obstacle respectively.

Table 3.9 gathers the parameters that control the positions and the geometrical dimensions of these obstacles. The definition of these parameters is illustrated in Figure 3.28 and presented as following:

- $VO_u$  is the vertical distance from the upper wall of the working section to the upper extremity of the obstacle.
- $VO_l$  is the vertical distance from the upper wall of the working section to the lower extremity of the obstacle.
- $dO_iO_j$  is the distance between two consecutive obstacles.

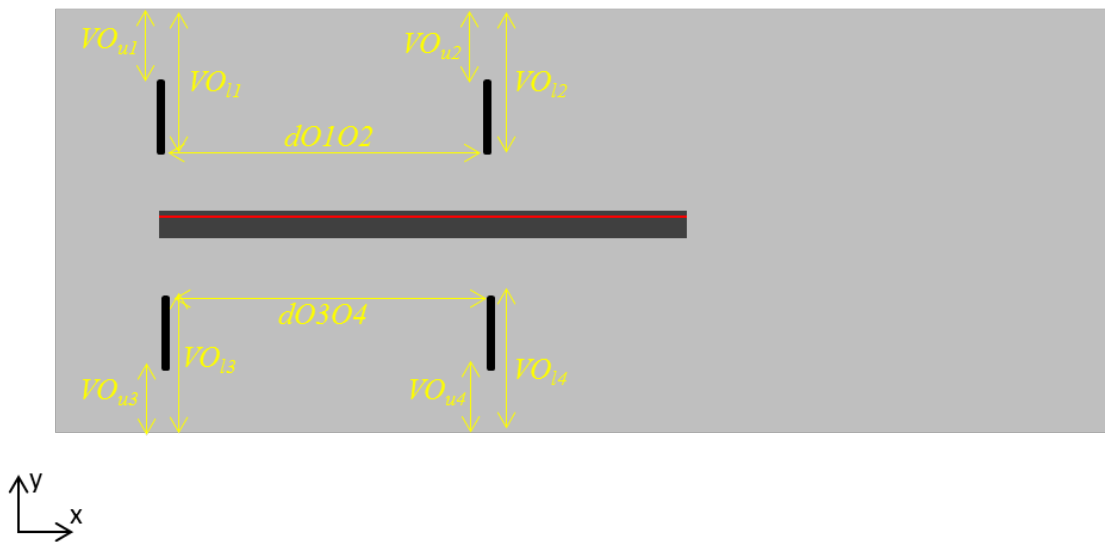


Figure 3.26 Definition of the geometric design parameters

Table 3.9 Assigned values for the geometric design parameters

Geometric parameter	Actual Value
$VO_{u2} = VO_{u3} = VO_{u4} = VO_{u1}$	0.085 m
$VO_{l2} = VO_{l3} = VO_{l4} = VO_{l1}$	0.15 m
$dO_3O_4 = dO_1O_2$	0.3 m

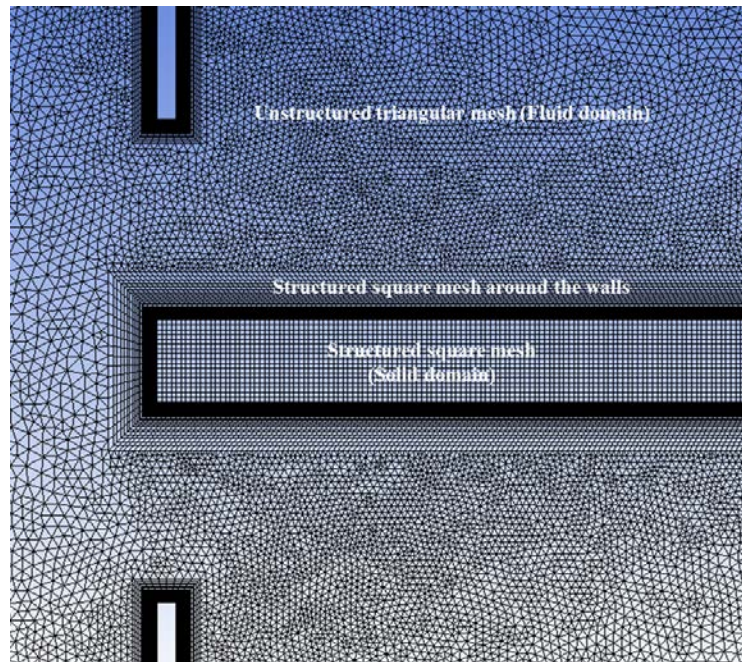
### 3.4.2 Governing equation and numerical method

The various steps followed in this section, i.e. the choice of the turbulence model, the definition of the different materials and the choice of the solver, are identical to those applied in the case of a single mold and two molds. Table 3.10 shows the setting up of the aerodynamic and thermal boundary conditions (Figure 3.27). They can be modified after according to the real experimental operating conditions.

**Table 3.10 Definition of the aerodynamic and thermal boundary condition**

Inlet			Outlet		Mold
$U_{\infty}$ (m/s)	$TI$ (%)	$T_{\infty}$ (K)	$P_{relative}$ (Pa)	$T_{\infty}$ (K)	$HP$ (W/m <sup>2</sup> )
33.7	1.1	300	0	300	2000

Concerning the mesh, it was constructed in the same manner as for the case of a single mold and two molds: the fluid domain was meshed with unstructured triangular grids and a structured square mesh was used for meshing the solid domains of the “Mold 1” as well as to create a finer mesh near the surface walls (Figure 3.29) such that  $y^+$  is below unity. Table 3.11 mentions the quality of the constructed mesh according to the quality criteria defined previously (Orthogonal quality and Skewness).

**Figure 3.27 Zoom on the constructed mesh in the computational domain**

**Table 3.11 Quality of the constructed mesh**

	Orthogonal quality		Skewness	
	Average	Standard deviation	Average	Standard deviation
	0.93	$8.1 \times 10^{-2}$	0.14	0.15
<b>Constructed mesh</b>				

### 3.4.3 Verification of the numerical model

The constructed numerical model has shown a numerical convergence of the investigated physical phenomena such as the velocity magnitude and the heat transfer coefficient in the computational domain as obtained previously for the other configuration studies. At the end of the calculations, the energy and the mass balance have been verified as well.

### 3.4.4 Numerical results and discussion

The obtained numerical results issued from the constructed numerical model will be presented in *chapter 4*.

### **3.5 Partial conclusion**

In this chapter, three different numerical models that represent different configurations studies have been realized using the CFD tool ANSYS FLUENT 16.0®. These numerical models allow the study of a single mold, two molds and a representative mold within the working section of the model autoclave. They were built in a manner to respect the actual dimensions and boundary conditions of the performed experimental works. The key features that can affect the convergence and the accuracy of the numerical computations, such as the mesh and the turbulence model, have been carefully selected. In fact, a finer structured mesh has been defined near the mold walls such that  $y^+$  is in the order of unity to suitable resolve the near wall region while using the SST  $k-\omega$  turbulence model. The obtained aerodynamic and thermal numerical results, mainly the structure of the separated-reattached flow region and the  $HTC$  distribution around a single mold, have been compared to previous researches findings. The comparison between the behaviors of the investigated physical phenomena has shown a good agreement, and thus the performed numerical simulations can be validated as a first step. The final validation will be presented in *chapter 4* while comparing the numerical results to the experimental ones.

## List of references

- [1] N.J. Smale, J. Moureh, G. Cortella, A review of numerical models of airflow in refrigerated food applications, *Int. J. Refrig.* 29 (2006) 911–930. doi:10.1016/j.ijrefrig.2006.03.019.
- [2] L. Jiao, Z. Yan-xuan, G. Pi-hai, G. Chang-tao, Numerical simulation and PIV experimental study of the effect of flow fields around tube artificial reefs, *Ocean Eng.* 134 (2017) 96–104. doi:10.1016/j.oceaneng.2017.02.016.
- [3] P. Singh, B.V. Ravi, S. V. Ekkad, Experimental and numerical study of heat transfer due to developing flow in a two-pass rib roughened square duct, *Int. J. Heat Mass Transf.* 102 (2016) 1245–1256. doi:10.1016/j.ijheatmasstransfer.2016.07.015.
- [4] H. Yanaoka, H. Yoshikawa, T. Ota, Numerical simulation of laminar flow and heat transfer over a blunt flat plate in square channel, *J. Heat Transfer.* 124 (2002) 8–16. doi:10.1115/1.1420715.
- [5] J. Wen, H. Yang, G. Jian, X. Tong, K. Li, S. Wang, Energy and cost optimization of shell and tube heat exchanger with helical baffles using Kriging metamodel based on MOGA, *Int. J. Heat Mass Transf.* 98 (2016) 29–39. doi:10.1016/j.ijheatmasstransfer.2016.02.084.
- [6] H.B. Nahor, M.L. Hoang, P. Verboven, M. Baelmans, B.M. Nicolai, CFD model of the airflow, heat and mass transfer in cool stores, *Int. J. Refrig.* 28 (2005) 368–380. doi:10.1016/j.ijrefrig.2004.08.014.
- [7] Z. Khatir, H. Thompson, N. Kapur, V. Toropov, J. Paton, Multi-objective Computational Fluid Dynamics (CFD) design optimisation in commercial bread-baking, *Appl. Therm. Eng.* 60 (2013) 480–486. doi:10.1016/j.applthermaleng.2012.08.011.
- [8] Ansys, Lecture 7: Turbulence modeling, (2015).
- [9] M.L. Hoang, P. Verboven, J. De Baerdemaeker, B.M. Nicolai, Analysis of the air flow in a cold store by means of computational fluid dynamics, *Int. J. Refrig.* 23 (2000) 127–140. doi:10.1016/S0140-7007(99)00043-2.
- [10] J. Moureh, D. Flick, Airflow pattern and temperature distribution in a typical refrigerated truck configuration loaded with pallets, *Int. J. Refrig.* 27 (2004) 464–474. doi:10.1016/j.ijrefrig.2004.03.003.
- [11] J. Moureh, D. Flick, Airflow characteristics within a slot-ventilated enclosure, *Int. J. Heat Fluid Flow.* 26 (2005) 12–24. doi:10.1016/j.ijheatfluidflow.2004.05.018.
- [12] A. Nady, M. Said, C.Y. Shaw, J.S. Zhang, Computation of room air distribution, *ASHRAE Trans. Symp.* 101 (1995) 1065–1077.
- [13] Q. Chen, Comparison of different k- $\epsilon$  models for indoor air flow computations, *Numer. Heat Transf. Part B.* (1995) 353–369.
- [14] D.C. Wilcox, *Turbulence Modeling for C.F.D.*, DCW Industries, Inc., La

- cañada, California, 1994.
- [15] F.R. Menter, Eddy viscosity transport equations and their relation to the k- $\epsilon$  model, *J. Fluids Engineering*. 119 (1997) 876–884.
  - [16] B.E. Launder, On the modeling of turbulent industrial flows, in: *Proc. Comput. Methods Appl. Sci.*, Elsevier, 1992: pp. 91–102.
  - [17] M. Nallasamy, Turbulence models and their applications to the prediction of internal flows - A review, 15 (1987) 151–194. doi:10.1016/S0045-7930(87)80003-8.
  - [18] The Engineering ToolBox, (n.d.). [https://www.engineeringtoolbox.com/air-properties-d\\_156.html](https://www.engineeringtoolbox.com/air-properties-d_156.html).
  - [19] M. Kiya, K. Sasaki, Free-stream turbulence effects on a separation bubble, *J. Wind Eng. Ind. Aerodyn.* 14 (1983) 373–386. doi:http://dx.doi.org/10.1016/0167-6105(83)90039-9.
  - [20] R. Hillier, N.. Cherry, The effects of stream turbulence on separation bubbles, *J. Wind Eng. Ind. Aerodyn.* 8 (1981) 49–58.
  - [21] A. Kondjoyan, F. Péneau, H.-C. Boisson, Effect of high free stream turbulence on heat transfer between plates and air flows: a review of existing experimental results, *Int. J. Therm. Sci.* 41 (2002) 1–16. doi:10.1016/S1290-0729(01)01299-6.
  - [22] H. Schlichting, *Boundary-Layer Theory*, 7th ed., New York, 1979.
  - [23] C. Zones, B. Conditions, *Introduction to ANSYS FLUENT*, (2010) 1–22.
  - [24] Lecture 5: Solver settings, 2015.
  - [25] N. Djilali, I.S. Gartshore, Turbulent flow around a bluff rectangular plate. Part I: experimental investigation, *J. Fluids Engineering*. 113 (1991) 51–59.
  - [26] T. Ota, A Survey of Heat Transfer in Separated and Reattached Flows, *Appl. Mech. Rev.* 53 (2000) 219–235. doi:10.1115/1.3097351.
  - [27] T. Ota, M. Itasaka, A separated and reattached flow on a blunt flat plate, *J. Fluids Eng.* 98 (1976) 79–86.
  - [28] M. Kiya, K. Sasaki, Structure of a turbulent separation, *J. Fluid Mech.* 137 (1983) 83–113.
  - [29] T. Ota, Y. Asano, J. Okawa, Reattachment length and transition of the separated flow over blunt flat plates, *Bull. JSME.* 24 (1981) 941–947.
  - [30] T. Ota, N. Kon, Heat transfer in the separated and reattached flow on a blunt flat plate, *J. Heat Transfer.* 96 (1974) 459–462.
  - [31] E.M. Sparrow, S.S. Kang, W. Chuck, Relation between the points of flow reattachment and maximum heat transfer for regions of flow separation, *Int. J. Heat Mass Transf.* 30 (1987) 1237–1246. doi:10.1016/0017-9310(87)90157-8.
  - [32] T. Ota, N. Kon, Heat transfer in the separated and reattached flow over blunt flat plates - Effects of nose shape, *Int. J. Heat Mass Transf.* 22 (1979) 197–206.



- [33] PCM INNOVATION, (n.d.). <https://www.pcminnovation.com/en/molds-for-composites/>.
- [34] T.W. Simpson, J.D. Peplinski, P.N. Koch, J.K. Allen, On the use of statistics in design and the implications for deterministic computer experiments, in: Proc. 1997 ASME Des. Eng. Tech. Conf., Sacramento, California, 1997: pp. 1–14.
- [35] G.G. Wang, S. Shan, Review of metamodeling techniques in support of engineering design optimization, *J. Mech. Des.* 129 (2006) 370–380. doi:10.1115/1.2429697.
- [36] J. Sacks, W. Welch, T. Mitchell, H. Wynn, Design and analysis of computer experiments, *Stat. Sci.* 4 (1989) 409–423. doi:10.2307/2245858.
- [37] R. Jin, W. Chen, T. Simpson, Comparative studies of metamodeling techniques under multiple modeling criteria, in: 8th Symp. Multidiscip. Anal. Optim., 2000: pp. 1–13. doi:10.2514/6.2000-4801.
- [38] A. Navid, S. Khalilarya, H. Taghavifar, Comparing multi-objective non-evolutionary NLPQL and evolutionary genetic algorithm optimization of a DI diesel engine: DoE estimation and creating surrogate model, *Energy Convers. Manag.* 126 (2016) 385–399. doi:10.1016/j.enconman.2016.08.014.
- [39] A.A. Giunta, L.T. Watson, A comparison of approximation modeling techniques: polynomial versus interpolating models, in: 7th AIAA/USAF/NASA/ISSMO Symp. Multidiscip. Anal. Optim., 1998: pp. 1–13. doi:10.2514/6.1998-4758.
- [40] J.R. Koehler, A.B. Owen, Computer Experiments, in: *Handb. Stat.*, Elsevier Science, New York, 1996: pp. 261–308.
- [41] N.A.C. Cressie, *Statistics for Spatial Data*, Wiley & Sons, New York, 1993.
- [42] N. Hu, P. Zhou, J. Yang, Comparison and combination of NLPQL and MOGA algorithms for a marine medium-speed diesel engine optimisation, *Energy Convers. Manag.* 133 (2017) 138–152. doi:10.1016/j.enconman.2016.11.066.
- [43] T. Okabe, Y. Oya, G. Yamamoto, J. Sato, T. Matsumiya, R. Matsuzaki, S. Yashiro, S. Obayashi, Multi-objective optimization for resin transfer molding process, *Compos. Part A.* 92 (2017) 1–9. doi:10.1016/j.composesa.2016.09.023.



*Chapter 4*  
*Flow Field Structure and  
Convective Heat Transfer  
Distribution around  
Molds*



## Table of contents

<i>Chapter 4 Flow Field Structure and Convective Heat Transfer Distribution around Molds .....</i>	<i>149</i>
<b>4.1 STUDY OF ONE MODEL MOLD.....</b>	<b>153</b>
4.1.1 Study of the flow field .....	153
4.1.1.1 Procedure of the study .....	153
4.1.1.2 Results of the flow field.....	154
4.1.2 Study of the convective heat transfer coefficient.....	160
4.1.2.1 Procedure of the study .....	161
4.1.2.2 Thermal results .....	163
4.1.2.2.1 Infrared thermography .....	163
4.1.2.2.2 Thermocouples acquisition .....	169
4.1.2.2.3 Determination of the convective heat transfer distribution ( $\phi_{cx}$ ) .....	170
4.1.2.2.4 Determination of the $HTC$ distribution .....	171
4.1.3 Summary of the results .....	174
<b>4.2 STUDY OF THE INTER-PART SHADOWING PHENOMENON .....</b>	<b>176</b>
4.2.1 Study of the flow field .....	177
4.2.1.1 Procedure of the study .....	177
4.2.1.2 Results of the flow field.....	178
4.2.2 Study of the convective heat transfer coefficient.....	184
4.2.2.1 Procedure of the study .....	184
4.2.2.2 Thermal results .....	184
4.2.2.2.1 Infrared thermography .....	184
4.2.2.2.2 Determination of the $HTC$ distribution .....	186
4.2.3 Summary of the results .....	187
4.2.4 Parametric study of $d$ .....	189
<b>4.3 STUDY OF THE “REPRESENTATIVE MOLD” .....</b>	<b>193</b>
4.3.1 Study of the flow field .....	193
4.3.2 Study of the convective heat transfer coefficient.....	195
4.3.3 Parametric study and optimization.....	195
4.3.3.1 Creation of the experimental design (DOE) .....	197
4.3.3.1.1 Design variables.....	197
4.3.3.1.2 Choice of the type of the design space.....	198
4.3.3.1.3 Objectives functions .....	199
4.3.3.1.4 Summary.....	199
4.3.3.2 Surrogate model.....	199
4.3.3.3 Optimization study .....	203
<b>4.4 PARTIAL CONCLUSION .....</b>	<b>209</b>
<b>LIST OF REFERENCES.....</b>	<b>210</b>



## **4.1 Study of one model mold**

The validation work of the model autoclave performed in *Chapter 2* enables to move to the next step of interest which is the installation of a model mold within the working section for performing experimental measurements.

As explained previously, these experimental measurements consist of investigating the local flow field structure and the *HTC* distribution around the mold using the PIV technique and the developed thermal measurement methodology explained in *Chapter 2*.

### **4.1.1 Study of the flow field**

#### **4.1.1.1 Procedure of the study**

The constructed model mold called “Mold 1”, shown in section 2.6, was installed within the working section of the model autoclave.

The installation of the mold creates normally pressure drop within the test section. Given this fact, PIV measurements of the velocity field have been performed near the inlet for the motor frequency of interest  $f = 80$  Hz. These PIV measurements have been carried out as the same manner as those performed for the validation works. The obtained flow characteristics, for  $f = 80$  Hz, were 32 m/s and 1.1% for the free stream velocity and turbulence intensity respectively against 33.7 m/s and 1.1% in the case of an empty working section. The corresponding volume flow rate was  $Q = 14\,500$  m<sup>3</sup>/h. It should be noticed that the obtained free stream velocity, i.e.  $U_{\infty} = 32$  m/s, results in a Reynolds number of  $1 \times 10^6$ , based on the mold length, and that respects also the dynamic similarity condition.

For investigating the velocity field around the mold, the laser of the PIV system was installed above the upper wall of the working section. The emitted laser sheet was generated in a manner to be normal to the upper surface of the mold near the center region, and thus it is located in the (xy) plane (Figure 4.1). This laser position enables the measurement of two components of the velocity field,  $u$  and  $v$ . The camera was installed in front of the laser sheet with a distance of 54 cm from the side wall of the working section (Figure 4.1). It was calibrated in a manner to capture the leading edge of the “Mold 1”. The size of the obtained image is  $18.8 \times 18.8$  cm<sup>2</sup>.

Then, tracer particles were seeded in the flow and it took few minutes to obtain a homogeneous density distribution of the tracer particles within the working section in a steady-state regime. The time delay between the illumination pulses was defined at 10  $\mu$ s according to the volume flow rate and the spatial resolution of the images. The

power supplier for the heater inserted inside the mold was not on and thus the aerodynamic measurements were performed in isothermal regime.

Thereafter, the PIV acquisition of 2 232 double-frame images was performed in the illuminated investigated spot (Figure 4.1). More details about the generated data and the Matlab post-processing of the results have been explained previously in section 2.4.4.

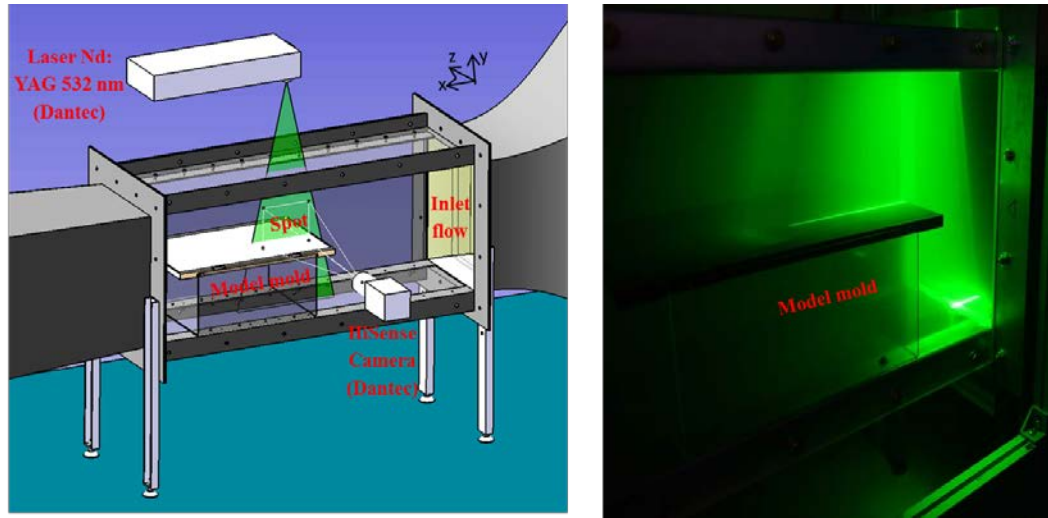


Figure 4.1 PIV measurements in the (xy) plane of the velocity field around the model mold

#### 4.1.1.2 Results of the flow field

Figure 4.2 and Figure 4.3 show the time-averaged velocity magnitude linked to the mean streamlines of the flow field around the leading edge of the “Mold 1”. These fields were obtained thanks to the performed PIV measurements and the numerical computations respectively and post-treated using the Matlab routines.

It should be noticed that the numerical simulations have been carried out according to the operating experimental conditions: the flow characteristics at the inlet were defined as boundary conditions and the calculations were made in isothermal regime. The other numerical options such as the choice of the turbulence model, the mesh, the solver, etc. have been carefully explained in *chapter 3*.

The time-averaged velocity magnitude ( $VM$ ) was calculated according to the formula shown in the Equation 4.1.

$$VM(x, y) = \sqrt{U(x, y)^2 + V(x, y)^2} \quad \text{Equation (4.1)}$$

The reference point ( $x/e=0$ ,  $y/e=0$ ) corresponds to the leading edge corner of the mold where  $e$  is the thickness of the plate (17 mm).

The obtained time-averaged velocity streamlines show the appearance of a separation bubble or a separated-reattached flow region over the leading edge of the mold. The separated shear layer occurred from the beginning of the mold ( $x/e=0$ ) and reattached at some location ( $x/e$ ) between 5 and 6. This distance represents in fact the time-averaged reattachment length ( $X_r$ ) of the separated-reattaching flow region. This flow field structure is consistent with the air flow description on a blunt flat plate provided by the previous research studies exposed in section 1.4, and illustrates by an example shown in Figure 4.4.

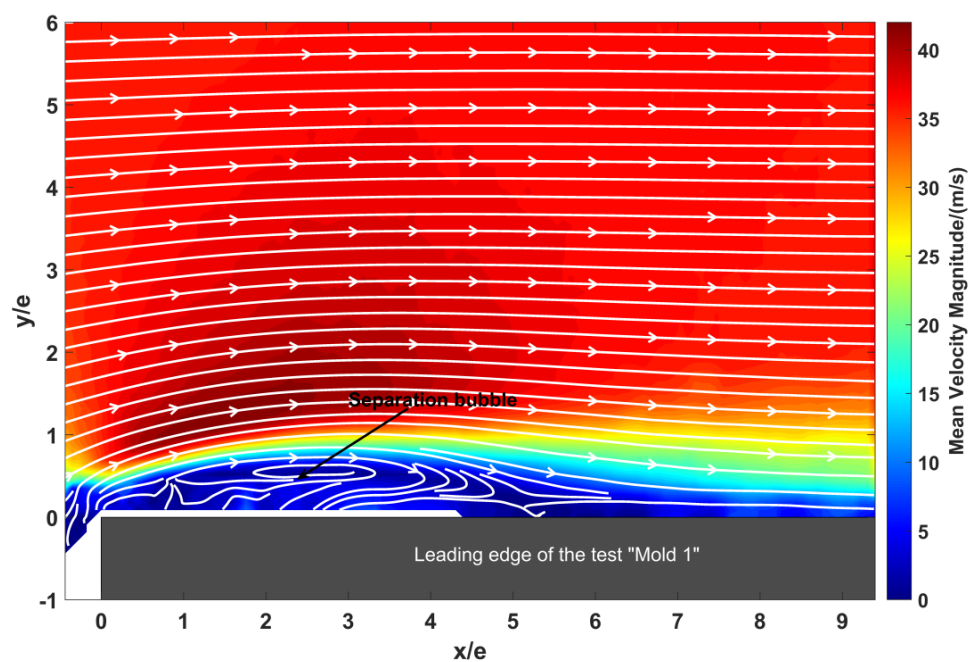


**Figure 4.2** Contour of the time-averaged velocity magnitude + time-averaged velocity streamlines: PIV result

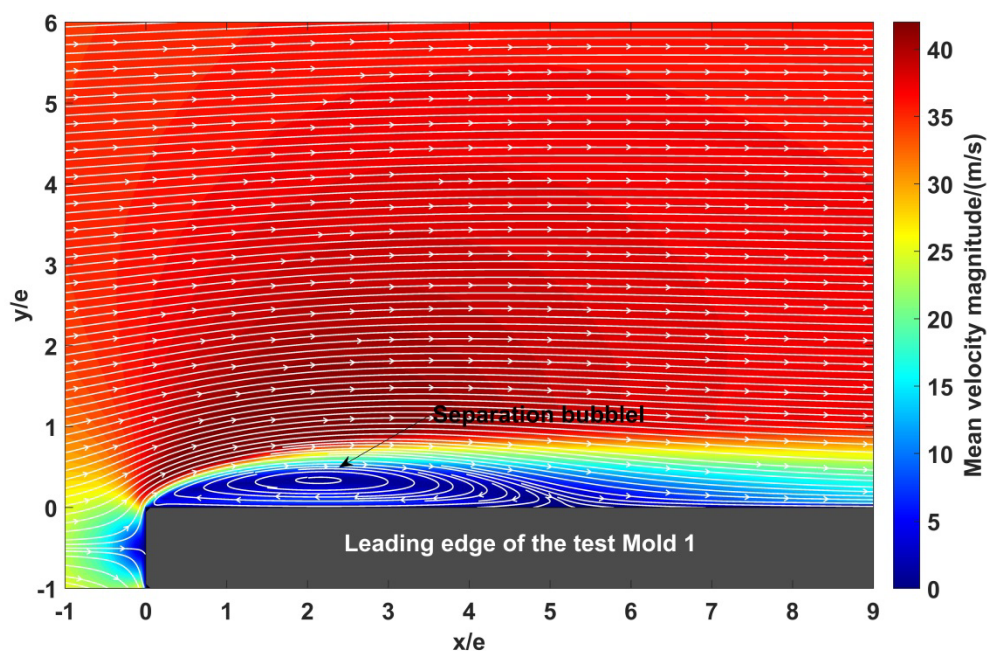


Figure 4.3 Contour of the velocity magnitude + velocity streamlines: CFD result

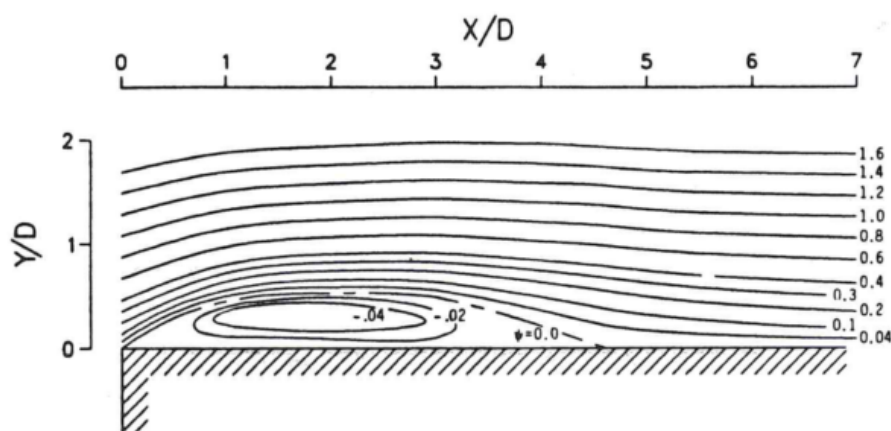
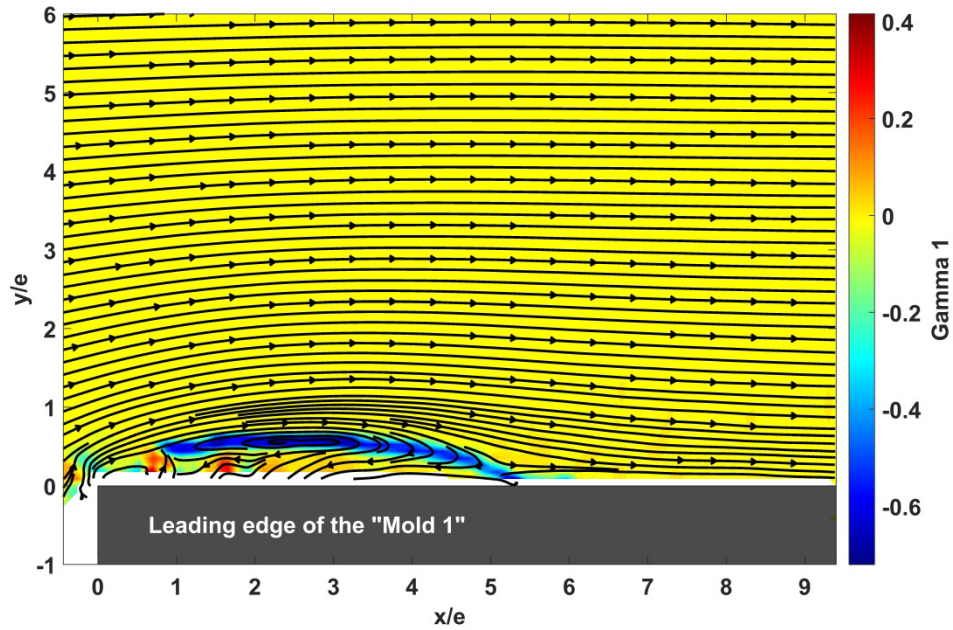


Figure 4.4 Mean streamlines obtained by the measurement of Djilali et al. [1]

This separation bubble was identified also by using a vortex identification algorithm developed by Graftieaux *et al.* [2] and which allows the calculation of gamma 1 ( $\Gamma_1$ ). The field of  $\Gamma_1$  is shown in Figure 4.5.





**Figure 4.5 Contour of  $\Gamma_1$ : PIV result**

The applied algorithm succeeds also to detect the recirculation region or the separation bubble over the leading edge of the mold, from  $x/e = 0$  and until some location ( $x/e$ ) between 5 and 6. This separated-reattached flow region can be detected by observing the important values of  $\Gamma_1$  field.

Further, the profiles of the normalized mean and fluctuating longitudinal velocity profiles,  $U/U_\infty$  and  $u_{rms}/U_\infty$  respectively, were plotted in the boundary layer developed around the "Mold 1" for different dimensionless  $x$ -positions ( $x/e$ ) (Figure 4.6 and Figure 4.7). The experimental profiles derived from the PIV measurements (rounds) were plotted against the numerical ones issued from the numerical model exposed in *chapter 3*.

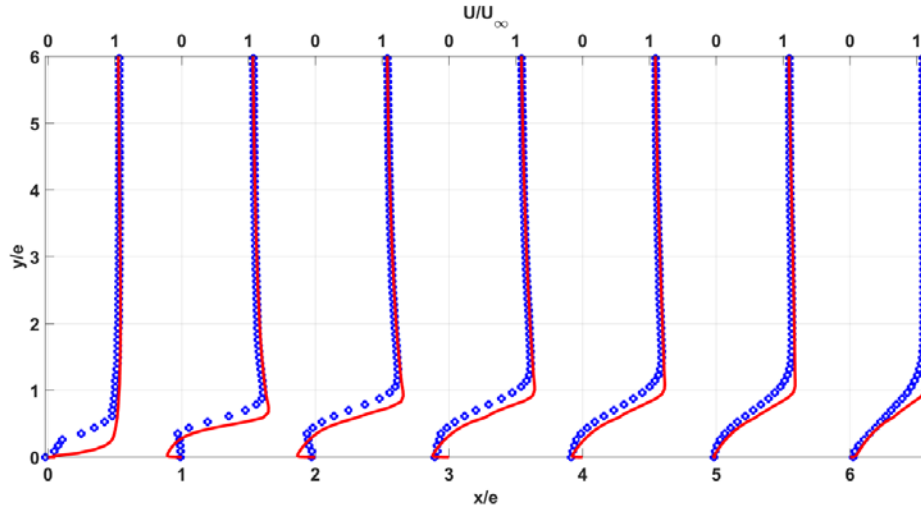


Figure 4.6 Mean longitudinal velocity profiles  $U$ :  $\circ$ , PIV;  $—$ , CFD

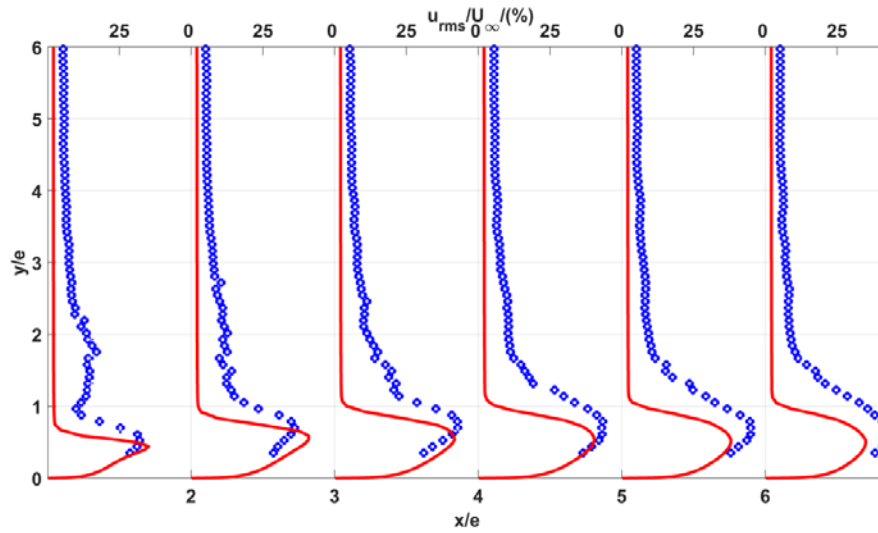


Figure 4.7 Fluctuating (r.m.s) longitudinal velocity profiles  $u_{rms}$ :  $\circ$ , PIV;  $—$ , CFD

The experimental profiles of mean velocities plotted in Figure 4.6 show again that at the beginning of the mold, i.e.  $x/e = 0$ , and until a distance  $x/e$  between 5 and 6, the normalized  $x$ -velocities ( $U/U_\infty$ ) near the wall present negative values. The presence of such inflexions points in these profiles indicates the existence of backflow velocities and thus the appearance of the separated-reattached flow region.

On the other hand, the profiles of the turbulence intensities (Figure 4.7) show the presence of significant values near the wall region which reach over 25%. However, the turbulence intensities decay fairly rapidly in the outer region of the shear layer. The presence of such high turbulence intensities indicates again the formation of separation bubbles over the leading edge of the mold [3].

It should be noted that the PIV turbulence intensity values near the wall have shown a non-statistical convergence and therefore they were not taken into consideration. This can be due to the fact that the accuracy of the PIV measurements near the wall is difficult to maintain. This difficulty arises from problems of laser reflection on the wall which can affect the quality of the recorded images and thus the accuracy of the analyzed velocity data.

The time-averaged reattachment line, founded previously between  $x/e = 5$  and  $x/e = 6$ , is defined more precisely as the location where the time-averaged wall shear stress ( $\overline{\tau_w}$ ) over the length of a plate vanishes [1]. Experimentally, it was found that the PIV system is unable to measure accurately the velocities at the wall surfaces and thus to measure the wall shear stresses. Such measures require the use of a micro-PIV system. Given this fact, it was decided to determine the location of the reattachment length ( $X_r$ ) by determining the longitudinal position of the point where the velocities, near the mold surface, pass from negative to positive values indicating then the vanishing of the separation bubble. Figure 4.8 shows the profile of the normalized  $x$ -velocities ( $U/U_\infty$ ) over the length of the mold surface and obtained from the nearest position ( $y/e$ ) to the wall:  $y/e = 0.09$ . From the plotted profile, it can be observed that the transition from negative to positive values occurs at  $x/e=5.2$  which represents in fact the position of the time-averaged reattachment line. Therefore, the reattachment length ( $X_r$ ) is located at  $x = 5.2e = 88.4$  mm according to the PIV measurements and for  $Re = 3.6 \times 10^4$  based on the plate thickness.

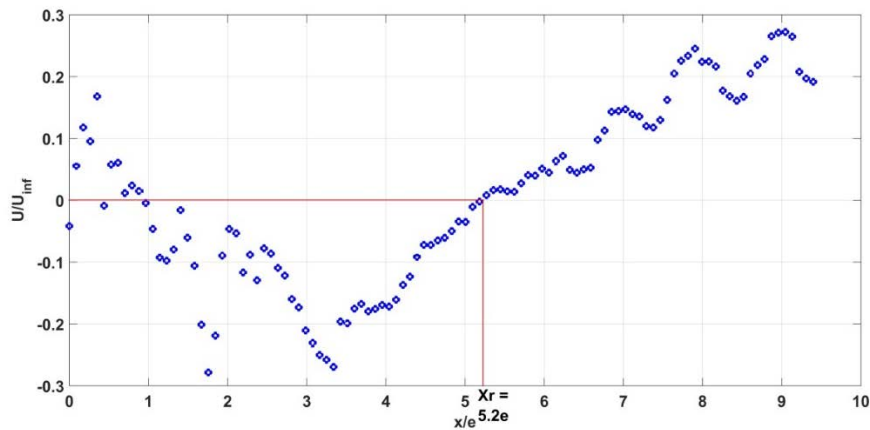


**Figure 4.8 Mean longitudinal velocity near the mold surface: PIV results**

Numerically, the reattachment length ( $X_r$ ) was determined by plotting the profile of the wall shear stress over the mold surface (Figure 4.9). It was found that  $\overline{\tau_w}$  vanishes at  $x/e=5.6$ . Thus, the reattachment length ( $X_r$ ) is located at  $x = 5.6e = 95.2$  mm according to the numerical simulation.

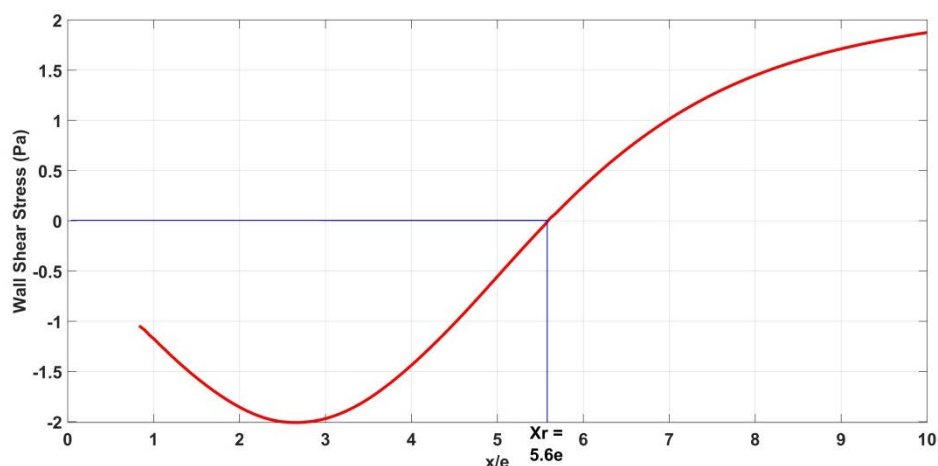


**Figure 4.9 Distribution of wall shear stress coefficients: CFD results**

The velocity field results derived from the numerical simulation show a quite good agreement with the PIV measurements, especially concerning the appearance of the separated-reattached flow region characterized by a reattachment length ( $X_r$ ), as well as the behaviors of the velocity profiles within the boundary layer. More precisely, the numerical model has succeeded to predict the value of  $X_r$  with a percentage deviation of 8% against the experimental one. Therefore, it can be deduced that the performed numerical simulations of the turbulent flow field around the rectangular box mold are validated thanks to the experimental measurements.

Despite this agreement in behaviors between the numerical and the experimental profiles, it should be noticed that the experimental free stream turbulence levels, shown in Figure 4.7, do not match the numerical ones and small discrepancies occur. This discrepancy could be explained as following: the numerical free stream turbulence intensities were obtained according to the defined inlet turbulence level. The latter was obtained in turn by the validation work results shown in Table 2.11 and which were issued from PIV acquisition images at 30 cm far from the side wall of the working section. On the other hand, the velocity profiles, shown in Figure 4.6 and Figure 4.7, were issued from PIV measurements where the camera was located 54 cm far from the side wall. Thus, this discrepancy may be due to the fact that moving away the camera from the investigated spot could reduce the signals captured by the camera sensors and emitted by the particles leading then to PIV errors [4].

### 4.1.2 Study of the convective heat transfer coefficient

The next step, after the investigation of the flow field structure around the model mold, was the study of the convective heat transfer coefficient ( $HTC$ ) distribution.

#### 4.1.2.1 Procedure of the study

The experimental procedure adopted for the measurement of the local *HTC* was carefully presented and explained in section 2.6.3.

However, for the thermal study, it was decided to replace the “Mold 1”, used above for the aerodynamics measurements, by the second mold called “Mold 2” presented in section 2.7. “Mold 2” was used instead of the “Mold 1” as it is shorter and thus an infrared thermography of the total length of the “Mold 2” can be performed. This decision was justified as well by the fact that the “Mold 1” and the “Mold 2” are both rectangular boxes sufficiently long ( $l_{Mold\ 1} > l_{Mold\ 2} \gg X_r$ ) and with identical thickness ( $e$ ). Therefore it was assumed that the flow field behavior and the *HTC* distribution over the two molds are identical.

The structure and the geometry of the “Mold 2” are shown in Figure 4.9.

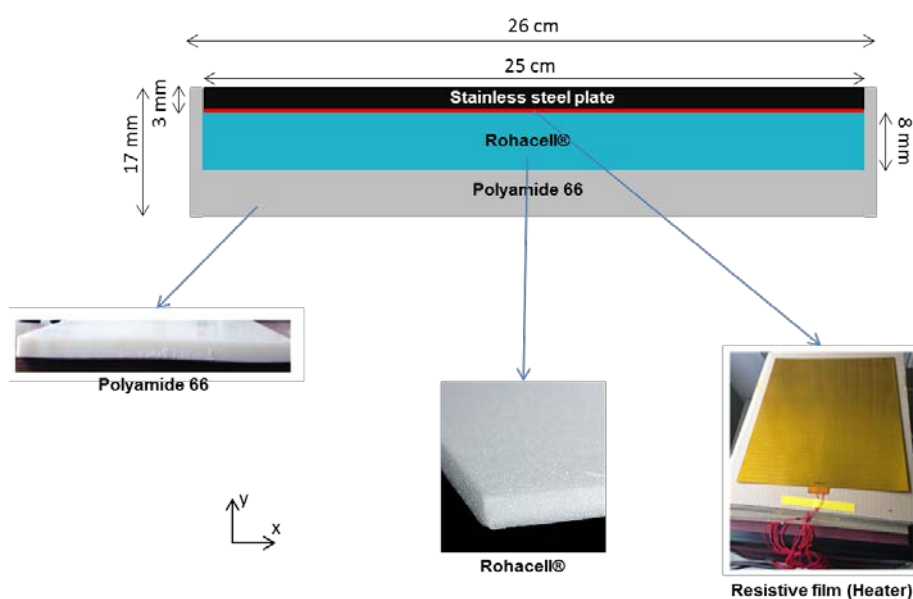


**Figure 4.10 Structure of the “Mold 2”**

Figure 4.11 shows the instrumentation of the “Mold 2” by the thermocouples according to the adopted methodology.

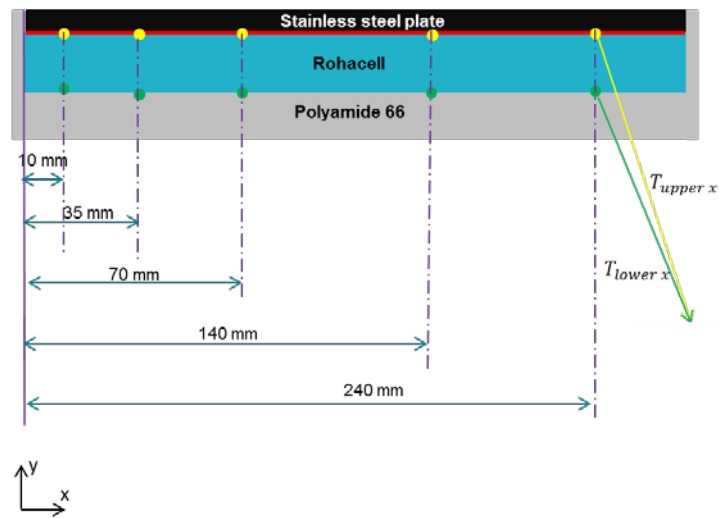


**Figure 4.11 Installation of the 10 thermocouples within the “Mold 2”**

In fact, “Mold 2” is equipped with ten thermocouples: five thermocouples at the upper surface of the Rohacell foam plate and five thermocouples at the lower surface. The positions of these thermocouples (Figure 4.11) were chosen in a manner to measure accurately the global behavior of the *HTC* distribution around the mold surface, especially over the leading edge where a separated-reattached flow region was found to occur.

The “Mold 2” was then installed within the working section of the model autoclave and below the calibrated infrared camera (Figure 4.12).

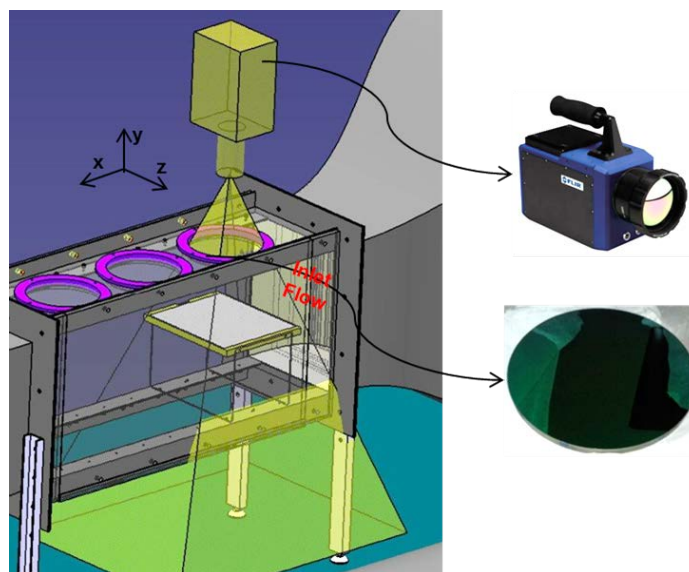


**Figure 4.12 Principle of infrared camera measurements**

Mold 2 was heated by applying a heating power ( $HP$ ) to the film resistive heater using an electrical power supply.  $HP$  was defined at  $1800 \text{ W/m}^2$ . On the other hand, the regulating valve of the cooling heat exchanger was turned on, and the desired air temperature was fixed at  $23^\circ\text{C}$  thanks to the PID regulator. Simultaneously, the mold was cooled by the air that flows at  $Q = 14\,500 \text{ m}^3/\text{h}$ .

Then thermal acquisitions of the temperatures, provided by the thermocouples and the infrared camera, were carried out. As mentioned previously, the thermal study is performed in the steady-state regime. The obtaining of the steady-state regime during the experiment was verified, for example, by visualizing the temperatures evolution of the thermocouples inserted within the “Mold 2”.

#### 4.1.2.2 Thermal results

##### 4.1.2.2.1 Infrared thermography

Figure 4.13 shows the contour of the time-averaged temperature field of the upper surface of the “Mold 2” measured by the infrared imaging camera. These measurements were performed in the  $(xz)$  plane (Figure 4.12). The obtained temperature field is issued based on the average of 300 thermal images, recorded in the steady state regime. The reference point ( $x/e=0, z/e=0$ ) corresponds to the middle of the leading edge of the “Mold 2”. The circular appearance of the obtained temperature field is due to the use of the circular optical silicon window.

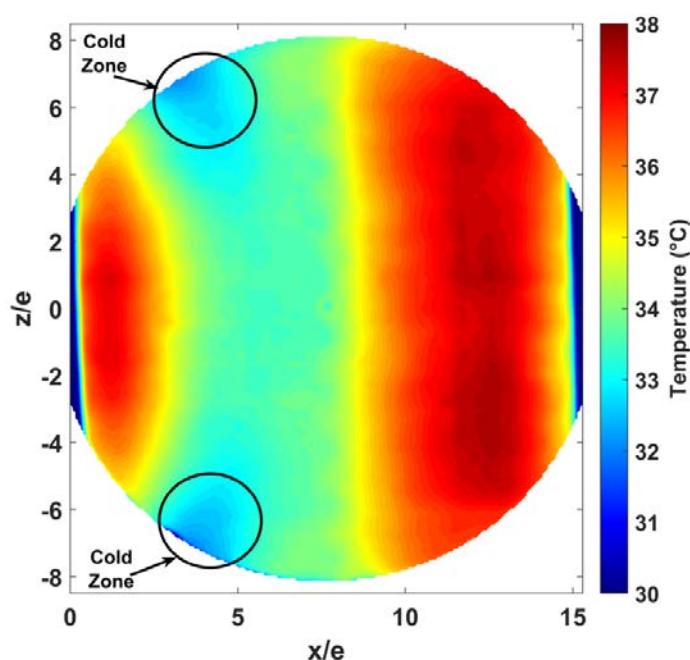


Figure 4.13 Contour of the time-averaged temperature field of the upper surface of the heated “Mold 2”



#### 4.1.2.2.1.1 Study of the side wall effects

The obtained contour of the temperature field shows a one-dimensional (1D) temperature field that depends mainly on the longitudinal position ( $x/e$ ) near the center region of the plate. That indicates that the convective heat transfers are one dimensional in the surrounding of the center region.

However, near the side walls of the plate at the longitudinal position  $x/e = 4$ , two “Cold Zones” appear, in which the temperatures are remarkably lower than those near the center region for the same longitudinal position (Figure 4.13). This observation indicates that the temperature field and thus the convective heat transfers have shown to be two-dimensional (2D) near the side walls of the mold.

The appearance of these “Cold Zones” can be explained by the side wall effects reported by the authors Yanaoka *et al.* [5] and explained in section 1.3. Indeed, and according to the authors, the side wall effects are explained by the presence of horseshoe-vortices formed near the side walls of a flat blunt plate (Figure 4.14). These horseshoe-vortices cause an increase of the streamwise velocity and also the transverse one near the side walls resulting then in the presence of a curved reattachment line of the reattachment region.

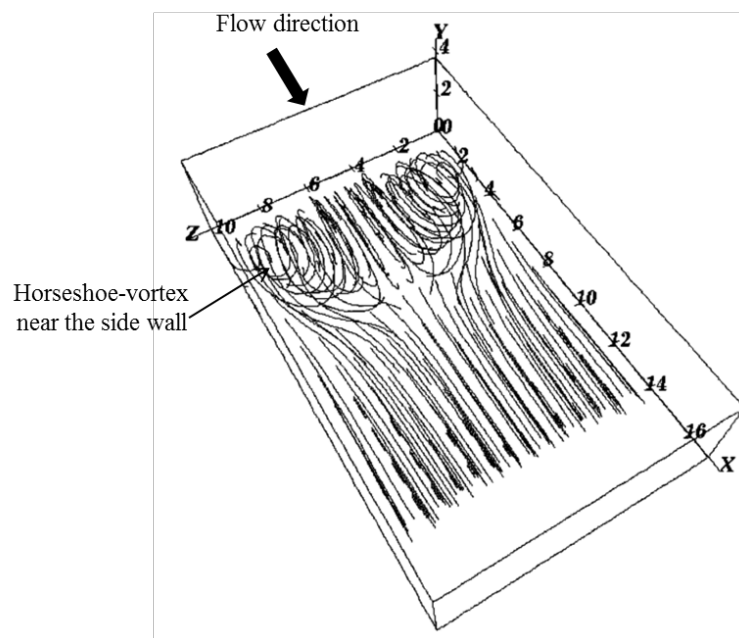


Figure 4.14 Mean velocity streamlines over a bluff blunt plate [5]

In addition, they stated that these horseshoe-vortices formed near the side walls have great effects upon the heat transfers in the redeveloping region. In fact, these flows bring a great increase of Nusselt number near the side walls than the center



region (Figure 4.15). However, they concluded that the recirculation region and the convective heat transfer remain two-dimensional and one-dimensional respectively in the center region (Figure 4.15).

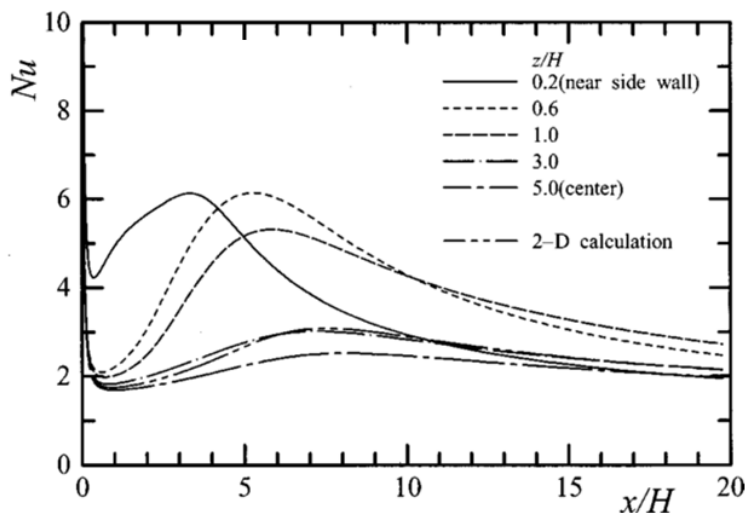
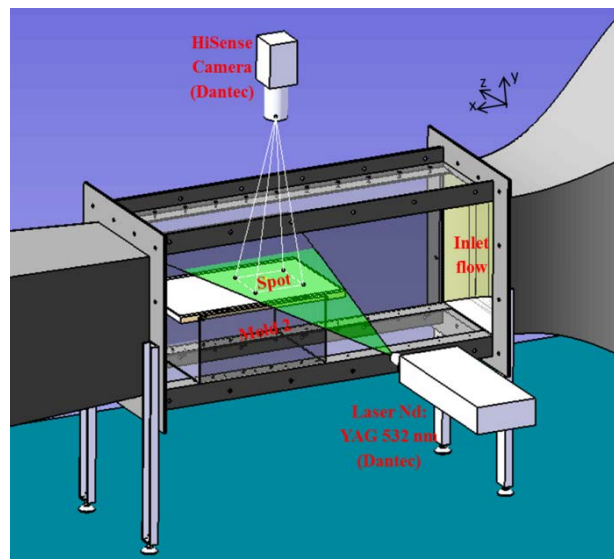


Figure 4.15 Nusselt number distribution [5]

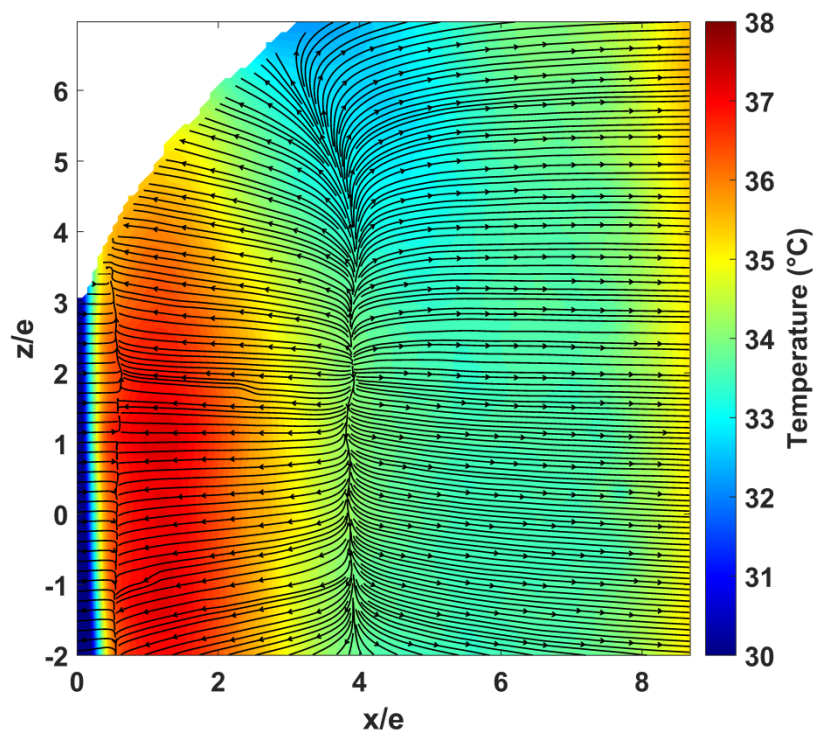
In order to verify this assumption, it was decided to investigate the flow field over the plate in a ( $xz$ ) plane.

This investigation has been performed using the PIV system. The laser was placed in front of the side wall of the working section in a manner that the emitted laser sheet is parallel to the upper surface of the “Mold 2” in the ( $xz$ ) plane (Figure 4.16). The laser sheet was at  $y/e = 0.3$  above the upper surface of the “Mold 2”. On the other hand, the camera was installed above the upper wall of the working section and calibrated in front of the upper surface of the “Mold 2”. The investigated illuminated spot was located between  $x/e=0$  and  $x/e=9$ , and between  $z/e= -2$  and  $z/e=7$  according to the defined coordinate system of the upper surface (Figure 4.13). The size of the obtained image is  $(14.88 \times 14.88)$  cm<sup>2</sup>.



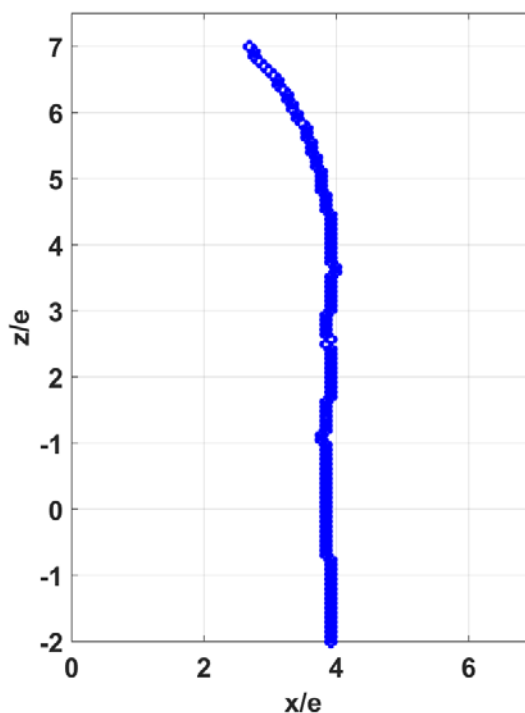
**Figure 4.16** PIV measurements in a  $(xz)$  plane of the velocity field around the “Mold 2”

Figure 4.17 shows the obtained time-averaged velocity streamlines based on the velocity components  $U$  and  $W$ . These velocities were derived from the PIV measurements. These streamlines were linked with the obtained time-averaged temperature field of the upper surface of the “Mold 2” in the investigated spot.



**Figure 4.17** Time-averaged velocity streamlines + Contour of the time-averaged temperature field

The observation of the change in the direction of the velocity streamlines allow to deduce the separation line of the recirculation region. It was located at  $x/e = 4$ . This reattachment line was determined by detecting, for each position  $z/e$ , the position  $x/e$  of the inflexion point where the velocity ( $U$ ) changes from a negative to a positive value. The obtained separation line of the recirculation region is plotted in Figure 4.18 and which corresponds to the intersection between the investigated ( $xz$ ) planar spot with the separation bubble, it means for  $y/e = 0.3$ .



**Figure 4.18 The curved reattachment line of the recirculation region**

The examination of the obtained reattachment line indicates that the latter is constant until  $z/e = 4.5$  from which it becomes curved. Then, the curved behavior of the reattachment line was located near the side wall and it matches closely the position of the “Cold Zones” where temperatures were remarkably lower (Figure 4.13 and Figure 4.17).

Therefore, it can be concluded that the appearance of such curved reattachment line is due to the presence of horseshoe-vortices near the side walls according to the side wall effects phenomenon description presented previously.

It can be deduced also, based on the aerodynamic and thermal results plotted in Figure 4.17, that the flow field is two-dimensional (2D), i.e. it depends on ( $x$ ) and ( $y$ ), and that the convective heat transfers are (1D), i.e. it depends on ( $x$ ) near the center

region of the mold. This result confirms the conclusion reported by the authors Yanaoka *et al.* [5].

Given this fact, the temperature profile ( $T_{mx}$ ), used after for the deduction of  $HTC$ , will be extracted near the center region. The details for the calculation of  $T_{mx}$  are listed below.

#### 4.1.2.2.1.2 Measurement of $T_{mx}$

The mean temperature profile ( $T_{mx}$ ) was calculated according to the Equation (4.2). The region  $-2e < z < 2e$  represents the near center region of the mold where the temperature field was found to be 1D.

$$T_{mx}(x) = \frac{1}{\Delta z} \int_{z=-2e}^{z=2e} T_{mx}(x, z) dz \quad \text{Equation (4.2)}$$

Figure 4.19 shows the obtained curve of the temperature profile ( $T_{mx}$ ). The experimental profile (cross), obtained thanks to the infrared thermography, is plotted against that issued from CFD computations (line). Uncertainties on the experimental temperatures is assumed to be  $0.5^\circ\text{C}$ .

The interpretation of the obtained temperature profiles will be presented below with the analysis of the  $HTC$  results.

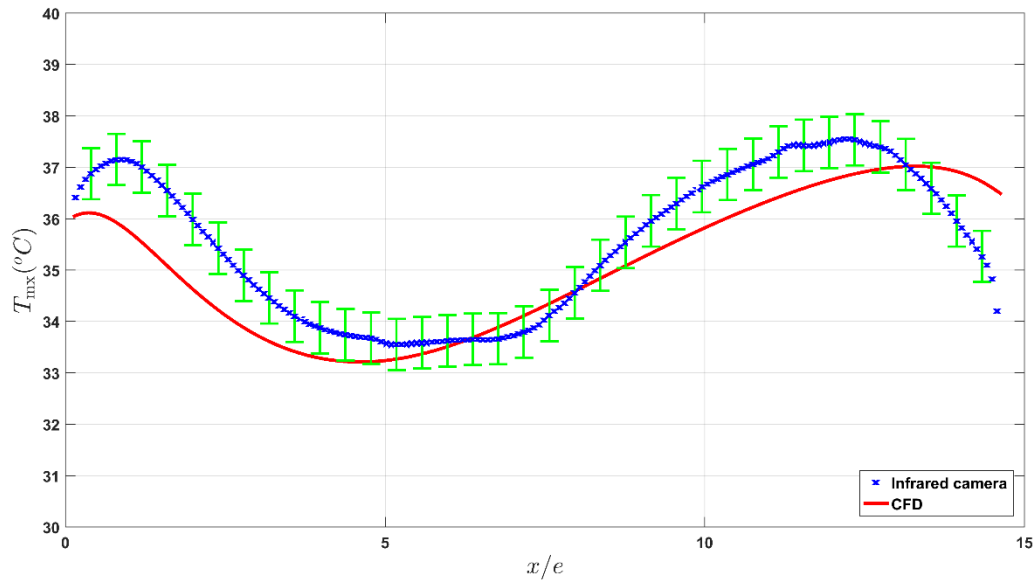


**Figure 4.19** The time-averaged temperature profile ( $T_{mx}$ ) of the “Mold 2”

#### 4.1.2.2.2 Thermocouples acquisition

The acquisition of the ten thermocouples signals (Figure 4.11) was performed during the infrared thermography measurements in the steady state regime. The reach of the steady state regime can be verified by obtaining a constant evolution of the temperatures given by the thermocouples (Figure 4.20). The obtained temperatures were used then to deduce the heat fluxes density  $\phi_{lx}$  and  $\phi_{hx}$  according to the Equation (4.3) and Equation (4.4).

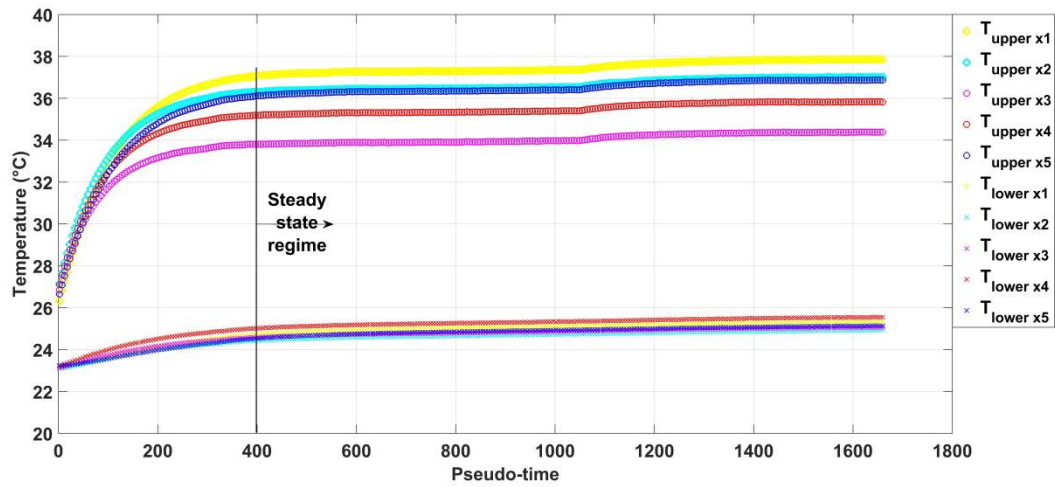


Figure 4.20 Thermocouples acquisition of temperatures during the experiment

$$\phi_{lx}(x = x_i) = \left( \frac{\lambda_{Rohacell}}{e_{Rohacell}} \right) \cdot (T_{upper}(x = x_i) - T_{lower}(x = x_i)) \quad \text{Equation (4.3)}$$

$$\phi_{hx}(x = x_i) = HP - \phi_{lx}(x = x_i); x_i \in [1,5] \quad \text{Equation (4.4)}$$

The five obtained values of  $\phi_{lx}$  and  $\phi_{hx}$  are plotted in Figure 4.21. They show the curves of the heat fluxes distribution along the length of the mold. In addition, the experimental results (cross) were plotted against the numerical ones (line). The low values of  $(\phi_{lx})$  with respect to those of  $(\phi_{hx})$  indicate that the mold was well insulated on its lower and lateral surfaces as planned. In fact these measured heat losses represent 5% of the total injected heating power:  $HP = 1800 \text{ W/m}^2$ . Table 4.1 shows the space-average values of the obtained fluxes over the length of the mold. The uncertainties were calculated based on the standard deviation calculation.

Table 4.1 Comparison between numerical and experimental findings

	CFD	Experimental
$\overline{\phi_{hx}} \text{ (W/m}^2\text{)}$	$1\,729 \pm 8$	$1\,718 \pm 8$
$\overline{\phi_{lx}} \text{ (W/m}^2\text{)}$	$70 \pm 8$	$79 \pm 8$

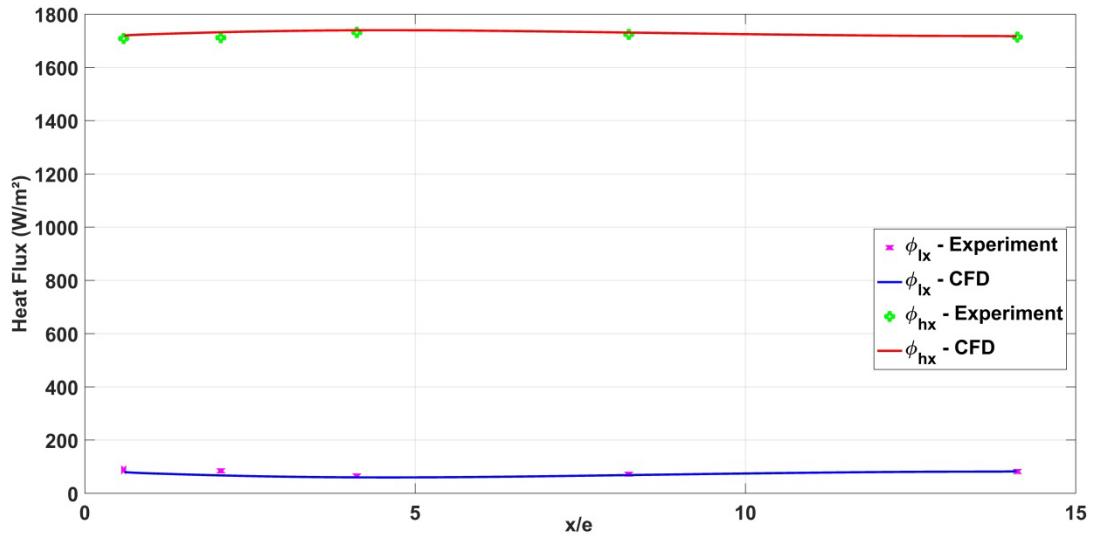


Figure 4.21 Local distribution of the heat fluxes  $\phi_{hx}$  and  $\phi_{lx}$

The comparison between the curves of the experimental heat fluxes and those obtained from the numerical calculations (lines) show a very good agreement quantitatively and qualitatively (Table 4.1).

#### 4.1.2.2.3 Determination of the convective heat transfer distribution ( $\phi_{cx}$ )

The experimental thermal physical quantities obtained previously  $\phi_{hx}$  and  $T_{mx}$  were used then as boundary conditions in the numerical thermal model applied on the stainless steel plate, as explained before in section 2.6.3.2. The used numerical model is shown in Figure 4.22. The energy equation in the computational domain was solved by using Finite Element Analysis (FEA) methods carried out on COMSOL Multiphysics 4.3a® software. It should be noted that the small variations of the  $(\phi_{hxi})_{xi \in [1,5]}$  values (in order of 0.5%) with respect to the average value  $(\overline{\phi_{hx}})$ , as shown in Table 4.1, allow to use  $\overline{\phi_{hx}}$  value as boundary condition in the thermal model instead of using the local function  $\phi_{hx}$ .

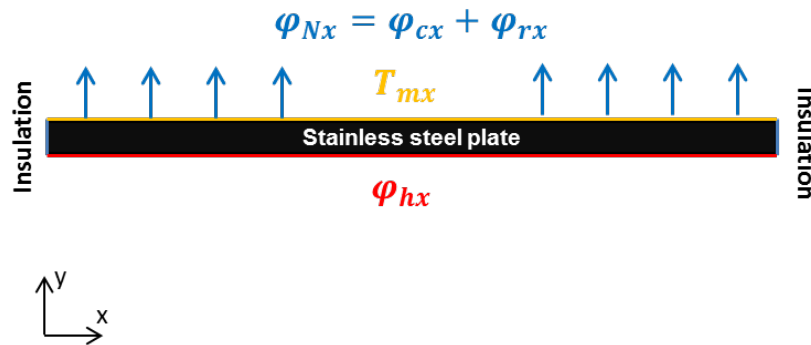


Figure 4.22 Descriptive schema of the numerical model

The resolution of the energy equation in the computational domain allows the determination of the normal heat flux ( $\varphi_{Nx}$ ) distribution over the upper surface of the “Mold 2”.  $\varphi_{Nx}$  represents in fact the sum of the local convective and radiative heat transfers  $\varphi_{cx}$  and  $\varphi_{rx}$  respectively.

$\varphi_{rx}$  is determined according to the Equation (2.14) and Equation (2.15). Thus, the local distribution of the convective heat transfer ( $\varphi_{cx}$ ) is determined according to the Equation (2.16).

#### 4.1.2.2.4 Determination of the *HTC* distribution

The experimental measurements performed previously, for a heating power  $HP = 1800 \text{ W/m}^2$ , allow the obtaining of the distribution of the temperature ( $T_{mx}$ ) and the convective heat transfer ( $\varphi_{cx}$ ) around the upper surface of the “Mold 2”. These physical quantities are essential to calculate the local convective heat transfer coefficient (*HTC*) according to the linear formula of Newton’s (Equation (4.5)).

$$\varphi_{cx}(x) = HTC(x) \cdot (T_{mx}(x) - T_{\infty}) \quad \text{Equation (4.5)}$$

However, and as explained previously in section 2.6.3.3, the *HTC* value at each longitudinal position ( $x/e$ ) was determined accurately by using the regression linear fitting data method. The method was applied on a data that contains three different values of  $T_{mx}$  against three different values of  $\varphi_{cx}$  for each position ( $x/e$ ). The free-stream temperature of the air can be deduced as well.

This method is represented by the Equation (4.6). It is illustrated also by the Figure 4.23 obtained for  $x = 7.5e$ .

$$\begin{bmatrix} T_{1\ mx} \\ T_{2\ mx} \\ T_{3\ mx} \end{bmatrix} (x) = \frac{1}{HTC(x)} \begin{bmatrix} \varphi_{1\ cx} \\ \varphi_{2\ cx} \\ \varphi_{3\ cx} \end{bmatrix} (x) + T_{\infty} \quad \text{Equation (4.6)}$$

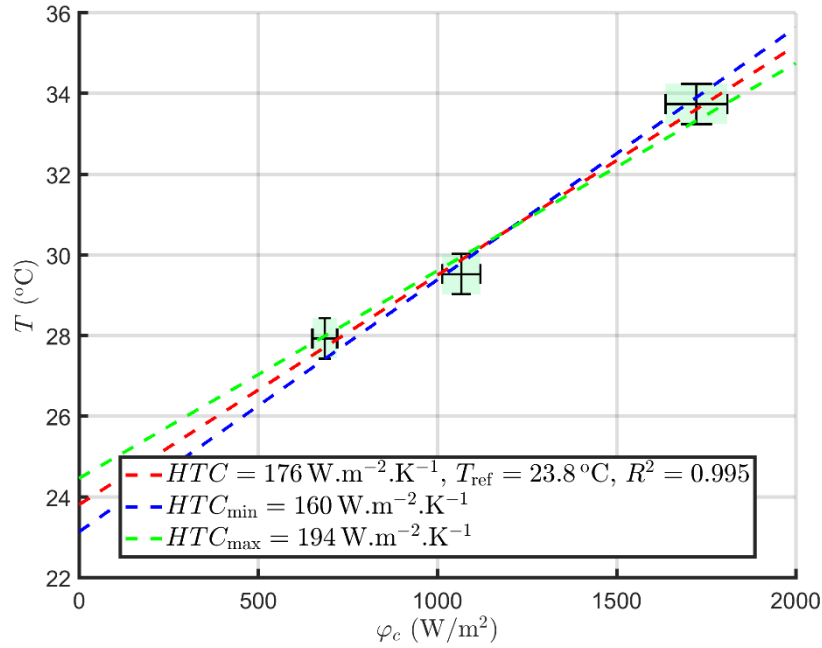


**Figure 4.23 Fitting data**

These three different values of temperatures and convective fluxes were provided by modifying three times the heating power ( $HP$ ) of the heater. For each heating power, the temperatures and the convective fluxes are deduced in the same way to that presented in section 2.6.3 and applied above for  $HP = 1\,800\text{ W/m}^2$ . The two other used heating powers were  $1\,110\text{ W/m}^2$  and  $714\text{ W/m}^2$ .

Assuming an absolute uncertainty of  $0.5^\circ\text{C}$  on the temperatures measured by the infrared camera and a relative uncertainty of 5% on the convective heat flux  $\phi_c$ , these uncertainties have been propagated through the linear regression process to estimate the uncertainty on the convective heat transfer coefficient  $HTC$ . The deviation observed in calculation of  $HTC$  is  $16\text{ W/m}^2/\text{K}$  for this particular x point, the absolute uncertainty on  $HTC$  is chosen to  $20\text{ W/m}^2/\text{K}$ .

Figure 4.24 shows the  $HTC$  distribution on the upper surface of the “Mold 2”. The experimental curve (round) was plotted against the numerical one (line). The free stream air temperature was found to be  $23.8^\circ\text{C}$  according to the regression linear fitting data method.



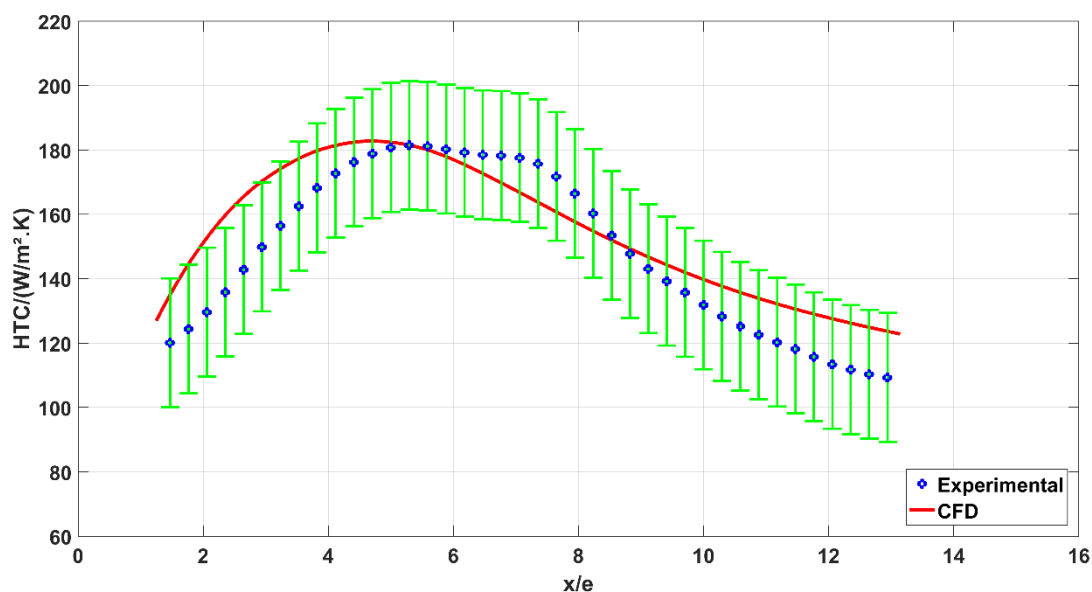


Figure 4.24 *HTC* distribution on the upper surface of the mold

The obtained numerical and experimental *HTC* profiles show the same behavior. In fact, *HTC* increases starting from the beginning of the mold and reaches a maximum value at  $x/e = 5.2$ , for the experimental profile, against  $x/e = 4.7$  for the numerical one.

This behavior of the *HTC* distribution could be explained by the velocity field showed previously around the mold. Indeed, the appearance of a separation bubble over the leading edge of the blunt flat plate and characterized by high turbulence intensities enhances heat exchanges that achieve a maximum value near the time-averaged reattachment point, which was obtained by the experimental test, or somewhat upstream of it which was the case for the numerical result [6,7]. The reattachment length was found previously to be  $5.2e$  and  $5.6e$  according to the experimental and the numerical aerodynamic results respectively.

On the other hand, the reattachment and thus the growing of the shear layer thickness after the reattachment point contribute to an increase in the thermal resistance. This increase of the boundary layer thickness reduces the convective heat exchanges which can explain the decreasing behavior of *HTC* after the reattachment point.

The space-average of *HTC* and  $T_{mx}$  over the length of the “Mold 2” and issued from the experimental measurements as well as from the numerical CFD model are given in Table 4.2.

**Table 4.2 Comparison between numerical and experimental findings**

	CFD	Experimental	Deviation
$\overline{HTC}$ (W/m <sup>2</sup> .K)	155	149 (+/- 20)	4 %
$\overline{T_{mx}}$ (°C)	35	36	1°C

Furthermore, the maximum values reached by  $HTC$ , experimentally and numerically, were found to be consistent with the estimated value calculated using the correlation proposed by Ota *et al.* [8] (Table 4.3). The correlation is represented by the Equation (4.7) and was exposed in section 1.3. The air properties ( $\lambda$  and  $\nu$ ) were calculated at ambient conditions of temperature and pressure.

$$Nu_{max} = \frac{HTC_{max} \cdot Xr}{\lambda} = 0.0919 \left( \frac{U_{\infty} \cdot Xr}{\nu} \right)^{0.734} \quad \text{Equation (4.7)}$$

**Table 4.3  $HTC$  near the reattachment point**

	CFD	Experimental	Correlation	Deviation
$HTC_{max}$ (W/m <sup>2</sup> .K)	183	182 (+/- 20)	196	7 %

The comparison between the experimental results and the numerical ones shows that the performed CFD simulations are able to predict quite accurately the distribution behavior of the temperature and the local heat transfer coefficient around the mold. In addition, the space-average values of  $HTC$  and  $T_{mx}$  around the “Mold 2” issued from the CFD approach fit well with those obtained from the experimental measurements (Table 4.2).

The radiative heat transfer coefficient can be calculated also as mentioned above, according to the Equation (2.15), and the obtained value was found to be small compared to the convective one:  $\overline{HTC_r} \approx 6 \text{ W/m}^2 \cdot \text{K}$ .

### 4.1.3 Summary of the results

Despite that the experimental aerodynamic and thermal results are derived from two different experimental approaches, they have been found to be correlated and the obtained aerodynamic findings were able to interpret the thermal ones such as the appearance of the side wall effects and the behavior of the  $HTC$  distribution.

In turn, these aerodynamic and thermal results have shown a good respect for the observations reported by the previous research studies, such as the development of a separated-reattached flow, the appearance of side wall effects, the behavior of  $HTC$  and the estimation of the maximum  $HTC$  value. Therefore, that indicates that the designed and fabricated model autoclave operates well as it is able to reproduce scientific physical phenomena.

On the other hand, the thermal and aerodynamic results derived from the numerical model exposed in *chapter 3* have shown a good agreement with the experimental findings. Thus, the constructed numerical model using the CFD tool ANSYS Fluent can be validated.

Based on the behavior of the convective heat transfer coefficient shown in Figure 4.24, it can be deduced that the *HTC* distribution is not uniform around the mold. This result signifies that during an autoclave manufacturing process, the convective heat transfer rates from the heated pressurized gas to a processed composite piece are not uniform. This non-uniformity of *HTC* distribution can be aggravated with the use of molds of more complex geometries and aerodynamically unfavorable shapes. This heterogeneity can result therefore in the presence of thermal gradients inside the manufactured composite part impacting then its quality at the end of the curing cycle.

## 4.2 Study of the inter-part shadowing phenomenon

The inter-part shadowing effects were investigated by installing the two molds of different sizes “Mold 1” and “Mold 2” within the working section of the model autoclave. The “Mold 1” was placed forward whereas the “Mold 2” was installed behind at a distance “ $d$ ” of the 1<sup>st</sup> one.  $d$  is considered as a parameter study. In this investigation,  $d$  is first fixed to 3.2 cm and a parametric study over the value of  $d$  will be performed later.

Figure 4.25 shows a CAD drawing that illustrates the experimental conditions of the installation of the two molds. On the other hand, Figure 4.26 shows the corresponding numerical model.

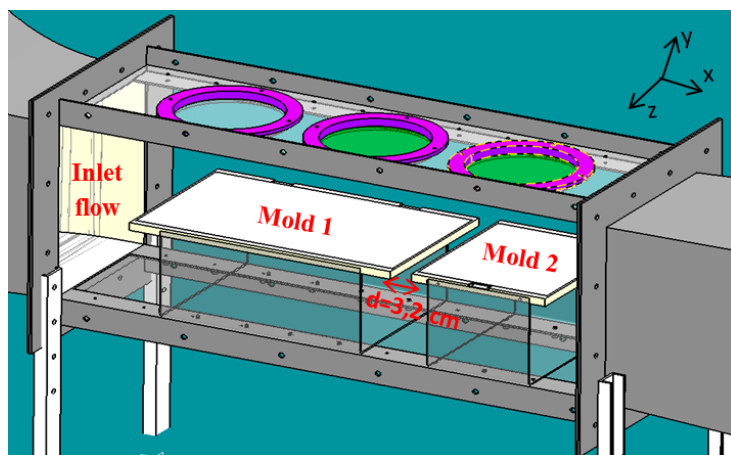


Figure 4.25 CAD drawing of the inter-part shadowing effects study

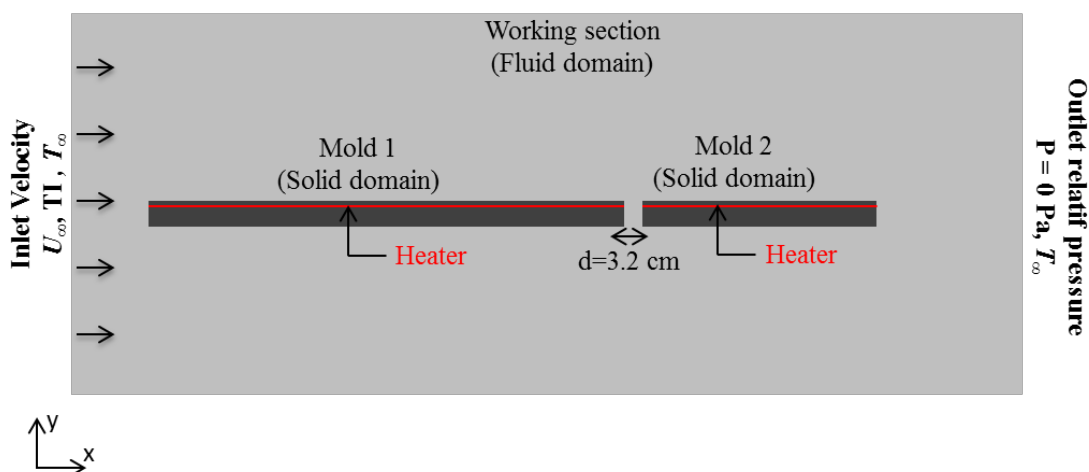


Figure 4.26 The computational domain for the inter-part shadowing effects study

The investigation of the shadowing effects consisted in studying first the velocity field behavior and the  $HTC$  distribution on the “Mold 2” according to the adopted

experimental and numerical methods explained previously, and which were already applied for the study of a single mold in section 4.1.

Then, the obtained aerodynamic and thermal results were compared to those obtained on the “Mold 1”. Indeed, it was assumed that the “Mold 2”, located behind the “Mold 1”, has no impact on the physical phenomenon over the “Mold 1”. Given this fact, the thermal and the aerodynamic results obtained previously in the case of a single mold have been considered applicable on the “Mold 1” for the inter-part shadowing study.

## **4.2.1 Study of the flow field**

### **4.2.1.1 Procedure of the study**

Figure 4.27 illustrates the installation of the PIV system for the performing of the aerodynamic measurements over the “Mold 2” placed at the back.

The laser of the PIV system was installed above the upper wall of the working section and thus the emitted laser sheet is normal to the upper surface of the “Mold 2” near the center region, and it is located in the ( $xy$ ) plane (Figure 4.27). The camera was installed in front of the laser sheet with a distance of 56 cm from the side wall of the working section (Figure 4.27). It was calibrated in a manner to capture the leading edge of the “Mold 2”. The size of the obtained image is  $(19.6 \times 19.6) \text{ cm}^2$ .

The generated volume flow rate ( $Q$ ) was found to not vary according to the Flowmeter measurement, i.e.  $Q = 14\,500 \text{ m}^3/\text{h}$ . The power supplier for the heaters inserted inside the “Mold 1” and the “Mold 2” was not on and thus the aerodynamic measurements were performed in an isothermal regime.

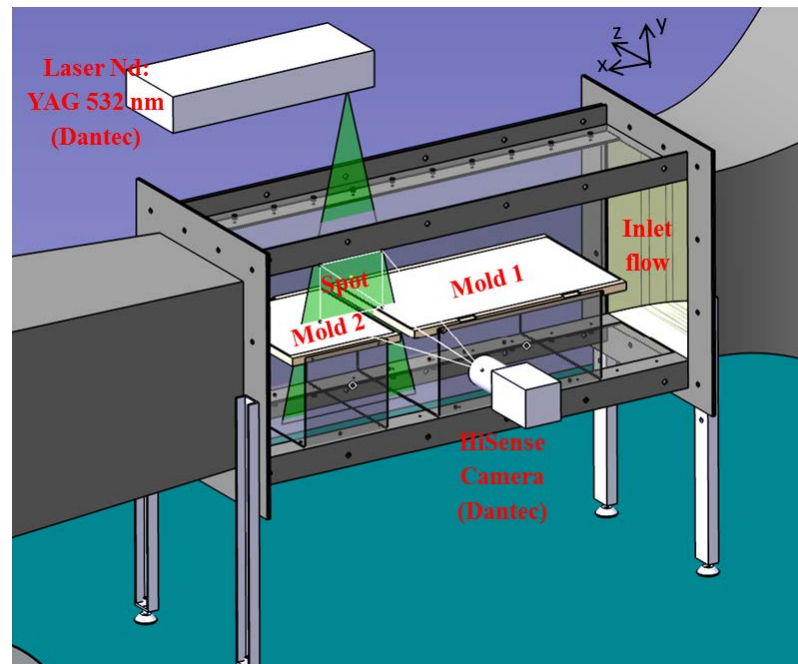


Figure 4.27 PIV measurements of the velocity field around “Mold 2” in the (xy) plane

#### 4.2.1.2 Results of the flow field

Figure 4.28 and Figure 4.29 show the time-averaged velocity magnitude linked to the mean streamlines of the flow field that leaves the trailing edge of the “Mold 1” and strikes the leading edge of the “Mold 2”. These fields were obtained thanks to PIV measurements and numerical simulations respectively. The velocity magnitude was calculated according to the Equation (4.1) above. The reference point ( $x/e=0$ ,  $y/e=0$ ) corresponds to the leading edge corner of the “Mold 2” ( $e = 17$  mm).

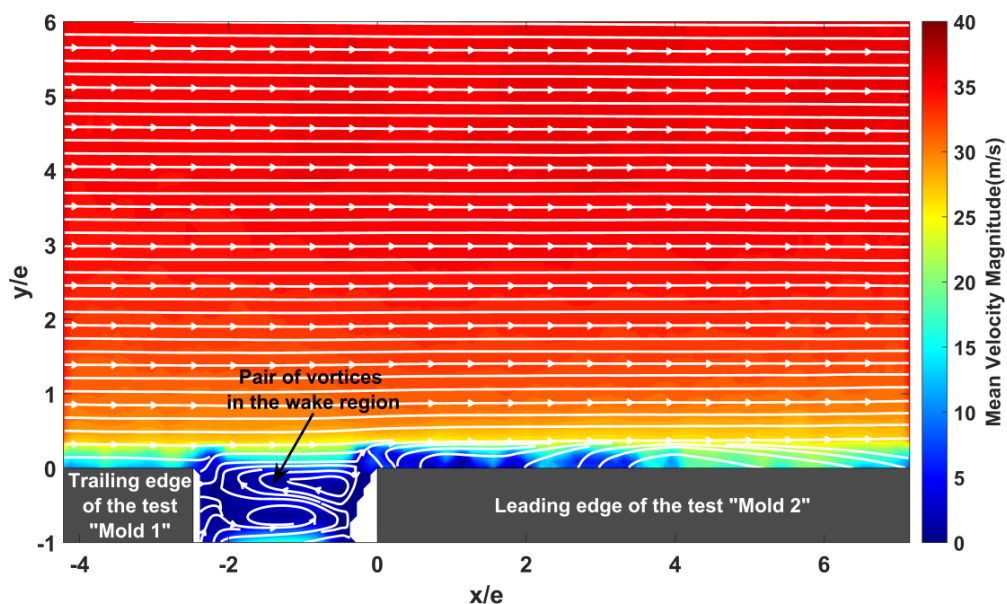


Figure 4.28 Contour of the time-averaged velocity magnitude + time-averaged velocity streamlines: PIV result

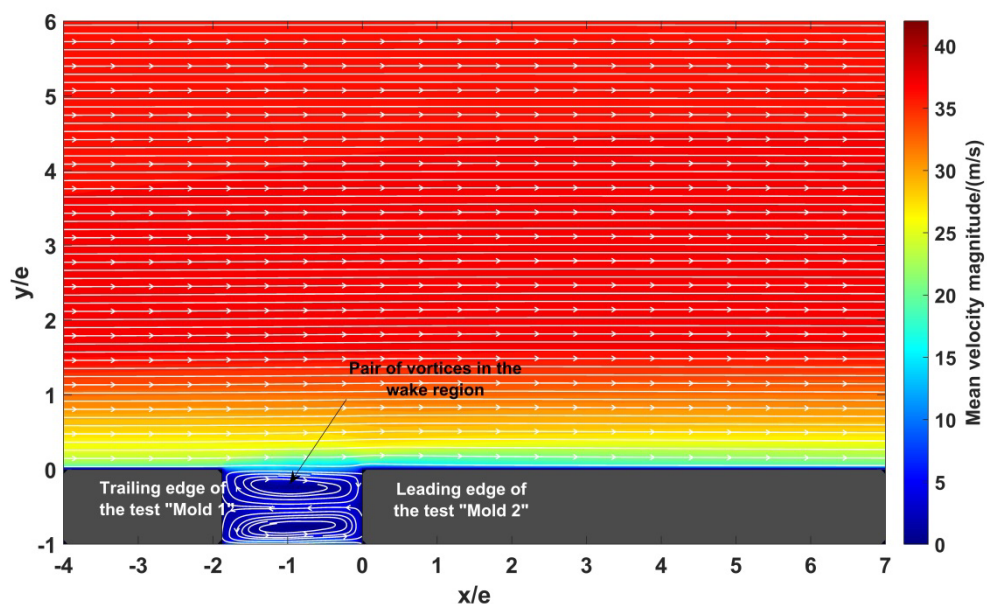


Figure 4.29 Contour of the velocity magnitude + velocity streamlines: CFD result

Based on the streamline velocities, it can be seen the creation of two vortices in the wake region behind the “Mold 1”. These two vortices have been detected more precisely by examining the important values of  $\Gamma_I$  field that are present in this wake region (Figure 4.30 and Figure 4.31). These vortices were located between the two molds: between  $x/e = -2.2$  and  $x/e = -5.5$  (Figure 4.31). The centers of these two vortices have been determined as well. The center of the positive recirculation was



located at  $x/e = -1.2$  and  $y/e = -0.6$ , while the center of the negative one was located at  $x/e = -0.6$  and  $y/e = -0.2$ .

Concerning the flow structure over the Mold 2, the obtained behavior of the time-averaged velocity streamlines as well as the presence of small  $\Gamma_I$  values show the no-appearance of a significant recirculation region or a separation bubble over the leading edge of the “Mold 2”, contrary to what was found over the “Mold 1” (Figure 4.2).

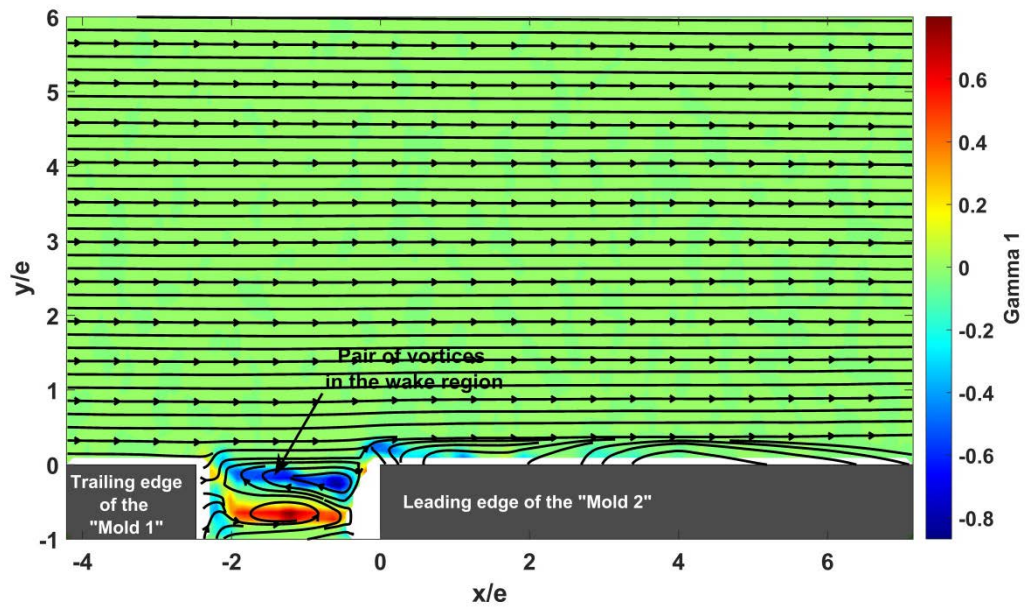


Figure 4.30 Contour of  $\Gamma_I$ : PIV result



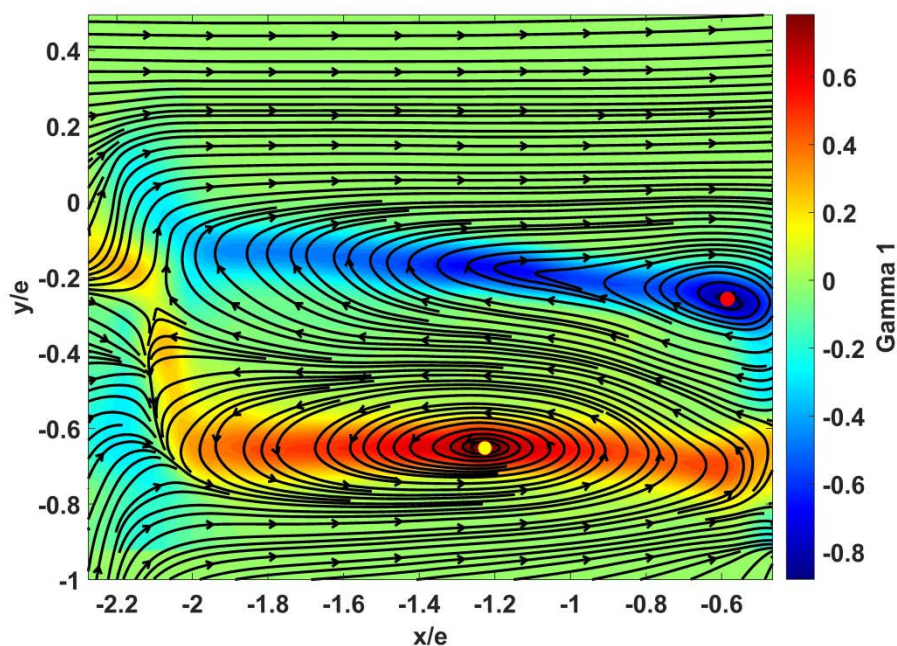


Figure 4.31 Zoom on the pair of vortices in the wake region

This behavior of the flow field was verified also by plotting the profiles of the normalized mean and fluctuating longitudinal velocity profiles  $U/U_\infty$  and  $u_{rms}/U_\infty$  in the boundary layer developed around the “Mold 2” and for different dimensionless x-positions ( $x/e$ ) (Figure 4.32 and Figure 4.33 respectively). These profiles were derived from the PIV measurements (rounds) as well as from the CFD calculations (lines).

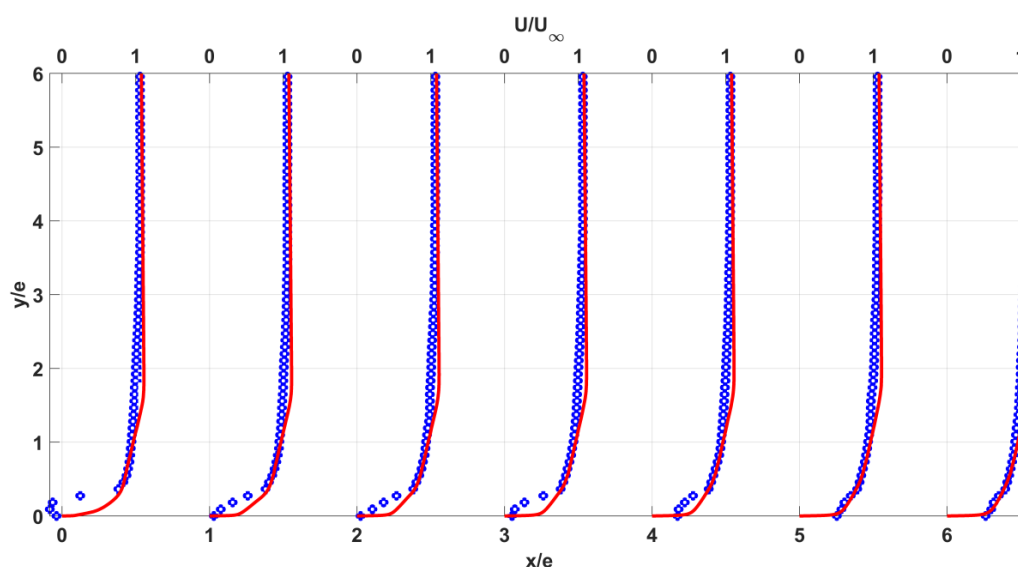
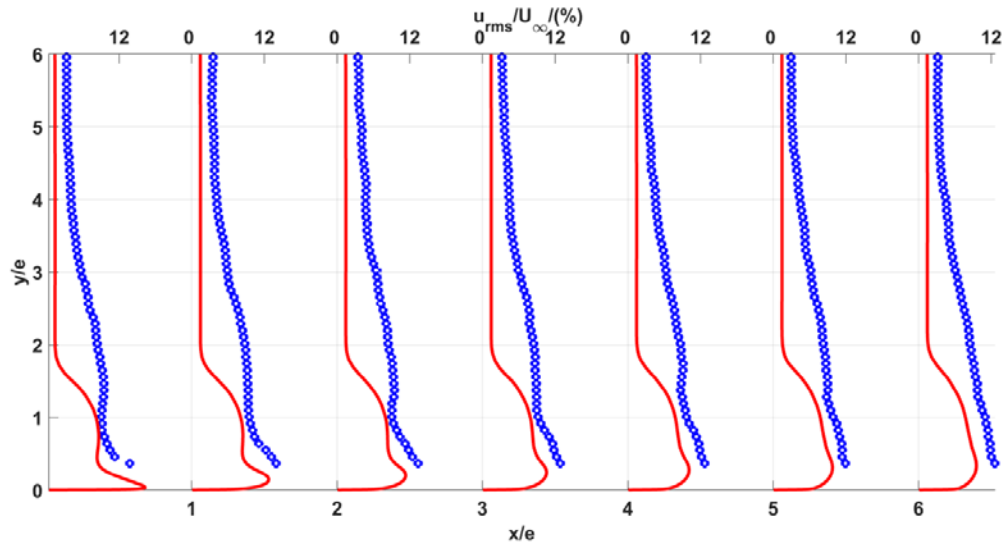


Figure 4.32 Mean longitudinal velocity profiles  $U$  on “Mold 2”:  $\circ$ , PIV; —, CFD



**Figure 4.33 Fluctuating (r.m.s) longitudinal velocity profiles  $u_{rms}$  on “Mold 2”:**  
 ○, PIV; —, CFD

Near the wall and throughout the “Mold 2”, Figure 4.32 shows positive values of the mean  $x$ -velocity, excepted for  $x/e = 0$ , with no presence of inflexions points. That indicates the non-existence of backflow velocities and thus the non-development of a separation bubble. This finding can be verified also by observing the relatively low values of turbulence intensities (Figure 4.33) compared to those obtained over the “Mold 1” (Figure 4.7).

Furthermore, the distribution of the normalized  $x$ -velocities ( $U/U_\infty$ ) extracted near the wall and over the length of the mold (Figure 4.34) shows positive values, excepted for  $x/e = 0$ , which indicates again the no-appearance of a significant separation bubble. Numerically, the positive values of  $\bar{\tau}_w$  (Figure 4.35) leads to the same conclusion about the flow field structure over the Mold 2.

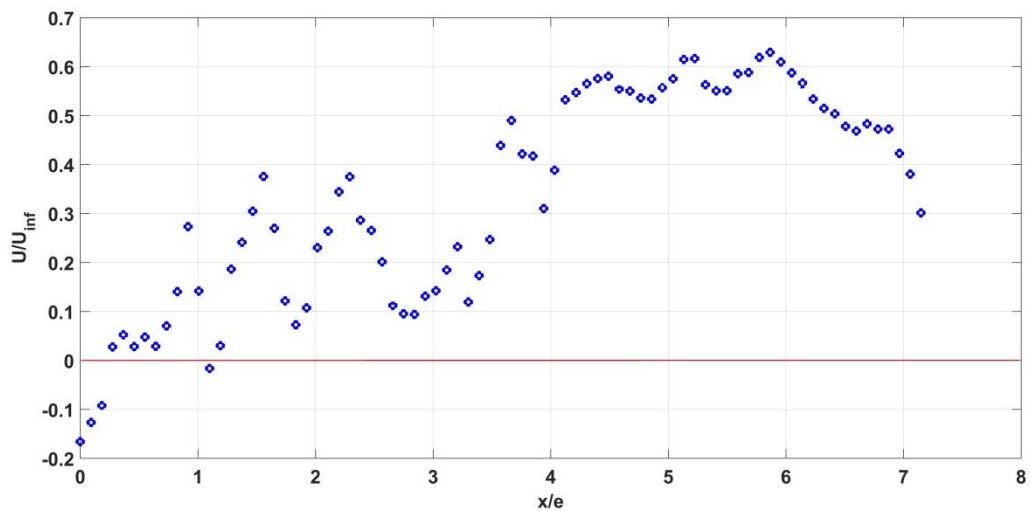


**Figure 4.34 Mean longitudinal velocity near the mold surface: PIV results**

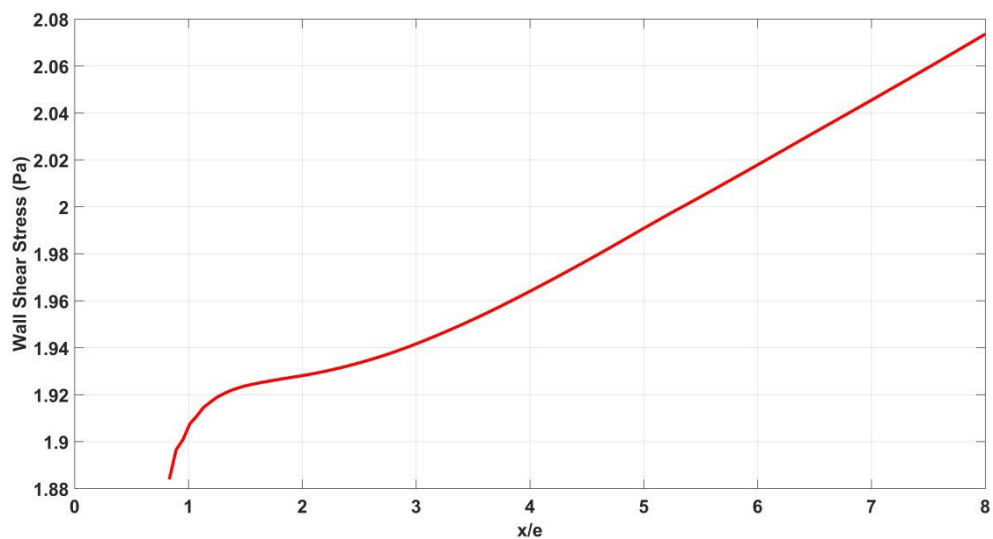


**Figure 4.35 Distribution of wall shear stress coefficients: CFD results**

The overall aerodynamic analysis of the flow field exposed above, experimentally and numerically, allow to conclude that there is no-existence of an important separated-reattached flow region over the leading edge of the “Mold 2” contrary to what was found over the “Mold 1”. On the other hand, the comparison between the experimental velocities profiles (rounds) and those derived from the CFD calculations (lines) shows again a good agreement. The PIV turbulence intensity values near the wall were not taken into consideration due to a non-statistical convergence.

## 4.2.2 Study of the convective heat transfer coefficient

### 4.2.2.1 Procedure of the study

The followed procedure for the investigation of the convective heat transfer coefficient distribution, over the “Mold 2” at the back, is the same as that explained in section 4.1.2.1 in the case of a single mold. It should be recalled that “Mold 2” was heated by applying a heating power ( $HP$ ) of  $1800 \text{ W/m}^2$ . The cooling air circulated at the same volume flow rate mentioned above with a controlled temperature of  $25^\circ\text{C}$ .

### 4.2.2.2 Thermal results

#### 4.2.2.2.1 Infrared thermography

Figure 4.37 shows the time-averaged temperature field distribution of the upper surface of the “Mold 2” obtained thanks to the infrared thermography (Figure 4.36).

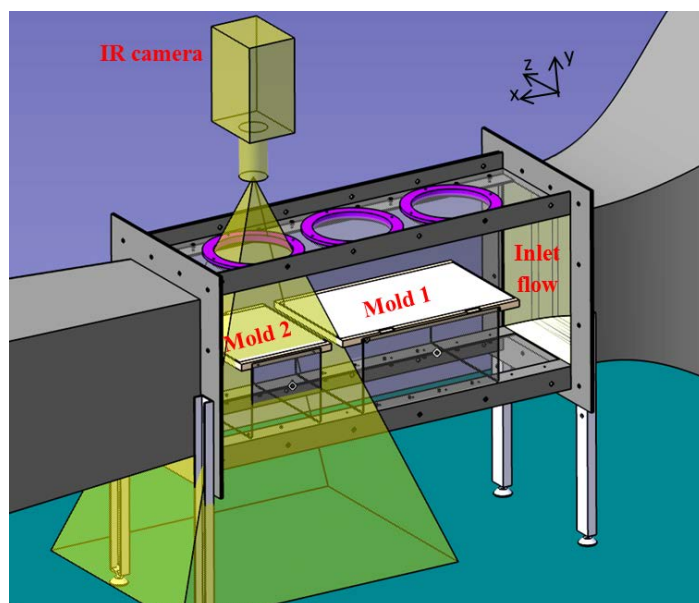
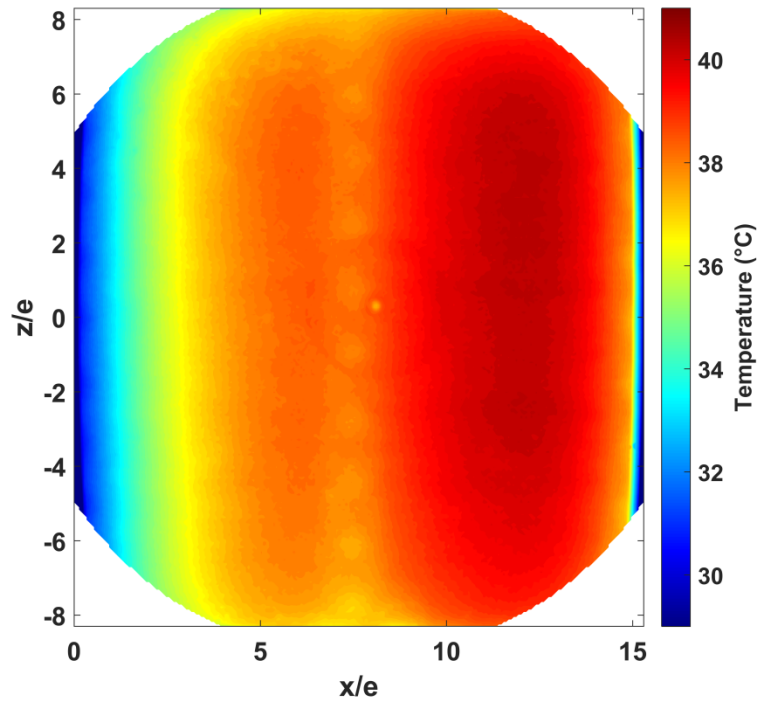


Figure 4.36 Infrared thermography of the upper surface of the test “Mold 2”



**Figure 4.37** Contour of the time-averaged temperature field of the upper surface of the heated “Mold 2”

The obtained temperature field of the upper surface shows a one-dimensional field with no-appearance of “Cold Zones” around the side walls, contrary to what was found before for the mold placed at the front (Figure 4.13), and thus the no-appearance of side walls effects.

However, this field reveals a temperature drop between  $x/e=6$  and  $x/e=8$  and along  $z/e$ . This appearance is due probably to a detachment of the film resistive heater from the stainless steel plate at this location because of the excessive use and heating of the mold (thermal fatigue). Consequently, an air gap can be formed between the heater and the plate at this location, resulting then in a bad contact resistance and therefore the appearance of lower temperature values between  $x/e=6$  and  $x/e=8$ . As a result, these temperature values were considered inoperable. Thus they were not taken into account for the measurement of  $HTC$  values (Figure 4.38, Figure 4.39 and Figure 4.40).

The obtained contour of the temperature field was used then to deduce the temperature profile ( $T_{mx}$ ) extracted near the center region of the mold. Figure 4.38 shows the plotted curve of ( $T_{mx}$ ).

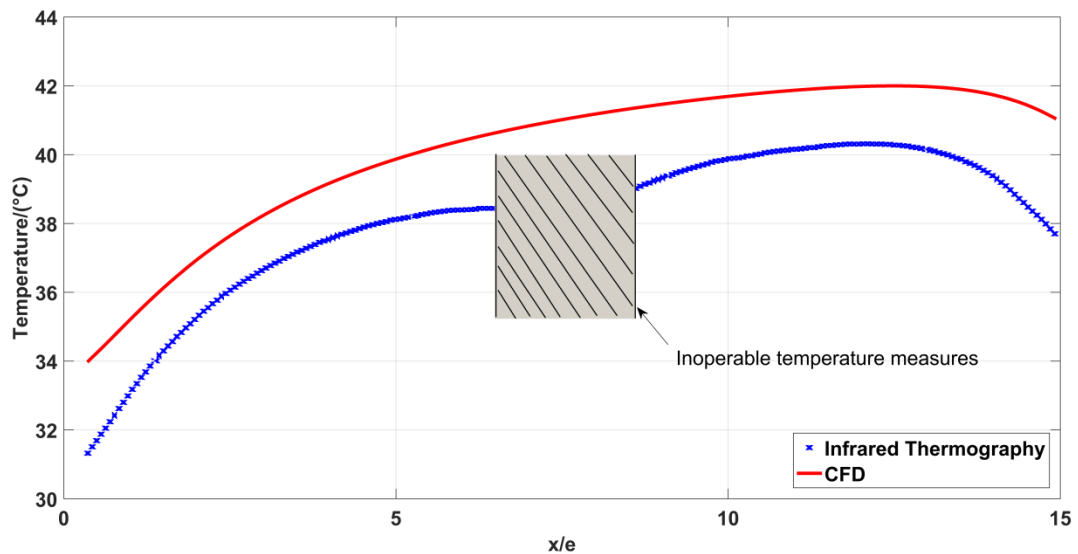


Figure 4.38 The time-averaged temperature profile ( $T_{mx}$ ) of the “Mold 2”

#### 4.2.2.2.2 Determination of the $HTC$ distribution

The determination of the convective heat transfer coefficient distribution over the “Mold 2” is the same as that applied in section 4.1.2.2.

Figure 4.39 shows the  $HTC$  distribution on the upper surface of the “Mold 2” placed at the back. The experimental curve (rounds) was plotted against that derived from the performed numerical simulation (line).

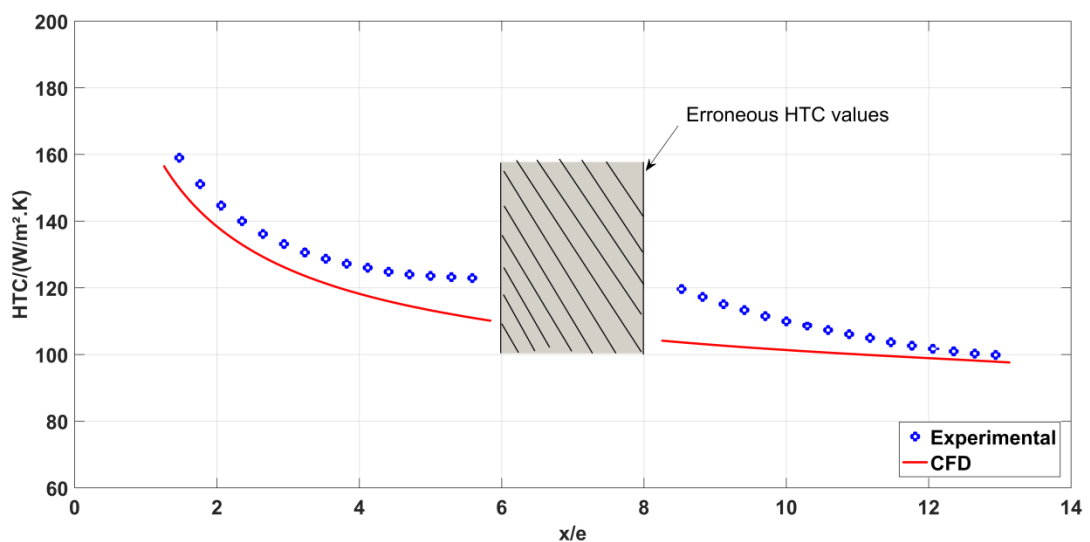


Figure 4.39  $HTC$  distribution on the “Mold 2”

The experimental and the numerical curves show the same evolution.  $HTC$  was continuously decreasing along the “Mold 2” which explains the monotonic increasing temperature profile ( $T_{mx}$ ) in Figure 4.38. This behavior of  $HTC$  could be explained again by the velocity profiles obtained previously around the “Mold 2”. Indeed, the no-appearance of a separation bubbles on one hand, and the existence of low velocities and turbulence intensities near the wall on the other hand, result in reducing values of  $HTC$ .

The space-average of  $HTC$  and  $T_{mx}$  over the length of the “Mold 2”, and issued from the experimental measurements as well as from the numerical CFD model are plotted in Table 4.4.

**Table 4.4 Comparison between numerical and experimental findings**

	CFD	Experimental	Error
$\overline{HTC}$ (W/m <sup>2</sup> .K)	111	120 (+/- 20)	7.5 %
$\overline{T_{mx}}$ (°C)	40	38	2 °

The comparison between the experimental results and the numerical ones shows that the performed CFD simulations are able again to predict quite accurately the distribution behavior of the temperature and the local heat transfer coefficient around the mold. In addition, the space-average values of  $HTC$  and  $T_{mx}$  around the “Mold 2”, issued from the CFD approach, fit well with those obtained from the experimental measurements (Table 4.4)

The radiative heat transfer coefficient between the “Mold 2” and its surrounding was calculated and it was found again to be small compared to the convective one:  $\overline{HTC_r} \approx 6 \text{ W/m}^2.K$ .

### 4.2.3 Summary of the results

In order to examine the inter-mold shadowing effects, the experimental  $HTC$  curve obtained for the first 26 cm of the “Mold 1” was plotted against that obtained for the “Mold 2” (Figure 4.40). As explained previously, the curve of the  $HTC$  around the “Mold 1” is in fact the curve obtained previously in section 4.1.2.2.4 in the case of a single mold within the working section.

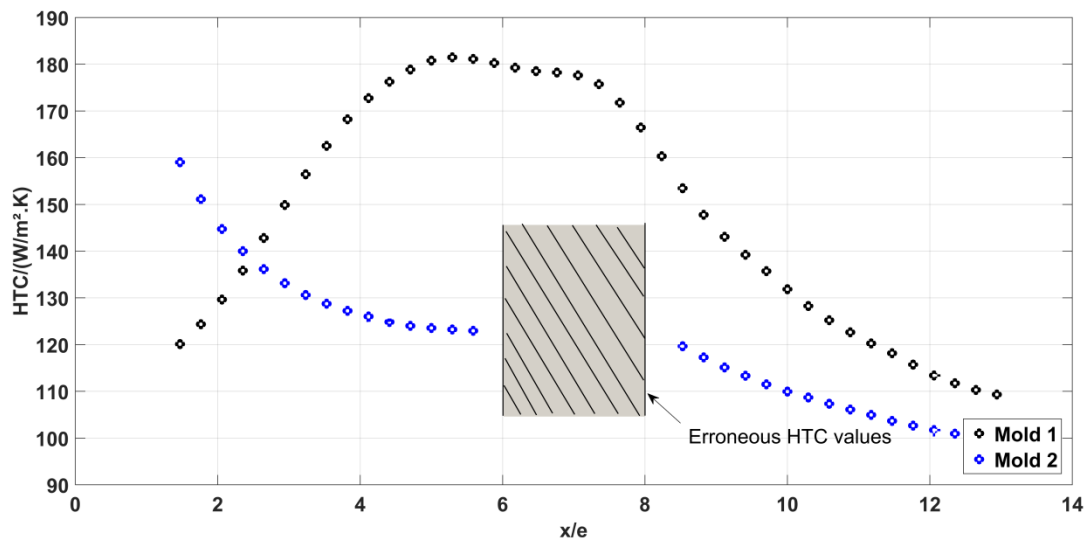


Figure 4.40 *HTC* distribution behavior on the “Mold 1” and the “Mold 2”

It can be clearly seen that the obtained *HTC* distribution behaviors on the “Mold 1” and “Mold 2” are not identical. Furthermore, the *HTC* values over the “Mold 1” showed to be more important than those obtained on the “Mold 2”. This can be seen by the space-average values shown in Table 4.5.

Table 4.5 *HTC* Comparison between Mold 1 and Mold 2

	Mold 1	Mold 2	Percentage deviation
$\overline{HTC}$ (W/m².K)	149 (+/- 20)	120 (+/- 20)	20 %

These differences in *HTC* behaviors and values are explained by the differences in behaviors and values of the developed velocity profiles over the “Mold 1” and “Mold 2”.

The comparison between the developed velocity and *HTC* profiles over the “Mold 1”, placed at the front, and those over the “Mold 2” placed at the back highlights the effects of the inter-part shadowing.

Indeed, during the autoclave manufacturing process of multiple composite parts of complex shapes and various sizes, the large parts placed at the front can block the gas flow to the small parts installed at the back. In such situations, the thermal effects of the inter-part shadowing can be aggravated. Such effects can contribute to important differences of convective heat transfer coefficient distribution between the various parts, resulting therefore in a simultaneous production of multiple composite items with different qualities at the end of the curing cycle.

The inter-part shadowing effect can exist as well in the case of manufacturing of a single mold with a complex shape and aerodynamically unfavorable geometry or with



excessive support structures. In such situations, various stagnation points can exist and blocking then the flow to other surfaces of the mold. Therefore, a non-uniform distribution of the convective heat transfer coefficient appears over the mold resulting then in temperature gradients within the composite items.

#### 4.2.4 Parametric study of $d$

Based on the above findings concerning the presence of inter-mold shadowing effects, it was decided to perform a parametric study that consists of varying the distance  $d$  between the two molds. The main objective of this study is to investigate the impacts of the distance  $d$  on the shadowing effects behaviors, especially concerning the convective heat transfer coefficient distribution, and to try also to found a position of the molds that allows to overcome these effects.

Experimentally, the size of the working section as well as the used installation system for the molds have limited the number of the configuration studies. In total, four configurations have been tested and which are defined in the Table 4.6 below. The “Multi-H” represents the performed tests where the two plates were placed at the same height or the same horizontal level within the test section. In this case, two distances were tested:  $d = 3.2$  cm (the already exposed case above) and  $d = 12.8$  cm. On the other hand, the “Multi-V” signifies the performed tests where the “Mold 2” was placed at a distance  $d$  behind the “Mold 1” and 3 cm above the “Mold 1”.

**Table 4.6 Definition of the tested configuration studies**

Multi-H	$d=3.2$ cm
	$d=12.8$ cm
Multi-V	$d=3.2$ cm
	$d=12.8$ cm

Figure 4.41 shows the obtained experimental  $HTC$  curves over the Mold 2 for the various tested configurations defined above.

These curves indicate that in the case of Multi-H, increasing the distance  $d$ , from 3.2 to 12.8 cm, and thus moving away the mold at the back from the mold at the front allows the intensification of the convective heat transfer coefficient just over the beginning of the backward mold. Thereafter, the difference between  $HTC$  values decreases and tends to be negligible at the end of the mold.

However, in the case of Multi-V, this effect of the distance  $d$  was found to be reversed. In fact, decreasing the distance from 12.8 cm to 3.2 cm was able to increase the  $HTC$  values of the “Mold 2” at the back.

The comparison between the Multi-H configuration and the Multi-V configuration shows clearly that placing the mold at the back above the first mold is able to increase the convective heat exchanges with the backward mold.

However, the various tested positions, either in Multi-V or Multi-H configurations, have failed to reproduce the same  $HTC$  behavior over the “Mold 2” than that over the “Mold 1” (black). Therefore, the different tested configurations have failed to overcome the inter-part shadowing effects.

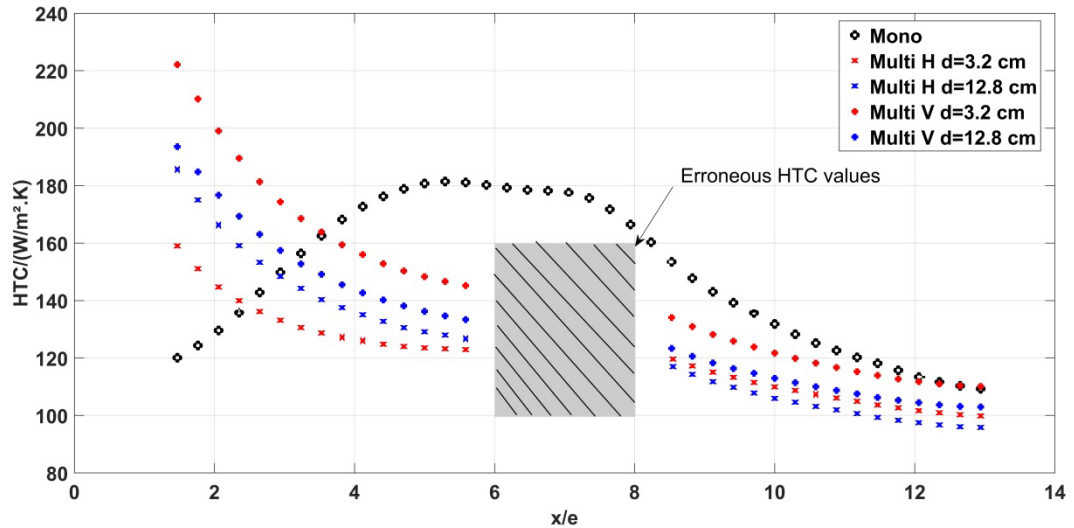
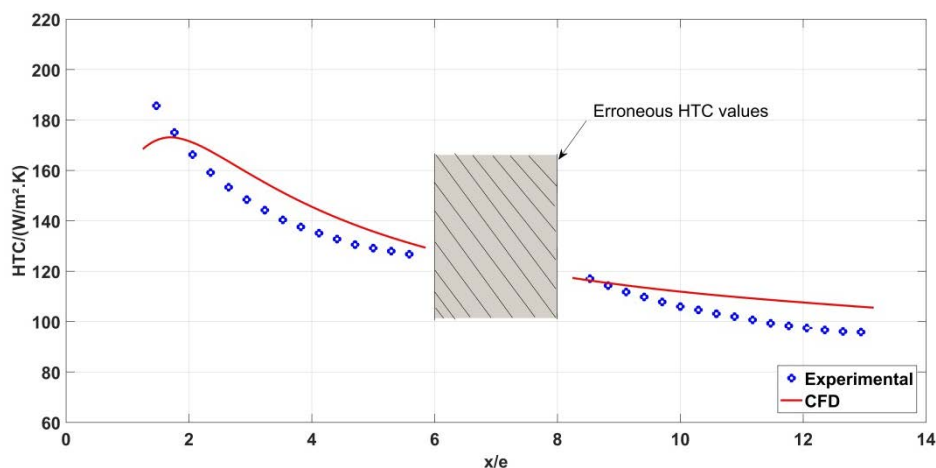


Figure 4.41  $HTC$  distribution over the Mold 2

The numerical  $HTC$  curves for the different tested configurations have been plotted against the experimental ones in Figure 4.42, Figure 4.44 and Figure 4.45.

In the case of Multi-H, the numerical  $HTC$  results show that increasing the distance  $d$  from 3.2 cm to 12.8 cm was able to modify the  $HTC$  behavior over the mold at the back. Indeed, Figure 4.42 shows that the numerical  $HTC$  profile is not monotonically decreasing contrary to what was found for  $d=3.2$ cm:  $HTC$  increases at the beginning of the mold and reaches a maximum value at  $x/e=1.8$ . Afterwards,  $HTC$  decreases. This behavior can be due to the appearance of a separated-reattached flow region over the leading edge as shown previously for the case of a single mold. This assumption was verified by plotting, numerically,  $\overline{\tau_w}$  distribution over the “Mold 2” in Figure 4.43. The obtained profile shows that  $\overline{\tau_w}$  vanishes at  $x/e=2$  allowing then the deduction of the presence of a separated-reattached flow region over the mold and

characterized by  $Xr = 2e$ . However, this numerical finding represents, for the first time, a discrepancy in the  $HTC$  behavior with the experimental result.



**Figure 4.42**  $HTC$  distribution over the Mold 2 for Multi-H,  $d= 12.8$  cm

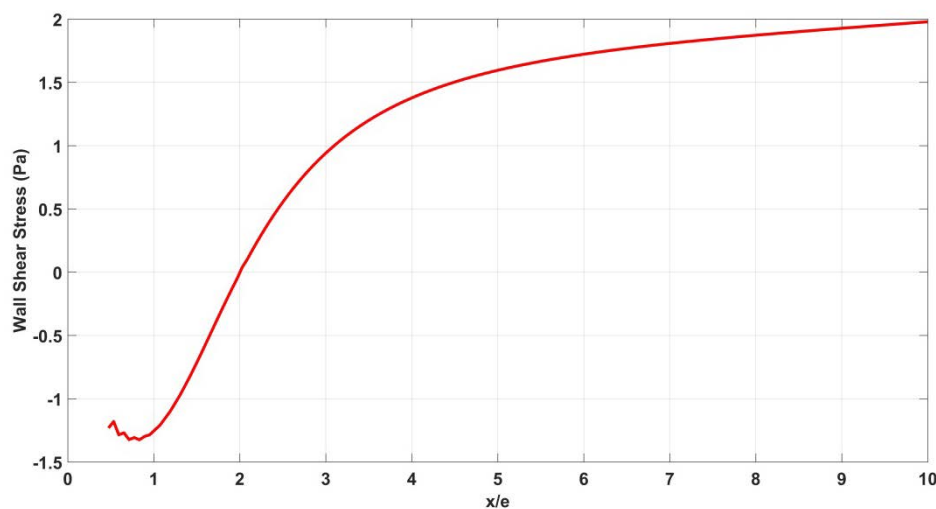


**Figure 4.43**  $\bar{\tau}_w$  distribution over the Mold 2 for Multi-H,  $d= 12.8$  cm

The discrepancy between the numerical and the experimental  $HTC$  behavior was found to be more aggravated in the Multi-V configuration study. In fact, the numerical  $HTC$  behaviors show the appearance of a non-negligible separation bubble over the leading edge of the “Mold 2” (Figure 4.44 and Figure 4.45). This finding cannot be deduced experimentally where the  $HTC$  curves remains monotonically decreasing.

Therefore, the comparison between the numerical and the experimental findings during this parametric investigation has revealed that numerical computations are

unable, in some cases, to predict quite accurately the behaviors of the flow field and the *HTC* distribution over the mold at the back. This may be due to the complex structure of the vortices formed in the wake region behind the “Mold 1” [9], especially at high Reynolds number, make difficult then to predict quite accurately the vortices shedding using 2D RANS numerical calculations.

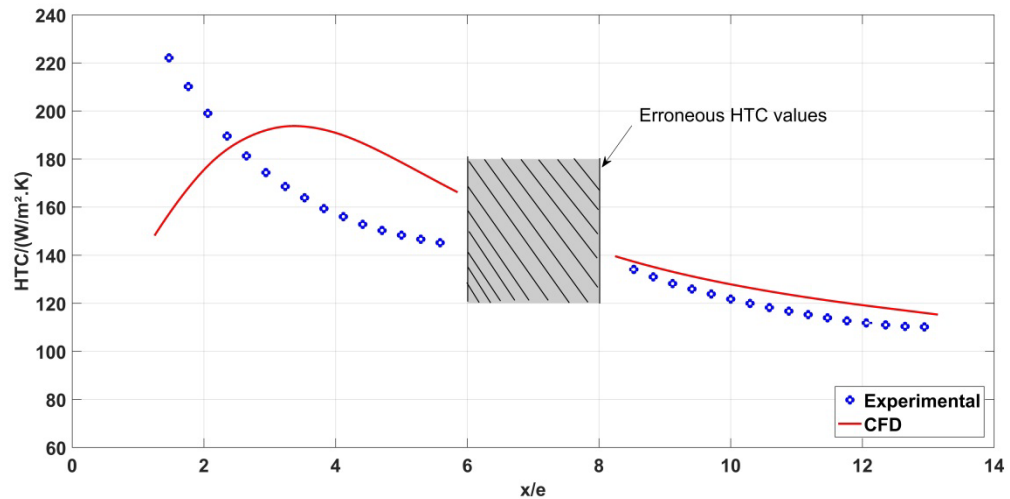


Figure 4.44 *HTC* distribution over the Mold 2 for Multi-V,  $d= 3.2$  cm

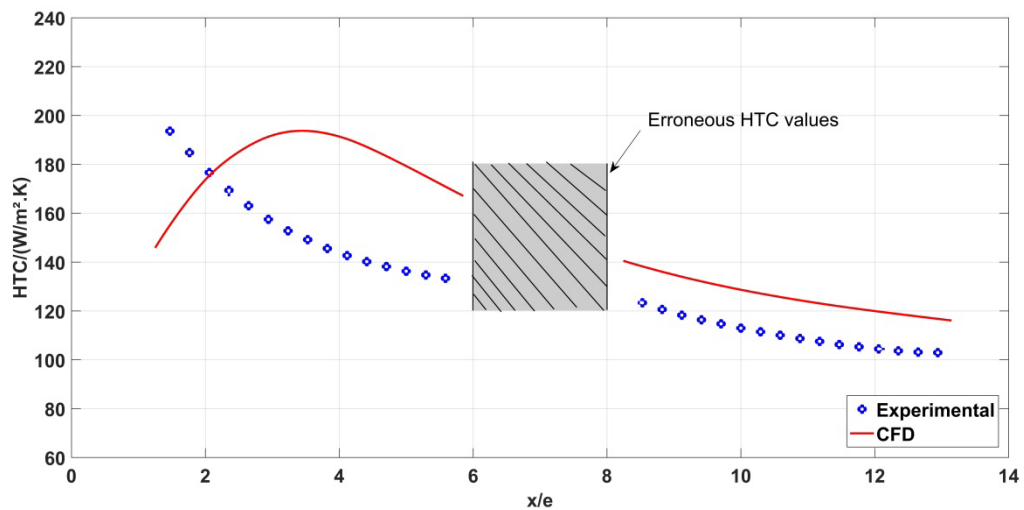


Figure 4.45 *HTC* distribution over the Mold 2 for Multi-V,  $d= 12.8$  cm

### **4.3 Study of the “representative mold”**

In this section, the computational calculations of the flow field and the convective heat transfer coefficient distribution around the mold equipped with obstacles are presented. The results are issued from the numerical model exposed in section 3.4.

#### **4.3.1 Study of the flow field**

Figure 4.46 shows the contour of the velocity magnitude as well as the streamlines issued from the CFD simulation around the Mold 1 surfaces and the obstacles. The faces of the solid domains are colored in black. The obtained behavior of the velocity field indicate that the presence of the obstacles contribute to the existence of dead zones characterized by low velocities. In addition, these obstacles, despite their simplified geometry, contribute to the existence of a complex flow field in the working section of the model autoclave and around the mold surface.

Such finding leads to deduce that in the case of an autoclave molding of composite pieces placed on molds equipped with excessive support structure of complex geometries and aerodynamically unfavorable shapes, more complex and non-uniform flow field can be present. Such flow is difficult to describe and to measure which explain the limited studies of the flow field within autoclaves in the literature. Furthermore, such flow can disturb the convective heat transfer coefficient distribution around the molds surfaces leading then to important heterogeneities.

However, this obtained flow field must be validated by experimental measurement.

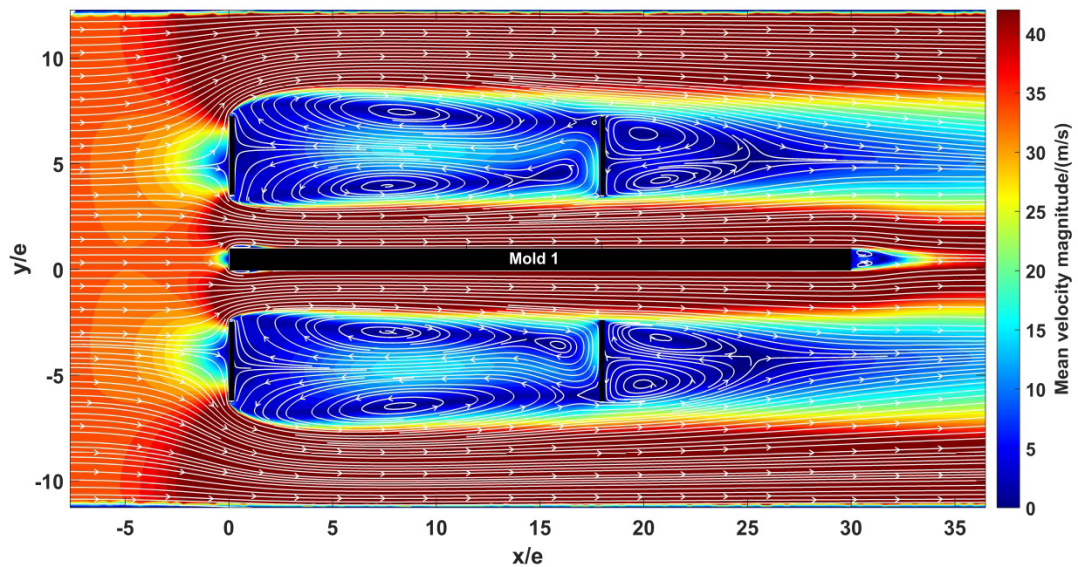


**Figure 4.46** Contour of the velocity magnitude in the working section

The obtained aerodynamic result shows also the appearance of a small separated-reattached flow region over the leading edge of the Mold 1. This flow structure can be deduced also by examining the wall shear stress behavior plotted in Figure 4.47 and which vanishes at  $x = 1.5e$ . This distance represents the reattachment length ( $X_r$ ) of the recirculation region as explained previously.

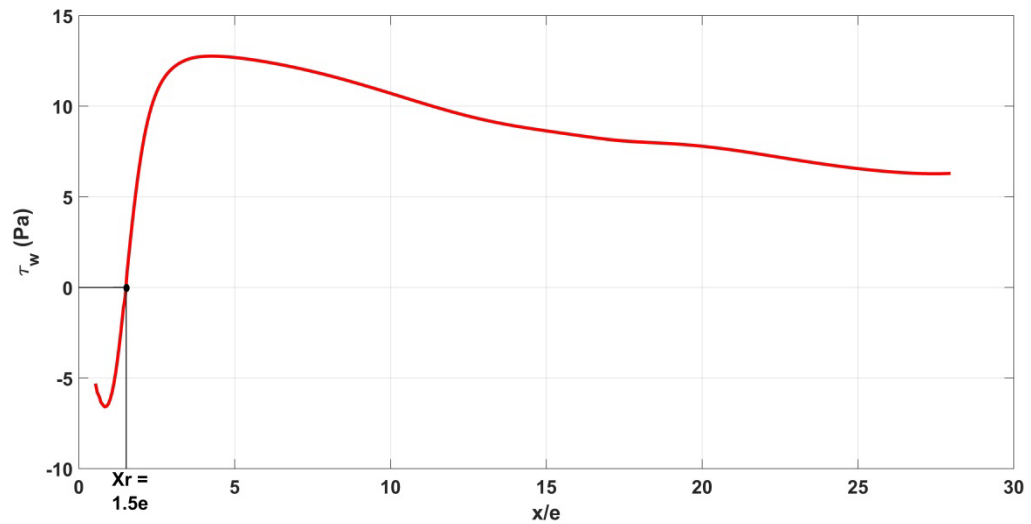


**Figure 4.47** Wall shear stress distribution over the upper surface of the Mold 1

### 4.3.2 Study of the convective heat transfer coefficient

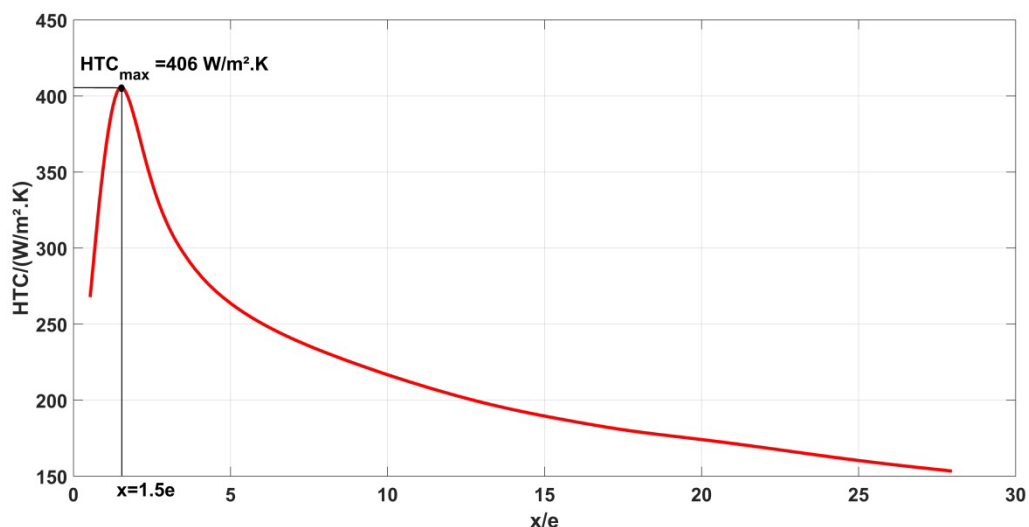


**Figure 4.48** *HTC* distribution over the upper surface of the “representative mold”

The obtained profile of *HTC* in Figure 4.48 and extracted over the upper surface of the Mold 1, presents a parabolic behavior similar to that obtained in Figure 4.24. The notable difference is that the *HTC* reaches a maximum value at  $x = 1.5e$ . This position corresponds to the reattachment length of the separated-reattached flow region as shown above.

However, the obtained behavior shows a non-uniform distribution of the convective heat transfer coefficients over the mold. During autoclave molding, such heterogeneities can contribute to the presence of thermal gradients within composite pieces. These thermal gradients are responsible, in most case, of the appearance of residual stresses that can affect the mechanical properties of composite parts and thus their qualities at the end of the process.

Given this fact, optimization work based on a parametric study was performed in order to improve the intensity as well as the uniformity distribution of the convective heat transfer coefficients over the mold surface.

### 4.3.3 Parametric study and optimization

The performed parametric study aims to investigate the impact of the geometrical design of the installed obstacles over the behavior of the velocity field, and thus over the *HTC* distribution around the mold surface.

The geometrical design of these obstacles signifies more precisely the dimensions and the positions of the holes within the obstacles as well as the separating distance



between the obstacles, i.e. between the first and the second one and between the third and the fourth one. Thus, the geometrical design involves the definition of numerous and various parameters.

Therefore, the desired investigation requires the study of the impact of these parameters and their combinations on the physical phenomena of interest. Such investigation dictates then the carrying out of numerous numerical simulations in order to take into account the various possibilities of these parameter combinations. This methodology of work is time consuming and the cost can be too prohibitive. Consequently, a new approach is required.

Based on the above discussion, it was decided to resort then to a new technique called “metamodeling techniques” or “approximate models”. In fact, the metamodeling techniques consist first of running simulations, automatically by the CFD tool, at a set of sampling points defined in an experimental design space called “Design of Experiments” (DOE). These sampling points represent practically different combinations of values assigned to the defined input parameters. The latter called also design variables. Then, metamodels or surrogate models (interpolations) are used to describe the relationship between resulting physical quantities of interest, called also output parameters or objective functions, and the input parameters or design variables. These metamodels provide quickly the approximated values of the output parameters, everywhere in the analyzed design space, without having to perform a complete and expensive simulation. Therefore the metamodeling techniques allow fast surrogates or approaches for the objective functions that can be used later for optimization.

The metamodeling techniques can replace then the existing numerical simulations and allow a more rapid optimization process because they provide [10][11]:

- a better understanding of the relationship between the design variables and the objective functions. This relationship is typically difficult to establish when running numerical calculations randomly.
- facilitated integration of domain dependent computer codes. This means that there is no need to work with the codes themselves but rather simple approximations of them.
- fast analysis and more efficient tools for optimization and exploration of the design space by using the approximations rather than the expensive numerical computations themselves.

In the following, the application of the metamodeling techniques for the parametric study of the “representative mold” is exposed and detailed.



### 4.3.3.1 Creation of the experimental design (DOE)

The creation of the experimental design space requires the definition of:

- the design variables (input parameters)
- the design space
- the objective functions (output parameters)

#### 4.3.3.1.1 Design variables

The main design variables or the input parameters used to modify the geometric design of the obstacles have been presented in section 3.4.1. They are recalled in Figure 4.49.

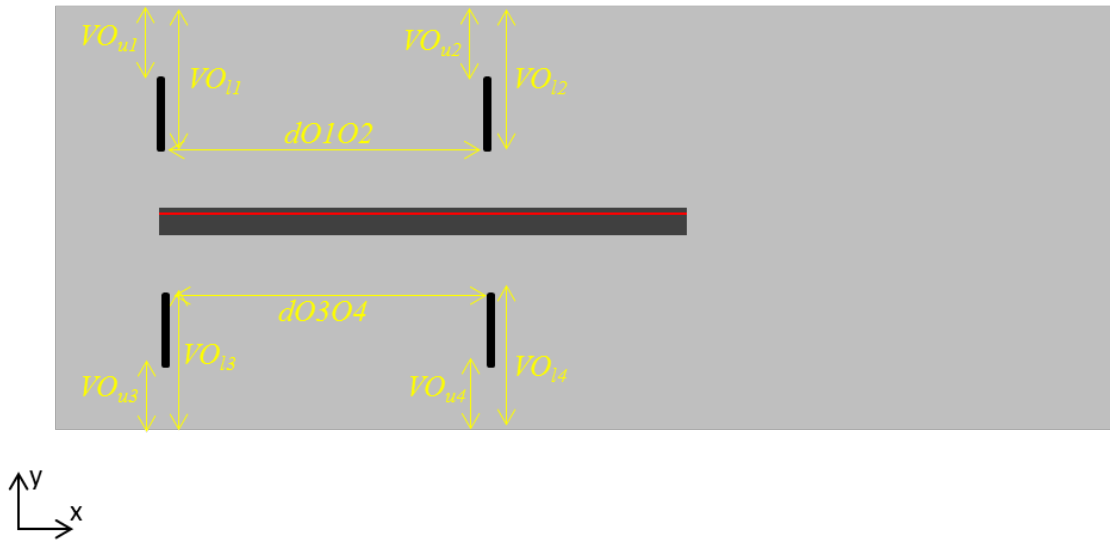


Figure 4.49 Definition of the geometric design parameters

These main design parameters allow then the variation of the size and the position of the obstacles holes as well as the distance between the different obstacles as explained previously.

In order to reduce the number of the input parameters and then to reduce the time consuming of numerical computations, it was decided that the parameters of the geometrical design of the other obstacles, i.e.  $O_2$ ,  $O_3$ , and  $O_4$ , follow the same variation of those of the obstacle one ( $O_1$ ), it means that:

- $VO_{u2} = VO_{u3} = VO_{u4} = VO_{u1}$
- $VO_{l2} = VO_{l3} = VO_{l4} = VO_{l1}$
- $dO_3O_4 = dO_1O_2$

Another advantage of this decision is that the geometrical designs of the lower obstacles (the third and the fourth one) are modified in the same manner as those of the upper obstacles (the first and the second one) allowing then the obtaining of a

symmetrical flow and thus a symmetrical  $HTC$  distribution between the upper and the lower surface of the “representative mold”.

To create the limits of the design space, each of these design parameters must be defined in a search range or an interval which allows the assignment of different values to these input parameters and thus the creation of different combinations. These intervals are defined as follows (Equation (3.12)):

$$\begin{aligned} 0.01 \text{ m} < VO_{ul} < 0.15 \text{ m} \\ VO_{ul} < VO_{ll} < 0.17 \text{ m} \\ 0.01 \text{ m} < dO_1O_2 < 0.5 \text{ m} \end{aligned} \quad \text{Equation (3.8)}$$

These ranges were defined in a manner to cover the largest amount of combinations possible between the input parameters without creating issues in the geometrical model and thus in the constructed meshes.

#### 4.3.3.1.2 Choice of the type of the design space

Various methods and algorithms exist to spread the created sample points in the design space. The classical and widely used methods include “Factorial or Fractional Factorial”, “Central Composite Design” (CCD), “Box-Behnken”, “Alphabetical Optimal”, and “Plackett-Burman” designs [12]. However, these classical methods tend to spread the sample points around boundaries of the design space and leave a few at the center. According to the authors Sacks *et al.* [13], a good experimental design tends to fill the design space rather than to concentrate on the boundary. They also stated that these classical methods can be inefficient or even inappropriate to represent the sampling points in the design space. On the other hand, Simpson *et al.* [14] confirmed that a consensus among researchers was that a design should be “space filling”.

Two types of “space filling” sampling methods are relatively among the most often used in the literature [12]: these are “Orthogonal Arrays” and the various “Latin Hypercube designs”. The latter was employed by several researchers [15,16] as it avoids clustering samples. In fact, in a “Latin Hypercube designs”, the points are randomly generated in a square grid across the design space, but no two points share the same value. In addition, it allows the achievement of a more uniform space distribution of points, i.e. maximizing the distance between points.

Based on the above discussion, it was decided to use in this study the “Latin Hypercube designs” method, provided by the CFD tool ANSYS Fluent, to create efficiently the design space that contains the sampling points. In total, 126 sample points were constructed in the design space.

#### 4.3.3.1.3 Objectives functions

The objectives functions are in fact the output parameters that represent the resulting physical quantities of interest. In this study, it is interesting to investigate the impact of the geometric design parameters defined above on the convective heat transfer coefficient ( $HTC$ ) distribution over the mold surface. Given this fact, two output parameters were defined:

- $\overline{HTC}$  which is the space-mean of  $HTC$  values over the length of the upper surface of the mold.
- $\sigma (HTC)$  which is the standard deviation of the  $HTC$  values over the length upper surface of the mold.

In fact, these two defined output parameters, i.e.  $\overline{HTC}$  and  $\sigma (HTC)$ , allows to visualize more precisely the impacts on the intensity and the distribution behavior respectively of the convective heat transfer over the mold surface.

#### 4.3.3.1.4 Summary

After the creation of the design space that contains the 126 sampling points according to the input parameters and their search ranges, numerical simulations were performed automatically by the CFD tool ANSY Fluent for each of these 126 sampling points. At the end of each simulation, the values of  $\overline{HTC}$  and  $\sigma (HTC)$  were determined and correspond in fact to each tested geometrical design of the obstacles.

#### 4.3.3.2 Surrogate model

After selecting an appropriate experimental design (DOE) and performing the necessary computer runs for each sample point, the next step involves choosing an approximating model or a fitting method in order to describe the relationship between the resulting objective functions and the design variables as explained before.

The most popular techniques of surrogate models are the “Second-Order Response Surface” models and “Kriging” models [17]. The difference between the two methods is that the “Response Surface” modeling typically employs least squares regression to fit a polynomial model to the sampled data while “Kriging” models are chosen to interpolate the data and are fit using maximum likelihood estimation [18].

In fact, the polynomial models are popular for a number of reasons one of which is that they provide a compact and explicit functional relationship between the output and the input parameters. In addition, the method of least squares used in creating the models is relatively computationally inexpensive and straightforward. Originally these polynomial modeling methods were developed to produce smooth approximation models of response data contaminated with random error found in

typical physical (stochastic) experiments. Due to the ease of use of the polynomial modeling methods, these techniques migrated to the field of deterministic computer experiments where there is no random error (i.e., response data are identical each time the simulation is repeated). The applicability of using these methods in modeling deterministic response data was the subject of debate in the statistical community, some aspects of which were addressed by Simpson *et al.* [11].

Since computer experiments typically lack random error, Sacks *et al.* [13] proposed, in response to this issue, the use of a more appropriate and perhaps more “statistically sound” interpolation models to approximate response data obtained from deterministic computer simulations. Their interpolation models are based on techniques known as “Kriging”. The validity of the “Kriging” model is not dependent on the existence of random error and may be better suited for applications involving computer experiments because it can either honor the data, providing an exact interpolation, or smooth the data [19]. Further, the interpolation model of “Kriging” response surface has a very flexible shape and is capable of modelling complex surfaces.

In general, the “Kriging” models are more accurate for nonlinear problems and they are also flexible in either interpolating the sample points or filtering noisy data [12]. On the contrary, the polynomial or “Response Surface” models are easy to construct, clear on parameter sensitivity, and cheap to work with but are less accurate than the “Kriging” models and they do not interpolate the sample points [14].

Based on the above discussion, it was decided to use the “Kriging” surrogate method and which is provided by the CFD tool ANSYS in order to interpolate the data.

Figure 4.50 and Figure 4.51 illustrate for example the response surfaces that describe the relationship between the determined objective functions of interest, i.e.  $\overline{HTC}$  and  $\sigma (HTC)$ , and defined design variables, i.e.  $VO_{ul}$ ,  $VO_{ll}$ . The square points shown on the presented surfaces are the sample points created in the design space.

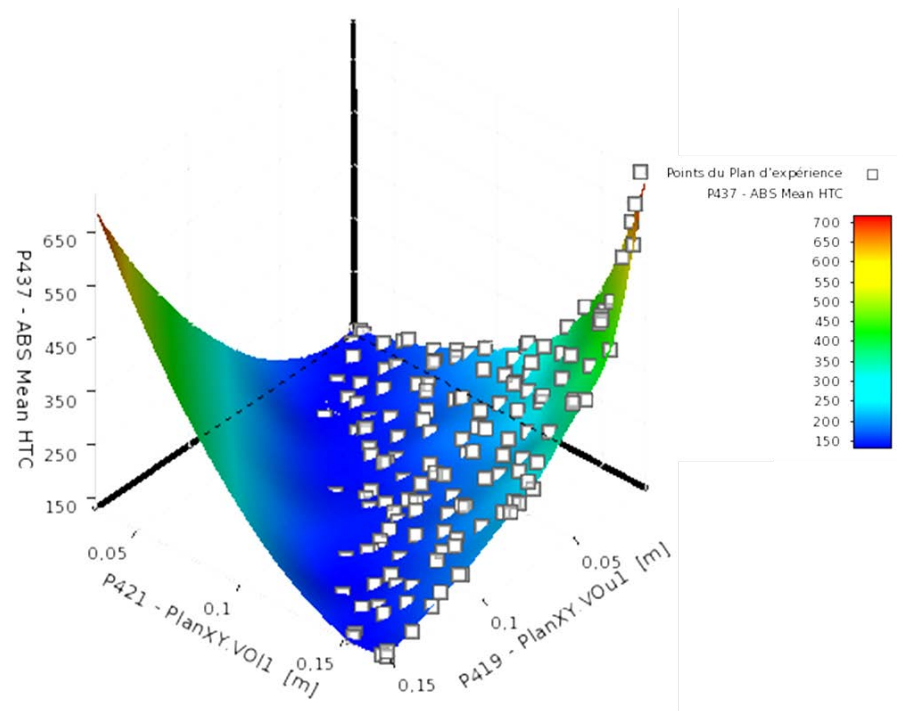


Figure 4.50 Response surface of  $\overline{HTC}$  against  $VO_{ul}$  and  $VO_{ll}$ .

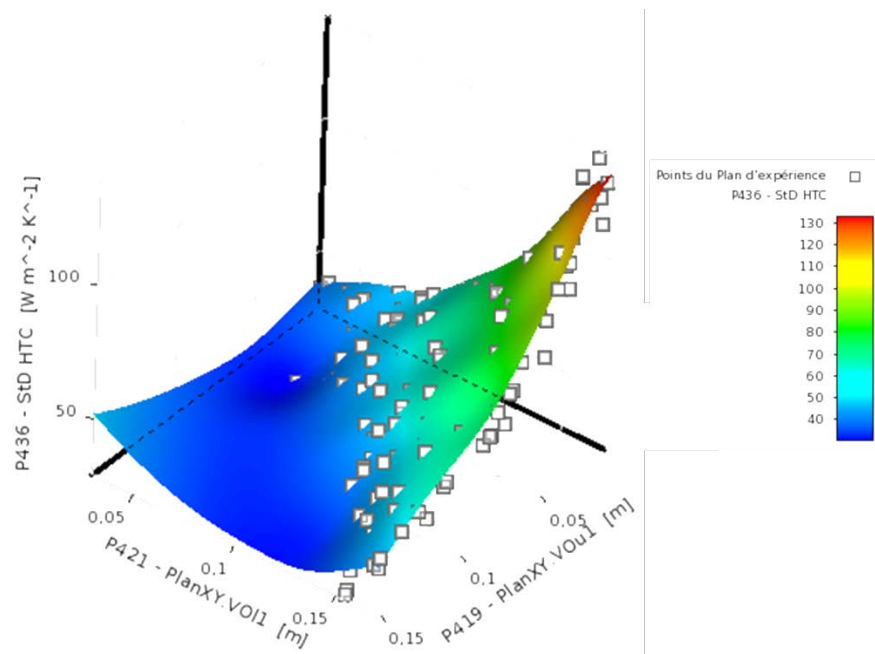


Figure 4.51 Response surface of  $\sigma(HTC)$  against  $VO_{ul}$  and  $VO_{ll}$

The quality of the approximation and the goodness of fit of the obtained surfaces can be verified by examining some criteria. These criteria are listed in Table 4.7. It

shows also the calculated values for each of these criteria for the DOE points located in the obtained surfaces above.

**Table 4.7 Approximation quality of the applied metamodel**

Approximation quality	$\overline{HTC}$	$\sigma (HTC)$
Coefficient of Determination ( $R^2$ ) (Best value = 1)	1	1
Maximum Relative Residual (Best value = 0)	0	0
Root Mean Square Error (Best value = 0)	$1 \times 10^{-4}$	$4.4 \times 10^{-6}$
Relative Maximum Absolute Error (Best value = 0)	0	0
Relative Average Absolute Error (Best value = 0)	0	0

In addition, the goodness of fit can be verified by using what is called “Verification Points”. In this study 10 validation points were constructed. For each of these validation points, the values of the output parameters, i.e.  $\overline{HTC}$  and  $\sigma (HTC)$ , were calculated directly on one hand by means of CFD computations, and on the other hand by using the response surfaces shown previously and based on the “Kriging” metamodel. The results are shown respectively in Figure 4.52 and Figure 4.53. The comparison between the CFD and “Kriging” values shows that the interpolation model predicts quite well the physical quantities of interest.

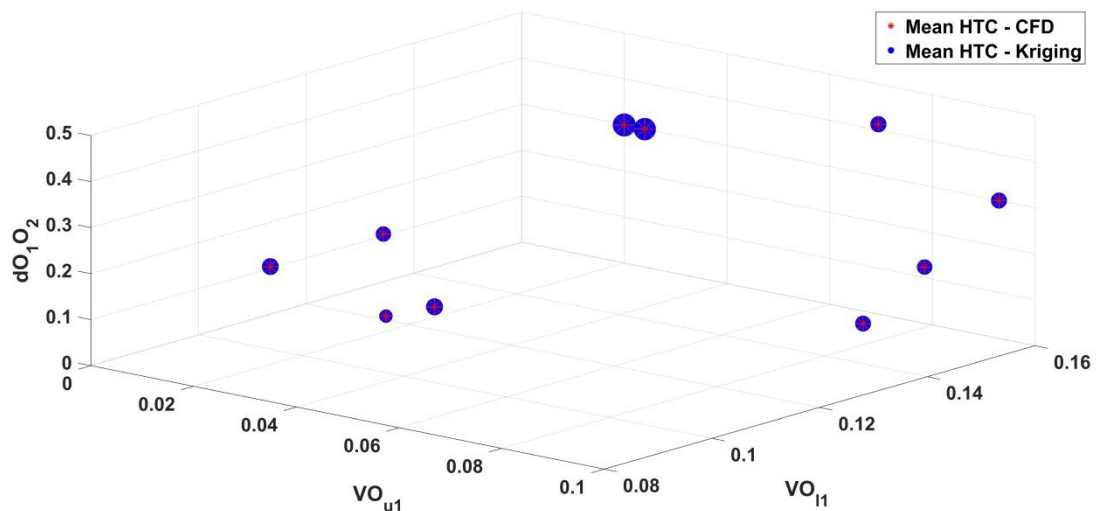


**Figure 4.52 CFD Vs Metamodel  $\overline{HTC}$  on the validation points**

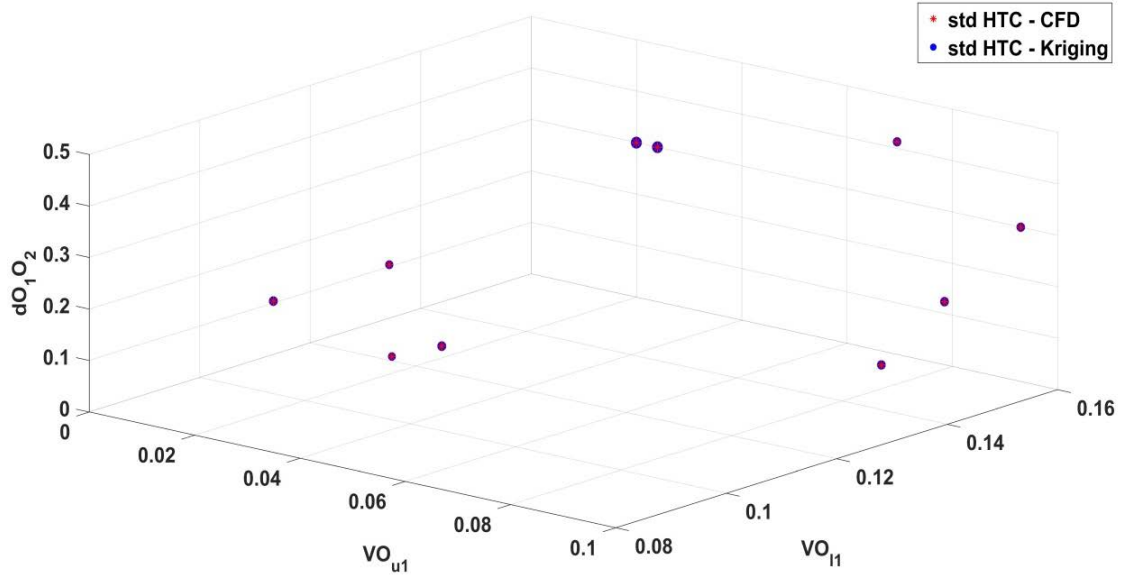


Figure 4.53 CFD Vs Metamodel  $\sigma(HTC)$  on the validation points

Therefore, based on the obtained results shown in Table 4.7, Figure 4.52 and Figure 4.53, it can be deduced that the “Kriging” model has succeeded to interpolate well the generated data.

The ability to establish a relation between the objective functions of interest and the defined design variables allows to go further and to perform an optimization study. The optimization study, based on the use of an optimization algorithm, enables to search into the obtained surface and then to find what is called “candidate points”. These candidates points represent in fact optimal geometrical designs of the obstacles that allow to meet certain criteria and constraints defined for the objective functions.

#### 4.3.3.3 Optimization study

In this study, we are interested to perform an optimization work that aims essentially to increase the intensity of the convective heat transfer coefficients ( $HTC$ ) on one hand, and to minimize its heterogeneity distribution on the other hand. In the case of an autoclave molding, such constraints allow respectively to increase the convective heat transfer rates and then to reduce the curing cycle time of a manufactured composite part as well as to improve its quality. Therefore it can result in an increase of the quality/cost ratio of a composite item.

Mathematically, these criteria are defined as following:

- Maximizing  $\overline{HTC}$

- Minimizing  $\sigma (HTC)$

To carry out an optimization problem, various optimization methods and algorithms exist. Among them, the widely used one is the “Multi-Objective Genetic Algorithm” (MOGA). In fact, the algorithm MOGA is a global optimization method [15] that offer more and better feasible Pareto designs. It offers broader and finer solutions but it is more time consuming [20]. In addition, several other researchers [10,16,21] have employed the MOGA algorithm to perform design optimization studies.

The MOGA algorithm was then applied coupled with the metamodeling technique result showed above in order to obtain the optimal geometric designs of the obstacles according to the criteria defined previously.

At the end of the optimization processes, a candidate point was generated. This candidate point is given in Table 4.8.

**Table 4.8 The suggested candidate point issued from the optimization study**

Candidate points	$VO_{ul}$ (m)	$VO_{ll}$ (m)	$dO_1O_2$ (m)	CFD		Metamodel	
				$\overline{HTC}$ (W/m <sup>2</sup> .K)	$\sigma (HTC)$ (W/m <sup>2</sup> .K)	$\overline{HTC}$ (W/m <sup>2</sup> .K)	$\sigma (HTC)$ (W/m <sup>2</sup> .K)
Point 1	0.01	0.17	0.4	764	125	747	116

Figure 4.54 shows the new optimal geometric design of the “representative mold” according to the suggested candidate point.

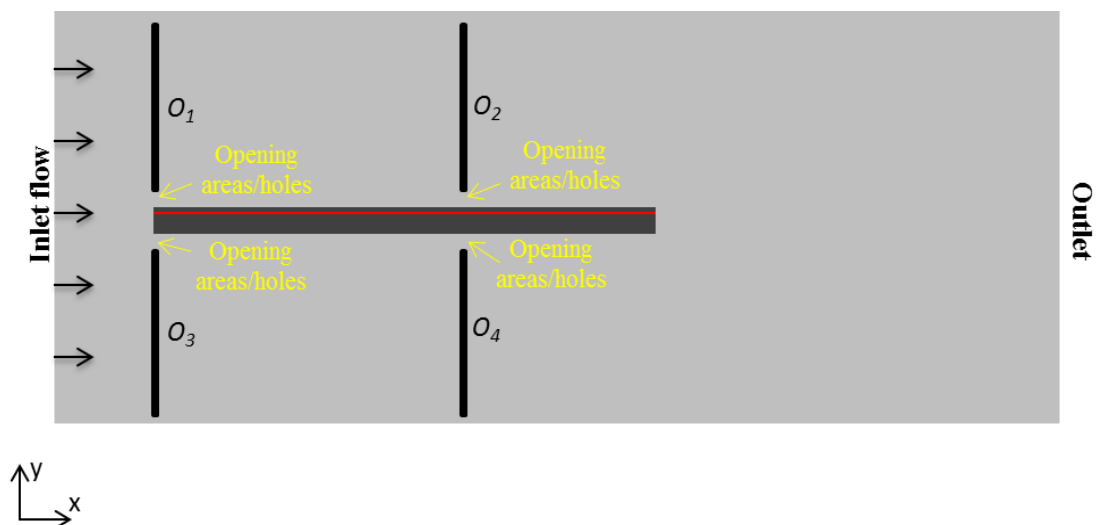


**Figure 4.54 The obtained optimal geometric design of the obstacles**



It can be clearly seen that the new geometric design, proposed by the optimization algorithm, consists of using long obstacles with keeping small holes or opening areas near the mold surfaces (Figure 4.54). With this design, the air flow is blocked inside the working section due to the high pressure drop created by these obstacles, and thus the air flow is forced to pass through these small opening areas. Therefore, and according to the mass conservation principle, the air flow passes through these inlets with high velocity. This can be observed by the obtained new velocity field shown in Figure 4.55.

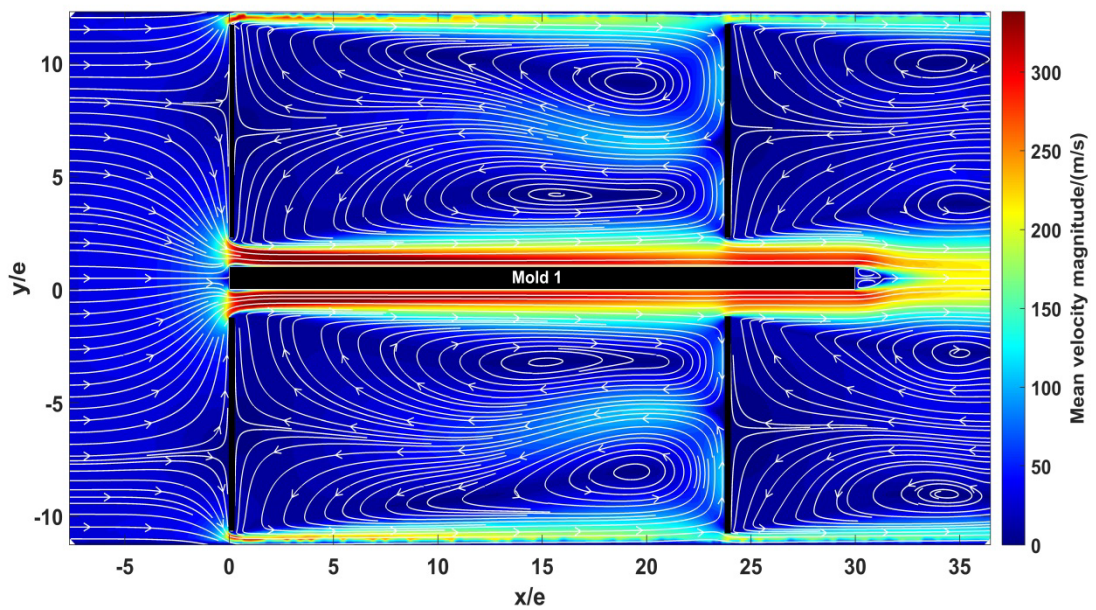


**Figure 4.55** Flow field around the new design of the representative mold

The remarkable increase in velocity magnitude over the mold surfaces is able to increase also notably the convective heat transfer coefficient ( $HTC$ ) values. The new distribution of  $HTC$  after optimization is plotted in Figure 4.56. Similarly,  $HTC$  reaches a maximum value at  $x=0.7e$  and which corresponds to the position of the reattachment length deduced in Figure 4.57. Afterwards,  $HTC$  decreases. However, at  $x=22.7e$ ,  $HTC$  undergoes a change in the behavior and shows an increasing evolution. This change is due to the second obstacle ( $O_2$ ) located at the same position  $x/e$ . In fact, the obstacle is closer to the mold surface than in the former design (Figure 4.49 vs Figure 4.54) leading then to modification in the velocity field. This can be observed also by plotting the wall shear stress distribution in Figure 4.57.

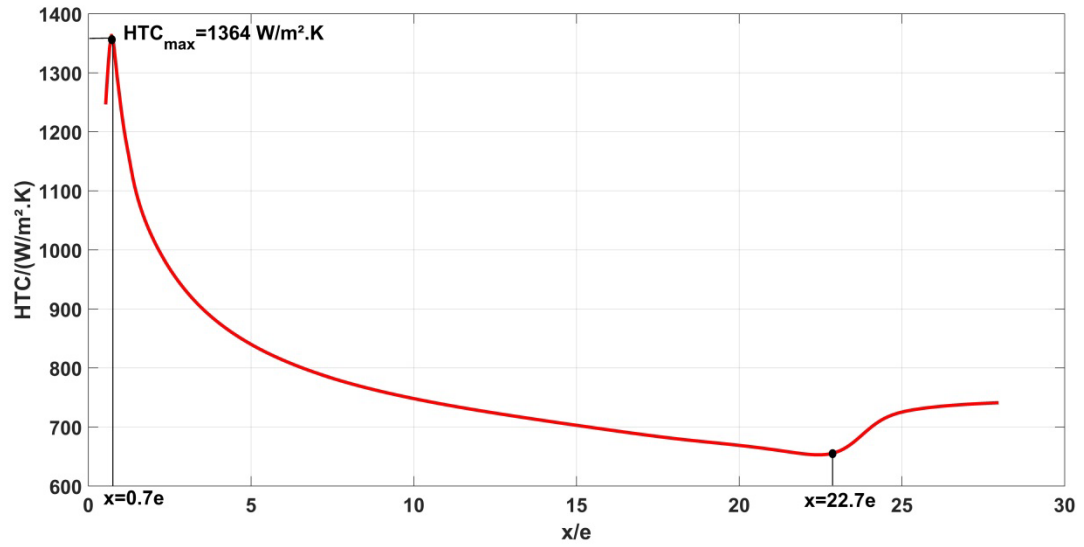


Figure 4.56 The new *HTC* distribution over the upper surface of Mold 1

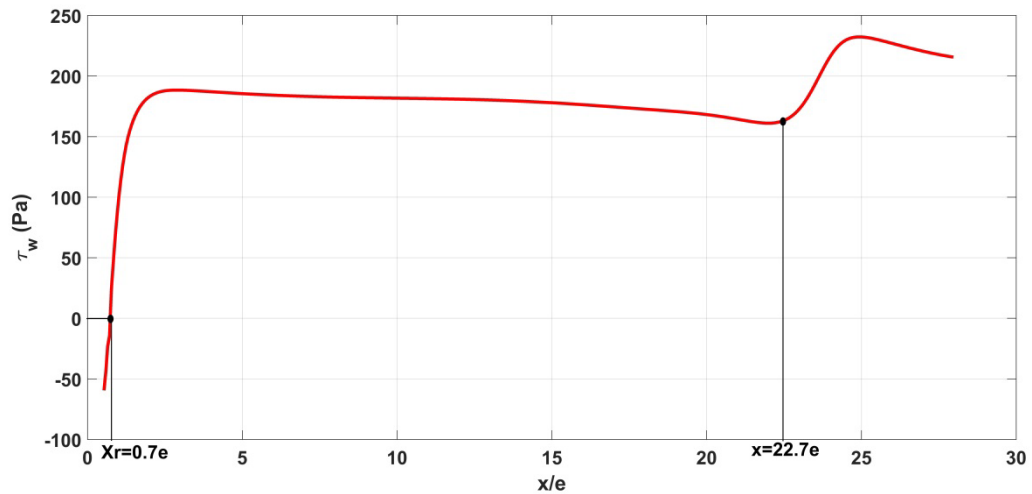
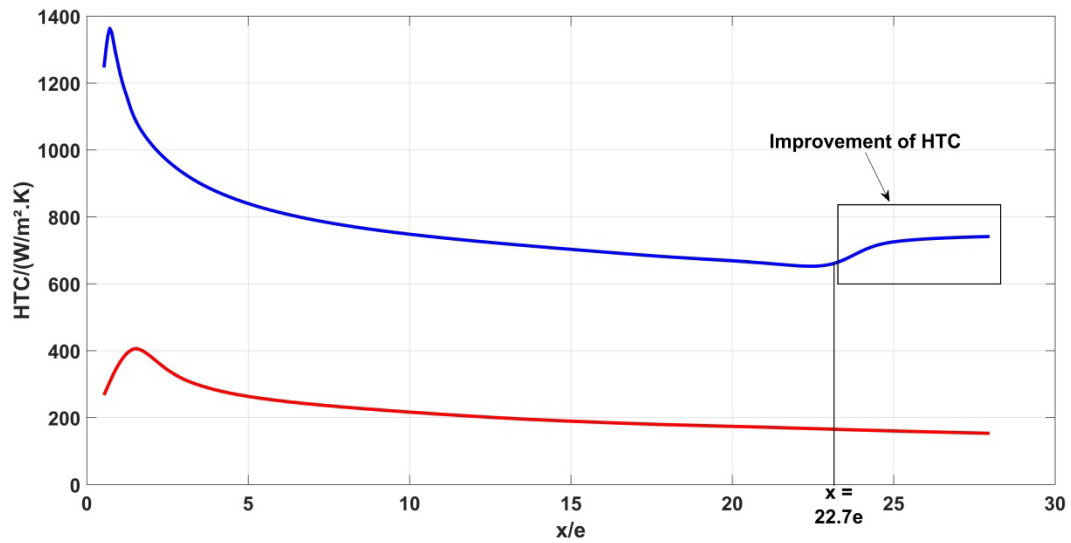


Figure 4.57 The new wall shear stress distribution over Mold 1

As mentioned before, this optimal design allows the intensification of the convective heat transfer coefficient around the mold surfaces in comparison with the former design. This intensification brought by the optimal solution can be deduced by plotting the *HTC* behaviors (Figure 4.58) obtained from the former design (red) against that obtained one from the new geometric design (blue).



**Figure 4.58** HTC over the upper surface of Mold 1: optimal design vs former design

Indeed, the new optimal design allows an increasing of 263% of the space-average  $HTC$  values ( $\overline{HTC}$ ) over the mold surface in comparison with the value obtained from the basic design (Table 4.9).

**Table 4.9**  $HTC$  comparison between the former and the new design

	$\overline{HTC}$ (W/m <sup>2</sup> .K)	$\sigma (HTC)$ (W/m <sup>2</sup> .K)	$CV$ (%)
Former design	210	59	28
New optimal design	764	125	16

To judge the improvement of the uniformity of the  $HTC$  distribution, and given the fact that these distributions were issued from two different configurations (former Vs new) and then from two different data, it was decided to resort to another statistical measure, rather than the standard deviation ( $\sigma$ ). The used statistical measure is the coefficient of variation ( $CV$ ) that measure the dispersion of data points in a data series around the mean. The coefficient of variation represents the ratio of the standard deviation to the mean ( $\sigma (HTC)/\overline{HTC}$ ), and it is a useful statistic for comparing the degree of variation from one data series to another, even if the means are drastically different from one another.

It was found that the coefficient of variation decreased with the new optimal design (Table 4.9). That means that the dispersion of the  $HTC$  values around the mean over the mold surface decreased, which can lead to deduce that the uniformity of the convective heat transfer coefficients has been improved with the new geometric design. This finding can be deduced also by noticing the change in the  $HTC$  behavior

at  $x=22.7e$ . In fact, this change indicates that *HTC* is not henceforth monotonically decreasing after the reattachment of the recirculation region as obtained previously for the other configuration studies. Therefore, this improvement of *HTC* values after the recirculation-reattachment of the flow is able to reduce the heterogeneity. Moreover, it leads to deduce also that installing more than two obstacles above the upper surface of the mold, with optimized design, can improve the *HTC* values at various locations in the reattachment region and thus can improve the *HTC* uniformity.

At the end of the performed optimization work, it can be concluded that the obtained findings bring a new way to enhance the distribution behavior and the values of the convective heat transfer coefficient over molds surfaces. In the case of an autoclave molding, such solution is able to reduce the time of the curing cycle on one hand, and to improve the quality of manufactured composite parts on the other, leading then to increase in the quality/cost ratio for the composite manufacturers. However, this gain in the quality/cost ratio on one hand can be affected by potential extra charges on the other hand. These extra charges can be due to the increase in the motor fan power in order to overcome the pressure drops generated by installing obstacles around molds.

The overall results issued from the numerical model of the “representative mold” as well as from the optimization study require validation works by means of experimental measurements as made previously for other configuration studies.

#### **4.4 Partial conclusion**

In this chapter, the developed experimental and numerical methodologies for the investigation of the flow field structure and the convective heat transfer around molds were applied. Different configurations were tested such as the installation of one or multiple molds within the working section of the model autoclave as well as the use of a “representative mold”. The aerodynamic and thermal findings have been found to be correlated and the velocity fields were able to interpret the thermal phenomena. In the case of a single mold study, these findings have been compared to those reported by the previous research works and the comparison has shown a good agreement. These correlations between the aerodynamic and the thermal findings and between the literatures indicate again that the model autoclave has been well designed and it is able to produce physical phenomena. Also, comparison works between the experimental results and those derived from the numerical model have been performed. These comparison works have shown that the constructed 2D RANS numerical model was able to predict quite well the investigated physical phenomena, with exceptions are made in the case of complex flow structures such as the presence of wake regions. However, the main conclusion is the presence of no-uniform distribution of the convective heat transfer coefficients over the molds. This heterogeneity can contribute to the presence of thermal gradients within the composite pieces. These thermal gradients are responsible of the presence of residual constraints which can affect the mechanical properties of the composite items and therefore their qualities. In the case of manufacturing of several composite parts simultaneously, different heat transfer coefficient distribution can occur between the parts leading then to the production of different composite items with different qualities. Furthermore, it was found that the separation distance between molds has an impact on the convective heat transfer coefficients over the backward molds, but the *HTC* behaviors still difference from that one over the forward mold. In the case of a mold equipped with obstacles, the MOGA optimization algorithm combined with “Kriging” metamodel have succeeded to propose a new geometric design that allows the intensification of the convective heat transfer coefficient and the minimizing of their heterogeneity distribution over the mold surface. However, the obtained result requires a validation work by means of experimental tests. The latter will be performed in future works.

## List of references

- [1] N. Djilali, I.S. Gartshore, Turbulent flow around a bluff rectangular plate. Part I: experimental investigation, *J. Fluids Engineering*. 113 (1991) 51–59.
- [2] L. Graftieaux, M. Michard, N. Grosjean, Combining PIV , POD and vortex identification algorithms for the study of unsteady turbulent swirling flows, *Meas. Sci. Technol.* 12 (2001) 1422–1429.
- [3] M. Kiya, K. Sasaki, Structure of a turbulent separation, *J. Fluid Mech.* 137 (1983) 83–113.
- [4] H. Huang, D. Dabiri, M. Gharib, On errors of digital particle image velocimetry, *Meas. Sci. Technol.* 8 (1997) 1427–1440.
- [5] H. Yanaoka, H. Yoshikawa, T. Ota, Numerical simulation of laminar flow and heat transfer over a blunt flat plate in square channel, *J. Heat Transfer*. 124 (2002) 8–16. doi:10.1115/1.1420715.
- [6] T. Ota, N. Kon, Heat transfer in the separated and reattached flow on a blunt flat plate, *J. Heat Transfer*. 96 (1974) 459–462.
- [7] E.M. Sparrow, S.S. Kang, W. Chuck, Relation between the points of flow reattachment and maximum heat transfer for regions of flow separation, *Int. J. Heat Mass Transf.* 30 (1987) 1237–1246. doi:10.1016/0017-9310(87)90157-8.
- [8] T. Ota, N. Kon, Heat transfer in the separated and reattached flow over blunt flat plates - Effects of nose shape, *Int. J. Heat Mass Transf.* 22 (1979) 197–206.
- [9] J.H. Gerrard, The mechanics of the formation region of vortices behind bluff bodies, *J. Fluid Mech.* 25 (1966) 401–413. doi:10.1017/S0022112066001721.
- [10] J. Wen, H. Yang, G. Jian, X. Tong, K. Li, S. Wang, Energy and cost optimization of shell and tube heat exchanger with helical baffles using Kriging metamodel based on MOGA, *Int. J. Heat Mass Transf.* 98 (2016) 29–39. doi:10.1016/j.ijheatmasstransfer.2016.02.084.
- [11] T.W. Simpson, J.D. Peplinski, P.N. Koch, J.K. Allen, On the use of statistics in design and the implications for deterministic computer experiments, in: *Proc. 1997 ASME Des. Eng. Tech. Conf., Sacramento, California, 1997*: pp. 1–14.
- [12] G.G. Wang, S. Shan, Review of metamodeling techniques in support of engineering design optimization, *J. Mech. Des.* 129 (2006) 370–380. doi:10.1115/1.2429697.
- [13] J. Sacks, W. Welch, T. Mitchell, H. Wynn, Design and analysis of computer experiments, *Stat. Sci.* 4 (1989) 409–423. doi:10.2307/2245858.
- [14] R. Jin, W. Chen, T. Simpson, Comparative studies of metamodeling techniques under multiple modeling criteria, in: *8th Symp. Multidiscip. Anal. Optim.*, 2000: pp. 1–13. doi:10.2514/6.2000-4801.
- [15] A. Navid, S. Khalilarya, H. Taghavifar, Comparing multi-objective non-

- evolutionary NLPQL and evolutionary genetic algorithm optimization of a DI diesel engine: DoE estimation and creating surrogate model, *Energy Convers. Manag.* 126 (2016) 385–399. doi:10.1016/j.enconman.2016.08.014.
- [16] Z. Khatir, H. Thompson, N. Kapur, V. Toropov, J. Paton, Multi-objective Computational Fluid Dynamics (CFD) design optimisation in commercial bread-baking, *Appl. Therm. Eng.* 60 (2013) 480–486. doi:10.1016/j.applthermaleng.2012.08.011.
- [17] A.A. Giunta, L.T. Watson, A comparison of approximation modeling techniques : polynomial versus interpolating models, in: 7th AIAA/USAF/NASA/ISSMO Symp. Multidiscip. Anal. Optim., 1998: pp. 1–13. doi:10.2514/6.1998-4758.
- [18] J.R. Koehler, A.B. Owen, Computer Experiments, in: *Handb. Stat.*, Elsevier Science, New York, 1996: pp. 261–308.
- [19] N.A.C. Cressie, *Statistics for Spatial Data*, Wiley & Sons, New York, 1993.
- [20] N. Hu, P. Zhou, J. Yang, Comparison and combination of NLPQL and MOGA algorithms for a marine medium-speed diesel engine optimisation, *Energy Convers. Manag.* 133 (2017) 138–152. doi:10.1016/j.enconman.2016.11.066.
- [21] T. Okabe, Y. Oya, G. Yamamoto, J. Sato, T. Matsumiya, R. Matsuzaki, S. Yashiro, S. Obayashi, Multi-objective optimization for resin transfer molding process, *Compos. Part A* 92 (2017) 1–9. doi:10.1016/j.compositesa.2016.09.023.





# *General Conclusion and Perspectives*



In this thesis study, a new approach has been developed which allows an accurate knowledge of the convective heat transfer coefficient distribution around molds during an autoclave process. Such knowledge enables the production of more appropriate boundary conditions around molds, and thus an accurate prediction of the thermal history of composite pieces.

The developed new approach consists of using an autoclave model designed and fabricated based on the respect of similarity conditions against an actual commercial autoclave. The developed autoclave model allows the carrying out of experimental tests with different volume flow rates. This can be advantageous for investigating various encountered cases within an actual autoclave as well as for studying different autoclaves with different characteristics. The obtained test bench is in fact a closed-wind tunnel which contains mainly a test section or a working section where molds of various shapes and geometries can be installed. During the thesis study, simple molds of rectangular box shape have been used.

Furthermore, experimental aerodynamic and thermal measurement methodologies have been developed for the analysis respectively of the velocity fields and the convective heat transfer coefficients around the molds. These methodologies are based on the use of non-intrusive measuring instruments such as the PIV technique and the infrared imaging.

The PIV system has first been employed to validate the flow field within the empty working section according to the set of specifications defined during the design works. The validation tasks have shown a good respect of the fixed set of specifications, in particular the obtaining of a uniform and steady velocity field. In addition, they permitted the characterization of the flow in terms of free stream velocity and turbulence intensity for the different tested volume flow rates. The obtained low turbulence levels allow the validation of the autoclave model as a high quality closed-loop wind tunnel.

The validation of the model autoclave as an operational test bench has enabled then the investigation of different molding configuration cases that can be encountered during an autoclave process. Three cases have been under the scope: the mono-loading which consists of studying one single mold within the working section, the multi-loading which consists of installing two molds to study the inter-part shadowing effect and the mold with support structure.

Aside the development of an experimental study, Computational Fluid Dynamics (CFD) computations of the investigated physical phenomena have been carried out by using the commercial CFD code ANSYS Fluent. Different numerical models have been constructed in order to simulate the different configuration studies. The computational domain and the boundary conditions were defined in a manner to respect the experimental conditions. The flow field was solved using the RANS

approach with the use of the SST  $k-\omega$  turbulence model. This turbulence model enables to solve suitably the near wall region with large gradients with the use of finer mesh near the surfaces.

In the case of a single mold installed inside the model autoclave, the PIV measurements of the flow field around the mold has shown the appearance of a two-dimensional separated-reattached flow region near the center region of the mold. Near the side walls, the appearance of horseshoe-vortices has been detected. The velocity streamlines and turbulence intensity profiles have shown the formation of a separation bubble from the leading edge of the mold and characterized by the time-mean reattachment length ( $X_r$ ). The latter was found to be equal to  $5.2e$ , according to the experimental measures, against  $5.6e$  for the numerical simulations for a Reynolds number of  $4 \times 10^4$  based on the mold thickness. According to the numerical investigations, the characteristic length ( $X_r$ ) was found to decrease with increasing turbulence intensity but it was  $Re$ -independent starting from about  $2.4 \times 10^4$ . The analysis of convective heat transfer coefficients ( $HTC$ ) around the mold surface has shown a non-uniform distribution. The maximum value is located near the reattachment position ( $X_r$ ).

The overall aerodynamic and thermal results derived from the numerical model have shown a good agreement with the experimental tests, allowing then the validation of the performed calculations. Moreover, the description of the flow field structure and the  $HTC$  distribution around the mold matches well the conclusions reported by previous research studies of a bluff blunt plate. The main conclusion at the end of this investigation is that, as expected, the convective heat transfer rates are not uniform over the mold surfaces. Consequently, in the case of an actual autoclave manufacturing process with the use of more complex molds shapes, this heterogeneity of convective heat transfer distribution can be more aggravated. Such situation may lead to the presence of thermal gradients within the manufactured composite parts affecting then their mechanical properties and thus their qualities at the end of the process.

The multi-loading investigation has revealed the presence of inter-part shadowing effects. Indeed, the flow field structure and the  $HTC$  distribution over the mold placed downstream have shown a different behavior from those around the mold placed upstream. More precisely, no significant separation bubble has been observed and the  $HTC$  distribution has shown a different behavior along the length of the second mold. In addition, the  $HTC$  values over the mold downstream were about 20% lower than those around the mold upstream. As for the single mold study, the comparison between the experimental results and the numerical ones issued from the corresponding numerical model has shown a good agreement qualitatively and quantitatively. It can be deduced from the shadowing effects investigation that placing

several molds together can engender non-identical curing degrees and therefore the production of different qualities at the end of the curing cycle.

A more realistic industrial case, where a mold equipped with its supports structure, has been studied. A simplified approach was adopted and consisted of installing obstacles around the mold of rectangular box shape. As a first step, the study was performed numerically. The numerical results have shown a complex flow field in the computational domain and characterized by the presence of dead zones downstream the obstacles. In the case of an actual autoclave molding with the presence of a more complex structure, the complexity and the non-uniformity of the flow can be more aggravated which can explain the limited studies that aim to measure the flow field within actual autoclaves. Such flow can significantly perturb the convective heat transfer rates around the molds by reducing their intensities and their uniformity. Based on this fact, an optimization study has been carried out to find an optimal design geometry of the obstacles. The optimization study was based on the use of the optimization algorithm MOGA (Multi-Objective Genetic Algorithm) coupled with metamodeling techniques provided by the used CFD tool. The optimization work has succeeded to converge to an optimal solution according to the defined criteria and it provided a new geometric design of the obstacles. The obtained new design of the obstacles has enabled the intensification of the convective heat transfer coefficient by about 260% on one hand, and on the other hand the reduction of its heterogeneity distribution percentage from 28% to 16%, against the former design. Therefore, such solution can be promising in order to reduce the manufacturing time and cost of a composite item as well as to enhance its quality. Consequently, it can be helpful at the end to increase the quality/cost ratio of composite parts manufacturers.

However, the head losses generated by the obstacles in the optimized configuration can be prohibitive in terms of blower power. An additional objective to the optimization study should then be added: minimizing the head losses. A good compromise between maximizing and making uniform the convective heat transfer and minimizing the head loss generated by additional obstacles should give a better idea to obtain an adequate optimized solution to the manufacturer's point of view.

These last CFD results as well as the optimization findings requires certainly a validation work by means of experimental tests, as done previously for the mono-and multi-loading studies. These tests will be performed in future works.

Furthermore, the presence of dead zones due to the obstacles or to more complex mold geometries and characterized by low velocities invites to consider the possibility of the appearance of the mixed convection, especially near the molds surfaces. The mixed convection depends mainly on the flow velocity and the surface temperature, and it involves a strong coupling between the velocity field and the heat transfer mechanisms. The appearance of the mixed convection is able to modify the velocity

profile near the wall region affecting then the convective heat transfer rates. Based on these facts, it will be interesting in future works to investigate the surface temperature and the air flow velocity conditions under which the mixed convection appears. Such investigation can be performed thanks to the developed test bench as it allows the testing of various volume flow rates combined with various surface temperatures of the molds.

The fabricated model autoclave and its associated instrumentations can be advantageous also in the future for the analysis of convective transfers around representative molds of industrial items that can be manufactured within autoclaves, especially in the aeronautical field, such as airplane wing, airplane nose, airplane fuselage, etc.

In addition, the convective transfer analysis that can be carried out thanks to the implemented experimental tools is helpful to acquire a more accurate knowledge of the boundary conditions around molds during an autoclave process. These obtained boundary conditions can be useful hence to develop numerical models that aim to predict, with more precision, the thermal history of a composite piece placed on a mold. The predicted temperature field within a composite material with specific properties can give answers on the levels of the present thermal gradients and how the latter can affect the mechanical properties and thus the quality of a composite piece. Briefly, such work can allow the establishment of a correlation between the heterogeneity degrees of the convective heat transfer coefficient distribution and the quality degrees of the manufactured part. The obtaining of such correlation can be important to determine the best thermal conditions to produce high quality composite items.

# **Appendix A**

## *Design of the Model Autoclave*





## Table of contents

<b><i>Appendix A Design of the Model Autoclave.....</i></b>	<b><i>219</i></b>
<b>A.1 INTRODUCTION .....</b>	<b>223</b>
<b>A.2 DESIGN GUIDELINES.....</b>	<b>223</b>
A.2.1 Contraction.....	223
A.2.1.1 Contraction ratio .....	224
A.2.1.2 Cross-sectional shape.....	224
A.2.1.3 Contraction length .....	224
A.2.1.4 Wall shape .....	225
A.2.1.5 Final design of the contraction .....	225
A.2.2 Flow conditioners (Settling chamber).....	226
A.2.2.1 Settling duct.....	226
A.2.2.2 Honeycomb.....	226
A.2.2.3 Screens .....	227
A.2.2.4 General arrangement of the screens and the honeycomb .....	229
A.2.3 Diffuser .....	229
A.2.4 Optional components .....	231
A.2.4.1 Wide angle diffuser.....	231
A.2.4.2 Turning sections.....	232
A.2.5 Cooling heat exchanger.....	233
A.2.6 Drive system (fan).....	233
<b>A.3 PRESENTATION OF THE DESIGNED MODEL AUTOCLAVE.....</b>	<b>235</b>
<b>LIST OF REFERENCES.....</b>	<b>238</b>



## **A.1 Introduction**

As explained in *chapter 2*, the concept of the model autoclave should represent a closed wind tunnel with the obtaining of a uniform flow and low turbulence levels at the inlet of its working section. In the field of closed wind tunnels, the obtaining of such flow should pass through the respect of the design guidelines of the main wind-tunnel components. The latter include essentially the flow conditioners, the contraction, the test section, the diffuser, the drive system (fan), and other optional components (Figure A.1).

In the following, these design guidelines will be exposed. Then, they will be applied in order to size main components that should be implemented in the model autoclave in order to meet the flow specifications.

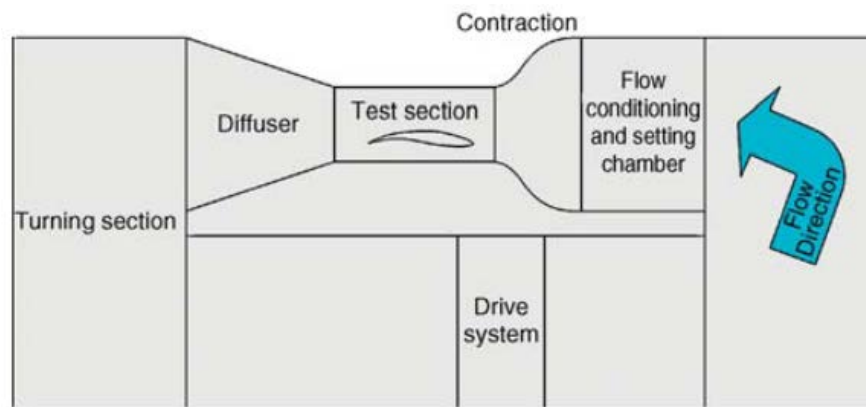


Figure A.1 Schematic of a closed-circuit wind tunnel

## **A.2 Design guidelines**

### **A.2.1 Contraction**

In a wind tunnel, the contraction plays a critical role in determining the flow quality in the test section by reducing both mean and fluctuating velocity variations to a smaller fraction of the average velocity, leading then to the production of a uniform and steady stream at its outlet. The outlet of a contraction corresponds to the inlet of the test section as it placed generally upstream of it (Figure A.1).

However, these flow characteristics and the final turbulence intensity levels in the test section are dictated by the size and shape of the contraction [1]. The most important parameters in determining the design and the shape of a contraction are the

contraction ratio ( $c$ ), the length of the contraction ( $l$ ), the cross-sectional shape and the wall shape.

### A.2.1.1 Contraction ratio

The contraction ratio is defined by the inlet cross section area to the outlet cross section area ratio ( $c=A_{inlet}/A_{outlet}$ ). It was found that contraction ratios between about 6 and 9 are normally used. More precisely, Bell *et al.* [2] recommended a contraction ratio of about 7.7.

Based on this fact,  $c$  was fixed at 7.7 for the contraction implemented in the model autoclave, upstream of the designed working section. Therefore, the inlet cross section area can be determined according to Equation (A.1).

$$\begin{aligned} A_{outlet} &= A_{working\ section} = 0.126\text{ m}^2 \\ A_{inlet} &= 7.7 \times A_{outlet} = 0.882\text{ m}^2 \end{aligned} \quad \text{Equation (A.1)}$$

### A.2.1.2 Cross-sectional shape

In any contraction with a non-circular cross-section, the flow near the walls tends to migrate laterally, especially near corners of a polygonal section. However, the investigations of Mehta *et al.* [3] show that this does not cause a problem in a well-designed rectangular contraction.

Further, it is recommended to keep the same cross-sectional aspect ratio between the inlet and the outlet. This condition, represented by Equation (A.2), allows the determination of the width ( $L_{inlet}$ ) and the height ( $H_{inlet}$ ) of the inlet section of the used contraction.

$$\begin{aligned} H_{inlet}/L_{inlet} &= H_{outlet}/L_{outlet} = 1.27 \\ A_{inlet} &= H_{inlet} \times L_{inlet} = 0.882\text{ m}^2 \\ H_{inlet} &= 1.058\text{ m}, L_{inlet} = 0.833\text{ m} \end{aligned} \quad \text{Equation (A.2)}$$

### A.2.1.3 Contraction length

The length of a contraction should be sufficiently small to minimize boundary layer growth and cost, but long enough to prevent flow separation. In this context, the authors Bell *et al.* [2] recommended in their work that a contraction length ( $l$ ) should be 0.89 times its inlet height ( $H_{inlet}$ ).

Given this guideline, the length ( $l$ ) was found to be about 0.94 m.

#### A.2.1.4 Wall shape

The smoothness in contour shape of a contraction plays an important role in determining the flow characteristics within a test section. In this context, various research works [4,5] have been carried out in order to find analytical solutions or theoretical design, such as matched polynomials methods, for the conception of the wall shape of a contraction.

Bell *et al.* [2] recommended in his work a 5<sup>th</sup> order polynomial function (Equation A.3) for the design of a contraction wall shape in the case of a small and low speed wind tunnel, i.e.  $A_{test\ section} < 0.5\ m^2$  and  $U_{\infty} < 40\ m/s$ . These latter requirements match the specifications of the working section of the model autoclave.

The recommended wall shape was found to be free of separation and provides flow uniformity in the test section. The 5<sup>th</sup> order polynomial function was therefore employed to determine the wall shape of the implemented contraction in the model autoclave.

$$y(x) = H_{inlet} - (H_{inlet} - H_{outlet})[6(x/l)^5 - 15(x/l)^4 + 10(x/l)^3] \quad \text{Equation (A.3)}$$

#### A.2.1.5 Final design of the contraction

The application of the set of the design guidelines exposed above allows the determination of the used contraction in the model autoclave (Figure A.2).

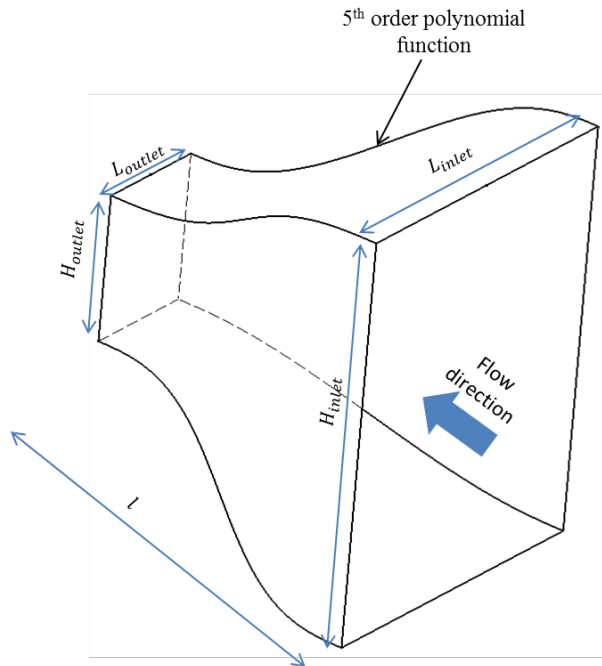


Figure A.2 Schematic of the sized rectangular contraction used in the model autoclave

### A.2.2 Flow conditioners (Settling chamber)

The flow conditioning section or the settling chamber contains normally a settling duct, honeycomb and screens. It is placed upstream of the contraction in a wind tunnel (Figure A.1). An example of a settling chamber is shown in Figure A.3.

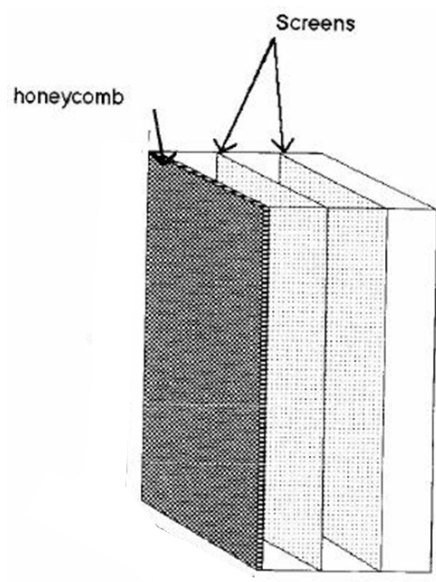


Figure A.3 Schematic of a settling chamber

#### A.2.2.1 Settling duct

Given the fact that the settling duct is placed upstream of a contraction, thus the dimensions of the contraction inlet dictate the cross section dimensions of the rectangular settling duct. Therefore, the dimensions of the required settling duct for the model autoclave are 1.058 m in height and 0.833 m in width.

On the other hand, the settling duct length ( $l$ ) depends on the arrangement of the screens and honeycomb installed inside it. The principle of this arrangement and thus the deduced length are exposed in section A.2.2.4.

#### A.2.2.2 Honeycomb

Theoretically, the honeycomb aligns the flow with the axis of the working section and breaks up larger-scale flow unsteadiness [6]. In fact, it removes swirl from the incoming flow and minimizes the lateral variations in both mean and fluctuating velocity [3].

Honeycomb comes in different shapes such as circular, square, and hexagonal cross sections. Among these, hexagonal is usually the cross-sectional shape of choice,

as it has the lowest pressure drop coefficient [7]. An example of a hexagonal cross section honeycomb is shown in Figure A.4.

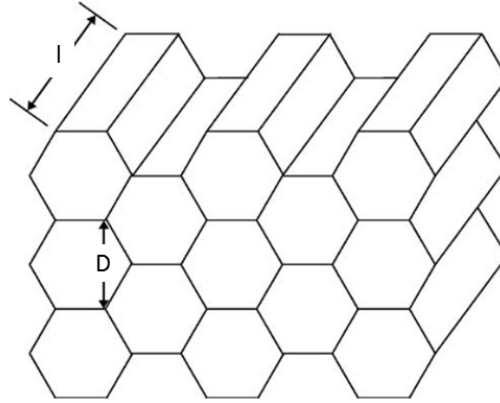


**Figure A.4 Schematic of a hexagonal honeycomb section [6]**

Honeycomb cells have been shown to have the best performance with a length ( $l$ )-to-diameter ( $D$ ) ratio of between 7 and 10 [3]. For maximum overall benefit, the cell size should be about 6-8 times its diameter.

The honeycomb section should have sufficient structural rigidity to withstand applied forces during operation without significant deformation. Given this fact, aluminum honeycombs are to be preferred for their high performance.

Based on these design guidelines, the characteristics of the selected honeycomb to be installed inside the settling chamber of the model autoclave are presented in Table A.1.

**Table A.1 Characteristics of the used honeycomb**

	Material	Cross section shape	$D$ (mm)	$l$ (mm)	$l/D$	$L$ (m)	$H$ (m)
<b>Selected Honeycomb</b>	Aluminum	hexagonal	3.2	25	7.8	1.058	0.833

### A.2.2.3 Screens

Tensioned screens, normally made of metal wires interwoven to form square or rectangular meshes, are normally placed in the settling duct for the reduction of turbulence levels of the incoming flow. They break up the large-scale turbulent eddies into a number of small-scale eddies that subsequently decay [3].

Screens are normally characterized by two parameters [3]:  $K$  and  $\beta$  which represent the pressure drop coefficient and the screen open-area ratio respectively. The authors Mehta *et al.* [3] stated that low  $\beta$  ( $\beta < 0.57$ ) screens produce instabilities in the flow.

Further, it was found that placing multiple screens in the settling duct with varying porosity, with the coarsest screen being closest to the incoming flow and the finest screen being closest to the test section, has been shown to provide lower values of test section turbulence [6].

According to these design guidelines, it was decided to install three tensioned square metallic screens in the settling chamber of the model autoclave downstream of the installed honeycomb (Figure A.3): one coarse followed by two fines. Table A.2 gathers the characteristics of the selected screens. A schematic of a mesh cell is shown in Figure A.5.

**Table A.2 Characteristics of the installed screens**

	Quantity	$l$ (mm)	$D$ (mm)	$Q$ (m <sup>3</sup> /h)	Settling duct section (m <sup>2</sup> )	$U_{\infty}$ (m/s)	$\beta$
<b>Coarse screen</b>	1	3.168	0.8	15 286	$1.058 \times 0.833$	4.6	$0.84 > 0.57$
<b>Fine screen</b>	2	0.746	0.18	15 286	$1.058 \times 0.833$	4.6	$0.84 > 0.57$

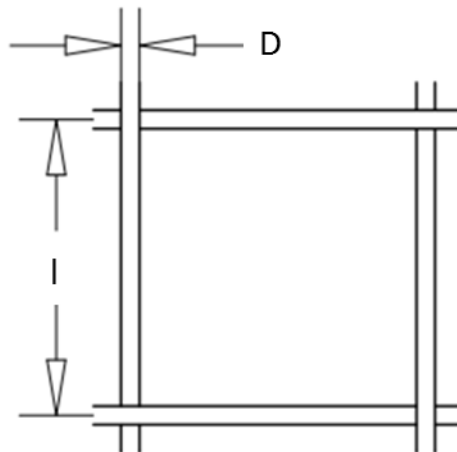


**Figure A.5 Schematic of a mesh cell**



#### **A.2.2.4 General arrangement of the screens and the honeycomb**

According to the authors Mehta *et al.* [3], the usual arrangement consists of installing the honeycomb near the entrance region of the settling duct followed by the screens.

Concerning the spacing between the screens inside the settling duct, it has been found that a screen combination with a spacing equivalent to about 0.2 settling chamber diameters performs successfully. The optimum distance between the last screen and the contraction entry has also been found to be about 0.2 cross-section diameters. The latter is about of 0.93 m calculated based on the diameter equivalent formula ( $D_{equivalent} = 4 \times A / Pe$ ). On the other hand, the honeycomb was installed upstream of the screens as mentioned above and far from the first coarse screen of about 0.2 cross-section diameters. This distance was respected also between the entrance region of the settling duct and the honeycomb.

Therefore, the application of these distance design guidelines results in a settling duct of about 0.93 m in length.

#### **A.2.3 Diffuser**

A diffuser is an expanding duct installed generally downstream of the test section in a wind tunnel. The primary objective of a diffuser is to recover fluid static pressure from a fluid stream while reducing the high-speed flow from the test section [6].

As with contraction sections, the flow through a diffuser depends on its geometry parameters defined by the area ratio between the outlet and the inlet of the diffuser, the diffuser angle ( $2\theta$ ), the wall contour and the diffuser cross-sectional shapes [3].

Given this fact, several authors [8–10] have investigated the effect of the diffuser geometry on the flow regimes. These effects are illustrated in the graph shown in Figure A.6(b).

The diffuser should be sized in a manner to obtain a “No appreciable stall” flow regime (Figure A.6). The latter signifies that the flow follows the diffuser contours and that the flow is steady with no existence of significant separation regions.

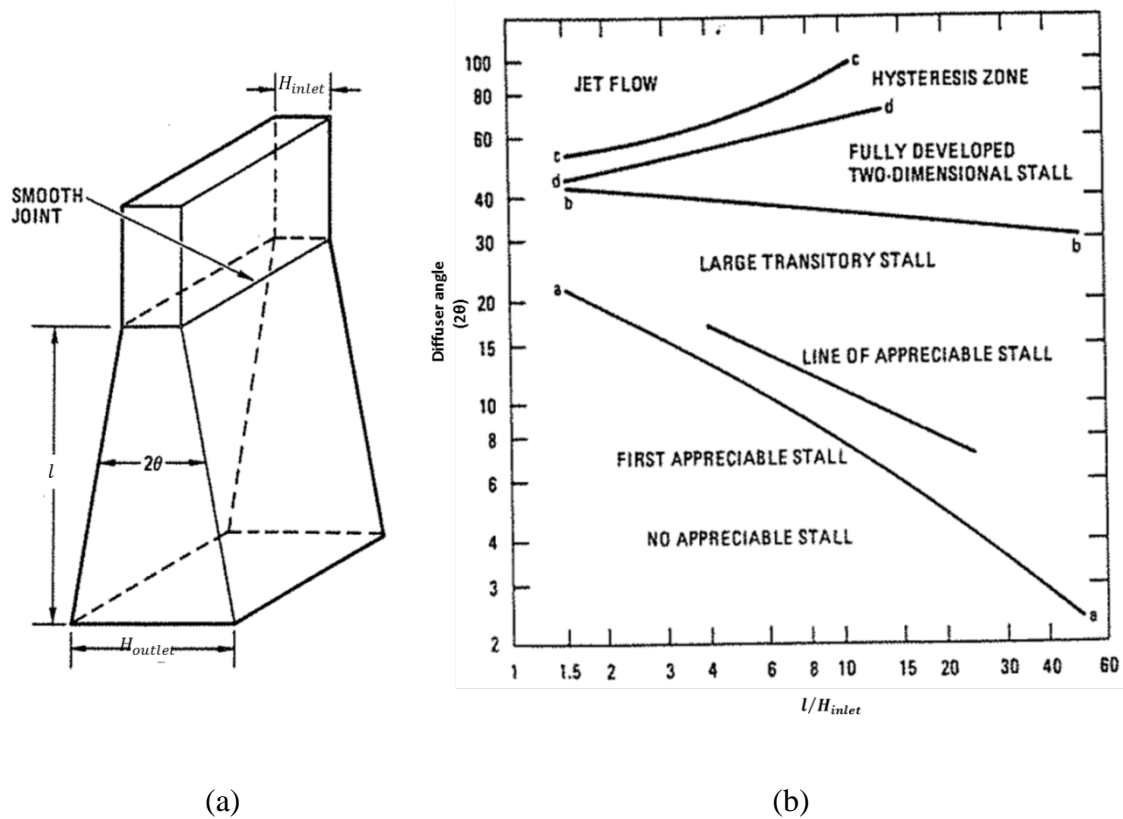


Figure A.6 (a) Schematic of a rectangular diffuser. (b) Flow regimes [11]

Therefore, the geometrical parameters of the rectangular section diffuser installed in the model autoclave were selected carefully in order to obtain a “No appreciable stall” flow regime. Table A.3 gathers these geometrical parameters.

Table A.3 Geometrical parameters of the diffuser

	Inlet section		$2\theta$ (°)	$l$ (m)	Outlet section		$l / H_{inlet}$
	$H_{inlet}$ (m)	$L_{inlet}$ (m)			$H_{outlet}$ (m)	$L_{outlet}$ (m)	
<b>Diffuser</b>	0.4	0.315	6	2	0.56	0.56	5

The inlet section of the diffuser is dictated by the working section. On other hand, the diffuser length ( $l$ ) was selected to be 2 m taking into consideration facility size constraints.  $2\theta$  was selected to be  $6^\circ$  as the diffuser angle ( $2\theta$ ) should be between  $5^\circ$ , for best flow steadiness, and  $10^\circ$  for best pressure recovery [3].

## A.2.4 Optional components

### A.2.4.1 Wide angle diffuser

The wide angle diffuser is normally installed upstream of the settling chamber in a wind tunnel.

As with contraction and diffuser sections, the flow through a wide angle diffuser depends on its geometry parameters. The four most important parameters are the area ratio ( $A_{outlet}/A_{inlet}$ ), the diffuser angle ( $2\theta$ ),  $N$  and  $K$  [11]. Where  $N$  and  $K$  are the number of screens within the diffuser and the associated pressure drop coefficient respectively.

Charts have been plotted for these relevant parameters in order to determine successful design rules, i.e. no separation and uniform outlet flow with an acceptable turbulence level.

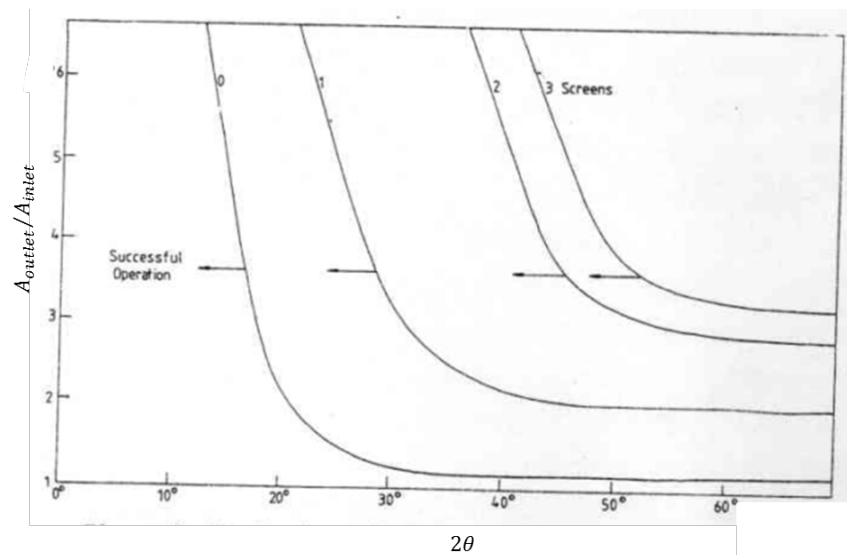


Figure A.7 Design boundaries for wide-angle diffusers [3]

For the model autoclave, it was decided not to install screens within the wide – angle diffuser for minimizing the pressure drops in the closed-circuit tunnel. Based on this fact, and taking into account the charts presented in Figure A.7,  $2\theta$  and the area ratio were selected in a manner to be in the “Successful operation” of the flow (Table A.4).

**Table A.4 Geometrical parameters of the wide angle diffuser**

	Inlet section		$2\theta$ (°)	$l$ (m)	Outlet section		$A_{outlet} / A_{inlet}$
	$H_{inlet}$ (m)	$L_{inlet}$ (m)			$H_{outlet}$ (m)	$L_{outlet}$ (m)	
<b>Wide angle Diffuser</b>	0.56	0.56	12	0.5	1.058	0.833	2.8

It should be noticed that the used wide-angle diffuser have a rectangular cross-sections for ease of construction. This cross-sections shape was dictated also by the cross-sections shape of the used settling chamber downstream.

#### **A.2.4.2 Turning sections**

In closed-circuit tunnels where the ducts are joined together by 90° bends (elbows), flow separation will occur, leading to significant pressure drop, flow unsteadiness, and noise generation.

Given these facts, turning vanes are installed in corner sections to mitigate these adverse effects. Collar [12] and Salter [13] developed some early designs for turning vanes. Gelder *et al.* [14] developed turning vanes with a low loss factor. The chord, thickness-to-chord ratio, shape, and the number of turning vanes determine the efficiency, as defined by flow losses, of the turning section.

However, it was found that the installation of such turning vanes in the turning sections of the model autoclave present some technical difficulties. On the other hand, it was found that using radius elbows without turning vanes can still highly efficient, in terms of pressure drops and flow steadiness, and is much easier and cheaper to fabricate and to install. At the same time, spatial constraints must also be considered, as a smaller turning radius will decrease efficiency rapidly. Thus, it was found that minimum recommended turning radius “ $R$ ” without turning vanes is  $R=L/2$ .  $L$  represents the elbow width.

In fact, a radius elbow without turning vanes and having a radius/width ( $R/L$ ) ratio of 1 is only 28% less efficient than the elbow with turning vanes. If the radius is increased to  $R/L=1.5$ , it will only be 12% less efficient, and if it is increased to  $R/L=2$ , it will have the same efficiency as the same size elbow with turning vanes.

These elbow design guidelines were taken into account during the design work of the model autoclave. It results then in a radius and rectangular cross-section elbow of width 0.56 m and radius 1.1 m. Four radius elbows were installed to complete the closed circuit of the model autoclave.

### A.2.5 Cooling heat exchanger

As explained in *chapter 2*, the convective heat transfer study, in the steady state regime, around a mold within the working section is carried out by heating the mold while the air flows at low controlled temperature.

Thus, the obtaining of a low controlled air temperature involves the installation of a cooling heat exchanger. The latter allows the evacuation of the heat load generated by the heated mold as well as by the drive system (fan) motor.

The sizing work of the heat exchanger requires first the determination of its nominal power. The latter includes, as mentioned previously, the power of the fan motor and the heating power injected in the mold. The nominal power of the drive system (fan) was estimated to be approximately 3 500 W according to the technical specifications of the existing commercial fans, for a nominal flow of about 15 286 m<sup>3</sup>/h. On the other hand, the maximum heating power planned to be injected in the mold is 2 000 W. This heating power will serve to heat the mold, thus the convective heat flux transferred to the circulating air is less than 2 000 W.

Based on these estimations, the nominal power of the cooling heat exchanger should be about 5 500 W. The selected cooling heat exchanger is an air-water heat exchanger and the cooling water is provided by the water circuit of the laboratory. Its temperature at the inlet of the heat exchanger is in the range of 15 – 20°C with a volume flow rate of about 1 m<sup>3</sup>/h. The nominal volume flow rate of the air is 15 286 m<sup>3</sup>/h defined previously. The geometrical dimensions of the heat exchanger were fixed at 1.058 m and 0.833 m in height and width respectively in order to be fitted in the model autoclave. These different elements have been transmitted to the supplier in order to obtain the final characteristics of the air-water cooling heat exchanger.

The proposed heat exchanger is a ribbed pipe heat exchanger that contains three vertical rows of fourteen copper tubes of 16.45 mm in diameter. Further, a PID regulator was installed and connected to a regulating valve in order to regulate the inlet volume flow rate of the water according to the desired air temperature in the closed circuit.

### A.2.6 Drive system (fan)

As in an actual real autoclave, a drive system or a fan must be installed in the model autoclave to ensure the air flow.

The work sizing of the fan was based on two essential parameters: the nominal volume flow rate ( $Q$ ) and the total pressure drop ( $\Delta P_t$ ). The nominal volume flow rate is 15 300 m<sup>3</sup>/h as showed previously. On the other hand, the total pressure drop in the

whole closed-circuit of the model autoclave was determined according to the following equation:

$$\Delta P_t = \sum_{i=1}^N \Delta P_i$$

**Equation (A.4)**

$$\Delta P_i = \frac{1}{2} K_i \rho U_{\infty}^2$$

$\Delta P_i$  represents the pressure drop due to each component of the model autoclave.  $N$  represents the total number of these components. The latter are showed in Figure A.8. The formula depends on the velocity within the cross-sections of each component as well as on its pressure drop coefficient ( $K_i$ ). The latter was calculated by using analytical formulas [15] based on the geometric dimensions and shapes of a component.

The total pressure drop in the whole model autoclave was found to be about 600 Pa for the nominal volume flow rate. Given these specifications, it was found to use an axial fan, instead of a radial one, as it is less power consuming and it provides a smaller size. Therefore, the selected fan, proposed by the constructor, is an axial fan with a diameter of 0.63 m and with a nominal power of about 3 500 W. Circular ducts, of the same diameter, were installed downstream of the fan (Figure A.8). In addition, the fan was equipped with a variable frequency drive in order to control and to vary the flow modes within the working section of the model autoclave.

A flow meter was installed in the circular duct in order to estimate the volume flow rate ( $Q$ ) of the air flow.

### **A.3 Presentation of the designed model autoclave**

The application of the different followed steps showed above, such as the application of the similarity laws for the design of the working section and the application of the various design guidelines for the sizing of the main components, results in a model autoclave represented by the CAD drawing in Figure A.8. A summary of the characteristics of the main components that constitute the designed model autoclave is presented in Table A.5. It can be clearly seen that the obtained model autoclave represents in fact a close-wind tunnel.

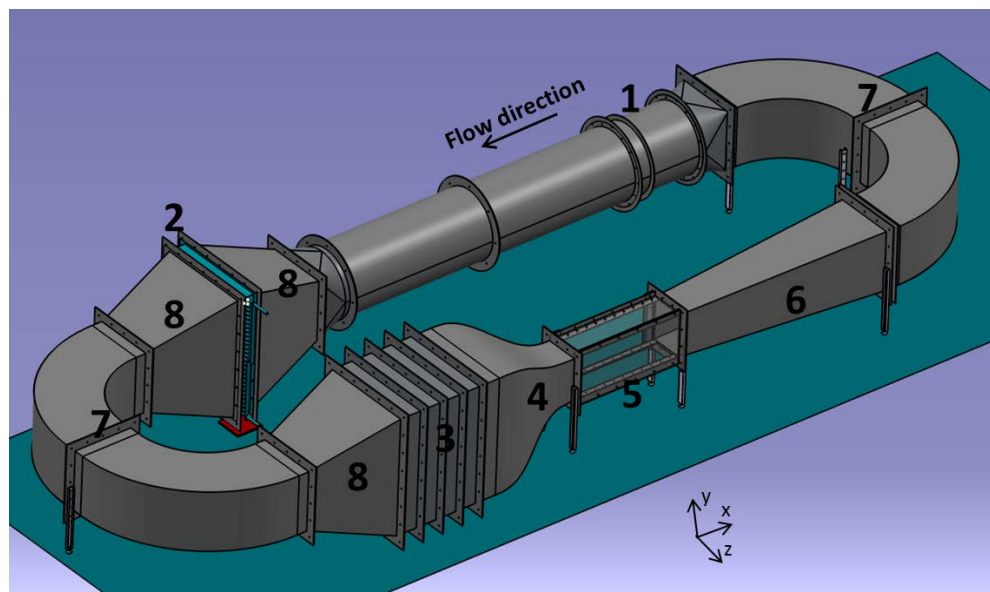


**Figure A.8 CAD schema of the designed model autoclave**

**Table A.5 Characteristics of the main components of the model autoclave**

Component	Noun	Characteristics
1	Axial fan	$D = 0.63 \text{ m}$
		Nominal flow ( $Q$ ): $15\,300 \text{ m}^3/\text{h}$
		Nominal Pressure drop ( $\Delta P$ ): $600 \text{ Pa}$
2	Heat exchanger	Nominal power: $5\,500 \text{ W}$
		$L \times H = 0.833 \times 1.058 \text{ m}^2$
3	Settling chamber	$l \times L \times H = 0.93 \times 0.833 \times 1.058 \text{ m}^2$
4	Contraction	Inlet section: $L \times H = 0.833 \times 1.058 \text{ m}^2$
		Outlet section: $L \times H = 0.315 \times 0.4 \text{ m}^2$
		$l = 0.94 \text{ m}$
5	Working section	$l \times L \times H = 1.07 \times 0.315 \times 0.4 \text{ m}^2$
6	Diffuser	Inlet section: $L \times H = 0.315 \times 0.4 \text{ m}^2$
		Outlet section: $L \times H = 0.56 \times 0.56 \text{ m}^2$
		$l = 2 \text{ m}$
7	Radius elbow	Square section: $L \times H = 0.56 \times 0.56 \text{ m}^2$
		$R = 1.1 \text{ m}$
8	Wide-angle diffuser	Inlet section: $L \times H = 0.56 \times 0.56 \text{ m}^2$
		Outlet section: $L \times H = 0.833 \times 1.058 \text{ m}^2$
		$l = 0.5 \text{ m}$

After obtaining and approving the final design of the model autoclave, the latter was manufactured and then installed. Figure A.9 shows the manufactured model autoclave which is in accordance with the CAD drawing showed above. Figure A.10 shows the working section of the model autoclave. The different components and ducts used in the model autoclave were fabricated of galvanized steel. On the other hand, the walls of the working section were made from acrylic glass (Plexiglas) in order to be transparent for the use of the PIV technique.

Also, Figure A.10 shows the installation of a model mold within the working section, for carrying out experimental measurements, and the mounting of the PIV technique.



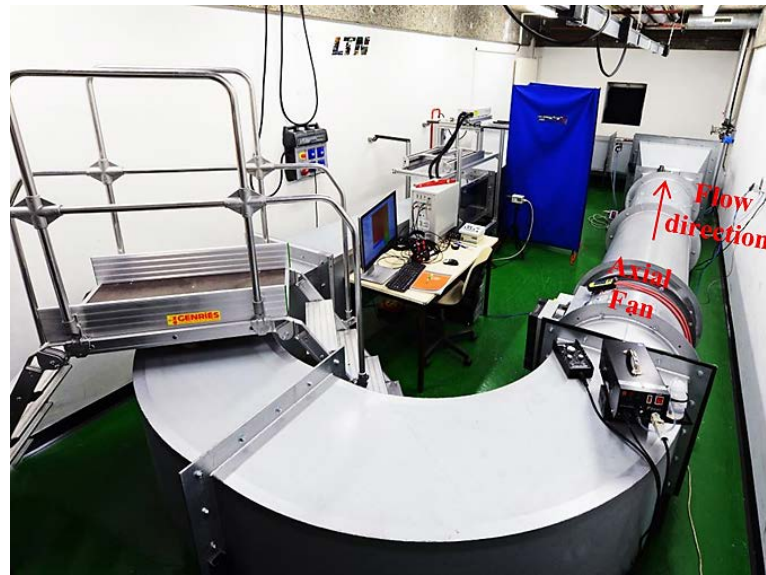


Figure A.9 Picture of the manufactured model autoclave

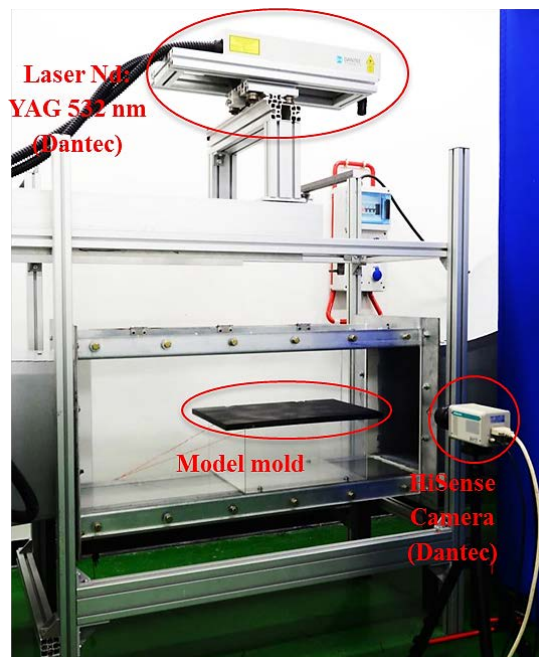


Figure A.10 Picture of the working section of the model autoclave

## List of references

- [1] G.I. Derbunivich, A.S. Zemskaya, E.U. Repik, Y.. Sosedko, Effect of flow contraction on the level of turbulence, in: *Izv. Akad. Nauk SSSR Mekh. Zhidk.*, Gaza, 1987: pp. 146–152.
- [2] J. H. Bell, R. D. Mehta, *Contraction design for small low-speed wind tunnels*, Stanford, 1988.
- [3] R.D. Mehta, P. Bradshaw, Design rules for small low speed wind tunnels, *Aeronaut. J.* 83 (1979) 443–453.
- [4] T. Morel, Comprehensive design of axisymmetric wind tunnel contractions, *J. Fluids Eng.* 97 (1975) 225–233.
- [5] Y. Su, Flow analysis & design of three-dimensional wind tunnel contractions, *AIAA J.* 29 (1992) 1912–1919.
- [6] L. Cattafesta, C. Bahr, J. Mathew, Fundamentals of wind-tunnel design, *Encycl. Aerosp. Eng.* (2010) 1–10. doi:10.1002/9780470686652.eae532.
- [7] J.B. Barlow, W.H. Rae, A. Pope, *Low-Speed Wind Tunnel Testing*, third ed., John Wiley & Sons, New York, 1999.
- [8] L.R. Reneau, J.P. Johnston, S.J. Kline, Performance and design of straight, two-dimensional diffusers, *J. Basic Eng.* 89 (1967) 141–150.
- [9] J.J. Carlson, J.P. Johnston, C.J. Sagi, Effects of wall shape on flow regimes and performance in straight, two-dimensional diffusers, *J. Basic Eng.* 89 (1967) 151–159.
- [10] C.R. Smith, S.J. Kline, An experimental investigation of the transitory stall regime in two-dimensional diffusers, *J. Fluids Eng.* 96 (1974) 11–15.
- [11] R.D. Blevins, Chapter 7: nozzles, diffusers, and venturis, in: N.Y.V.N. Reinhold (Ed.), *Appl. Fluid Dyn. Handb.*, New York, 1984: pp. 144–163.
- [12] A.R. Collar, *Some experiments with cascades of aerofoils*, 1937.
- [13] C. Salter, *Experiments on thin turning vanes*, 1946.
- [14] T.F. Gelder, R.D. Moore, J.M. Sanz, E.R. McFarland, Wind tunnel turning vanes of modern design, in: *24th Aerosp. Sci. Meet.*, 1986.
- [15] I.E. Idel’cik, *Memento des Pertes de Charge: coefficients de pertes de charge singulières et de pertes de charge par forttement*, First edi, Paris, 1968.

## **Appendix B**

### *Sensitivity of mesh and turbulence model*



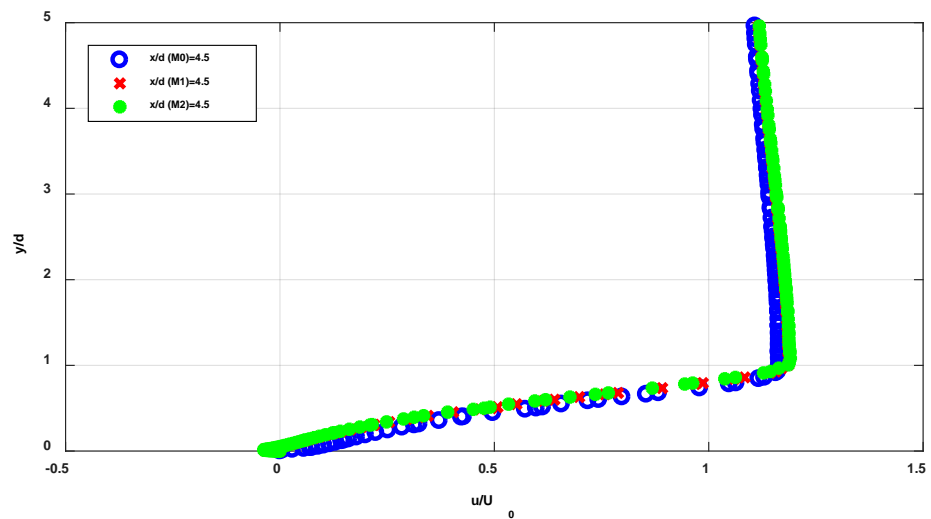
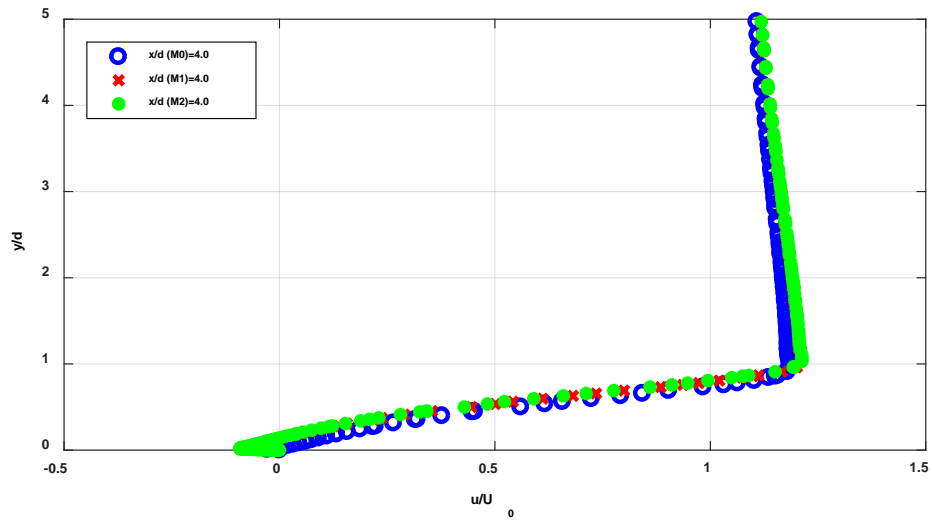
## Table of contents

<b><i>Appendix B</i></b>	<b><i>Sensitivity of mesh and turbulence model.....</i></b>	<b><i>239</i></b>
<b>B.1.</b>	<b>MESH EFFECT ON VELOCITY FIELD .....</b>	<b>243</b>
<b>B.2.</b>	<b>EFFECT OF TURBULENCE MODEL ON VELOCITY FIELD.....</b>	<b>245</b>



### B.1. Mesh effect on velocity field

The following figures show the evolution of the longitudinal normalized velocity profile ( $u/U_0$ ) in the boundary layer for several abscissa ( $x/d$ ) for three different meshes (Table B1).



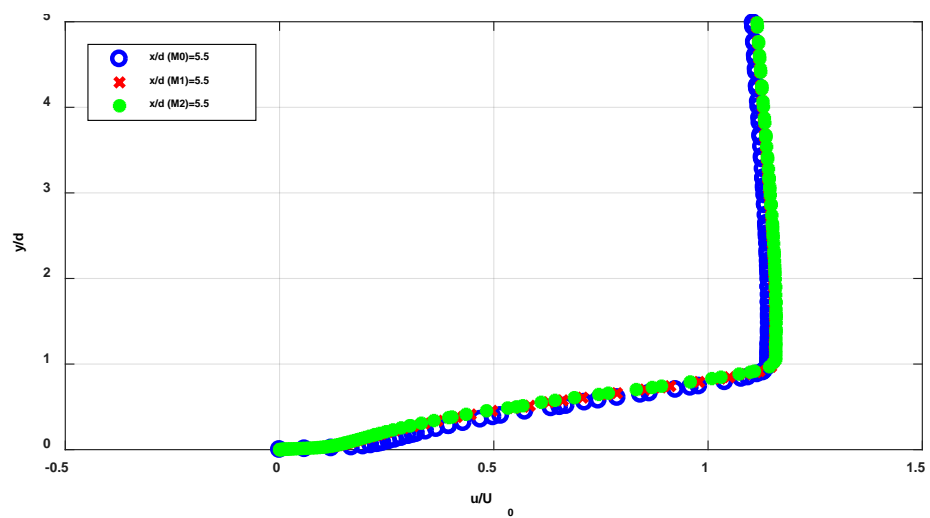
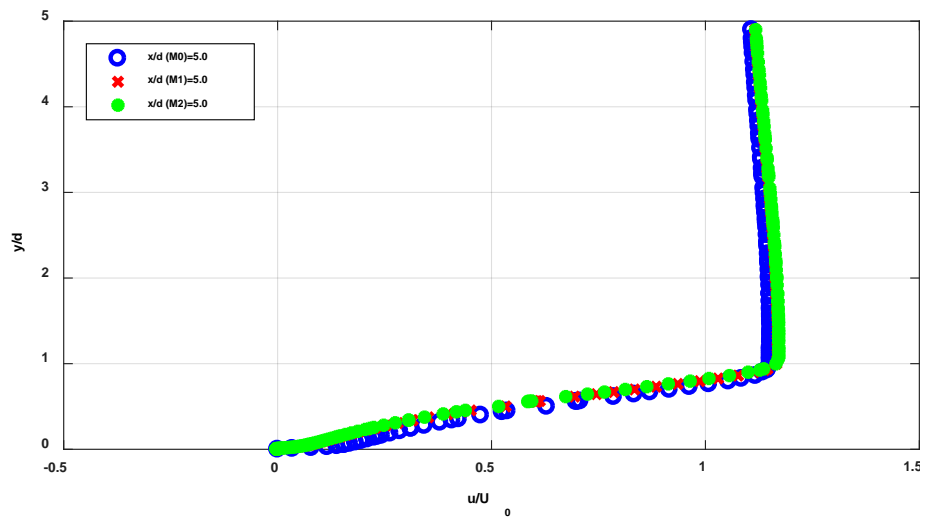


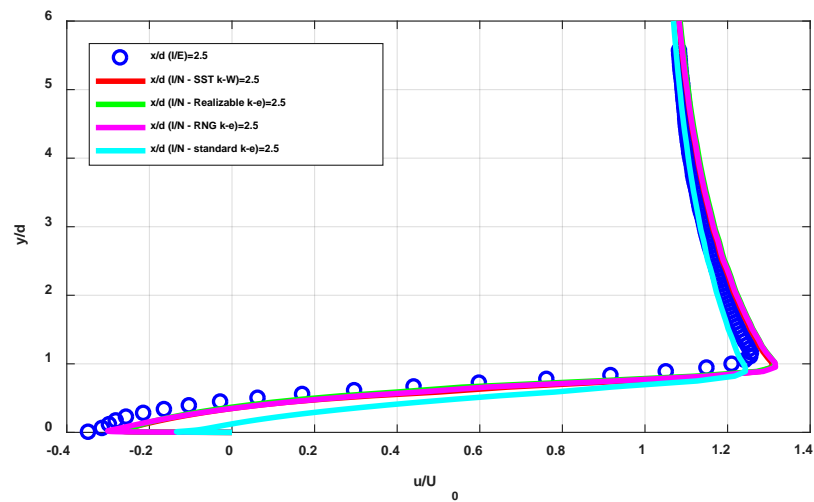
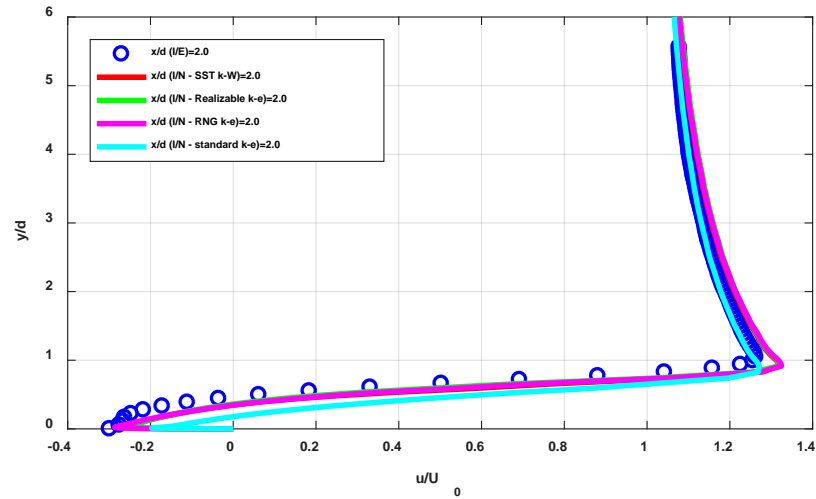
Table B.1 Mesh characteristics

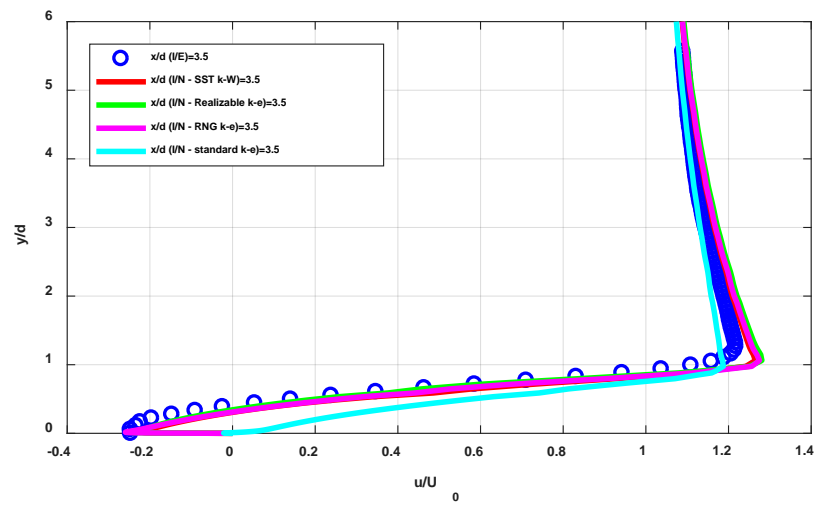
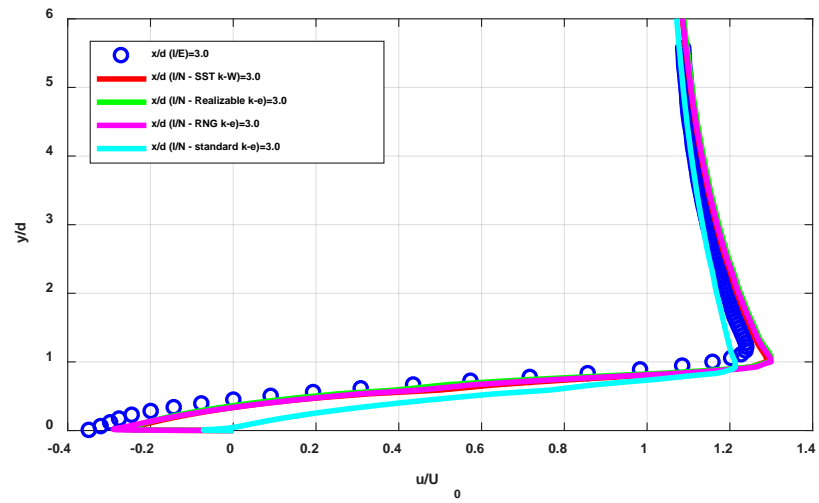
Mesh number	Number of nodes
<b>M0</b>	497 507
<b>M1</b>	600 614
<b>M2</b>	718 831



## ***B.2. Effect of turbulence model on velocity field***

The following figures show the evolution of the longitudinal normalized velocity profile ( $u/U_0$ ) in the boundary layer for several abscissa ( $x/d$ ) for different turbulence models.







**Titre :** Analyse des transferts convectifs autour de moules simples dans un autoclave

**Mots clés :** Écoulement turbulent, Convection, Autoclave modèle, Plaque rectangulaire épaisse, Simulation numérique, Optimisation.

**Résumé :** Ces dernières années, l'utilisation de matériaux composites légers et à hautes performances a considérablement augmenté dans de nombreux secteurs industriels. Toutefois, il est évident que le contrôle du champ de température et notamment la minimisation des gradients thermique et de transformation est indispensable à la bonne qualité des pièces. Parmi les différentes méthodes de fabrication existantes, la cuisson des pièces composites par autoclave est largement répandue notamment dans la filière aéronautique. Cette technique permet la réalisation de pièces composites techniques et de grande qualité. Au sein de l'autoclave, les transferts de chaleur sont majoritairement convectifs entre l'ensemble pièce composite plus moule et son environnement. Il s'avère donc nécessaire de connaître (voire d'optimiser) la distribution du coefficient d'échange convectif autour de ces moules. Pour apporter des éléments de réponse à cette problématique, nous présentons dans nos travaux une nouvelle approche consistant à effectuer des mesures expérimentales dans un « autoclave modèle » à échelle réduite, représentatif d'un autoclave industriel. Cet autoclave modèle a été conçu et fabriqué en se basant sur les lois de similitude. L'un des avantages de notre configuration est évidemment la facilité d'utilisation des instruments de mesure non intrusifs et fiables tels que la

PIV (Particle Image Velocimetry) pour la mesure du champ de vitesse, et la caméra infrarouge pour la détermination de la distribution des coefficients d'échange autour de moules simples et représentatifs. En parallèle, des modèles numériques qui représentent les configurations d'études expérimentales ont été construits avec le code CFD Ansys Fluent 16®. Les principaux résultats obtenus à partir de ce travail ont montré une distribution non uniforme des coefficients d'échange convectifs autour des moules. Cette hétérogénéité peut conduire à la présence de gradients de température importants au sein des pièces composites fabriquées qui peuvent affecter leur qualité finale. De plus, ces résultats indiquent que le chargement simultané de plusieurs pièces peut engendrer des degrés de cuisson différents entre elles. Cela peut contribuer à la production de pièces composites de qualités différentes. Une étude d'optimisation a conduit à proposer une conception géométrique optimale des supports de moules qui permet à la fois d'intensifier les coefficients d'échange convectifs et de minimiser les hétérogénéités. La comparaison entre les résultats numériques, aérodynamiques et thermiques, et ceux issus des mesures expérimentales a montré un bon accord permettant de valider le code de calcul.

**Title :** Analysis of convective transfer around simple molds inside a model autoclave

**Keywords :** Turbulent flow field, Convective heat transfer, Model autoclave, Flat blunt plate, Computational fluid dynamic, Optimization

**Abstract :** In recent years, the use of high performance and lightweight composites materials has increased considerably in many industrial sectors. However, the temperature distribution within composite parts produced using the current manufacturing methods plays a key role in determining the parts quality at the end of the process. Among the existing various fabrication methods, the autoclave molding is considered as one of the best methods to manufacture advanced and high quality composite parts. During autoclave molding, heat transfer between the composite parts and the surroundings is strongly coupled with the flow field around their molds and modeled through the convective heat transfer coefficient. The purpose of this study is therefore to develop a new approach for performing experimental measurements in order to analyze the local velocity field and convective heat transfer coefficient distribution around simple and representative industrial molds. The implemented experimental approach is based essentially on the use of a reduced scale autoclave designed thanks to similarity laws, and instrumented by means of non-intrusive measuring instruments such as Particle Image

Velocimetry (PIV) and infrared imaging. Furthermore, Computational Fluid Dynamics calculations of the flow field and convective heat transfer were performed using ANSYS Fluent 16.0®. This local investigation has revealed a non-uniform distribution of the convective heat transfer coefficient around the molds. This heterogeneity can directly impact the parts quality during an autoclave process in view of high temperature gradient. Furthermore, the study has shown the presence of shadowing effects during the process of several molds together which can lead to production of composite pieces with different qualities. An optimization study has permitted to propose an optimal geometric design of the supports of the molds that allows the intensification of the convective heat transfer coefficients and the reduction of the heterogeneities. The experimental and the numerical results were in good agreement, leading then to the validation of the performed numerical simulations.